

UNIVERSITÀ
DI PAVIA

UNIVERSITY OF PAVIA

FACULTY OF ENGINEERING

DEPARTMENT OF ELECTRICAL, COMPUTER AND BIOMEDICAL
ENGINEERING

Ph.D. DEGREE IN ELECTRONIC ENGINEERING

Ph.D. THESIS

**Analysis of multi-temporal spaceborne Earth observation data
to map selected land cover classes**

Ph.D. Candidate: **David Marzi**

Supervisor: Prof. Paolo Ettore Gamba

XXXV cycle - A.Y. 2021/2022

Abstract

Nowadays, the need for reliable, timely, high-resolution land cover maps is more than urgent if large-scale environmental problems are to be tackled effectively. Many different contexts would in fact benefit from such products, such as climate change, desertification, arctic greening, deforestation, urbanization, soil erosion, forest monitoring, conservation of biodiversity, urban area management, water resources management, agriculture, food security and many others. Due to the fact that the involved variables tend to change very rapidly in time and space, the availability of frequent and good quality global land cover products raises great interest.

Several regional/global thematic and land cover maps have been delivered and other are expected, but they often do not meet the specific requirements of various applications; this is mainly due to the fact that all the existing products have been generated from different satellite sensors (optical, radar or both), different sampling strategies, different types of mapped land cover types, different validation protocols, etc. Moreover, the spatial and/or temporal resolution of these products is often insufficient for some applications.

In this thesis work, we investigated how to leverage multitemporal optical and SAR data to characterize a very small set of classes rather than a full range of land cover types. Our work focuses on vegetation (including tree species, grasslands, shrublands and others), water bodies (including lakes, seas, rivers and others) and organic croplands (specifically, organic farming practices).

Regarding vegetation, the technical literature offers numerous well-established methodologies aimed at mapping vegetated land covers. On the contrary, approaches that use SAR sensors as the main source of data are definitely more scarce. For this reason, part of this thesis work will be devoted to analyze the potential of multitemporal SAR data to characterize several types of natural vegetation.

Regarding mapping of water bodies, the scientific literature provides several solutions based on optical and SAR data. However, almost all the analyzed methodologies have some limitations, mainly related to lack of automatism, impossibility to use the proposed method in other regions of interest, relatively low spatial resolution and others. Given the climate change community's need for timely information on the status of water bodies at the global level regardless of weather conditions, in this thesis a methodology aimed

at mapping water bodies using sequences of SAR data, that is able to overcome the most severe limitations of the existing methodologies, is proposed.

Finally, to characterize organic farmland, several aspects must be detected and monitored, including weed-killer operations, fertilization activities and tillage techniques. To do so, both multitemporal optical and SAR data are exploited to build small detection blocks, that will be part of a more complex organic farming monitoring system aimed at improving transparency and traceability within the organic food supply chain.

In general, results showed that SAR time series can be successfully employed to classify these land cover types. For instance, the proposed vegetation land cover mapping methodology achieved, on average, 71% overall accuracy with a standard deviation of about $\sigma = 14.2\%$ considering four very diverse test sites; the standard deviation justifies the obtained relatively low result, mainly caused to the very complex test site located in Siberia, without whom the accuracy pushes towards values near 80% and much lower standard deviation values ($\sigma = 5\%$). Still, the developed methodology showed great potential in characterizing vegetated areas.

Regarding the water bodies monitoring and mapping application developed in this thesis work, it was able to achieve, on average, 94.6% overall accuracy and standard deviation $\sigma = 10^{-3}\%$ using reliable ground truth data and considering the whole Lombardy region (North Italy) as test site. An additional independent validation process was carried out by an expert validation team from the European Space Agency (ESA), within the framework of the WorldWater project. Based on their validation, the proposed methodology achieved, on average, 93.4% overall accuracy over five very diverse and complex test regions. The methodology also showed great potential in monitoring temporary/seasonal water bodies.

Finally, regarding mapping of organic farming parcels, it has been demonstrated that multitemporal SAR data can also be used to detect some operations that are carried out within the crop field, like for example the type of tillage, that help characterize organic farmland as opposed to traditional farmland. Other farming practices that provide clues for organic vs. non-organic discrimination, such as weed-killing operations and fertilization, were instead better characterized using multitemporal optical data. The obtained results were analyzed qualitatively and were considered promising to monitor organic crop fields for transparency and traceability purposes within the whole supply chain and organic certification process.

Sommario

Oggi, per poter affrontare efficacemente i problemi ambientali su larga scala, la necessità di disporre di mappe di copertura del suolo affidabili e ad alta risoluzione spaziale e temporale è più che mai urgente. Infatti, numerosi contesti potrebbero trarre beneficio da tali prodotti come, ad esempio, il cambiamento climatico, la desertificazione, l'inverdimento dell'artico, la deforestazione, l'urbanizzazione, l'erosione del suolo, il monitoraggio delle foreste, la conservazione della biodiversità, la gestione delle aree urbane, la gestione delle risorse idriche, l'agricoltura, la sicurezza alimentare e molti altri. Siccome le variabili di interesse tendono a cambiare molto rapidamente nel tempo e nello spazio, la disponibilità di mappe di copertura del suolo frequenti e di buona qualità suscita un grande interesse.

Negli ultimi anni sono state prodotte diverse mappe tematiche e di copertura del suolo su scala regionale/globale le quali, tuttavia, spesso non soddisfano i requisiti imposti dalle applicazioni; ciò è dovuto principalmente al fatto che i prodotti esistenti sono stati generati da diversi sensori satellitari (ottici, radar o entrambi), diverse strategie di campionamento, diverse legende, diversi protocolli di validazione, ecc. Inoltre, la risoluzione spaziale e/o temporale di tali prodotti è spesso insufficiente per diverse applicazioni.

In questo lavoro di tesi è stato studiato come sfruttare dati multitemporali di tipo ottico e SAR (Synthetic Aperture Radar) per caratterizzare un insieme molto ristretto di classi, piuttosto che un'ampia gamma di tipi di copertura del suolo. Il lavoro presentato si concentra sulla vegetazione (tra cui specie arboree, praterie, arbusti ed altri), corpi idrici (tra cui laghi, mari, fiumi ed altri) e colture biologiche (in particolare, pratiche di agricoltura biologica).

Per quanto riguarda la vegetazione, la letteratura scientifica offre numerose metodologie consolidate, finalizzate alla mappatura delle coperture vegetative. Al contrario, gli approcci che sfruttano i sensori SAR come principale fonte di dati sono decisamente più rari. Per questo motivo, parte di questa tesi è dedicata all'analisi della potenzialità dei dati SAR multitemporali nel caratterizzare diversi tipi di vegetazione naturale.

Per quanto riguarda la mappatura dei corpi idrici, la letteratura tecnica fornisce diverse soluzioni basate sia su dati ottici che SAR. Tuttavia, la maggioranza delle metodologie analizzate presentano alcune limitazioni legate principalmente alla mancanza di automatismo degli algoritmi, l'impossibilità di utilizzare il modello in altre regioni di interesse,

alla risoluzione spaziale relativamente bassa ed altri. Dal momento che la comunità sul cambiamento climatico necessita di informazioni tempestive relative allo stato dei corpi idrici a livello non solo locale/regionale ma anche globale, e che sia indipendente dalle condizioni meteorologiche delle diverse aree del mondo, in questa tesi si propone una metodologia volta a mappare i corpi idrici sfruttando sequenze temporali di dati SAR, che sia in grado di superare le limitazioni più gravi presenti negli approcci esistenti.

Infine, per quanto concerne la caratterizzazione dei terreni agricoli biologici, occorre rilevare e monitorare diversi aspetti, tra cui le operazioni di diserbo, le attività di fertilizzazione e le tecniche di lavorazione del terreno. A tal fine, sia i dati ottici multitemporali che i dati SAR vengono sfruttati per costruire piccoli blocchi che faranno parte di un sistema di monitoraggio dell'agricoltura biologica più complesso, volto a migliorare la trasparenza e la tracciabilità all'interno della catena di approvvigionamento alimentare biologica.

In generale, i risultati hanno dimostrato che le sequenze temporali di dati SAR possono essere impiegate con successo nella classificazione dei diversi tipi di copertura del suolo di cui sopra. Ad esempio, la metodologia sviluppata per la mappatura della vegetazione ha raggiunto, in media, il 71% di accuratezza complessiva, con una deviazione standard di circa $\sigma = 14,2\%$ considerando quattro siti di prova aventi caratteristiche climatiche e geomorfologiche molto diverse tra loro; la deviazione standard giustifica il risultato relativamente basso, ottenuto principalmente a causa dell'area di test situata in Siberia, senza la quale l'accuratezza si spinge verso valori prossimi all'80%, con valori di deviazione standard decisamente inferiori ($\sigma = 5\%$). Tuttavia, la metodologia proposta ha mostrato un notevole potenziale nella caratterizzazione delle aree vegetative.

Per quanto riguarda l'applicazione di monitoraggio e mappatura dei corpi idrici sviluppata in questo lavoro di tesi, il modello proposto è stato in grado di ottenere, in media, il 94.6% di accuratezza complessiva e deviazione standard pari a $\sigma = 10^{-3}\%$, utilizzando dati affidabili di realtà a terra e considerando l'intera regione della Lombardia (nord Italia) come sito di test. Un secondo processo di validazione completamente indipendente è stato effettuato da un gruppo composto di esperti dell'Agenzia Spaziale Europea (ESA) nell'ambito del progetto "WorldWater". Sulla base della loro validazione, la metodologia sviluppata in questa tesi ha raggiunto, in media, il 93.4% di accuratezza complessiva, considerando cinque regioni del mondo estremamente diverse. L'algoritmo ha inoltre mostrato un notevole potenziale nel monitoraggio dei corpi idrici temporanei e stagionali.

Infine, per quanto riguarda la mappatura delle coltivazioni biologiche, è stato dimostrato che i dati SAR multitemporali possono essere utilizzati anche per rilevare alcune operazioni agricole effettuate all'interno del campo di coltura, come ad esempio il tipo di lavorazione del terreno impiegato, che contribuiscono a caratterizzare i terreni agricoli biologici rispetto a quelli tradizionali. Altre pratiche agronomiche che forniscono indizi per la discriminazione biologica vs. non biologica come le operazioni di diserbo e la fertilizzazione, sono state invece caratterizzate meglio utilizzando dati ottici multitemporali. I risultati ottenuti sono stati analizzati qualitativamente e sono stati considerati promettenti per lo sviluppo di sistemi di telerilevamento volti al monitoraggio dei campi coltivati a biologico, ai fini di una maggiore trasparenza e tracciabilità all'interno dell'intera catena di fornitura e del processo di certificazione biologica.

Acknowledgements

Apart from academics, very few people are aware of the astonishing efforts needed to get a Ph.D. in engineering. People think a Ph.D. student is a person that simply spends his time studying, and they usually believe that it is not comparable to a “normal” job. Well... they are right! Indeed, getting a Ph.D. and becoming a Doctor **it’s much harder**.

The life of a Ph.D. student is made of laboratory, reading, writing, analysis, teaching, “that’s broken”, planning, worrying, more reading, more worrying, “damn (to be polite), that didn’t work”, crying, deciding to quit, deciding not to quit, fear.

However, I did it! I finally got a Ph.D. in Electronic Engineering! On average, around 1% of the world’s population has a doctorate. So it seems like a Ph.D. is pretty rare, and it’s something to be proud of.

My utmost appreciation goes to my Ph.D. supervisor, *Prof. Paolo Gamba*, who believed in me since the very beginning of this path considering me no longer as a student, but as a colleague. Thanks to all the fellows at the Telecommunications, Microwave and Remote Sensing Laboratory of the University of Pavia.

A big thank-you to my beloved girlfriend, *Martina*, who every day kindly stands me despite my very stressful moments and supported me during these tough years. Thanks also to Martina’s Family: *Giovanna, Umberto and Giuseppe*.

Many thanks to my friends *Paolo* and *Gianluca*, old adventuring companions. Even if currently our different life paths prevent us from seeing each other as often as I would like, our true friendship assures us that we can always count on each other, regardless of the physical distance between us (and always remember to defend the ancient!).

Thanks *Javier* for your support (both technical and moral) and your faith in me. Our channel “Pausa caffè” was one of the best projects ever created!

Thanks to my friends *Stefano, Ylenia, Alessandro* and *Matteo*. You were a beacon of comfort for me in one of the most challenging periods of my life. Thank you for believing in me and welcoming me into your lives. May the force of the cast-iron be with you!

Thanks also to *Michela* and *Mariella*, my latin dance teachers and friends, who are always here for me.

I am extremely grateful to my parents, *Walter* and *Sandra* for always being on my side. They always supported my life decisions, since from my elementary school, allowing me to freely follow my dreams, whatever they were. I know you would do everything for me, even in difficult moments. I am also grateful to my brother and sister, *Lorenzo* and *Alice* for the never ending support and love.

Thanks to all my close relatives: *Anna, Marco and Riccardo. Anna and Adolfo. Laura and Nino.*

A particular thought goes to my grandmother *Chrissy* and my grandfather *Cicop*. I'm sure they're looking down from the sky proud of me and what I have become.

This does not mark the end of anything. This is just the end of a path. Exciting things are yet to come. . .

Contents

Abstract	i
Sommario	iii
Acknowledgements	vi
List of Figures	xi
List of Tables	xvii
1 Introduction	1
1.1 Vegetation Land Cover: challenges	1
1.2 Existing Land Cover products	2
1.3 Optical versus microwave remote sensing	5
1.4 The advantages of using multitemporal satellite data	8
1.5 Objectives of this dissertation	8
2 A review of land cover mapping methodologies based on space-borne time series data	11
2.1 Scientific literature review on vegetation land cover mapping	11
2.1.1 Optical-based vegetation land cover methodologies	11
2.1.2 SAR-based vegetation land cover methodologies	15
2.2 Scientific literature review on water body mapping	30
2.2.1 Optical-based water body mapping methodologies	30
2.2.2 SAR-based water body mapping methodologies	33
2.3 Scientific literature review on crop management using satellite data	45
2.3.1 Organic farming practices	45
2.3.2 The organic crops growing panorama	46
2.3.3 Relationship between crop management operations and spaceborne data	48
2.4 Overall considerations on the reviewed state-of-the-art methodologies	55
3 Vegetation land cover monitoring and mapping	57
3.1 The European Space Agency Climate Change Initiative (CCI+) project	57
3.2 Study areas	59
3.3 Sentinel-1 SAR data	64

3.4	Background of the proposed vegetation land cover mapping methodology	68
3.5	SAR data pre-processing	71
3.5.1	Leveraging of aggregated SAR time series	74
3.6	Features extraction	78
3.7	Medium resolution (MR) training set	79
3.7.1	High-resolution training set generation	84
3.8	Results and discussion	86
3.8.1	Comparison with other training set generation procedures	102
3.8.2	Selection of features suitable for land cover mapping	105
4	Inland water body monitoring and mapping	111
4.1	Background of the proposed inland water body mapping methodology	111
4.2	SAR data pre-processing for water detection	115
4.3	Extraction of water-related SAR features	116
4.4	Training the k-means model	118
4.5	Automatic water cluster extraction	120
4.6	Post-processing of the clustering result	122
4.7	Results and discussion	123
4.7.1	Consistency analysis	124
4.8	Validation of the proposed method on the Lombardy region	127
4.9	The ESA WorldWater Round Robin	132
4.9.1	Sample-based validation	136
4.9.2	Object extraction accuracy	137
4.9.3	Results and discussion	139
4.9.4	Takeaway messages	143
4.10	Seasonal water body monitoring and mapping	145
4.10.1	Example of permanent and seasonal water body mapping: the Monte Cotugno reservoir	149
5	Organic farming characterization	153
5.1	The Italian Space Agency (ASI) “MultiBigSARData” project	155
5.2	Detection of weed-killer activities using optical data	157
5.2.1	Space-based monitoring of organic compliance on rice	157
5.2.2	Study area	158
5.2.3	Sentinel-2 multispectral data	161
5.2.4	Results and discussion	162
5.3	Tillage assessment using SAR data	167
5.3.1	Backscattering models	168
5.3.2	Data and case study	173
5.3.2.1	Data	173
5.3.2.2	Case study	175
5.3.3	Preliminary conclusions	176
5.4	Detection of fertilization operations using multispectral data	178
5.4.1	The Joint Research Centre (JRC) “Geospatial Intelligence Against Nitrate Pollution” (GEOINT) project	178
5.4.2	Scientific literature review on manure detection using spaceborne data	179

5.4.2.1	Target Detection in Hyperspectral data	183
5.4.3	Development of a manure detection methodology	186
5.4.3.1	Analysis with Sentinel data	187
5.4.3.2	Analysis with Planet data	189
5.4.3.3	The proposed manure detection methodology	192
5.4.3.4	EOMI analysis	194
5.4.3.5	An additional experiment	200
6	Conclusions	204
6.1	Conclusions	204
6.2	Future work	208
6.3	Published works during the Ph.D. course	209
Bibliography		211

List of Figures

2.1	Charts of the Pearson correlation coefficient computed between SAR backscatter intensity and AGB in case of (a) evergreen species and (b) species. Image source: [92].	18
2.2	Feature extraction based on LRW composite images time series. \tilde{x}^N is the spatial median of the N -th LRW composite, Q_1^N is the spatial 25% percentile of the N -th LRW image, and Q_3^N is the spatial 75% percentile of the N -th LRW image (computed inside a mask).	23
2.3	Generation of image composites from series of images acquired every 12 days.	24
2.4	Feature selection procedure. Image source: [85].	29
2.5	False color composite of average SAR backscatter (red), minimum SAR backscatter (green) and standard deviation (blue) for the Netherlands. Dataset: Envisat ASAR Wide Swath Mode. Image source: [43].	35
2.6	On the left: comparison between single-date Sentinel-1 image (top) and temporal mean composite (bottom). On the right: comparison between single-date (clouded) Sentinel-2 image (top) and temporal median composite (bottom).	38
2.7	(a) RADARSAT-2 HV-polarized image, acquired over the Prairie Pothole Region; (b) variance texture image; (c) water boundaries extracted by thresholding the variance image; (d) segmented image generated using SLIC superpixel algorithm; (e) water bodies and superpixel segmentation; (f) final water bodies after intersection between detected water bodies and water boundaries.	41
2.8	Principle of water seeds placement for the watershed algorithm. They are identified in blue as the topographic minimum of catchment basins.	42
2.9	Temporal dynamic of NDVI for the test sites. The x-axes represent the number of days after GBH treatment. Day 0 is the day of GBH treatment. The y-axes represent the mean value of the NDVI of the appropriate study site.	50
2.10	Interaction between SAR signals and the different growing stages of rice crops.	52
3.1	Overview of all the test regions: Siberia (tile 42WXS), Italy (tiles 32TNR and 32TPP), Amazonia (tile 21KUQ) and Africa (tile 37PCP). The background image is the visualization of the OpenStreetMap basemap.	60
3.2	Detailed overview of the Amazonian tile (21KUQ). The red, dashed line represents the Sentinel-2 tile boundaries, and the background image is the ESRI World Imagery base map.	61

3.3	Detailed overview of the African tile (37PCP). The red, dashed line represents the Sentinel-2 tile boundaries, and the background image is the ESRI World Imagery base map.	62
3.4	Detailed overview of the Siberian tile (42WXS). The red, dashed line represents the Sentinel-2 tile boundaries, and the background image is the ESRI World Imagery base map.	63
3.5	Detailed overview of the Italian tile (32TNR). The red, dashed line represents the Sentinel-2 tile boundaries, and the background image is the ESRI World Imagery base map.	64
3.6	Detailed overview of the Italian tile (32TPP). The red, dashed line represents the Sentinel-2 tile boundaries, and the background image is the ESRI World Imagery base map.	65
3.7	3D model of the Sentinel-1A satellite.	66
3.8	Basic radar block diagram.	67
3.9	Sketch of the TOPSAR acquisition geometry. T_B is the burst duration and ω_r is the steering angle rate (image credit: DLR).	68
3.10	A simplified block diagram of the proposed land cover mapping procedure. Part of the pre-processing chain is pre-implemented in Google Earth Engine; whereas, the radiometric correction and speckle noise reduction steps were added to the chain.	70
3.11	Sentinel-1 RGB color composite (Red: σ_{VV}^0 (dB), Green: σ_{VH}^0 (dB) Blue: VV/VH power ratio) over the region of interest before (a) and after correction with model 1 (b) and model 2 (c), as well as the difference of model 1–model 2 for the VV polarised bands stretched between -5 and 5 dB (d). Regions of active layover and shadow are overlaid in black and white (b,c) as well as in red and blue (d).	73
3.12	Algorithm of the multitemporal despeckle filtering used in the proposed land cover classification methodology.	74
3.13	Overview of the classification model aimed at assessing the potential of temporally aggregated Sentinel-1 SAR time series.	76
3.14	Visual comparison between (a) the 2018 European Space Agency (ESA) CCI LC map at 300 m spatial resolution and the LC maps obtained by using (b) a single scene acquired on 2018.04.27, (c) single image obtained averaging in time all available images for year 2018, (d) a multitemporal stack of all the 2018 images, (e) a set of 4 seasonal images obtained by averaging 3 images per season, (f) a set of 4 seasonal images obtained by averaging 5 images per season. Black areas in (a) represent classes discarded from the classification.	76
3.15	Extraction of textural features from seasonal mean composites, using a 5×5 kernel. Note that this features extraction procedure is not limited only to four seasons, but it can be applied on N seasonal collections. . . .	79
3.16	Extraction of temporal features from 24-days denoised clusters. Note that this procedure is applied to both VV and VH channels, separately (therefore two 24-days based collections are generated).	80
3.17	Visual example of how the erosion operation works on the MRLC map, based on a 3×3 pixels kernel. The left image is the original, non eroded map, while the right one is the erosion output. Note that in both maps, black regions represent classes that were not selected to be classified. . . .	83
3.18	Block diagram of the high-resolution training set generation procedure. . .	85

3.19	Main outputs of the training set generation procedure: in (a) is shown the eroded MRLC map; in this example, the aquatic vegetation is selected and clustered (b) using a k -Means clusterer with $k = 3$. Finally, in (c) the most abundant cluster is extracted and sampled with 10 m scale.	86
3.20	Chopping of training set issue caused by low overlapping degree between region of interest and each SAR image belonging to the original time series.	87
3.21	Simplified concept scheme of a random forest classifier.	88
3.22	Spatial distribution of the validation points in (a) Siberia (tile 42WXS), (b) Italy (central Italy tile, 32TPP), (c) Amazonia (tile 21KUQ) and (d) Africa (tile 37PCP). The color code is reported in Table 3.3	90
3.23	Phenology tracking of classes in multitemporal Sentinel-1 SAR data (note that the tiles do not always contain the same number of classes).	91
3.24	Qualitative results for the four test areas. Columns refer to 1) the Google Satellite basemap view, 2) the annual mean composite derived by all the VH-channel images overlapping the tile of interest, 3) the CGLS map at 100 m resolution and 4) the obtained classification result with 10 m pixel spacing.	92
3.25	Small sample areas inside each test site: on the left a multispectral Sentinel-2 image of each area, at the center the CGLS map, and on the right the result of the proposed procedure.	93
3.26	Mean feature vectors for each class in each test site (class color legend as in Table 3.3).	100
4.1	Overview of the complete procedure designed to extract water bodies from Sentinel-1 SAR data sequences.	115
4.2	Set of features extracted from a Sentinel-1 time series, suitable for water detection in SAR data.	117
4.3	Main outcomes of the training set generation procedure: (a) shows the original CGLS map at 100 m spatial resolution; the “water” class is then extracted (b) from the MR map and eroded (c). Finally, the eroded water class is randomly sampled inside and outside water regions (d) to generate a balanced set of points. The Iseo Lake, located in the Lombardy region in North Italy, was used in this example.	119
4.4	Main steps of the water cluster selection procedure: (a) shows the satellite view of the example scene; the (b) CGLS map at 100 m resolution is loaded, and a negatively buffered (100 m) multi-polygon layer (c) is generated. Then, a frequency histogram is computed over the clustered result (d) inside the multi-polygon layer. The most frequent cluster is then associated to the water class (e), and extracted as the final HR water map (f).	121
4.5	Benefits of the slope filtering: (a) shows the satellite view of the scene, while (b) and (c) show how false positive occurrences were removed, hence improving classification results.	123
4.6	Qualitative results over very small areas inside the considered tiles. The images on the left show samples from the 100 m spatial resolution water layer in the CGLS map; the images on the right show instead the output of the proposed methodology with a spatial resolution of 10 m in Siberia (top), Amazon (middle) and Italy (bottom). In all the cases, water regions are colored in light blue and overlapped to the Google Satellite basemap.	125

4.7	From left to right, visual comparison among the water layer of the Globcover, the Copernicus Global Land Cover (CGLS) map, the JRC Global Surface Water Mapping Layer and the results of the proposed approach (10 m).	126
4.8	The Lombardy region, northern Italy. Red solid line represents the political boundaries of the region.	129
4.9	Visual comparison between (a) the validation set and (b) the extracted water bodies map for the whole Lombardy region. Both sets are presented in blue, whilst the red solid line represents the boundaries of the Lombardy region (the white background allows to better highlight water bodies and the differences between the two sets).	131
4.10	Spatial distribution of omitted water points (black dots) for a specific classification run. Red solid line represents the boundaries of the Lombardy region and blue areas represent water bodies from the DUSAF 6.0 dataset. Black dashed boxes “a” and “b” show examples of foreshortening/layover effects and morphological operation issued, respectively (see Figure 4.11).	132
4.11	Spatial distribution of omitted water points for a specific classification run. Case 1: foreshortening and layover; case 2: small water bodies not extracted or canceled by morphological operations. Omission points lay on the background image which is represented by the Google Maps layer (over which the boundaries of the Lombardy region, in red, are superimposed).	133
4.12	Overview of the WorldWater pilot Countries and test sites: Colombia, Gabon, Greenland, Mexico and Zambia.	134
4.13	All the test sites used in the ESA WorldWater Round Robin.	135
4.14	Overview of the WorldWater pilot Countries and test sites: Colombia, Gabon, Greenland, Mexico and Zambia.	135
4.15	Accuracy statistics from the WorldWater Round Robin test sites, individually and overall, summarized by model input data type (OA = Overall Accuracy; UA = User Accuracy; PA = Producer Accuracy).	140
4.16	False colour PlanetScope QuickLooks and associated water classifications for each test site used in the object-based validation approach.	141
4.17	False colour PlanetScope QuickLooks and associated water classifications for each test site used in the object-based validation approach.	142
4.18	Qualitative results for the five WorldWater Round Robin test sites: Colombia (tile 18NYL), Gabon (tile 32MND), Greenland (tile 22WET), Mexico (tile 14QKH) and Zambia (35LNC). Background optical images are taken from the Google Satellite basemap, except for the second column, which shows the annual mean VH composite image for each tile of interest (the grey-scale composite is obtained by setting -30 dB and 0 dB for minimum (black) and maximum (white) σ^0 values respectively). The scale bar is shown only once for full view of the tiles and for the detailed, zoomed region.	144
4.19	Scheme of the proposed seasonal water body mapping algorithm (which is a variation of the original water body mapping model).	148
4.20	Final stage of the permanent/seasonal water body mapping algorithm, that aims at generating the final water map based on the frequency of water presence, per pixel.	149
4.21	The Monte Cotugno reservoir in the Potenza province, Basilicata region, South Italy.	150

4.22	The Monte Cotugno reservoir in the Potenza province, Basilicata region, South Italy.	150
4.23	Final high resolution (10 m) permanent/seasonal water body map generated over the Monte Cotugno reservoir.	151
4.24	Vector layer showing the extent of the analyzed water body for each month (year of interest: 2019). Note that there are some false positive occurrences around the reservoir, due to the absence of post-processing steps.	152
5.1	Scheme of the NDVI time series extraction procedure.	159
5.2	Ground truth (GT) polygons representing conventional rice fields.	160
5.3	NDVI time series of all fields sowed with the S. Andrea rice variety. Coloured vertical lines mark the dates where major agricultural operations were carried out.	164
5.4	NDVI time series of all fields sowed with the Luna CL rice variety. Coloured vertical lines mark the dates where major agricultural operations were carried out.	165
5.5	NDVI time series of all fields sowed with the Sole rice variety. Coloured vertical lines mark the dates where major agricultural operations were carried out.	166
5.6	Procedure for the extraction of the roughness index parameter Z_s	174
5.7	Typical paddy field SAR backscatter time series. Vertical axis values are in dB.	174
5.8	Boxplot of roughness values Z_s for paddy fields, urban areas and water. Z_s is in \log_{10} units for clearer visualization.	177
5.9	Reflectance values decrease after EOM treatment over five sites (four with GWC and one without EOM treatment). Image source: [63]	180
5.10	Boxplots of EOMI ₂ pixels values before (B) and after (A) EOM spreading. The Sentinel-2 acquisition dates are 25 Jul (orange), 2 Aug (green) and 4 Aug (blue). Image source: [63]	181
5.11	Mean reflectance of sample fields before (2 Aug) and after (4 Aug) cattle manure application. Image source: [63]	182
5.12	Typical buffalo breeding farm. Yellow boxes contain manure areas, whereas green boxes represent metal roofs. Image source: [203]	183
5.13	Classification product based on the described work and intermediate results. a) shows the detection of manure areas. b) shows the detection of metal roofs. In c) the detected manure areas were filtered based on a proximity analysis applied on metal roofs. Finally, in d) photointerpretation was carried out to recognize buffalo breed facilities.	184
5.14	Test sites used to develop the manure detection algorithm.	187
5.15	Average spectral shifts registered in the two fields of interest, before and after manure application.	189
5.16	RGB composites of Sentinel-2 before and after images of the test sites.	190
5.17	Average spectral shifts registered in the two fields of interest, before and after manure application (using Planet data).	191
5.18	Example of bad quality cloud mask generated for the L2A Sentinel-2 image acquired on the 1 st of January 2022.	193
5.19	Radiometric calibration issues, encountered for both study sites and for the same period.	194

5.20	Visual comparison among different products. a) is the L1C RGB composite of the whole Sentinel-2 tile, b) is L2A RGB composite of the whole Sentinel-2 tile, c) and d) are zoomed regions around FOI ₁ field, respectively, and e) is the RGB composite of a Planet image, acquired the same date as the Sentinel's ones (6 th of January).	195
5.21	Histograms of spectral values a) before and b) after radiometric calibration issues.	196
5.22	From top to bottom: 1) EOMI time series without any type of cloud filtering, 2) time series obtained by filtering the metadata to consider only images with 60% or less of overall cloud coverage, and 2) EOMI time series obtained by selectively filtering clouded pixels only inside the crop field (FOI ₁).	197
5.23	Map of EOMI values of FOI ₁	198
5.24	From top to bottom: 1) EOMI time series without any type of cloud filtering, 2) time series obtained by filtering the metadata to consider only images with 60% or less of overall cloud coverage, and 2) EOMI time series obtained by selectively filtering clouded pixels only inside the crop field (FOI ₂).	199
5.25	Map of EOMI values of FOI ₂	200
5.26	Two possible approaches aimed at spotting out potential manure spreading activities during winter months.	201
5.27	An additional site used to test the proposed manure detection algorithm. .	202

List of Tables

1.1	Available global land cover products subdivided in two groups: the first group relates to general LC products; whereas, the second group is devoted to thematic LC products.	4
3.1	List of available SAR satellites.	66
3.2	Classification improvements [%] with respect to the worst result, occurring when only a single SAR image is provided in input to the classifier.	77
3.3	The class legend used in the proposed land cover mapping methodology.	81
3.4	Accuracy results for the selected test site using independently extracted high resolution validation points. The table reports the overall accuracy (OA) values for the CGLS map and for the maps produced by the proposed procedure, the number of validation pixels per class (px) and the class producer’s accuracy (pa). Note: the symbol “-” means there are no MR points in that tile for a specific class.	95
3.5	Accuracy results for the selected test site using independently extracted high resolution validation points. The table reports the overall accuracy (OA) values for the maps produced by the proposed procedure, the number of validation pixels per class (px) and the class producer’s accuracy (pa) in three different cases. Case 1 refers to the application of the training set generation procedure, as described in Section 3.7.1; Case 2 reports the results when only a classical morphological erosion filter is applied to the MRLC map; Case 3 shows the values obtained using applying a Multiclass Border Reduction Filter (MBRF) on the MRLC map. Note: the symbol “-” means there are no MR points in that tile for a specific class.	104
3.6	Accuracy results obtained by changing the set of input SAR features.	107
4.1	Available global water surface products subdivided in two groups and sorted by increasingly coarser spatial resolution: the first group relates to projects focusing only on water bodies extraction; whereas, the second group is devoted to projects aimed at generic Land Cover (LC) mapping.	113
4.2	Confusion matrices for the three regions of interest, generated based on test points collected from the three different reference maps: the CCI Globcover (300 m), the CGLS (100 m) and the JRC (30 m). “W” and “NW” stand for water and non-water respectively.	127
4.3	Overall accuracy (OA), <i>water</i> producer accuracy (PA_w) and <i>non-water</i> producer accuracy (PA_{nw}) for each study case using CCI Globcover (300 m), the CGLS (100 m) and the JRC (30 m) map as references (all the values are in percentage [%]).	128

4.4	Results from the ESA WorldWater project validation process. “w” and “nw” stand for water and non-water respectively, whereas PA, UA and OA stand for Producer Accuracy, User Accuracy and Overall Accuracy respectively (in percentage [%]).	143
4.5	Summary of object extraction accuracies. The accuracy metrics are maximum overlap area (A_{max}) and quality (A_{qual}) as a joint balanced measure of correctness (A_{cor}) and completeness (A_{com}). The overall score is the product between A_{max} and A_{qual}	143
5.1	Rice fields and corresponding geo-location, sowed variety (SA = S. Andrea, LCL = Luna CL, SO = Sole), type of sowing (dry-seeding or water sowing), sowing date and weeding dates. Geographic coordinates are expressed in decimal degrees.	160
5.2	NDVI values statistics of the individual fields at two representative dates.	161
5.3	Spectral bands for the Sentinel-2 sensors (S2A & S2B).	163
5.4	Roughness parameter estimation for each rice field. σ_{VV}^0 max is the maximum backscatter coefficient of the entire times series in decibels [dB], Z_s is the surface roughness parameter in centimeters [cm] and the “Date” column reports the date at which the maximum backscatter value was registered along the rice growth season (year 2018).	176
5.5	Description of PlanetScope bands.	190

Chapter 1

Introduction

1.1 Vegetation Land Cover: challenges

Land Cover (LC) products play a key role in many different contexts, from climate change to food security [1–3]. Recognized as an essential climate variable [4], LC maps are in fact very important sources of information, that allow to better understand the relationship between human activities and changes occurring from the local to the global scale. Being a measure of the land surface change mainly due to human activities - that translates into pressure on ecosystems and biodiversity - Land Cover Change (LCC) provides fundamental information that can be employed, for example, in climate change studies, environmental health, urban area management, resource management, biodiversity conservation, food security, forest carbon and many others [5, 6]. For all these reasons, there exists a strong demand for frequent, high quality land cover maps at the global scale.

The features of vegetated land cover tend to change rapidly due to the natural phenology of the observed vegetation¹. This aspect represents a challenge in terms of product validation, as an accurate assessment of the quality and reliability of the generated maps turns out to be a difficult task. This limitation becomes even more critical when the main objective is mapping and monitoring of broad areas; in fact, previous work focussed on monitoring small, local areas and/or short periods of time, making it difficult to compare results (for instance, due to differences in satellite data sources and mapping methods) and to quantify the actual changes, in a reliable way.

¹Land cover maps represent spatial information on different types (classes) of physical coverage of the Earth's surface, e.g. forests, grasslands, croplands, lakes, wetlands, etc.

In general, automatic or semi-automatic monitoring and mapping algorithms strongly depend on the quality and quantity of reference sample data sets, and their capability to generate meaningful statistics. Reference or “ground truth” data are generally collected by means of in-situ campaigns, where professionals are tasked with interpreting, manually collecting and labelling ground truth data [7]. The high reliability of manually collected reference data comes however from campaigns that are usually very expensive, in terms of both time and resources.

Other LC mapping approaches are instead based on reference data that has been collected by previous, existing LC maps [8]. Of course, this latter approach is much more efficient and time-effective, but the final quality of results strongly depends on the quality of the involved LC map.

1.2 Existing Land Cover products

In recent years, several regional and global land cover maps have been produced based on many different spaceborne remote sensing data, such as multi- and hyper-spectral data and Synthetic Aperture Radar (SAR) data. Some of the most widely used low-spatial resolution products (i.e., from 300 m to 1 km) are the European Space Agency (ESA) Climate Change Initiative (CCI) global land cover map at 300 m resolution [9], the Global Land-Cover map (GlobCover) at 300 m resolution [10], the Moderate Resolution Imaging Spectroradiometer (MODIS) land-cover map at 500 m resolution [11], the Global Land-Cover Classification map (GLC2000) at 1 km scale [12] and the International Geosphere-Biosphere Programme (IGBP) land cover map at 1 km resolution [13].

However, in many contexts such as climate change, urban extent monitoring, resource managements and agriculture, these coarse spatial resolutions are not enough to provide spatial details that are needed to carry out studies on them. In fact there exists great interest in mapping and monitoring land cover types and their changes with finer spatial resolution for improved characterization.

Many efforts have been done to improve classification accuracy of land cover maps, based on the most recent spaceborne Earth Observation (EO) missions. Finer-resolution products have been released, most of them having spatial resolution ranging from 10 to 30 m scale. Citing the most famous ones: the GlobeLand30 [14] at 30 m scale produced using Landsat 4 and 7, the Finer Resolution Observation and Monitoring of Global

Land Cover (FROM-GLC) [15] generated using Landsat Thematic Mapper (TM) and Enhanced Thematic Mapper Plus (ETM+), the Global Land-Cover product with Fine Classification System (GLC_FCS30) [16] at 30 m spatial resolution based on Landsat data, the ESA CCI Land Cover Sentinel-2 map (ESA-S2-LC20) of Africa at 20 m resolution [17], the Finer Resolution Observation and Monitoring of Global Land Cover at 10 m scale (FROM-GLC10) [18] and, finally, the ESA WorldCover product at 10 m resolution for year 2020 [19], generated based on Sentinel-1 and -2 data (released in late 2021).

Many different thematic high-resolution land-cover products have also been delivered. For example, regarding urban areas extent, available data sets include the ESA Global Human Settlement Layer (GHSL) [20, 21], the Normalized Urban Areas Composite Index (NUACI) product [22], the annual maps of Global Artificial Impervious Areas (GAIA) [23] and the Global 30 m impervious surface product using multi-source and multi-temporal data sets in 2020 (MSMT_IS30-2020) product [24].

Regarding inland water bodies data sets, we can cite the 30 m resolution Landsat Global Inland Water product (GLCF-GIW) [25], the Global 3-second/1-second Water Body Map (G3WBM and G1WBM) [26] at 90 m scale, the European Commission Joint Research Centre (JRC) Global Surface Water dataset [27] at 30 m resolution and the Global Land Analysis and Discovery (GLAD) Global Surface Water Dynamics (GSWD) product [28]. For cropland land cover maps, the most widely used reference products include the Global Food Security-Support Analysis Data (GFSAD) at 30 m scale [29], the Global Cropland Area Database (GCAD30) at 30 m spatial resolution based on Landsat and MODIS data [30], and the 30 m Finer Resolution Observation and Monitoring Global Cropland (FROM-GC) dataset [31].

Finally, regarding global forest land cover, there exist several thematic products, such as the Global 2010 Tree Cover (treecover2010) [32] at 30 m scale, the Global Forest Cover Change (GFCC) [33] product by NASA at 30 m spatial resolution and the 30 m resolution Global Forest Cover (GFC30) [34], based on Landsat-8 imagery. Table 1.1 summarizes all the described relevant products found in the technical literature.

These high spatial resolution land cover and thematic maps were developed based on different satellite sensors (optical or radar) and classification approaches and, as a consequence, significant differences exist among the various products, in terms of accuracy and overall spatial agreement. Moreover, the efforts made to build reference data sets

Dataset	EO sensor(s)	Res.	Year(s)
General Land Cover products			
International Geosphere-Biosphere Programme (IGBP) land cover map [13]	Advanced Very High Resolution Radiometer (AVHRR)	1 km	1992 - 1993
Global Land-Cover Classification map (GLC2000) [12]	SPOT 4	1 km	2000
Moderate Resolution Imaging Spectroradiometer (MODIS) land-cover map [11]	MODIS	500 m	2001-2020
Global Land-Cover map (GlobCover) [10]	MERIS (ENVISAT mission)	300 m	2009
European Space Agency (ESA) Climate Change Initiative (CCI) global land cover map [9]	MERIS (ENVISAT mission)	300 m	1992-2018
GlobeLand30 [14]	Landsat 4 and 7	30 m	2000, 2010, 2020
Finer Resolution Observation and Monitoring of Global Land Cover (FROM-GLC30) [15]	Landsat Thematic Mapper (TM) and Enhanced Thematic Mapper Plus (ETM+)	30 m	2011-2020
Global Land-Cover product with Fine Classification System (GLC_FCS30) [16]	Landsat-8	30 m	2015
ESA CCI Land Cover Sentinel-2 map (ESA-S2-LC20) of Africa [17]	Sentinel-2A	20 m	2016
Finer Resolution Observation and Monitoring of Global Land Cover (FROM-GLC10) [18]	Sentinel-2A	10 m	2017
ESA WorldCover product [19]	Sentinel-1 and -2	10 m	2020-2021
Thematic Land Cover products: urban areas			
ESA Global Human Settlement Layer (GHSL) [20, 21]	Sentinel-1 and -2	10 m - 1 km	1975, 1990, 2000, 2015, 2018, 2020
Normalized Urban Areas Composite Index (NUACI) product [22]	Landsat-5	10 m - 1 km	1990, 2010
Global Artificial Impervious Areas (GAIA) [23]	Landsat TM, ETM+ and Landsat-8	30 m	1985, 2018
Global impervious surface product (MSMT_IS30-2020) [24]	Landsat-8, Sentinel-1 and VIIRS NTL	30 m	2015
Thematic Land Cover products: water bodies			
Landsat Global Inland Water product (GLCF-GIW) [25]	Landsat TM and ETM+	30 m	2000
Global 3-second/1-second Water Body Map (G3WBM and G1WBM) [26]	Landsat TM and ETM+	90 m	2015
JRC Global Surface Water dataset [27]	Landsat-5 TM, Landsat-7 ETM+ and Landsat-8 OLI	30 m	1984-2015
Global Land Analysis and Discovery (GLAD) Global Surface Water Dynamics (GSWD) product [28]	Landsat-5 TM, Landsat-7 ETM+ and Landsat-8 OLI	30 m	1999-2018
Thematic Land Cover products: cropland			
Global Food Security-Support Analysis Data (GFSAD) [29]	Landsat-8	30 m	2015
Global Cropland Area Database (GCAD30) [30]	Landsat and MODIS	30 m	1990, 2010
Finer Resolution Observation and Monitoring Global Cropland (FROM-GC) dataset [31]	Landsat TM, Landsat ETM+ and MODIS	30 m	2010
Thematic Land Cover products: forests			
Global Tree Cover (treecover2010) [32]	Landsat-7 ETM+	30 m	2010
Global Forest Cover Change (GFCC) [33]	Landsat-7 ETM+	30 m	2000-2015
Global Forest Cover (GFC30) [34]	Landsat-8 OLI	30 m	2018

TABLE 1.1: Available global land cover products subdivided in two groups: the first group relates to general LC products; whereas, the second group is devoted to thematic LC products.

for validation of high-resolution global land cover maps were limited due to strong inconsistencies mainly between legends, sampling strategies and validation procedures used. Despite the efforts that were made aimed at improving mapping accuracy in the last few decades, the above listed 30 m spatial resolution global land cover maps still suffer from a relatively low accuracy. For this reason, some of the maps do not match the requirements of many applications [13].

1.3 Optical versus microwave remote sensing

Spaceborne remote sensing data can help monitor the ground surface at a large scale by providing precise and timely information on the status of different land cover types (classes). These data are generally divided into three categories:

- Optical data: multi-spectral and hyper-spectral data;
- Microwave data: Synthetic Aperture Radar (SAR) data acquired using carrier frequencies typically in the range from L- to X-band (from ~ 1 to ~ 12.5 GHz);
- Fused data: the result of considering together optical and SAR data and/or auxiliary data sources, such as weather stations and other sensors. The operation of merging these different data sources is termed "data fusion".

The information retrieved by optical data strongly differs from that derived by SAR sensors: on the one hand, optical sensors are passive instruments that can capture information from the visible and near-infrared regions of the electromagnetic spectrum, thus providing clues on the surface composition. On the contrary, SAR sensors are active instruments, which gather information from the microwave region of the spectrum regarding the shape, orientation and dielectric properties of a target. Naturally, each source of data has its own advantages and limitations, discussed in this section.

Thanks to satellites carrying multispectral sensors such as Landsat, Landsat Thematic Mapper, SPOT (Satellite Pour l'Observation de la Terre) and MODIS (Moderate Resolution Imaging Spectroradiometer), the remote sensing community had at its disposal more than forty years of optical imagery at the global scale. In general, medium- and high-spatial-resolution data (≤ 300 m) are used for small-scale mapping (regional to national

scale); however, thanks to the steadily increasing computational power and number of geospatial cloud computing platforms, even global land cover mapping became feasible using high resolution satellite data.

Even if these sensors are not able to provide finer spatial details, the main advantage is represented by their coverage capability; in fact, these satellites can map a specific region of the Earth on a daily (or near-daily) basis, allowing scientists to analyze temporally dense time sequences of multispectral data. Optical data time series are capable of capturing both slow and fast land cover changes and can overcome cloud cover issues [35]. In fact, cloud cover strongly limits the use of optical products; Cloud issues can be reduced using image compositing, with the consequent cost of constraining multitemporal change analysis. Optical-based methodologies are also limited by the similarities in spectral reflectance across a landscape, meaning that different crops or tree species that have similar phenological features may be indistinguishable in optical data; for this reason, similar land cover characteristics enhance the inability to distinguish land cover types and land uses, and employment of complex hyperspectral data analysis may be considered.

Moreover, optical sensors only interact with upper surfaces; this means that vegetation canopies obscure the terrain beneath and crops obscure agricultural soil, limiting the inferences of land cover and land use to only when these are well correlated with the characteristics of the top layers. Finally, changes in the spectral properties of the soil and atmosphere can also prevent the inference of land and vegetation properties. However, optical data are the most commonly found and easily accessible spaceborne Earth Observation (EO) data, and are often used to explore unique spectral characteristics of a target using, for example, spectral indices. Optical data are very easy to interpret and to apply, but obtaining enough optical data without cloud interference at a large scale remains a challenge [36].

On the other hand, microwaves in the widely-used SAR wavelength range (approximately a few centimetres to meters) are not affected by smoke, atmospheric haze, dust, cloud cover and rain and thus they are suitable for monitoring regions dominated by cloudy and rainy weather, during night and day time. However, the use of microwave sensors for LC mapping purposes has not been used as widely as that of optical sensors, especially for global mapping [37]. In fact, most of the past and current SAR sensors

have been used for regional-scale monitoring and mapping. Among these, we can cite the European Remote Sensing 1 and 2 (ERS-1 and -2), the Advanced Land Observation Satellite (ALOS), the Advanced Synthetic Aperture Radar (ASAR), the Japanese Earth Resources Satellite (JERS-1), RADARSAT-1 and -2. Related to land cover, several studies tackled a large variety of topics: land cover classification [38, 39], forest cover classification [40], grassland monitoring [41], woodlands monitoring [41], deforestation mapping and monitoring [42], water body monitoring [43, 44], urban area monitoring [45] and others.

Also in the case of land use, few studies have been carried out on: urban land use [46], agricultural areas classification [47], crop monitoring (for example, rice crops) [48, 49] and many others.

However, similarly to optical sources, several critical aspects affect radar data. For instance, speckle noise increase measurement uncertainty and can lead to poor classification accuracy; to limit speckle noise, spatial and/or temporal filters are required. Topography also represent a critical issue: over morphologically complex regions such as mountains and hills, in fact, geometric and radiometric distortions emerge (such as foreshortening and layover effects caused by radar shadows).

Until few years ago, monitoring land cover dynamics at medium-to-high resolution was limited by the lack of available high temporal and spatial resolution satellite imagery. As the most widely accessible medium to high spatial resolution optical satellite products, Sentinel-2 and Landsat products are often used to create merged products with high temporal resolutions. SAR data availability has also increased since the launch of Sentinel-1A and B on 3rd April 2014, and 25th April 2016, respectively. This was the first operational SAR mission of the European Commission's Copernicus program, which provides an unprecedentedly large amount of free data even for commercial use. Sentinel-1, in particular, is designed for continuous near-real-time land monitoring and offers dual-polarized mode (VV/VH) SAR images with a global spatial resolution of 5m to 20m at least every 5-6 days on any place on the Earth.

1.4 The advantages of using multitemporal satellite data

Earth Observation models allow to efficiently and rapidly monitor, identify, map and assess land cover at different spatial and temporal scales. In turn, correct identification of the different types of land cover allows to build reliable monitoring applications.

Including sequences of spaceborne data within land cover mapping algorithms can provide clues on the stability of the classes and their change in time. Thanks to the ever increasing number of Earth Observation satellites, time series data has become the dominant form of remote sensing data for monitoring changes on the land surface [50], allowing to detect finer changes and to provide their temporal patterns.

As previously discussed in Section 1.2, several regional and global land cover maps have been generated that, however, need to be frequently updated and validated; this is a challenging task, especially in highly heterogeneous regions. Time sequences of remotely sensed data have the potential to generate wide-area land cover products, that are able to capture the complexity of the changes occurring on the Earth surface. Time series data have been employed in many studies, such as forest disturbance [51] using Landsat data, water body mapping using Landsat data [52], annual land cover changes characterization using MODIS data [53], flood monitoring with Sentinel-1 SAR imagery [54], crop mapping using Sentinel-2 data [55], and many others. Moreover, intra-annual sequences of remotely sensed data can provide useful information on the phenological stages of different land covers, allowing to better characterize them and identify finer differences across the years.

All in all, methodologies based on time series have been demonstrated to outperform single-date approaches in many applications, such as Above-Ground Biomass (AGB) estimation [56], forest cover loss quantification [57], land cover mapping [58, 59] and many others.

1.5 Objectives of this dissertation

In this thesis, we will focus on the characterization of three different land cover types leveraging the features hidden inside temporal sequences of satellite data. The three types are vegetation, water and organic cropland; specifically, the *vegetation* macro-class includes several types of natural vegetated land covers, such as different tree species,

grassland, shrubland, etc. Regarding the *water* class, this includes only inland water bodies, such as lakes, rivers, small seas and reservoirs. Lastly, in the case of *organic cropland*, particular attention will be devoted to the characterization of farming practices carried out within organic crop fields, such as weed-killing and fertilization operations and tillage monitoring; these are clues that help discriminating organic cropland from traditional cropland.

Regarding vegetated land cover mapping, findings from the scientific literature convey a clear message: in general, approaches based on sequences of optical data outperform those based on SAR time series [60–62]. Consequently, as can be observed from Chapter 2, the technical literature offers plenty of methodologies aimed at characterizing vegetated land cover types using optical data. On the other hand, very few studies leverage dense sequences of SAR data to characterize vegetated land covers; moreover, these studies also present several limitations that this thesis will try to overcome. Given this context, we decided to explore in this thesis work the untapped potential of multitemporal SAR data in characterizing natural vegetation species.

Regarding water bodies monitoring and mapping, also in this case the technical literature offers a large variety of methodologies aimed at characterizing water land cover using multitemporal optical data. However, it turned out that all the analyzed work suffers several limitations. The most critical limitation is represented by clouds; for example, flood monitoring applications strongly suffer from cloud issues, as generally bad weather is associated to flood risk. Flooded vegetation can also represent a limitation, as optical sensors cannot sense soil beneath vegetation. Since almost three-fourths of the Earth surface is continuously covered by clouds, it is difficult to develop systems aimed at generating frequent water maps for any region of the World. Many methodologies also lack of automatism and cannot be transferred to other regions of interest, as their parameters are locally tuned. Lastly, there are currently no methodologies able to generate frequent, high-resolution (<30 m) water bodies maps at very large (up to global) scale. SAR-based methodologies are also present in the literature (but fewer than optical-based ones), still they have several limitations in terms of spatial and temporal resolution, lack of automatism, reference data sets generation and many others that will be deeply discussed in Chapter 2. Based on all the above considerations, in this thesis we will assess the potential of multitemporal SAR data to build a fully automated, global-scale, high-resolution water body monitoring and mapping application that aims at overcoming the most severe limitations found in the technical literature.

Finally, regarding characterization of organic farming practices, the selection of the most suitable source of data strictly depends on the parameter that needs to be monitored. For instance, multispectral data can be successfully use to detect fertilization operations [63, 64], classify crops [65] and monitor weed-killer activities [66]. On the other hand, SAR data can provide useful information regarding the type of tillage [67], the estimation of flooding periods in case of aquaculture [68], the determination of harvesting dates [69], yield forecasting [70] and discrimination of different species of the same crop [71]. In this thesis, we will focus mainly on monitoring three very important aspects that mostly characterize organic farming, i.e., assessing the type of utilized tillage technique using SAR time series data, detecting weed-killer activities in sequences of multispectral data and monitoring fertilization operations through pairs of multispectral data. Consequently, in this last part of the thesis, we proposed a new methodology to characterize organic farming by a multisource approach, i.e., using both optical and radar data.

Chapter 2

A review of land cover mapping methodologies based on space-borne time series data

2.1 Scientific literature review on vegetation land cover mapping

2.1.1 Optical-based vegetation land cover methodologies

The technical literature offers plenty of vegetation mapping approaches which are based on optical data. In the first part of this section, a brief review of land use and land cover mapping using optical data is carried out; specifically, this will include a summary of the relevant knowledge related to classification models, training sample strategies, segmentation algorithms, geographical areas and others.

In recent years, several analysis techniques and algorithms were developed, aimed at characterizing land cover and land cover changes. In [72], the Authors discussed the most used techniques for land cover classification at the regional/global level; their review study showed that the Random Forest (RF) classifier is one of the preferred technique by the Remote Sensing community, as it can handle high data dimensionality, it is a fast algorithm and, more importantly, it is insensitive to overfitting.

The work cited in [73] presented both opportunities and challenges represented by the use

of satellite images time series on large scale for land cover mapping; the main outcome of this study was that leveraging time series in land cover mapping approaches allows to gather information on the class stability and their transition.

In [74] guidelines on the choice of different pixel-based image classification processes were provided. The Authors shown that the highest improvement in terms of overall accuracy is given by the inclusion of textural information within the classification frameworks (with an average increase of about 12.1% OA). Moreover, the study demonstrated that the use of ancillary data such as topographic information, also have the potential to complement existing spectral information.

Regarding machine learning models, in [75] an overview of machine learning from an applied point of view is given; specifically, the Authors focussed on several machine learning approaches, such as Support Vector Machines (SVM), Decision Trees (DT), Random Forests (RF), Boosted Decision Trees (BDT), Artificial Neural Networks (ANN) and k -Nearest Neighbours (k -NN). For each approach, issues concerning the choice of the most suitable algorithm, training data requirements, user-defined parameter selection (and optimization), features space and computational costs were analyzed.

In [76] the Authors provided an overview of different Earth Observation data sets, spatial/spectral/temporal features of satellite data and approaches employed in land use and land cover classification. They also provided recommendations on how to generate accurate LC maps, depending on the source of data and on the region of interest. An important outcome of the study relates to the temporal resolution; as a matter of fact, temporal information play a fundamental role in detecting class changes and their dynamics, as frequent remotely sensed data allow to monitor crop types, natural vegetation such as forest cover, phenological stages, urban areas, and many others.

The study reported in [77] characterized the forest vertical structure for estimating forest water storage capacity from multitemporal, Sentinel-2 optical imagery and topographic data using an Artificial Neural Network (ANN) with fourteen input neurons (generated based on satellite data).

In [78], the Authors proposed an algorithm based on adaptive thresholds (decision trees) to generate land cover maps, computed from very high-resolution WorldView-2 images and according to the different input samples from the study area.

Based on decision trees, the Authors of [11] generated land cover products through an ensemble supervised classification algorithm applied on MODIS time series data.

In [79], multi-annual series of MERIS image composites were used within a Gaussian

Maximum Likelihood (GML) classifier, aimed at minimizing classification errors based on Bayes' theorem of decision making.

All in all, as also mentioned in [80], the majority of the related works found in the technical literature takes advantage of time series spaceborne data, multitemporal analysis and two main classification approaches, namely, pixel-based classification and object-based classification. In the former case, multi-/hyper-spectral time series data are used to monitor single pixels' trends along time, while in the latter, pixel's neighbourhood relations for segmentation and classification are analyzed using the GEographic Object-Based Image Analysis (GEOBIA) approach. Moreover, object-based classification procedure are often used together with machine learning algorithms such as random forests and support vector machines.

Currently, the majority of the studies that can be found in the scientific literature rely on Vegetation Indices (VI) to build their classification frameworks, in order to assess the nature of the land cover composition and its changes in time. The most common VIs used in those studies are generated based on reflectance values gathered from the visible and near-infrared regions of the electromagnetic spectrum. The Normalized Difference Vegetation Index (NDVI) [81] is computed based on the red and near-infrared bands, and is extremely sensitive to vegetation's chlorophyll, allowing to track plants' growth; the Soil-Adjusted Vegetation Index (SAVI) [82] also relies on the red and near-infrared bands, and represents an improvement of the NDVI index, as it minimizes soil brightness issues through a correction factor; the Enhanced Vegetation Index (EVI) [83] relies on the blue, red and near-infrared bands and accounts for atmospheric noise, thus preventing saturation over highly vegetated areas; lastly, the Normalized Difference Water Index (NDWI) [84] uses the green and near-infrared bands to highlight water bodies and to measure vegetation water status; all the cited indices are the most widely used in optical-based classification approaches; however, some variations of the same have been designed to account for some limitations and improve their sensitivity.

Time sequences of optical data were successfully employed in many vegetation land cover mapping applications. In [85], a comparison of land cover maps generated based on time sequences of Sentinel-1 SAR data, Sentinel-2 multispectral data and Landsat-8 multispectral data was provided (in terms of overall accuracy). Several vegetation types were mapped, such as grasslands, shrublands, rangelands and pastures. The Authors used

several vegetation indices mentioned above, together with some modifications of them to enhance detection of specific species; it has been shown that different composite generated based on Sentinel-2 data led to better results, compared to the (single) use of the other two sources of data. This study demonstrates that temporal aggregation is a promising tool for integrating large amounts of data in an efficient way and that it can compensate for the lower quality of automatic image selection and cloud masking. It also shows that combining data from different sensors can improve classification accuracy.

The work reported in [86] analyzed the potential of Sentinel-2's red-edge bands to generate land cover maps, compared to Landsat-8 capability in accomplish the same task. To this aim, three different machine learning algorithms were used, such as random forest, stochastic gradient boosting and support vector machine. A relatively wide range of classes were analyzed, such as cereals, legumes, shrubland, forest, settlement, bare soil and water, and it was found that classification based only on Sentinel-2's red-edge bands achieved better results compared to those obtained using only Landsat-8 data.

In [87] the relationship between eight vegetation indices generated from Sentinel-2 data was evaluated, in order to characterize three forest and two grassland areas in Australia, assessing how much Gross Primary Productivity (the most important component of terrestrial carbon flux) variations can be explained by Sentinel-2's red-edge bands.

The Authors of the work reported in [88] used Landsat time series data to characterize burned pastures, tilled pastures and forests using a random forest classifier obtaining very good results, and demonstrating (once again) that the detection of temporally irregular events is possible using dense sequences of cloud-free observations. As a matter of fact, involving time series in land cover classification algorithms reduces limitation represented by cloud cover.

The work cited in [89] a Support Vector Machine (SVM) applied to several spectral indices was used to classify the morphologically complex heterogeneous land cover patterns of cities, focussing on the discrimination between bare soil and built-up regions in Istanbul. The Authors showed that a multi-index approach (i.e., a combination of three spectral indices, namely, the NDTI, NDVI_{re} and MDDWI) was able to significantly improve the separation between urban areas and bare soils, also enhancing the distinction between other major land cover classes, such as water and vegetation.

In [90], the Authors generated annual land cover maps containing eight classes, such as woody formation, forest, swampy region and flooded grassland, grassland, farming, non-vegetated areas and water; to this aim, data from Landsat sensors Thematic Mapper

(TM), Enhanced Thematic Mapper Plus (ETM+) and the Operational Land Imager and Thermal Infrared Sensor (OLI-TIRS), on board of Landsat 5, Landsat 7 and Landsat 8, respectively were used to train a random forest classifier.

All the above mentioned studies represent only a tiny fraction of the large number of published papers on vegetation classification approaches based on time sequences of optical data. In general, they showed that optical data can be successfully employed to characterize vegetated land cover types, especially if time series data are used. On the other hand, the scientific literature review carried out in this Chapter also revealed lack of methodologies aimed at classifying vegetation species using multitemporal SAR data. Moreover, as mentioned in the introduction of this thesis, in the case of natural vegetation several studies demonstrated that optical time series based methodologies outperform those based on SAR time series [60–62].

Given all the above considerations, in the present thesis the potential of multitemporal SAR data in characterizing vegetated land covers at large (up to global) scale is assessed. Specifically, while being well aware of the advantages of optical data compared to SAR data, in this dissertation we will try to understand how to leverage SAR data to obtain results comparable to those obtained with optical-based classification approach. To this aim, the relevant findings from the technical literature are deeply analyzed in the next section.

2.1.2 SAR-based vegetation land cover methodologies

The first analysed work is reported in [91]. In this study, the estimation of tropical forest structural characteristics was assessed in Vietnam, using ALOS-2 SAR data, an L-band microwave sensor. Particular attention was paid on the effects of the polarization and seasonality of the SAR data on forest biomass estimation. The Authors showed that combinations of HH and HV polarizations used to feed linear regression models did not improve the biomass estimation with respect to use the HV channel alone. They also demonstrated that the HV backscatter intensity correspondent to the dry season (February) was much more sensitive to the amount of biomass, compared to the rainy season (October) HV backscattering intensity. In fact, it has been noticed that SAR data acquired during the wet season, hence, in heavily humid conditions, was not significantly sensitive to the biomass.

Regarding the methodology used for the biomass estimation, this relies on two parameters that are related to the geometrical structure of the vegetation (forest). These parameters are the diameter of the tree trunk (D) measured at 1.3 m from ground and the total height (H) of the tree (both measured using lasers-based measuring tools). This sampling was made for all trees that have trunk diameter greater than 5 cm inside a 1 hectare ($1ha = 100 \times 100m^2$) sample plot.

Then, the Above Ground Biomass (AGB) was computed by means of allometric equations (that provide biomass estimation), using D and H as input data. The AGB was computed separately for deciduous (2.1) and evergreen (2.2) trees, using the following equations.

$$AGB_{\text{deciduous}} = 0.14 \cdot D^{2.31} \quad (2.1)$$

$$AGB_{\text{evergreen}} = 0.098 \cdot e^{2.08 \cdot \ln(D) + 0.71 \cdot \ln(H) + 1.12 \cdot \ln(d_w)} \quad (2.2)$$

Where AGB is the Above Ground Biomass in kilograms [kg], D is the diameter of the trunk of the tree at 1.3 m above ground expressed in meters [m], H is the height of the tree in meters [m] and d_w is the wood density, expressed in tons per cubic meters [ton/m^3]. The equations for AGB estimation provide the actual amount of per-tree biomass, including branches and leaves, and the measure unit is [$Mg \cdot ha^{-1}$].

At this point, the mean backscatter intensity for both HH and HV polarizations has been computed over the $100 \times 100m^2$ reference plots, and the relationship between biomass and backscatter intensity was then analyzed by means of simple linear regression models. To this aim, the correlation coefficient R^2 and the Root Mean Square Error (RMSE) have been derived and used to evaluate the relationship between the two variables. The analysis shown that the HV backscattering intensity was more correlated to biomass, with respect to the other channel (or combination of polarizations, such as the ratio). Moreover, the correlation between biomass and backscatter intensity turned out to be stronger during dry season ($R^2 = 0.57$) with respect to the wet season ($R^2 = 0.34$). The study demonstrated the importance of selecting the best polarization and season for satellite-based biomass estimation.

Another very interesting study is reported in [92]. The Authors of this work wanted to perform fine-scale mapping of the AGB at the provincial level in Viterbo, Italy, using

ALOS-2 (L-band), Sentinel-1 (C-band) and Sentinel-2 (optical) multitemporal SAR data. Similarly to what has been made in the previous study, a simple linear regression analysis was carried out to assess the relationship between backscatter intensity and AGB. Results showed there exist quite good correlation between the two parameters, with $R^2 = 0.7$. The Authors demonstrated that the temporal information is very relevant, as it allows to discriminate between different types of trees (for example, it has been shown that broadleaf forests have different behaviours in yearly backscatter time series). They also declared that the models based on Sentinel-1 data could improve their capability in predicting AGB, if they are developed separately for each vegetation class (i.e., deciduous and evergreen classes).

The methodology relies on the use of SAR time series to map the AGB and on several parameters that were measured in situ, such as the diameter at breast height (DBH) of both living and dead stems with a diameter greater than 5 cm, the species, thirty height samples per main species per plot and the age of the trees. Regarding Sentinel-1 data, two different time sequences were generated: a sequence made of 10 three-month time windows (Jan-Feb-Mar, Feb-Mar-Apr, Mar-Apr-May, etc.) and a complete yearly time sequence made of all the available acquisitions for a specific year of interest. Then, for each stack, a mean composite image was generated. Moreover, polarization compositions were also tested, specifically the ratio and the product of VH (HV) and VV (HH) channels were computed for Sentinel-1 and ALOS-2. Whereas, for Sentinel-2, a single yearly mean composite was computed, and the NDVI and RENDVI vegetation indices were derived. To summarize, the features used in this work are the following:

- Sentinel-1 features: 10 three-months mean composites and one-year mean composite for VV, VH, VH/VV and $VH \cdot VV$ polarizations (for a total of 44 features);
- ALOS-2 features: one-year mean composite for HV, HH, HV/HH and $HV \cdot HH$ (for a total of 4 features);
- Sentinel-2 features: given the one-year mean composite, 10 bands and 2 vegetation indices were used as features (for a total of 12 values).

As shown in Figure 2.1a, in the case of evergreen trees the correlation between AGB and backscatter intensity in time remain almost unaltered along the whole year ($\rho \geq 0.75$)

for all the polarization channels (and compositions). While in the case of deciduous vegetation (Figure 2.1b), the correlation is lower for all the polarizations ($\rho < 0.7$).

Based on the analysis carried out in this paper, some conclusions can be drawn. First of all, it was observed that the leaves tend to provide the strongest backscatter contribute in C-band (5.405 GHz). In fact, the wavelength of the radar signal is comparable to the size of the leaves. In particular, the Authors demonstrated that Sentinel-1 C-band signals are sensitive to the phenology of deciduous vegetation, as the correlation between VH backscatter intensity and AGB for this type of tree varies greatly depending on the season. On the other hand, the correlation values in case of evergreen vegetation are high during the whole year.

Referring to Figure 2.1b, high correlation values occur in the period when the tree has developed leaves on it (high AGB), that contributes to the so-called “volume scattering”, which is much lower in the period in which the tree is leafless. In fact, when the leaves fall from the tree, the biomass decreases, whilst the backscatter intensity experience an overall increase due to a stronger “double-bounce” scattering mechanism that occurs at the trunk-ground interface. On the contrary, referring to Figure 2.1a, the persistent presence of leaves generates an almost constant volumetric backscattering intensity along the whole year.

Overall, this work demonstrated the potential of Sentinel-1 SAR data in monitoring and mapping biomass using high spatial resolution SAR data. The results suggests that multitemporal C-band SAR data is fundamental for characterizing broadleaf forests.

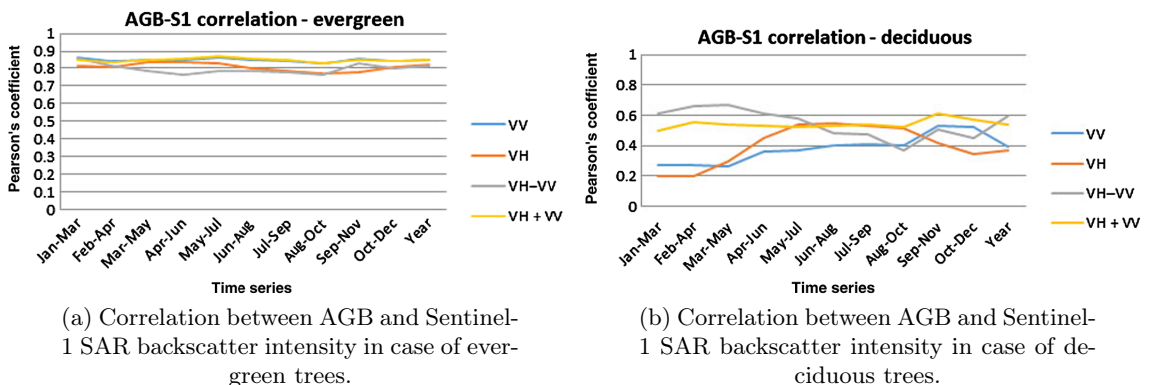


FIGURE 2.1: Charts of the Pearson correlation coefficient computed between SAR backscatter intensity and AGB in case of (a) evergreen species and (b) species. Image source: [92].

Notwithstanding the demonstrated ability of Sentinel-1 data in estimating AGB, the joint use of L-band data turned out to be necessary in order to improve AGB predictions.

Carrying on with the scientific literature review, a study is reported in [93] in which the Authors describe the important role of topographic variables in forest classification algorithms. Even if not directly related to the use of multitemporal SAR time series, this work provides interesting insights that can be exploited when forest classification is the task.

The Authors stated that, in general, performing detailed tree species classification using satellite data is very challenging mainly due to the limited availability of high-resolution remotely sensed data; moreover, the complex geometry of the different tree species and the lack of suitable classification approaches make this task difficult. In this work, it has been explored the potential of ZiYuan-3 (ZY-3) multi-spectral and stereo imagery from leaf-on and leaf-off season in order to distinguish land cover types, forest and tree species distributions. These classifications were made by testing six different classification algorithms, such as Artificial Neural Networks (ANN), k -Nearest Neighbors algorithms (kNN), Maximum Likelihood Classifiers (MLC), Support Vector Machines (SVM), Decision Tree algorithms (DT) and Random Forest classifiers (RF). The main results of this study can be here summarized:

- If only spectral bands are used to classify forest types, MLC outperforms other machine learning algorithms;
- Images acquire during leaf-off season lead to better classification performances than those acquired during leaf-on period. However, the combination of these images can significantly improve classification results by more than 10%. Of course, such improvement can be achieved only if bi-temporal data are used;
- The use of ancillary data such as spectral responses, textures and topographic information can improve the classification quality, especially when random forest and support vector machines are involved. By exploiting these variables, together with spectral data, it is possible to increase the classification result by more than 12%;

- The canopy height information may lead to better discrimination capabilities in the case of particular tree species. Accurate canopy height can be derived from LIDAR or space-borne stereo images and can improve forest classification;
- If general land cover mapping is the task, RF and SVM machine learning algorithms lead to the best classification accuracy, that is greater than 80%. If the focus is forest classification, then MLC outperforms RF and SVM, achieving more than 89% overall accuracy.

Based on the above discussion, this work demonstrated the need of specific classification approaches that correspond to different tree species, as no single classification method was able to achieve high classification accuracy on all the considered species. Moreover, this study highlights the importance of topographic variables such as elevation and slope, as they can discriminate classes having different spatial distribution (e.g., tree species living only at certain altitudes).

In study [94], the Authors leveraged on the joint use of Sentinel-1 and Landsat-8 time series to classify evergreen and deciduous broad-leaved forests, tropical monsoon forests, typical rain forests and others. On the one hand, Landsat-8 multispectral data can provide useful information for mapping and classifying forests; however, tropical areas, such as the Hainan Island in China analyzed in this work, are often covered by clouds, thus representing a critical limitation for optical data. On the contrary, SAR data can penetrate such harsh weather conditions and can provide useful information on forests able to characterize canopies.

The classification methodology relies on multitemporal Sentinel-1 and Landsat-8 time series and on field survey data; specifically a sampling campaign was conducted to collect more than 400 sample points, labelled with the specific type of forest.

Being a coherent imaging system, each pixel in SAR images represents the coherent addition of scatterers from a corresponding resolution cell; depending on the phase of the scatterers, they can interfere either in a constructively or destructively manner. This (unwanted) effect is called speckle noise, and translates into randomly bright and dark pixels (also known as “salt and pepper” effect), even within homogeneous regions. To reduce this effect, all Sentinel-1 data were pre-processed before actual use with a Refined

Lee filter (using a 7×7 kernel). The features used to feed the SVM algorithm are: one-year mean VV and VH composites for Sentinel-1, and Blue, Green, Red, NIR, SWIR and the NDVI vegetation index for Landsat-8.

Based on the SVM, the Authors proposed a two-stage classification strategy aimed at better distinguishing the different forest types. The first step consists of performing a “raw” classification aimed at distinguishing the main land cover types, present in the area of interest. These classes include open water, tropical forest, artificial forest, bare soil, coastal forest, artificial surface and other vegetation species. In this first step, the SVM was used, and images acquired in a similar period were used as input. At this point, a finer classification was carried out (again by using SVM) exploiting the multitemporal information. Thanks to this second stage, the natural tropical forest class can be clustered in finer, sub-classes, such as evergreen broad-leaved forest, tropical monsoon forest, evergreen and deciduous broad-leaved forest, typical tropical rain forest, evergreen coniferous forest and coastal forest.

Another very interesting paper found while reviewing the state-of-the-art methods for land cover classification using SAR time series is reported in [95]. The Authors of this work presented an analysis aimed at assessing the potential of using multitemporal C-band data for monitoring and classifying forests in northern Switzerland.

Previous studies on mixed temperate forest characterization focussed on the analysis of fully-polarimetric SAR data in order to associate a specific scattering mechanism to a specific forest type [38], or estimate forest density using supervised classifiers [96], whilst just few works analyzed long C-band backscatter time series over forest regions. The Authors of this research presented a methodology that aims at using VV and VH polarized Sentinel-1 imagery to classify one coniferous and two broad-leaved deciduous trees.

The analysis starts with the calibration of Sentinel-1 data; specifically, the data are radiometrically calibrated and terrain-geocoded, obtaining Geometrically Terrain Corrected (GTC, γ_E^0), using available Digital Terrain Models (DTM). Then, GTC data undergo a radiometric terrain correction using the procedure described in [97], that normalizes backscatter intensity values based on the illuminated local area (instead of using a simple ellipsoid model, as done for GTC products). The obtained terrain-corrected images (RTC, γ_T^0) have the advantage of being better interpretable over morphologically

complex areas, such as hills and mountains.

RTC images are then passed through a multitemporal despeckle filter aimed at reducing the speckle noise affecting them and increase the spatial resolution. Moreover, descending and ascending orbit RTC images acquired within a specific time window are combined by means of the Local Resolution Weighting (LRW, γ_{LRW}^0) approach to generate composite backscatter images (whose procedure is described in [98]). Specifically, it was observed that 24-days windows and a temporal sampling interval of 12 days turned out to be enough to observe phenology changes in backscatter time series, while also providing the complete coverage of the area of interest.

At this point, the LRW composite images were used to extract features that are useful to classify the different species within the study region. For each LRW image of the time sequence, several textural statistics are computed and plotted in time in order to carry out a preliminary analysis of the seasonal behaviour of the classes. These parameters are the median, 25% percentile and 75% percentile, and they are computed inside a specific ground truth mask related to a specific class (e.g., the evergreen forest class). Moreover, in order to better characterize the behaviour of the different classes, other temporal statistical parameters were derived from the time sequences of the three textural parameters previously computed. These parameters are: overall median of the medians, median of the 25% percentiles, median of the 75% percentiles, median of the medians during Winter (from the 1st of December to the 15th of March), median of the medians during Summer (from the 1st of June to the 25th of September) and the difference (delta) of the two latter variables (Winter minus Summer). To better clarify how all the features were extracted, the reader is referred to Figure 2.2.

Two additional descriptors are also derived, called “breakpoints”. These two parameters correspond to two specific dates on which structural changes in the annual time series are observed. Specifically, the first break date was set as the leaves emergency date; whereas the second break date was set as the fall of the leaves.

All the computed features were then used to feed a Random Forest (RF) classifier; the RF was chosen, as it was able to handle all the non-linear relationships that are present in the study data. Moreover, it was demonstrated in previous studies that RF classifiers fed with multitemporal C-band SAR data outperformed other types of classifiers.

Another paper that uses multitemporal Sentinel-1 time sequences is described in [99],

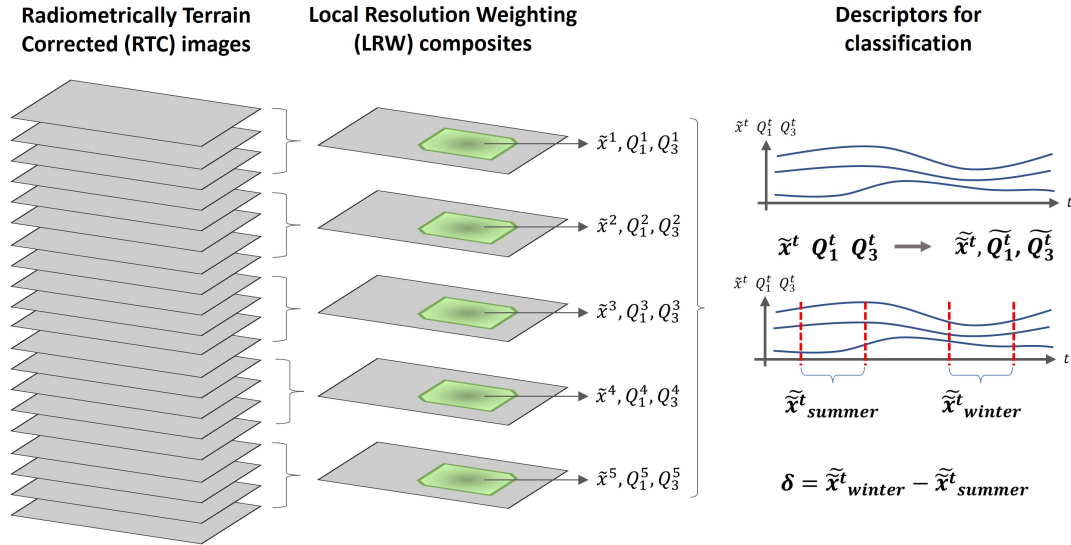


FIGURE 2.2: Feature extraction based on LRW composite images time series. \tilde{x}^N is the spatial median of the N -th LRW composite, Q_1^N is the spatial 25% percentile of the N -th LRW image, and Q_3^N is the spatial 75% percentile of the N -th LRW image (computed inside a mask).

where the Authors used joint Sentinel-1 and -2 (SAR and optical) data to generate crop maps in Belgium. The main finding of the study is that the combination of SAR and multispectral data always lead to better classification results, compared with single-sensor approaches. Moreover, the classification accuracy further increases from the beginning of the season (January) until June, as the differences between crops is maximum.

The developed methodology relies on a set of features extracted from Sentinel-1 and -2 time series. In particular, all the available Sentinel-1 images (from both A and B platforms) acquired within a 12-day window are used to generate a single image composite. Since each satellite has 12 days revisit time, there are at least two images in each 12-days time window. As shown in Figure 2.3, all the images belonging to each time window is converted from dB to natural units; then, a single mean composite is generated on a per-pixel basis and is re-converted to dB.

The averaging operation allowed to reduce speckle noise as it acted as a multitemporal filter, and to ensure the same amount of features for each single location within the study area. In this work, all the images acquired between the 1st of March and the 16th of August 2017 were used, resulting in a total of 60 ascending and descending VV and VH 12-day composites that were used as input features in the proposed classification procedure. It is important to note that, due to significant differences in terms of viewing

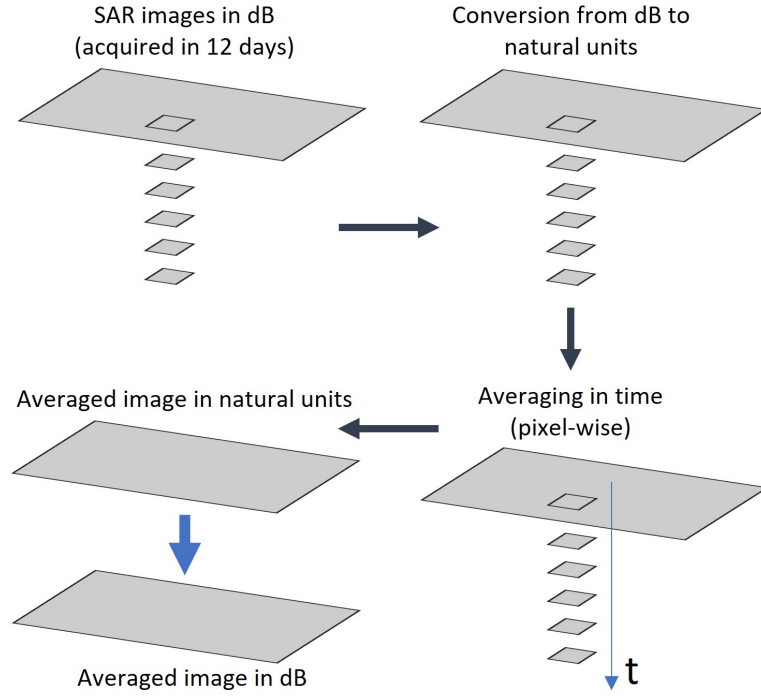


FIGURE 2.3: Generation of image composites from series of images acquired every 12 days.

angle between ascending and descending orbits, these were analyzed separately. Then, all the images undergone a speckle noise reduction through a refined Lee filter and the effects of incidence angle variations were reduced by means of a squared-cosine angle normalization, whose equation is reported below.

$$\sigma_{\theta_{ref}}^0 = \frac{\sigma_{\theta}^0 \cos^2(\theta_{ref})}{\cos^2(\theta)} \quad (2.3)$$

In Equation (2.3), which is a simplified incidence angle correction based on Lambert's law of optics, σ_{θ}^0 is the backscatter intensity measured under the observed incidence angle θ , and $\sigma_{\theta_{ref}}^0$ is the estimated intensity as it was measured with a reference incidence angle θ_{ref} .

Regarding Sentinel-2 optical data, after correcting them geometrically and atmospherically, a cloud-masking procedure was applied to each scene of the multitemporal stack. Then, the NDVI value was computed for each image, thus obtaining time sequences of NDVI values on a per-pixel basis. In order to overcome the loss of information due to

cloud coverage, the NDVI sequences were interpolated and smoothed using the pixel-wise weighted least squared approach, described in [100]. Such smoothing procedure was applied based on temporal windows of 10 days between the 1st of March 2017 and the 31st of August 201, for a total of 18 features used as input for a two-step Random Forest (RF) classifier.

The first classification step aims at classifying “macro-classes”, such as built-up, water, forest and crops. Whereas, in the second (and last) step, the “crop” class is split into different types: wheat, barley, rapeseed, maize, potatoes, beets, flax, grassland and others. To do so, the Authors of this work analyzed 18 different classification schemes:

1. In the first 6 schemes, only Sentinel-1 SAR data were used and the number of utilized images increased after each scheme:
 - (a) March;
 - (b) March - April;
 - (c) March - April - May;
 - (d) March - April - May - June;
 - (e) March - April - May - June - July;
 - (f) March - April - May - June - July - August
2. In the second group of 6 schemes, it was applied the same previous approach, but now using Sentinel-2 images.
3. In the third and last group of 6 schemes, it was applied the same previous approach, but now using both Sentinel-1 and -2 images.

For each classification scheme, the overall accuracy (OA) and Cohen’s kappa coefficient of agreement (k) were computed to assess the classifier performance. The proposed approach was able to achieve maximum OA of 82% and k coefficient of 0.77 when the March-to-July scheme based on both sources of data was used. The most important outcome of this study is the fact that the joint use of optical and radar data always leads to better results, compared with single-sensor based approaches.

In [101] the Authors used both multitemporal Sentinel-1 and -2 data to generate a 10-m spatial resolution land cover map for Iran with 13 classes, using a random forest classifier within the Google Earth Engine geospatial cloud computing platform. The Authors

also proposed a method based on Sentinel-2 data, that aims at migrating ground truth samples from a reference year to automatically generate a land cover map for any year of interest.

The methodology is based on the joint use of Sentinel-1 and -2 images acquired in year 2017, that are used to characterize 13 land cover types exploiting an object-based classification, in order to obtain “cleaner” results. The 13 classes were selected based on the thematic legend of a land cover map of year 2016, generated by the Iranian Space Agency (ISA) using low spatial resolution MODIS data (500 m). Ground truth data was collected manually by the Authors by photo-interpretation of the ISA LC map, cross-checking using high-resolution optical imagery that are available in Google Earth. The built dataset was then split in half, where 50% of it was used to train the random forest classifier, whereas the other 50% was used to validate the model.

The classes mapped by the Authors are: urban, water, wetland, kalut (Landforms created from soft riverbed and seabed sediment and silt through wind erosion), marshland, salty land (Areas with high soil salinity), clay, forest, outcrop (Unconsolidated deposits of bedrock and mountains appeared on the Earth’s surface), uncovered, plain (Plain bare soils without any vegetation cover), sand, farmland and rangeland.

Regarding the data selection, a total of 2.869 and 11.994 Sentinel-1 and Sentinel-2 images (acquired in year 2017) were used, respectively. In the case of Sentinel-1 SAR data, both VV and VH polarizations were selected. The main features that have been derived from these data are the mean and the median in the case of Sentinel-1 and -2, respectively. Specifically, a single, very large Sentinel-1 mosaic was generated by averaging all the acquisitions for each polarization. Similarly, a single median composite covering Iran was computed based on all Sentinel-2 acquisitions. In this case, all the images with cloud coverage greater than 10% were discarded from the computation, in order to create a stable and cloud-free composite. To reduce the computational processing cost, only some spectral bands were involved in the classification; in particular, for Sentinel-1 both VV and VH backscatter intensity values were used, while only the blue, green, red, NIR, RE and SWIR bands were utilized in the case of Sentinel-2 (so only 6 bands out of a total of 13). So in total, 8 features have been used as input variables in the random forest classifier, whose number of trees and node variables was chosen to be equal to the square root of the total number of variables (as suggested in [102]).

Since the RF classifier implemented in Earth Engine is pixel-based, the obtained result

was post-processed in order to produce an object-based LC map, which is much stable and led to better accuracy. To do so, a Simple Non-Iterative Clustering (SNIC) algorithm was applied to the Sentinel-2 median composite. Then, a majority voting technique was applied within each single segment extracted by the SNIC.

So in general, the methodology proposed by the Authors was able to accurately map the different land cover types, especially the forest class, which achieved alone a producer's accuracy of about 99.9%. For this reason, in future works, it is foreseen to split this class into sub-classes (enhancing the quality of the Iranian LC map).

In some studies, in order to produce land cover maps using multitemporal SAR data, the coherence information is exploited. An example of such approach is reported in study [103]. In particular, the Authors wanted to assess the performance of interferometric coherence compared to intensity information only when land cover mapping is the task. Seven different classification approaches were analyzed, including pixel- and object-based techniques and supervised and unsupervised classification methodologies. Following, some main conclusions:

- Interferometric coherence is a very important information when performing land cover classification; for three regions of interest analyzed in the study, an average of 75% overall accuracy was achieved;
- In general, coherence outperforms intensity for each considered scenario. However, using both sources of information led to better results, compared to those obtained by utilizing only one of them;
- If only the intensity information is used, then the VV channel performed better than VH channel in all the considered cases. Again, joint use of both polarizations is better;
- Also the training set plays an important role in land cover mapping. In fact, the higher the number of (good quality) training points, the higher the final map accuracy. In this study, the number of reference points was around 1% of the total image dimension and were randomly collected;
- As demonstrated in other studies, object-based approaches lead to better results with respect to pixel-based ones. However, the natural drawback of object-based methodologies is the loss of spatial detail.

Based on the above observations and on the findings of the study, the Authors demonstrated that coherence-based results provided higher accuracy than intensity-based approaches, when a temporal sampling of 6/12 days is considered.

In another study [104], the Authors demonstrated the utility of Sentinel-1A SAR data for the characterization of Land Use and Land Cover (LULC), to support natural resource management for land use planning and monitoring in Bac Lieu, a province of the Mekong Delta, in Vietnam.

In this work, 21 Sentinel-1 SAR images, all acquired in year 2016, are used; based on the methodology reported in [105], Grey Level Co-occurrence Matrices (GLCM) textures were computed based on the original stack of images. A GLCM is a second-order statistical texture measurement that considers the relationship between groups of two pixels. Specifically, the GLCM is a matrix of the frequencies of pixel pair values within a neighbourhood of a specific kernel size. Together with the original Sentinel-1 acquisitions, these textural images were used to train a random forest (RF) and a support vector machine (SVM) classifier, aimed at characterizing urban areas, forest, aquaculture and paddy rice fields. Therefore, 3 features are utilized for each image of the original stack: the VV and VH polarization images and the GLCM texture image.

Regarding the training reference points, 500 points were manually extracted from the official land use map of the Mekong Delta, also with the support of high-resolution imagery, such as Google Earth imagery and Planet data. The generated classification product was then post-processed in order to obtain a clearer map by means of a 8-neighbouring cells majority filter. Additionally, a class boundary smoothing and a region grouping algorithm was applied to further enhance the final result.

To validate the proposed methodology, 270 validation reference points were used and extracted in the same way as the training set. The study was able to achieve 91.8% and 94% overall accuracy during the dry and wet season, respectively. The Authors showed that multi-temporal Sentinel-1 SAR data is effective for land cover mapping and useful to understand spatial-temporal changes coastal landscapes, especially in tropical countries where frequent cloud cover obstructs optical remote sensing methodologies.

Another very interesting paper we found carrying out the scientific literature review is referenced in [85]. In this work, the Authors leveraged on the huge computational power of Google Earth Engine to classify wide areas ($100 \times 100 \text{ km}^2$ tiles) in the West of England. To do so, data sets were generated based on Sentinel-1, Sentinel-2 and

Landsat-8 images, acquired from October 2016 and September 2017 (so to highlight the seasonality of particular classes, such as crops).

Almost all the features used in this work were obtained by “temporal aggregation” of optical and SAR data over a specified time window. For instance, a “one-interval” dataset was obtained by reducing all the available images (acquired within the year of interest) to one single image composite. Whereas, a “two-interval” dataset was generated by aggregating images acquired in two different periods of the year of interest (e.g., two 6-months composites); in this way, two single image composites are generated. In Figure 2.4 the feature selection scheme used in this work is reported.

From Figure 2.4 it is possible to note that, in case of multispectral data, a cloud-masking algorithm was applied to each scene in order to obtain cloud-free image composites. In addition to the composites, elevation information was added to the set of features. Specifically, elevation, aspect and slope were used as features with the aim of enhancing the classifier performance and increasing the final accuracy. Different data sets were generated using different sensors; for example, the “s1_med4” dataset (based on Sentinel-1 data) was generated by subdividing the whole year of interest in 4 intervals of same length. Then, for each of the 4 obtained time series, a single median composite is computed for each polarization (VV, VH and VV-VH). So in this case, the number of features is equal to the number of composites multiplied by the number of bands (4 images times 3 bands).

Sentinel-1 data was pre-processed using a spatial Lee filter, aimed at reducing speckle noise; both channels were used as input features, together with the VV-VH combination,

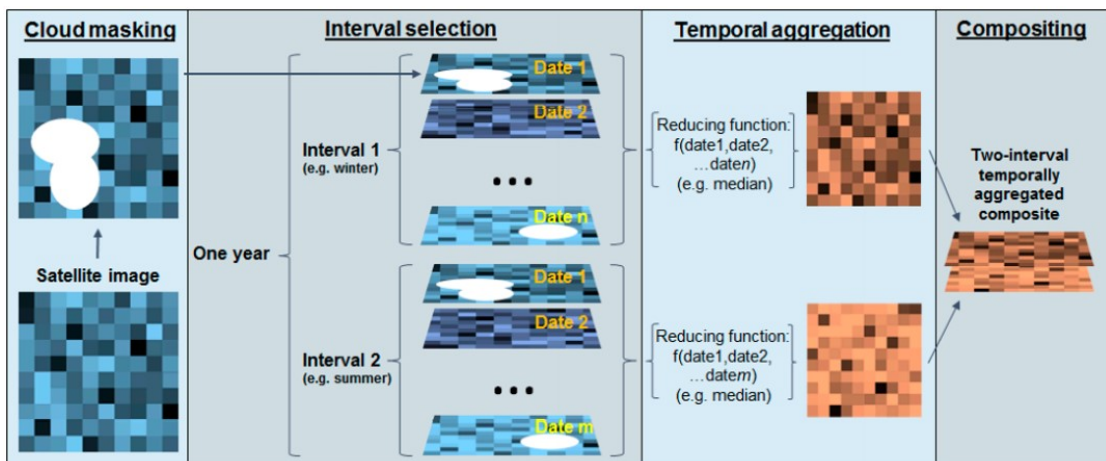


FIGURE 2.4: Feature selection procedure. Image source: [85].

that was demonstrated to play a key role in land cover classification procedures. Also the use of temporal SAR composites was demonstrated to be an excellent strategy to overcome some weather conditions, such a strong wind.

Regarding the training dataset, 10000 reference points were randomly collected for 13 classes from a local land use map (the UK Broad Habitat Land Cover Map) and used to train a random forest classifier. Results showed that joint use of optical and SAR data led to better results, compared with single-sensor methods. Specifically, combined data sets (S1/S2 or S1/S2/L8) outperformed single-sensor data sets, while data sets based only on spectral indices achieved the lowest accuracy levels. This study provides a very useful comparison of the accuracy among multi- and single-sensor data for land cover mapping, as well as providing a range of combinations and parameters that are used as features input for the classification model.

2.2 Scientific literature review on water body mapping

2.2.1 Optical-based water body mapping methodologies

In the context of climate change studies, increasingly detailed information on land cover and land use to precisely model and predict climate are needed. A fundamental land cover type that needs to be constantly monitored by the climate change community is water. Due to its typical spectral signature, water is well-distinguishable in multispectral data, and several spectral indices have been designed to detect water bodies by means of optical data, such as the Normalized Vegetation Index (NDVI), Normalized Difference Water Index (NDWI) [84], Modified Normalized Difference Water Index (MNDWI) [106] and the Automated Water Extraction Index (AWEI) [107].

In general, almost all the existing optical-based water bodies methodologies rely on the typical low reflectance values of water in the infrared bands which, compared to other land covers, is a unique feature. Based on this principle, a large number of algorithms have been developed that aim at extracting water bodies from time sequences of optical data. Moreover, water bodies represent a very dynamic type of land cover, as they rapidly change in time due to both natural and human-induced factors; therefore, approaches based on spatio-temporal analysis are widely used, as such technique is essential to assess the availability of water resources at the regional and global scale.

In [108], sequences of MODIS data were used to characterize short- and long-term lake inundations; the Authors of this work extracted water boundaries using the Floating Algae Index (FAI), which is computed based on the red and shortwave-infrared bands of the E.M. spectrum, and used it with a gradient method to detect the water/land interface of the inundation.

The work reported in [25] generated a global surface water dataset at 30 m scale through an automatic algorithm applied to Landsat surface reflectance values, spectral indices (both water and vegetation indices), terrain metrics and existing coarse-resolution water maps (based on MODIS data). The proposed methodology relied on a two-stages approach: the first stage, namely, the deductive stage, focussed on the generation of reference water pixels by comparing spectral (water-related) indices and topographic variables with MODIS water estimation at coarse resolution; the second stage, namely, the inductive stage, was based on decision trees aimed at optimizing and refine prior information.

In [109], decision trees were built based on multispectral bands to discriminate water bodies from other land cover types leveraging on Landsat data. The aim of the overall study was to map historical flood extents for inundation frequency estimation; despite the achieved good results, limitations related to the use of Landsat emerged in terms of revisit time and cloud coverage issues.

The Authors of [110] used a set of water-related spectral indices to characterize both flood extents, vegetation and moisture content based on pixel-based classification procedure applied to time sequences of MODIS data.

In [111], a fine-resolution water mask for North America, and that has been derived from Landsat data, has been presented. The methodology relies on dynamic thresholding of the mNDWI multispectral index.

The work carried out in [112] was about the use of time sequences of Landsat TM/ETM+ data to map the extent and dynamics of surface water and flooding based on random forest models (an ensemble classifier). Thanks to the high spatial and temporal resolution Landsat data, the Authors were able to quantify small scale changes of water bodies' extents.

In [113] several supervised classifiers such as Maximum Likelihood Classifier (MLC), Artificial Neural Networks (ANN) and Object-Based Image Analysis were employed to classify water, built-up, bare soil, low vegetation and forest land covers, based on Sentinel-2 time series.

The study reported in [114] demonstrated that spatio-temporal patterns were useful to characterize irrigated cultures using an object-based analysis applied to Sentinel-2 time series. The methodology relied on segmentation to obtain delineated fields, and on a random forest based classification step aimed at identifying croplands. Finally, a decision tree was in charge of distinguish irrigated crops and rain-fed crops based on NDVI time series.

In [115], the performance of Sentinel-2 multispectral data for detecting urban surface water was evaluated. Specifically, the Authors proposed an automatic classification approach based on dynamic thresholding and object-based segmentation, and different water indices were compared. Results showed that urban surface water can be successfully mapped using the modified NDWI (mNDWI).

The Authors of [116] proposed a novel water index computed on Sentinel-2's red-edge and shortwave infrared bands, namely, the SWI (Sentinel-2 Water Index). Their study showed that the SWI was able to provide better contrast than NDWI, and that a method based on the integration of SWI and Otsu algorithms could accurately extract different types of water bodies.

Similarly to what emerged from the technical literature regarding vegetation land cover mapping methods, also in the case of water body mapping, a large number of algorithms and approaches based on time sequence of multispectral data exists. However, all the above cited works have limitations. The most critical one is represented by cloud coverage; for instance, clouds are almost always associated to rainfall-induced flood events, exactly when inundation detection is important. Moreover, optical sensors cannot gather information from regions with water beneath vegetation. More in general, clouds represent a severe limitation for continuous monitoring and frequent water body map generation, especially at large scale. Finally, many of the cited works lack of automatism, they cannot be applied to other regions than the one used in the study and, often, the temporal and spatial resolution is not enough for several applications. On the other hand, SAR signals can penetrate almost all weather conditions and can thus monitor ideally any region of the Earth surface; depending on the operational frequency, SAR signals can also penetrate through vegetation and provide information regarding the condition of the soil beneath.

Compared to optical-based approaches, the technical literature does not offer a large number of methodologies aimed at classify water bodies extent at large (up to global)

scale and at high spatial resolution using time sequences of SAR data. Moreover, the existing approaches all have limitations, that are going to be discussed in the next Section. Given this context, in this thesis work the potential of multitemporal SAR data to map water bodies at the global scale is assessed. To this aim, in the following Section, a deep literature review on water body mapping using multitemporal SAR data is given.

2.2.2 SAR-based water body mapping methodologies

The first relevant work emerged from the literature review is reported in [117], where the Authors used Sentinel-1 SAR data to derive a land cover map for Lagos state, Nigeria. To this aim, a supervised pixel-based classification methodology was applied to the data. In this work, water bodies, bare land, vegetation and urban areas were classified by means of Maximum Likelihood Classification (MLC) algorithm that has been trained with manually collected reference points. The focus of this work was to determine the best features possible, when water body mapping is the task. Based on empirical approaches, the Authors identified VH as the best polarization to classify water class; however, the use of this channel alone was not suitable to classify, for instance, urban areas. Therefore, the final set of SAR features that turned out to lead to a better discrimination between classes is composed by VH, VV+VH and VV-VH polarization compositions. Despite the good obtained classification results, some confusion errors occurred. In fact, due to the similar geometric characteristics of water class, even lots of actual bare soil pixels were classified as water, and vice versa.

The Authors also noticed that their proposed methodology based on MLC, achieved lower accuracy values than other studies that extract water bodies using, for example, Otsu thresholding or k -means clustering approaches.

In [118] is described a methodology aimed at evaluating the potential of RADARSAT-1 data in monitoring and mapping flood water in flood-prone areas. In particular, the main goals of the work are to mapping inundated areas using multitemporal RADARSAT-1 data, to compute flood duration and to map the propagation of flood waves using multi-date flood maps. To this aim, HH-polarized images were used, as this polarization is less sensitive to minor vertical differences on the surface of the water (e.g., waves). These data were pre-processed in order to reduce speckle noise (by means of a median filter with kernel 3×3) and correct for geometric distortions (leveraging on manually

distributed ground control points, or GCPs). Since inundated areas appear in dark tone in SAR images, it is possible to separate them from non-inundated regions based on the roughness of the surface on water and land. To do so, the Authors converted SAR backscattering coefficients to Digital Numbers (DN), with 8 bit of radiometric resolution. Then, the flooded regions were extracted using a specific radiometric threshold.

The areas detected using such thresholding approach is a combination of flooded and permanent water areas. Therefore, it is necessary to eliminate permanent water bodies from the final flood map. To do so, a permanent water bodies map was generated based on a pre-flood image, acquired by the IRS-1C satellite. This paper describes a methodology aimed at effectively extracting flooded areas from SAR images and, based on the findings, the methodology can also be applied to extract permanent water bodies.

Another interesting study that uses a simple thresholding approach to classify permanent water bodies in multitemporal SAR data is reported in [43]. Here the Authors leverage on two very important features related to the characterization of water in radar data: low backscatter intensity and very high temporal variability. Specifically, in C-band, water bodies are characterized by low backscatter intensity values and by high temporal variability due to the waves (i.e., high standard deviation). These two features can be extracted from multitemporal SAR data and used in a water classification model. In this work, Envisat Advanced SAR (ASAR) Wide Swath Mode (WSM) data were considered and analyzed over six test sites, having different types of water bodies and land surfaces. Each SAR image was first multi-looked, terrain geocoded and speckle filtered using a multi-channel filter. Then, starting from the stack of SAR images, the overall (per-pixel) mean, minimum and standard deviation values were computed. Figure 2.5 shows an RGB composite, where the Red (R) channel is represented by the mean SAR backscatter image, the Green (G) by the minimum image and the Blue (B) by the standard deviation (i.e., temporal variability) image.

Referring to Figure 2.5, water bodies appear bluish due to the low minimum backscatter (thus, no green) and high temporal variability (thus, strong blue channel). On the other hand, other land cover types are characterized by a lower contribution of the blue channel, as they are more stable in time (e.g., urban areas).

The signature analysis carried out by the Authors suggested that a simple decision algorithm, based on the location of a measurement in terms of minimum and standard



FIGURE 2.5: False color composite of average SAR backscatter (red), minimum SAR backscatter (green) and standard deviation (blue) for the Netherlands. Dataset: Envisat ASAR Wide Swath Mode. Image source: [43].

deviation backscatter values, can be enough to separate permanent water bodies and other land cover types. The equation proposed by the Authors, and aimed at separating water and non-water classes, is:

$$y = 3.5x - 28 \tag{2.4}$$

where x is the standard deviation in dB, and y the minimum backscatter value in dB. Of course, the identified equation corresponds to the best classification results for the study area (the Netherlands). Furthermore, to reduce classification errors, all the pixel labelled as “water” that are located on slopes greater than 10 degrees are, instead, re-labelled as “non-water” class. The slope information was derived from the SRTM-3 Digital Elevation Model (DEM). The proposed methodology was able to achieve accuracy values on the order of 90%, even if several omission errors were made, due to the inability of the algorithm in detecting small water bodies.

In [119], the Authors demonstrated that the joint use of Sentinel-1 time series data and a metric based on the product of co- and cross-polarized channels can lead to an efficient support of the so-called “smart water management”. In particular, a methodology was developed to extract the waterline and estimate the extent of water-covered areas using

VV and VH polarizations and an unsupervised classifier.

The algorithm develops in two phases: enhancement of the separability between water and land, and edge detection method. Regarding the first step, this relates to the pre-processing of SAR data. Specifically, the data are multi-looked, speckle filtered, resampled and co-registered. Whereas, the second step aims at extracting waterlines exploiting Single- (SP) and Dual-polarization (DP) channels.

Exploiting dual-polarimetric data, it is possible to estimate waterline using different combinations of co- and cross-polarized channels; in this work, the Authors used the metric based on the product of co- and cross-polarized data (amplitude information) reported in Equation (2.5),

$$r = \langle |S_{VV}| \cdot |S_{VH}| \rangle \quad (2.5)$$

where $|\cdot|$ and $\langle \cdot \rangle$ represent the modulus and the spatial averaging, respectively. This metric was employed, as it was demonstrated in previous works to enhance sea/land contrast when coastline extraction is the task. Based on the experiment that have been carried out, the Authors of this article were able draw several conclusions:

- Sentinel-1 SAR data allow to track not only normal season trends, but also anomalies;
- Dual-polarization (DP) measurements lead to better results, compared with single-polarization ones. This fact was observed in terms of overall accuracy and quality of the extracted profile of the water body;
- In single-polarization data are used, then the co-polarized (e.g., VV) channel performs better than cross-polarized ones (e.g., VH), as the latter tends to overestimate water-covered areas, thus leading to numerous false positive occurrences;
- In general, time-series analysis can be successfully employed to discriminate permanent water bodies (such as reservoir areas) from regions covered by water only for a limited amount of time during the year.

Another interesting paper was found during the literature review, that deals with supervised learning models aimed at mapping inland water bodies using Sentinel data at the

state level [120].

In this work, the Authors exploited both SAR and multispectral Sentinel data for water body mapping. Even if the majority of the water mapping algorithms rely on optical data, the choice to include also SAR data is mainly driven by the fact that SAR signals can provide information almost in any weather condition, thus allowing constant monitoring of important water bodies or wetlands. Moreover, such data fusion for has been proved to be much more robust than single-sensor based approaches.

Regarding the proposed water body mapping methodology, first several pre-processing steps are carried out, in order to overcome some single-sensor limitations (i.e., cloud coverage for optical data and speckle noise for SAR data). An effective way to reduce speckle noise, without lose spatial details, is based on the generation of a temporal mean composite image. To this aim, all the Sentinel-1 SAR images acquired within a specific time window are temporally averaged on a per-pixel basis. As a result, the obtained composite is cleaner and more stable than single-date acquisitions.

Similarly, to limit the issue represented by clouds in Sentinel-2 optical data, a single temporal median composite is generated from a stack of images acquire within a specific time window. In this case, the median composite exhibits pixels whose values are in between very low reflectance values (dark, shadowed areas) and very high values (bright, clouded areas). To visually appreciate its effects, In Figure 2.6 an example of such compositing is reported.

Regarding Sentinel-1, both VV and VH channels (of the mean composite) are used as features; whereas, for Sentinel-2, all 10 and 20 m bands are used, together with two spectral indices: the Normalized Difference Vegetation Index (NDVI) and the Modified Normalized Difference Water Index (MNDWI), which is an extension of the NDWI.

Another interesting aspect of this work is represented by the methodology employed to sample reference, training data. In fact, in order to build a well-generalizing model, is is necessary to sample points belonging to a wide variety of water body types, from large lakes, to small and shallow rivers. To do so and, most importantly, to avoid time-expensive manual approaches, an automatic sampling procedure is proposed based on the use of the OpenStreetMap (OSM) layer. Specifically, only water bodies (such as rivers, lakes, etc.) are extracted from the layer and used for sampling reference points; moreover, to avoid selecting pixels on the water bodies boundaries, while ensuring selection of only “pure” water pixels, a negative buffering of 20 m has been applied on all the extracted

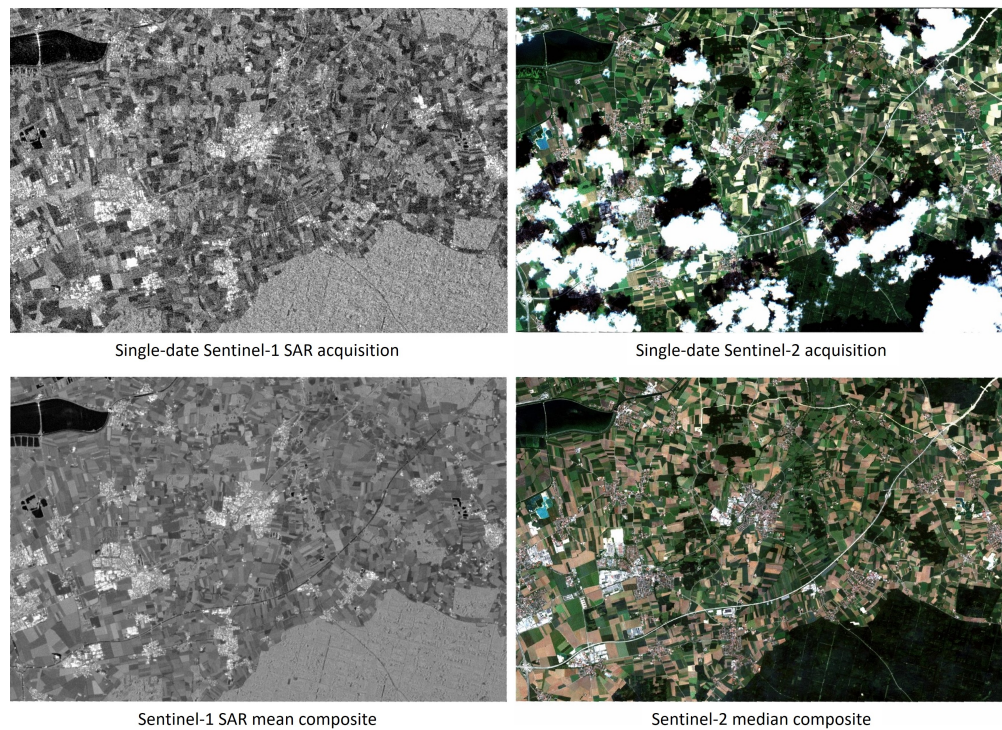


FIGURE 2.6: On the left: comparison between single-date Sentinel-1 image (top) and temporal mean composite (bottom). On the right: comparison between single-date (clouded) Sentinel-2 image (top) and temporal median composite (bottom).

water polygons. Then, all polygons with area greater than 10000 m^2 are removed from the list of water polygons, and the remaining are used for sampling. Finally, within the Google Earth Engine platform, a Support Vector Machine (SVM) with Radial Basis Function (RBF) kernel is trained with the training set built using the method described above.

Based on the achieved overall results (around 98%), the Authors concluded that a fully automatic large-scale water body monitoring and mapping is possible. To this aim, the configuration that exhibited the best results is a pixel-based fusion of Sentinel-1 and -2 data. They also stated that, in order to improve the proposed methodology, post-processing steps aimed at removing false positive occurrences should be implemented. Moreover, dedicated speckle noise filtering and cloud removal algorithms should be used, in order to unlock the possibility of weekly monitoring of water bodies.

In study [121], an automatic method for water cover detection based on the k -means clustering was developed within the Google Earth Engine cloud computing platform. The algorithm relies on Sentinel-1 SAR data, that were used to monitor surface water changes

from October 2014 to November 2018 in the protected area of the Upper-Kiskunsag Alkaline Lakes region in Danube-Tisza Interfluve, Hungary, with the aim of supporting nature protection planning.

Sentinel-1 SAR data is first of all pre-processed; specifically, SAR backscatter coefficients must be normalized, to account for incidence angle effects. In fact, backscatter values measured with a small incidence angle are higher than those measured with a larger angle, considering the same identical area. To limit incidence angle effects, the commonly-used technique is the cosine squared correction method, previously introduced in the present scientific literature review, whose equation is reported in (2.3).

The second step provides for the removal of all the SAR images acquired during strong wind conditions (with speed greater than 12 km/h), as waves induced by wind increase the surface roughness, thus increasing the intensity of the backscatter. To do so, the Authors used wind speed data extracted from the 20 km spatial resolution Climate Forecast System Version 2 (CFSV2) dataset.

The third step consists of the reduction of speckle noise using a refined Lee filter algorithm. Thanks to this procedure, it was able to reduce speckle noise, while maintaining high frequency details. Finally, the last step was to compute monthly mean composites from the “clean” stack of SAR images for both ascending and descending orbits, separately.

Regarding the classification procedure, this is based on the k -means clustering algorithm, with a number of clusters $k = 15$, using both VV and VH channels as input features. Whereas, regarding the training set, 10000 random pixels were collected over the area of interest. Given the clusterer result, water clusters were identified by visual inspection, prior knowledge of the study area and empirical threshold limits for backscatter values. Once the water cluster is correctly identified, it is extracted and converted to a binary raster layer, where ones represent water and zeroes non-water pixels.

In other works, fully-polarized SAR data are exploited to detect water bodies using a combination of radiometric thresholding and image segmentation. An example is reported in [122], where the Authors used quad-polarized RADARSAT-2 data for monitoring changes in surface water extent within wetlands or other areas.

First, all RADARSAT-2 images undergo a pre-processing step aimed at calibrating the data (from raw data to σ^0), reducing the effects of speckle noise using a polarimetric Lee filter, orthorectifying using the rational polynomial coefficients provided with the images

metadata and the Shuttle RADAR Topography Mission (SRTM) digital elevation model (DEM), and co-registering all the images by means of a Fast Fourier Transform (FFT) phase-matching algorithm. The final pre-processing step consists of a simple linear-to-dB conversion, to highlight the histogram tails of each image.

The methodology derived two different thresholds that are used for two different purposes: surface water detection and water boundary detection (in the description of this paper, we will focus only on the former one). To detect surface water, histograms of either HH or HV polarizations are generated and used to select a consistent threshold. Since several previous studies have shown that cross-polarized backscatter intensity values (VH and HV) are less affected by wind than co-polarized signals, in this study the Authors decided to use HV-polarized imagery, so to detect water regardless of the roughness conditions. However, the described methodology can be applied to any polarization, as it based only on the analysis of bi-modal distributions of SAR intensity values (i.e., water and non-water modes). The histogram is then log-scaled in the vertical axis to better visualize the low probability mode. At this point, a high-order polynomial fitting is performed, and the threshold is set to the local minimum between the two modes.

To group adjacent pixels with similar characteristics in the HV image, the SLIC superpixel algorithm was used. Based on an empirical approach, it was found that subdividing the entire image into 1000×1000 smaller tiles, each containing 3600 superpixels, was the best approach for identifying potential water bodies of any size. In order to build the final water map, the HV intensity image is segmented and all the pixels inside each superpixel are averaged. This average value is then compared with the previously found threshold and, if it is lower than such threshold, than the superpixel is labelled as “water”. To further improve the final classification result, water boundaries (obtained by thresholding the variance SAR image) are intersected with all the regions identified as water in the classification map; only those water regions that are adjacent to the boundaries are kept in the final water product. From Figure 2.7 it is possible to observe that the methodology also allows to cleanup the final result, as some misclassified superpixels (e.g., roads) are excluded from the final water product.

Another very interesting water body detection methodology is described in [123]. Here, the Authors used TanDEM-X quick-look images at 50 m spatial resolution acquired from 2011 to 2016, to generate a global water body layer exploiting the bistatic interferometric coherence as the main source of information.

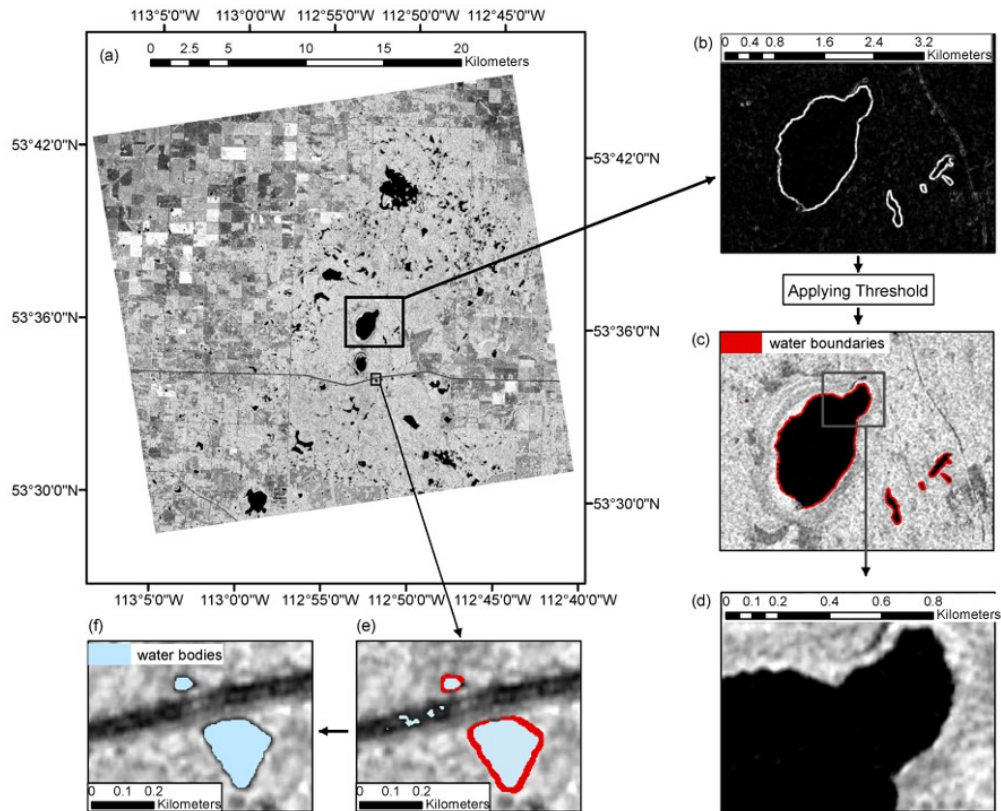


FIGURE 2.7: (a) RADARSAT-2 HV-polarized image, acquired over the Prairie Pothole Region; (b) variance texture image; (c) water boundaries extracted by thresholding the variance image; (d) segmented image generated using SLIC superpixel algorithm; (e) water bodies and superpixel segmentation; (f) final water bodies after intersection between detected water bodies and water boundaries.

SAR interferometry (InSAR), in fact, introduces the use of the interferometric coherence for water mapping purposes. Interferometric coherence is defined as the normalized cross-correlation coefficient between a pair of interferometric images, and represents the measure of the quality of an interferogram [124]. In InSAR data, water bodies usually exhibit very low coherence values and, in general, have a more stable behaviour and are less influenced by waves and wind (that causes the surface roughness to vary significantly).

In repeat-pass systems, the InSAR coherence is affected by temporal decorrelation, which causes the coherence to decrease, thus making almost impossible to discriminate unstable land cover classes (such as forests and crop fields) from water bodies. Whereas, in bistatic systems such as TanDEM-X, the pair of interferometric images is acquired at the same identical time. In this situation, InSAR data is no longer affected by temporal decorrelation.

The proposed algorithm can be summarized in three main steps: the first step relates

to the data preparation, in order to derive the input features, suitable for water detection in InSAR data. The second step deals with the placement of seed points for the detection algorithms. Finally, the last step deals with the actual classification of all the independent scenes and mosaicking of the final global map.

Regarding the data preparation step, this consists of masking out the typical geometric distortions affecting SAR data, i.e., layover and shadow regions. These regions were labelled as “non-water” in the images by filtering high slopes based on an empirical slope threshold set to 10 degrees. The second step consists of the placement of seeds, that must be performed before the application of the watershed segmentation algorithm. In this work, “seeds” are defined as the catchment basin present on a topographic surface.

Referring to Figure 2.8, the plotted surface represents the height of each single point in the map; therefore, if water is dropped on such surface, it will reach a minimum height and it will stop in that area. All the points of the surface that collect water drops (thus reaching a local minimum) are called seeds, and are used as starting points for detecting water bodies in the proposed algorithm.

Regarding the classification methodology, this relies on the watershed segmentation algorithm, a widely used approach in image segmentation applications. Being a non-parametric method, it has the advantage that no empirical threshold values are needed.

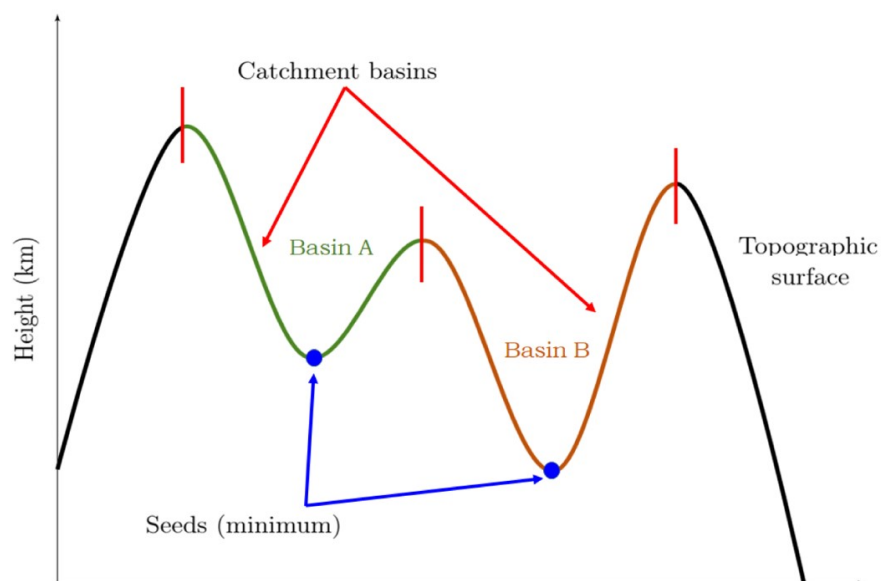


FIGURE 2.8: Principle of water seeds placement for the watershed algorithm. They are identified in blue as the topographic minimum of catchment basins.

Starting from the previously identified seeds, the watershed evaluates an input pixel as an elevation information. Then, each basin is iteratively “flooded”, and all the areas where the floods from different basins meet are identified as contours, representing the different partitions of the image, which can be now segmented. In this procedure, the topographic representation of the input pair of TanDEM-X images is obtained using a Scharr transform, a filter used to identify gradient edges and features by means of a 2-D kernel (representing the first derivatives).

Eventually, the described watershed algorithm is applied on the interferometric pair, and the resulting segmented regions (where the seeds were places) are identified as water bodies.

The final global water map is generated by mosaicking $1^\circ \times 1^\circ$ tiles. To generate such mosaic, a 3-dimensional data cube for each tile is created by stacking the water rasters on a latitude (ϕ) and longitude (λ) grid. Then, for each (ϕ, λ) coordinate, the probability to be water is computed. The final binary classification of water and non-water is performed by selecting a threshold of 35% on the probability value (based on empirical experiments): pixel values above such threshold are labelled as “water”, while pixels whose values are below the threshold are labelled as “non-water”. This final global water mosaic was validated by comparison with other existing global products, achieving high overall accuracy, with F-score index around 90% in case of tiles with water class covering more than 1% of the total tile area.

The work reported in [125], describes how the Authors leveraged on the computational power offered by Google Earth Engine to develop a large-scale water mapping system, based on a random forest classifier and joint use of Sentinel-1, Landsat-7 ETM+ and Landsat-9 OLI data.

Together with satellite data, auxiliary data were also used, including the SRTM at 30 m spatial resolution DEM, the Artificial Impervious Surface data of year 2015 and the Global Land Ice Measurements from Space (GLIMS) Glacier database. Moreover, the JRC GSW dataset was used to collect both training and validation points.

Regarding the satellite data, all the available Top-of-Atmosphere (TOA) Landsat-7 images, Surface Reflectance (SR) Landsat-8 images and Ground Range Detected (GRD) Sentinel-1 images were collected between January 2019 and June 2020. Landsat-7 images were used as the main source of information, while the Quality Assessment (QA) band of Landsat-8 was mainly used to remove clouds, snow and shadows in Landsat-7 images.

The SRTM elevation model was used to derive slope information, that was used to remove false positive occurrences over morphologically complex areas, such as hills and mountains, by means of a simple thresholding procedure. The GLIMS glacier dataset was used to remove glaciers pixels from the final water map, and the impervious surface data were used to remove built-up areas interference.

The proposed method can be summarized in four steps. In the first one, the training set was built by automatic sampling of the JRC GSW water product. In the second step, based on a combination of Landsat-7 and 8 and Sentinel-1 data, monthly images composites were created. The third step consists of extracting features suitable for surface water detection; these include spectral reflectance features, terrain characteristics, SAR backscatter features, textural features and spectral indices. In the final step, a random forest classifier was trained within each $5^\circ \times 5^\circ$ geographical tile, and the accuracy of the classification was assessed by comparing the obtained result with JRC GSW data.

In this work, the Author proposed an automatic reference points sampling procedure, as many previous studies leverage on visual interpretation and manual collection of sampling points. Of course, such approach represents a severe limitation when classifying wide areas is the task. Therefore, the JRC GSW dataset was used to automatically collect reference points, thanks to the fact that this dataset has high spatial resolution (30 m), is generated based on expert knowledge and it is updated every month. For each tile, the ratio between water and non-water training points was 1:3; specifically, 1000 water and 3000 non-water points were automatically sampled.

The features that have been used in this classification model were derived within the Google Earth Engine platform. After the removal of clouds, shadows and snow pixels, monthly median composites were generated based on Landsat-7 and Sentinel-1 imagery (the latter were down-sampled to 30 m, in order to match the spatial resolution of Landsat-7 data). Regarding the spectral bands, from Landsat-7 bands from B1 to B5 and B7 were selected, while bands from B2 to B7 were selected from Landsat-8 data. Moreover, spectral indices suitable for water detection were obtained, such as the NDWI, MNDWI, NDVI and NDBI. In addition to these indices, the NIR band was exploited to compute the GLCM matrix in order to extract local textural features, such as variance, dissimilarity and entropy.

Regarding Sentinel-1 SAR data, VV and VH monthly composites were generated and used as input classification features. The last input feature is represented by the slope

and aspect information; in this work, the slope was also used to clean up the final water map, by removing those pixels wrongly labelled as water by the classifier, and located over regions associated with slopes greater than 10 degrees.

2.3 Scientific literature review on crop management using satellite data

Remote sensing based methodologies play a very important role in crop classification, crop monitoring and yield assessment. Thanks to satellite technologies, in fact, it is possible to monitor the agricultural production system and the biological life cycle of crops. Moreover, as these parameters rapidly change in time, satellite-based approaches allow to promptly provide information related to the crop status thanks to the high revisit frequency of satellite constellations.

In the field of agriculture, satellite data can be employed in many applications, such as yield estimation, precision agriculture, crop stress monitoring, crop growth monitoring, land use changes, nutrient and water content estimation, Nitrogen levels monitoring, weed identification, crop disease monitoring and others.

In this thesis, particular attention will be devoted to the characterization of organic farming practices.

2.3.1 Organic farming practices

Unlike conventional farming practices, organic farming aims at producing food using natural substances and processes, resulting into limited environmental impact by encouraging maintenance of biodiversity, regional ecological balances, soil fertility, water savings and energy savings, and more.

Organic food is generally expensive, due to costly production practices, but still accepted by the consumer because of its features. Recently, the number of Italian organic rice producers has been growing at a pace that raised suspicion about the likelihood of such an “avalanche” transition and the full compliance of the actors involved with the strict regulations of the organic crop growing. This phenomenon is extremely harmful, to all “real organic” producers, and also to final consumers, increasingly wary of organic labels. In this framework, the market need that has been identified and assessed is twofold: 1)

genuine organic producers wish to provide supplemental evidence about the authenticity of their organic production; 2) organic food distributors wish to obtain independent assessment about self-declared organic producers.

This delicate type of agriculture requires great additional care in growing because, for instance, it is forbidden the use of chemicals in crop treatment: every single required action must be planned in advance in order to not compromise the harvest.

Within the framework of the Italian Space Agency (ASI) “MultiBigSARData” and the Joint Research Centre (JRC) “GEOINT” project, described more in detail in Chapter 5, methodologies aimed at supporting organic farming and monitor agronomic practices compliance using both spaceborne SAR and multispectral data are proposed. Specifically, the project focussed on organic rice crops monitoring and, to date, no works or projects on monitoring of organic cultures from space can were carried out; this aspect makes the work carried out in this Ph.D. thesis particularly innovative.

2.3.2 The organic crops growing panorama

In the context of preliminary works, several aspects of organic rice cultivation that may be monitored and assessed from space have been identified using the information provided by rounds of interviews with local farmers and producers. An important technical detail regards the sequence of the cultures; in a 4- to 5-year cycle, the practice of organic rice cultivation is characterized by the so-called “crop rotation”, which is mandatory for qualifying a crop as organic. The actual occurrence of such rotation can be assessed through satellite observation by analysing the Sentinels’ multi-annual data records on the monitored field. This technical aspect implies the identification from space of all the species emerging in the same field in a cycle of 4 to 5 years.

Another aspect, which is subject to monitoring from space, and which represents the real challenge in the organic crop field, is weed control. Such management must be planned largely in advance in order to avoid compromising the production, and it is based on three main alternative agronomic techniques: grooming, green mulching and transplanting.

The technique of green mulching involves using green manure, a mixture of plant materials, named “cover crops”, incorporated into the soil before or soon after the sowing phase to improve the soil. The interesting aspect for certification - and one that can be monitored from space - is that a possible, non-compliant, weedicide activity can be

detected from space thanks to drying up and yellowing of plants within 24-36 hours after the treatment. Therefore, a variation in the spectral response should emerge and be subject to space-based identification.

A third fundamental aspect which in particular regards aquatic cultivars, differentiating organic production from non-organic one, is the management of the water network. This is about planning inflow and drainage of water from the field chamber, and consequently about monitoring water level in the field (for example, in the case of rice crops). From a technical point of view, it is not possible to reliably detect water depth from satellite, still, we can determine the moment in time when the inflow and outflow of water takes place. Since the management of water is correlated to the specific agronomic technique used, this assessment is extremely significant in verifying whether the previously declared organic technique was actually implemented or not. This aspect can be successfully assessed by exploiting radar data. In fact, monitoring of water is reliable and effective using space-borne radar data; moreover, radar signals are insensitive to weather conditions and can therefore provide data in cloudy conditions as well.

Another very important aspect is related to tillage techniques. Tillage can indeed be performed with different techniques, resulting in diverse impacts on soil properties; *minimum tillage* is a typical organic technique minimizing stubble burial and overturning of clods. Organic agriculture favours minimum tillage because it reduces erosion and surface runoff. Different approaches to tillage translate into different features at the air-to-soil interface and different characteristics of the soil, thus activating different backscattering mechanisms during spaceborne radar observation.

As mentioned at the beginning of this section, in the process of building the state-of-the-art in organic crop monitoring and support to certification, we realized that no papers on monitoring of organic crops from space can be found in the scientific literature. Therefore, each of the required technical aspects related to organic farming practices were individually investigated. Note that some of the above discussed aspects have been deeply investigated and reported in Chapter 5; some other cannot fit into the framework of the present thesis. In particular, the topics that have been widely analyzed are weed-killer activities detection, surface roughness estimation (with special regards to plowing-and-harrowing as opposed to minimum tillage) and fertilization activities detection (such as

spreading of manure). A dedicated literature review on these topics is given in Chapter 5.

Since no previous studies on monitoring of organic farming practices have been carried out, in the next section some papers that analyzed the relationship between crop management operations and satellite data are described. Even if these studies are not directly related to organic farming monitoring, some of the described aspects provided us with clues on how to exploit such methodologies for organic crop monitoring purposes.

2.3.3 Relationship between crop management operations and space-borne data

The first analyzed study is reported in [65]. The authors proposed the development of a 3 color-coded warning alert system (green, yellow and red) for the management and control of direct aids to the farmers in the context of the Common Agricultural Policy (CAP). The system is based on the analysis of the crops' spectral response during their growth cycle and on machine learning techniques. The system is based on three main steps, and, at the end of each step, a warning colour is assigned to each analysed parcel. The steps are here summarized:

1. Use of Vegetation Indices (VI) temporal metrics allow to perform an initial validation of the farmers' declarations. This step is therefore aimed at identifying false declarations, i.e., crop fields that do not show their typical growth cycle along the season. This is achieved by analyzing the VI curves for each analyzed field. The monitored parameters are related to the most important stages of vegetative growth: onset of greenness, maturation stage and onset of senescence. These parameters can be extrapolated by the VI time series themselves, using the methods explained in [126]. Analyzing the VI temporal metrics and the corresponding Cumulative Density Functions (CDF), it is possible to select the best threshold for class separability. These metrics are the minimum and maximum value, the mean value, the standard deviation value, and the minimum and the maximum gradient value extracted from four different vegetation indices (NDVI, RedEdge Chlorophyll Index, NDWI and Brightness Index);

2. The interpolated surface reflectance (SR) time series and the “compliant” parcels identified in step 1 are used to train a random forest model. At this point, all the fields whose predicted crop is consistent with the declared crop (ground truth) are flagged as “compliant”. For the classifier, all the reference fields validated as truthful (compliant) in the step 1, were split into 75% training set and 25% validation set;
3. The final step consists of the refinement of the obtained classification. The misclassification occurrences to be corrected are represented by temporary crop fields being classified as vineyard or olive grove (due to the high representativeness of these two permanent crops in the polygons dataset). The purpose of this step is to identify whether a parcel corresponds to a temporary or permanent crop. To do so, an additional feature is added as an auxiliary input feature. This feature is the texture, extracted from a GLCM matrix. As a matter of fact, the texture allows to evaluate the crop density and shape (whereas, the vegetation index, such as the NDVI, enables the evaluation of the growth status). The texture feature was computed for each synthetic panchromatic band, resulting from blending different proportions of the visible blue (11%), green (59%) and red (30%) bands in the original time series, and only one of the possible textural features was used (the GLCM-Mean), computed using a kernel of size 3×3 .

Another interesting study found carrying out the literature review is described in [66]. In this work, the Authors showed a method aimed at detecting and monitoring weed management using glyphosate-based herbicides (GBH) in agricultural practices using Sentinel-2 time series. The main result of the study is that broadband NDVI calculated from S2 data showed explicit feedback after the herbicide treatment. The final goal of the study is to use the results to provide the necessary transparency about weed treatment in agricultural practices and to support environmental monitoring.

To this aim, Sentinel-2 data was acquired and processed to level L2A (Bottom Of Atmosphere, or BOA) and four spectral indices were computed, based on the scientific literature review. These spectral indices are derived from green (band 3), red (band 4) and NIR (band 8) regions of the spectrum. Whereas, the computed spectral indices are: NDVI (Normalized Difference Vegetation Index), GNDVI (Green Normalized Difference Vegetation Index), CVI (Chlorophyll Vegetation Index) and SAVI (Soil Adjusted Vegetation Index). For each test site and vegetation index, the following statistics were calculated: mean, median, quantile at 25% and 75%. The final results were compared

against reference fields, i.e., fields without glyphosate treatment. In Figure 2.9 an example of temporal dynamic of the NDVI index for each test site is shown.

From the plot of Figure 2.9, day 0 represents the day of GBH treatment. The main result is that all spectral indices decrease consequently over time after weed treatment. Just two days after treatment, it is possible to detect such operation due to a decrease of the indices values. The study demonstrated that the sensitivity of the NDVI index to herbicide applications clearly exists.

Regarding works related with fertilization detection and monitoring, it is interesting to report study [64]. The objective of this work is to measure the sensitivity of the NDVI signal to on-farm fertility treatments applied to five locally important crops: cotton, pearl millet, sorghum, maize and peanut.

The methodology can be summarized in four main blocks. In the first one, the seasonal temporal NDVI profiles are presented for each crop type and fertilization level. Then, the mean and standard deviation were computed from the NDVI time series for each crop type, from emergence to senescence. The second step consists of detecting the fertilization treatment at the field scale, for each crop and for each acquisition date. To this aim, the variance components are estimated using the ANOVA (ANalysis Of VAriance) variance

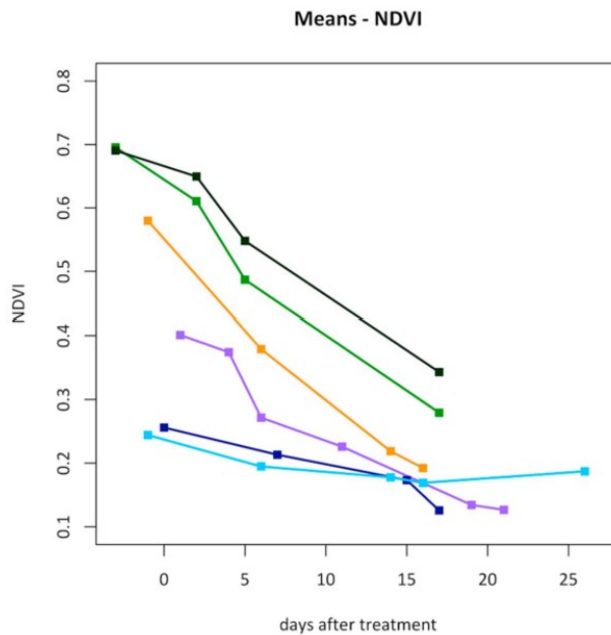


FIGURE 2.9: Temporal dynamic of NDVI for the test sites. The x-axes represent the number of days after GBH treatment. Day 0 is the day of GBH treatment. The y-axes represent the mean value of the NDVI of the appropriate study site.

decomposition method. The variance is decomposed for each field at each date (from crop emergence to harvest). For this method, the determination coefficients R^2 of a linear model estimates the part of variance which is caused by fertilization, with respect to the total variance. A higher median R^2 indicates a better discrimination of fertilization levels, using NDVI for a given crop at a given date.

The third block is about the assessment of the relationship between NDVI and plant growth (e.g., ground coverage fraction and height). Specifically, linear relationships between the variables were established for each crop type using least-squares. Finally, the last step consists of comparing the effects of fertilization treatments to variations occurring within and between fields in relation to position, farming practices and soil type. To this aim, a hierarchical linear model was set up for each crop type to decompose the total NDVI variance, in order to estimate the contributions of three components that cause variation: plot (induced by fertility treatments), field (induced mainly by other management factors) and landscape (mostly induced by environmental factors, such as soil, elevation and others).

A relevant analyzed work is reported in [69], where time series of coherence and backscatter coefficients were used to determine crop harvesting dates, leveraging on Sentinel-1 Single Look Complex (SLC) SAR data.

The main concept of the methodology relies on the features of radar images coherence: during the periods of time when fully developed vegetation is present in crop fields (or when farming operations are performed), very low coherence values are registered. On the other hand, when the field is harvested (and therefore it almost behaves as a bare soil) relatively high coherence values are measured. Such concept is exploited in this work, by associating the end of harvesting to a steep coherence increase.

The utilized Sentinel-1 SLC images were acquired from the 1st of May 2018 to the 28th of October 2018, every 12 days. Regarding the intensity information, as opposed to co-polarized data (VV and HH), VH-polarized images were used to detect harvest operations, as this polarization was demonstrated to better correlate backscatter intensity and vegetation-related parameter, such as the Leaf Area Index (LAI). Moreover, the cross-polarized channels are more sensitive to volume scattering than co-polarized ones. Whereas, coherence maps were generated based on VV-polarized imagery, as the VH-based coherence turned out to be less sensitive to changes within the crop field, based on several studies. Then, for each reference polygon (crop field), time series of averaged

backscatter intensity σ^0 and coherence C_{VV} values were generated.

Based on the experiments, time sequences of coherence values can behave mainly in two manners. The coherence can increase due to the ripening and drying up of the crops; then, during the harvesting period, it typically drops. After dropping, it starts to increase again, due to the static (post harvesting) condition. The second scenario is that coherence remains almost unaltered and with low values, until the end of the harvest operation, which causes the coherence to steeply increase. In order to claim a crop field “harvested”, at least 70% of the points randomly collected inside the field (around 30 points per polygon) must be labelled as “harvested”, based on the correspondent σ^0 and C_{VV} time sequences. Overall, the proposed methodology was able to estimate harvesting dates with a relatively high degree of accuracy, considering the temporal resolution of the Sentinel-1 constellation; in fact, the mean absolute error was 6.5 days (and can decrease if the temporal resolution of SAR satellites increases).

In [127], Sentinel-1 data are used to automatically map rice fields based on the features hidden in time series of backscatter values. In fact, as schematically depicted in Figure 2.10, different rice crops growing stages translate into roughness changes of the soil, that can be detected in SAR data.

Specifically, by means of the superpixel segmentation algorithm, the Authors of this work generated time sequences of backscatter values for each segment (rice field) considered in the study. The methodology can be summarized in the following five main steps:

1. Selection of ascending and descending VV- and VH-polarized Interferometric Wide Swath (IW) SAR data;

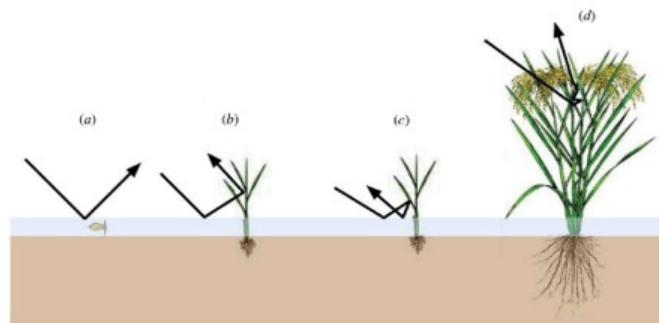


FIGURE 2.10: Interaction between SAR signals and the different growing stages of rice crops.

2. Pre-processing of the data by using the conventional Sentinel-1 data calibration chain, available within the SNAP software;
3. Segmentation of the rice fields using the Simple Linear Iterative Clustering (SLIC) algorithm;
4. Extraction of time series of backscatter value for each segment and for each date (averaging all the pixel values within the segment);
5. All the extracted time sequences are then classified using a 5-nodes decision tree, based on radiometric thresholds.

Notwithstanding the relatively effectiveness of this approach, the use of decision trees built based on the local geographical features makes the algorithm less flexible in terms of transferability to other regions of the World.

One of the most important operation that is performed in rice fields is the flooding of the rice field chamber. In the technical literature there exist numerous papers that automatically detect rice fields from space, leveraging the peculiar signal caused by such operation. Among the studies found in the literature, it is possible to cite the work in [68], where the Authors estimated flooding, emergency and growing dates based on SAR time series. The described methodology relies on multitemporal Sentinel-1 data and exploits the typical “V” shape of the SAR time series, caused by the field filled with water (thus, by a smooth surface), before plants emergency (the moment when crops break the water/air interface). After an analysis on these SAR time sequences, the Authors proposed a classification model based on radiometric thresholds (similarly to the study described above).

Another very interesting study is reported in [71]. Here, COSMO-SkyMed (CSK) data were used to automatically determine rice-cultivated ares, sowing dates and discriminate between short and long cycle varieties. The methodology relies on the three main phases, summarized below:

1. Analysis and interpretation of SAR data and in situ data. Regarding in situ data, these refer to sowing dates, harvesting dates, rice variety, plants height and phenological stages. Whereas, SAR data were calibrated and used to extract backscatter values based on the “age” of the plant, i.e., the crop status after sowing;

2. Extraction of SAR indicators for the identification of different varieties of rice. Specifically, SAR time sequences of HH- and (HH/VV)-polarized (ratio) CSK images were used to derive statistics; the maximum and minimum value derived from HH CSK sequences were used to identify rice fields, while the maximum value of (HH/VV)-polarized sequences were used to discriminate short and long cycle species (the maximum peak in the case of long cycle varieties shows up around 60 days after sowing, and has a value greater than ~ 10 dB with respect to the ~ 8 dB value registered around 50 days after sowing for short cycle varieties).
3. Determination of sowing dates leveraging the date corresponding to the sprouting stage, identified in HH/VV sequences. Sowing dates are determined based on the region of interest, agricultural practices (e.g., sowing or transplant) and incidence angle.

This study achieve good overall accuracy, which was around 92% in rice grown area, 96% on rice short or long cycle and a RMS error of 4.3 days in sowing date. Still, the non transferability of the methodology represents a strong limitation.

Another parameter that can be estimated from space is the yield of a crop field. Typically expressed in tons per hectare [$\frac{t}{ha}$], this parameter allows to discriminate an organic rice field from a conventional one, as they are characterized by very different yields. Study [70] leverages multitemporal Sentinel-1 SAR data and Sentinel-2 multispectral data to train an Artificial Neural Network (ANN) to make predictions on the yield of a given rice field. The methodology can be summarized in the following three steps:

1. Co-registration between SAR data and multispectral data; the latter were chosen based on a “minimum cloud coverage” criterion;
2. Sampling of ground truth data. Specifically, the NDVI and NDWI spectral indices derived from Sentinel-2 were used within a stratified random sampling procedure. These two indices were used to determine the health of rice fields along the different growing stages;
3. Training of the ANN network using VV- and VH-polarized Sentinel-1 SAR data. The RMS error is then considered to measure the difference between predicted and actual yield.

The methodology described in this study was able to achieve about 91% overall accuracy, when VH-polarized SAR data were used (VV-polarized data performed worse).

The methodology described in this study showed that using VH-polarized data instead of VV-polarized data lead to better results, with a coefficient of determination R^2 and root mean square error (RMSE) of 0.72 and 600.11 kg/ha, respectively. Whereas, for VV-polarization data the results were $R^2 = 0.26$ and $RMSE = 948.46 \text{ kg} \cdot \text{ha}^{-1}$. Overall, the study demonstrates that the effective use of ANN model may provide reliable yield estimation accuracy from remotely sensed imagery alone.

Given the carried out analysis of the most relevant studies for characterizing farming practices, it is clear that some parameters can be modelled using SAR data, some others require multispectral data. In general, all those operations that somehow modify the chemical composition of the soil (e.g., fertilization, weeding, etc.) are better detectable in optical data; on the other hand, operation that modify the soil from a physical point of view (e.g., tillage, harvest, etc.) can be characterized using SAR data.

2.4 Overall considerations on the reviewed state-of-the-art methodologies

Notwithstanding the demonstrated effectiveness of the studies in the technical literature, these present limitations. The most important ones - and that are going to be tackled in this thesis - can be here summarized:

- To date, most of the methodologies lack of complete automatism. Despite the degree of automatism, in fact, human intervention is always needed;
- Referring to the point above, training and validation data sets are usually built by means of experience, photointerpretation and manual collection of reference samples, to train a classification model and to validate it;
- In most cases, is not possible to transfer a classification model from a region of interest to another, without user intervention and without a-priori information. Generally, classification models and algorithms are tailored to a specific area of interest, and all the parameters are “tuned” based on that;

- Usually, land cover classification is performed over relatively small areas, mainly due to computational costs and to the non-transferability of the model to wider (or different) areas;
- Methodologies based only on optical data reduce their classification capabilities over strongly cloud-covered regions;
- Most of the studies based on SAR data do not account for terrain-induced geometrical distortions, thus they cannot be applied over morphologically complex regions (e.g., mountainous areas);
- Many land cover maps do not exploit the great potential of spatial and temporal resolution SAR data.

Chapter 3

Vegetation land cover monitoring and mapping¹

Based on the scientific literature review on vegetation land cover monitoring and mapping methodologies, in this Chapter an algorithm that aims at classifying several vegetation classes is presented and discussed in detail. The objective of the proposed algorithm is to overcome the most severe limitations found in previous studies, as discussed in Section 2.4.

3.1 The European Space Agency Climate Change Initiative (CCI+) project

The first part of this thesis was carried out within the framework of the European Space Agency (ESA) “Climate Change Initiative Extension (CCI+) Phase 1: New Essential Climate Variables (New ECVS).

¹this chapter is based on material published in the works:

- [128] Marzi, David, and Paolo Gamba. “Global Vegetation Mapping for ESA Climate Change Initiative Project Leveraging Multitemporal High Resolution Sentinel-1 SAR Data.” IGARSS 2020-2020 IEEE International Geoscience and Remote Sensing Symposium. IEEE, 2020.
- [129] Marzi, David, Shantanu Todmal, and Paolo Gamba. “Mapping Globally Using Multitemporal Sentinel-1 SAR: A Semiautomatic Approach.” 2021 IEEE International India Geoscience and Remote Sensing Symposium (InGARSS). IEEE, 2021.
- [130] Sorriso, Antonietta, David Marzi, and Paolo Gamba. “A General Land Cover Classification Framework for Sentinel-1 SAR Data.” 2021 IEEE 6th International Forum on Research and Technology for Society and Industry (RTSI). IEEE, 2021.

The main purpose of the CCI+ project is to continue the achievements made within the CCI (Climate Change Initiative) project, with the following new focus points of the CCI+ project:

- Developing new ECVs which are not included in the previous CCI project;
- Additional research and development studies on existing ECVs already established in the CCI project;
- Exploitation of the different ECVs;
- Supporting activities on knowledge exchange;
- Interaction between Earth Observation (EO) science community and climate science community;
- Prototype product generation and system definition.

These needs emerged, as long-term global EO archives are nowadays available to the scientific and user community from past, current and future ESA EO missions for climate change purposes. The CCI+ project aim at defining and validating innovative approaches for continuously generating and updating a comprehensive, long term set of ECV products, by focussing on the consistency and quality analysis from a climate model perspective.

Among the various ECV products, the “High Resolution (HR) Land Cover ECV” represents a new variable, which focusses on the impact of land cover (LC) and land cover changes (LCC) on climate changes, with the main objective of assessing in detail the role of the spatial resolution of the detected changes in order to support climate modelling research.

Even if it cannot be directly used as an input to climate change models, land cover is an essential climate variable to quantify surface energy, water fluxes and the sources of greenhouse gasses, to monitor variation in land use and land surface and to characterize the impacts of extreme events, such as floods, heatwaves, droughts, hurricanes and others.

Land cover change is, in fact, both a cause and a consequence of climate change, either when the change is induced by human beings or generated by natural events. The previous CCI project focussed on the generation of Moderate Resolution (MR) Land Cover

ECV maps at the global scale; specifically, the MRLC CCI provided annual LC maps at 300 m spatial resolution for years from 1992 to 2015. The CCI project introduced a new concept of global land cover mapping with respect to the past years, by considering a multi-sensor approach and generating time series of interoperable and consistent global annual products.

With the CCI+ project, the goal is to extend and improve this concept by increasing the spatial resolution of the obtained maps, which represents an innovation and an unprecedented attempt. From the climatological point of view, the consistency of the generated maps is vital to monitor and understand ongoing processes such as desertification, urbanization, soil erosion, deforestation, arctic greening and the influence of land cover changes on the physical climate system itself. Therefore, the possibility of using high resolution (10 to 30 m) remotely sensed data to produce land cover maps and detect changes opens the door to a wide range of possibilities for climate change analysis, including improved quantification of energy, water and carbon budgets of the terrestrial ecosystem.

3.2 Study areas

For the vegetation classification system described in this chapter and for the water extraction algorithm described in Chapter 4, almost the same test areas were involved, as they are areas of interest within the CCI+ project. The size of each area is equal to a standard Sentinel-2 tile, which corresponds to a size of $100 \times 100 \text{ km}^2$. Therefore, in this Section all the study areas are introduced and described at once.

As shown in Figure 3.1, the utilized test sites are located in Siberia (tile 42WXS), Italy (tiles 32TNR and 32TPP), Amazonia (tile 21KUQ) and Africa (tile 37PCP). These test sites were chosen as they offer completely different geo-morphology and climate, thus, they allow to test the effectiveness of the developed methodologies in very diverse conditions and environments.

The first region (tile 21KUQ), reported in Figure 3.2, concerns the Amazon basin which has for several decades focus the attention of the scientific community due to large deforestation rates and potential associated large-scale climate impacts. Agricultural expansion and climate variability have become important agents of disturbance in the Amazon basin, mainly in the southern and eastern portions. Although Amazonian forests



FIGURE 3.1: Overview of all the test regions: Siberia (tile 42WXS), Italy (tiles 32TNR and 32TPP), Amazonia (tile 21KUQ) and Africa (tile 37PCP). The background image is the visualization of the OpenStreetMap basemap.

have considerable resilience to moderate annual drought, the interactions between deforestation, fire and drought potentially lead to losses of carbon storage and changes in regional precipitation patterns and river discharge, with some signs of a transition to a disturbance-dominated regime.

This region is dominated by vegetation and hot tropical weather, and represents a perfect example of SAR data usefulness: in fact, due to such harsh climate, it is very difficult to obtain cloud-free optical images over this area. Temperature ranges from 22 to 40 °C, and the rainfall is persistent during most of the year, ranging from 200 to 320 mm every single month with an average of 89% of humidity.

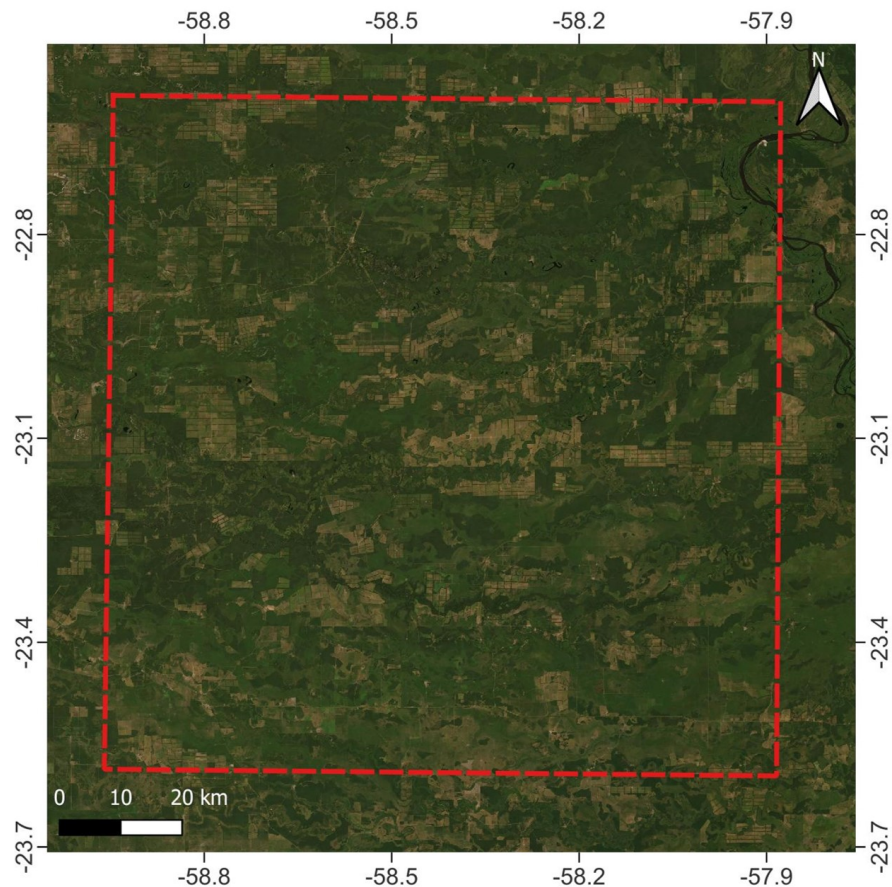


FIGURE 3.2: Detailed overview of the Amazonian tile (21KUQ). The red, dashed line represents the Sentinel-2 tile boundaries, and the background image is the ESRI World Imagery base map.

In Figure 3.3 the second region of interest (tile 37PCP) is reported; this is the Sahel band in Africa, including West and East Africa which is a very complex climatic region which experiences severe climatic events (droughts in the 70's and 80's and floods more recent) often attributed to climate warming and for which the future predictions (amplitude of the regional warming and rainfall changes) are very uncertain. Present climate and especially the position and seasonal dynamics of the monsoons (the West African and the Indian ones) are generally not correctly represented in most of the climate models. Recently, many studies highlighted the key role of the surface processes on the representation of the near surface meteorological variables and their consequences on the turbulence in the mixing layer and the initiation of the precipitation. In the eastern part of the Sahelian band, the role of El Niño in the initiation of dramatic drought events in the horn of Africa is also not really understood and deserves more work to better predict and help mitigation studies.

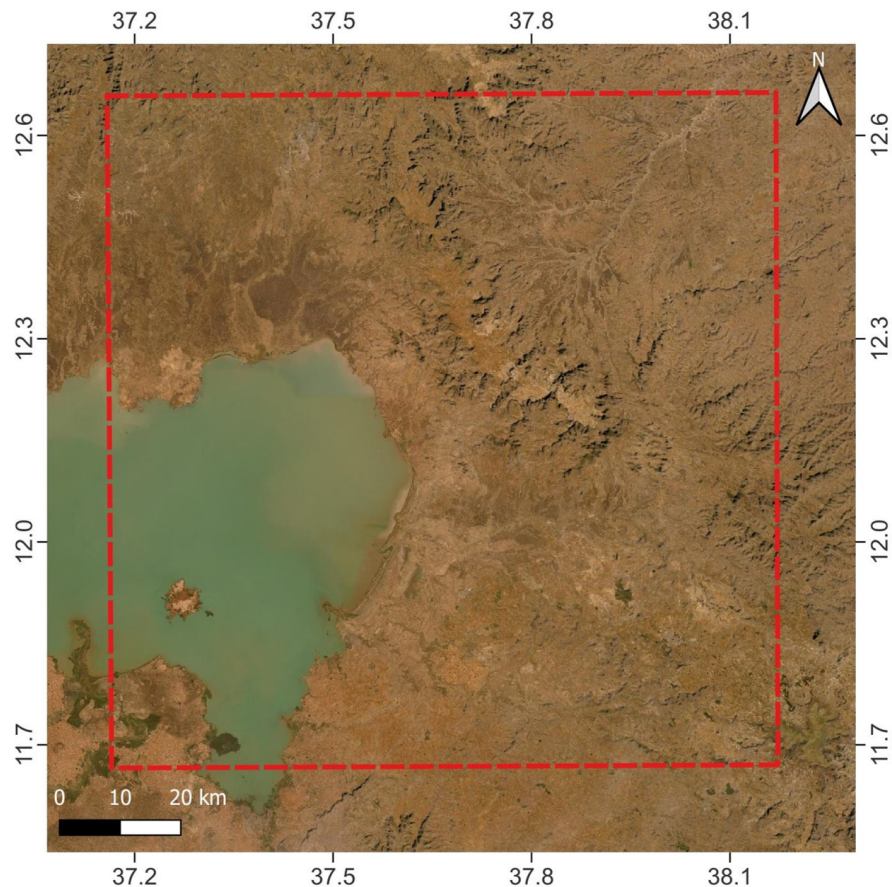


FIGURE 3.3: Detailed overview of the African tile (37PCP). The red, dashed line represents the Sentinel-2 tile boundaries, and the background image is the ESRI World Imagery base map.

The third region, represented in Figure 3.4 is situated in the northern high latitudes, for which future climate changes are expected to be particularly strong, a phenomenon known as “polar amplification”. In Siberia, complex climate feedbacks over land, implicating natural and human factors, may further amplify these changes and make this region as a possible hot spot of future climate changes. Siberia represents 10% of land surface and 30% of forested surfaces globally. The warmer temperatures and increased winter rainfall have promoted increases in biosphere’s activity and longer active seasons. Land cover changes have been reported with the displacement of the forest-shrubs-grasslands-transition zone to the north. In addition, changes in land cover may impact directly the fate of the carbon stored in permafrost. which in turn will affect long-term terrestrial carbon balance and ultimately climate change. From a morphological point of view, this region is characterized by many complex rivers and water bodies, covered with ice and snow for $\sim 75\%$ of the year. Extremely cold weather is dominant during the whole year,

with temperatures ranging from -40 to 20 °C. Again, the advantage of using multitemporal SAR data is clear: SAR signals can penetrate clouds and rain, ensuring periodic data acquisitions;

The last two considered regions, shown in Figures 3.5 and 3.6, are located in northern and central Italy, respectively. These regions were not considered by the CCI+ project, but given their diverse morphological characteristics compared to all the other sites, we decided to include them as test regions. Tile 32TNR (Figure 3.5) lies exactly in the middle of the Lombardy region, and is characterized by the so-called Mediterranean, with temperatures ranging from 20 to 35 °C during Summer (with the exception of the extreme hot temperatures reaching 45 °C and severe drought registered during the present Summer 2022), and from -1 to 10 °C in Winter. Clouds, fog and haze are often present, and the region includes a small minority of mountains areas in the north, that make it complex in terms of morphology. Finally, tile 32TPP (3.6) is located in the

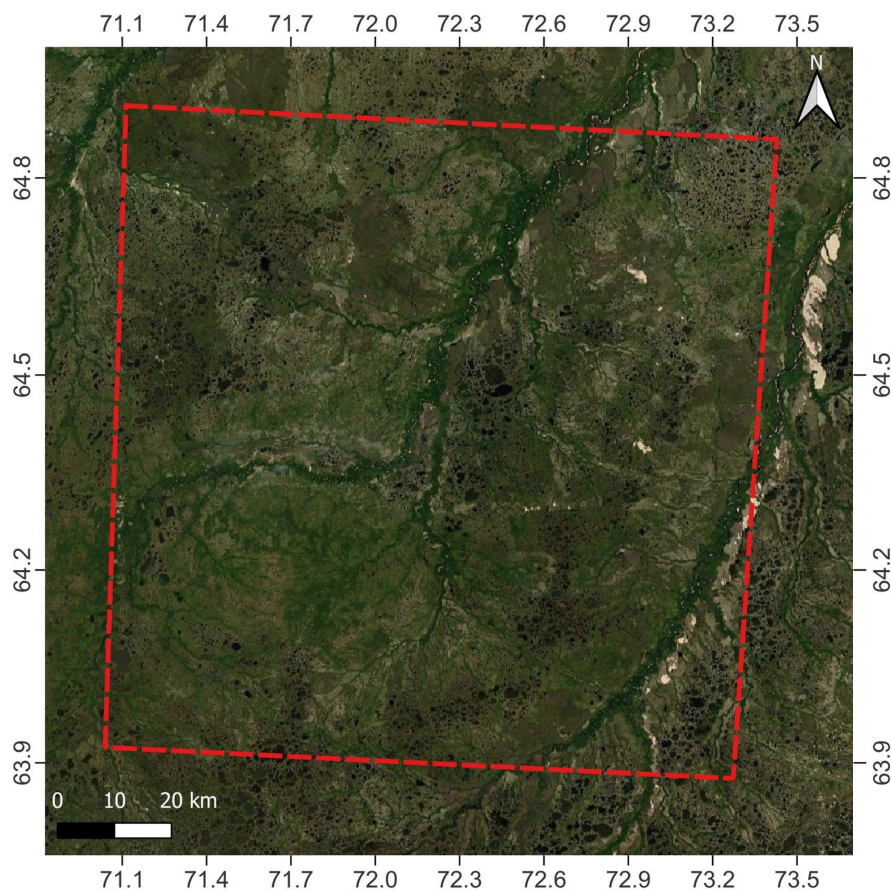


FIGURE 3.4: Detailed overview of the Siberian tile (42WXS). The red, dashed line represents the Sentinel-2 tile boundaries, and the background image is the ESRI World Imagery base map.

Tuscany region, central Italy. Here the climate is generally mild, with some differences depending on the geography of each area; the coast and valleys tend to have hotter summers than the hills or mountains although the coast benefits from breezes off the sea for cooler temperatures even in those warmer months. Temperature in Winter are, on average, around 7 °C along the coast, while they can range between 3.5 to 5.5 °C inland. Also this tile presents diverse morphological features, from few plains to hills (which characterize nearly two-thirds of the total area) and mountains chains.

3.3 Sentinel-1 SAR data

In Table 3.1 is provided a list of a number of available SAR sensors which can be used for land cover mapping and monitoring. However, among these satellites, the Copernicus' Sentinel constellation appeared to be the best source of data. Their free and open data

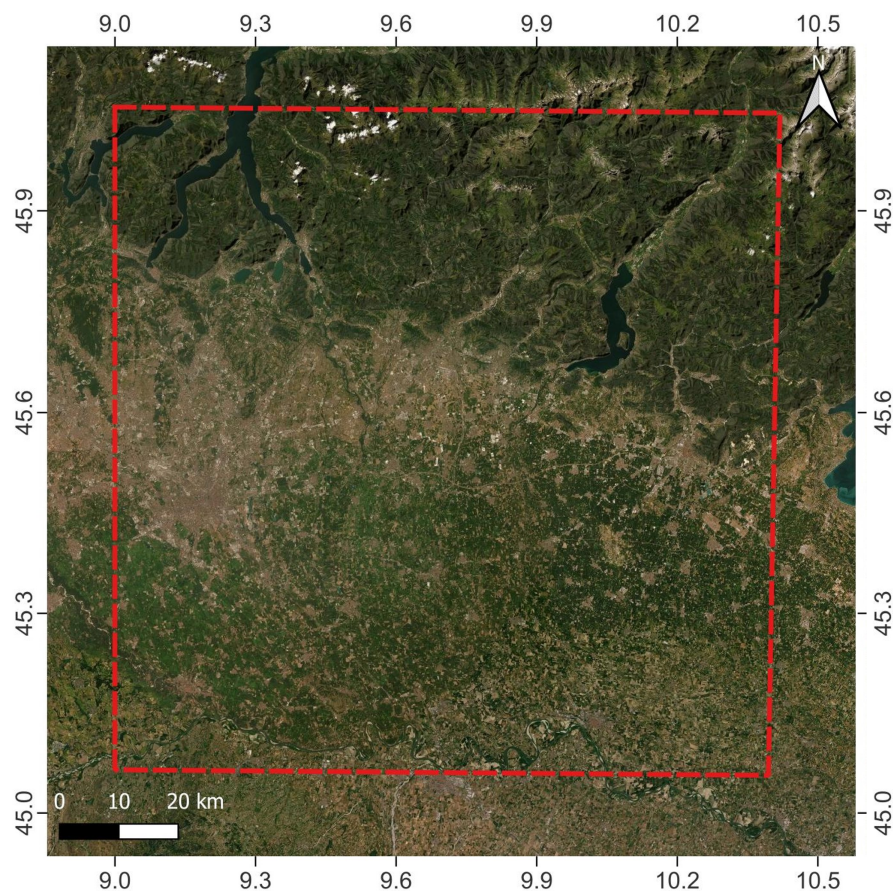


FIGURE 3.5: Detailed overview of the Italian tile (32TNR). The red, dashed line represents the Sentinel-2 tile boundaries, and the background image is the ESRI World Imagery base map.

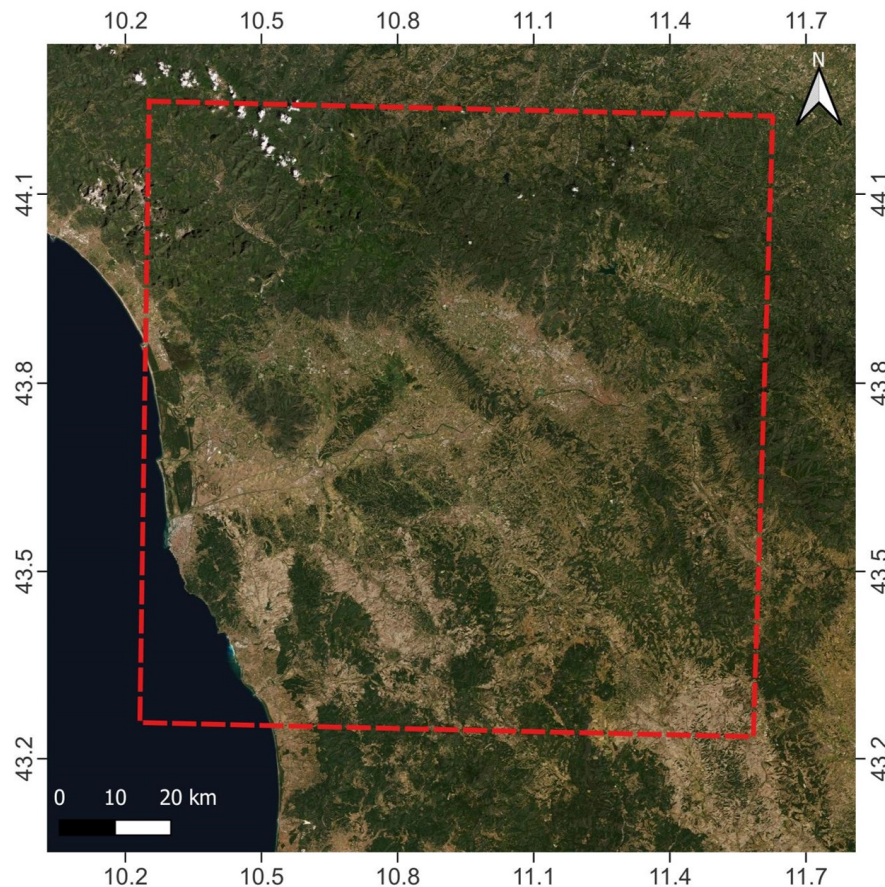


FIGURE 3.6: Detailed overview of the Italian tile (32TPP). The red, dashed line represents the Sentinel-2 tile boundaries, and the background image is the ESRI World Imagery base map.

policy, in fact, encourages EO data users to easily access and use the data anywhere in the World. Sentinel-1, in particular, provides freely accessible data, even for commercial use, at both temporal and spatial resolutions fully compatible with the application we intended to develop in this work. Therefore, Sentinel data was preferred over other expensive sources of data.

However, such open data also present limitations for our application. For instance, due to its dual-polarization nature, polarimetric analysis cannot be performed with Sentinel-1 data and, thus, it is not possible to investigate the scattering mechanism occurring on the target. Other sources such as TerraSAR-X, COSMO/SkyMed, Radarsat, would be able to provide more information fit for the scope, but would also imply much higher cost.

The Sentinel-1A SAR sensor, whose schematized structure is reported in Figure 3.7, operates in C-band with a central frequency of 5.405 GHz (Figure 3.8 reports a basic

Platform	Operation	Band	Polarization	Spatial resolution	Institution Country	Free data
Radarsat-2	2007-present	C	Quad-pol	3-100 m	NASA/JPL - USA	no
RISAT-1	2012-present	C	Dual- and Quad-pol	1-50 m	ISRO - India	no
Sentinel-1A/B	2014-present	C	Dual-pol	5-40 m	ESA - Europe	yes
ALOS-2	2014-present	L	Quad-pol	1-100 m	JAXA - Japan	no
Gaofen-3	2016-present	C	Quad-pol	1-500 m	CAST - China	no
SAOCOM-1/2	2018-present	L	Quad-pol	10-100 m	CONAE/ASI - Argentina	no
TerraSAR-X	2007-present	X	Quad-pol	0.25-40 m	GmbH - Germany	no
COSMO-SkyMed	2007-present	X	Dual-pol	1-100 m	ASI - Italy	yes (proposal)
COSMO-SkyMed 2 nd gen.	2020-present	X	Quad-pol	0.3-40	ASI - Italy	yes (proposal)

TABLE 3.1: List of available SAR satellites.

radar block diagram).

The platform was launched on 3rd of April, 2014, and its revisit time is 12 days at the equator on a polar orbit. The antenna aboard the satellite is right-looking and its incidence angles can vary from 29.1° to 46°. Such antenna is capable to provide a total radiometric accuracy within 1 dB. Regarding the polarization modes, Sentinel-1A can provide images acquired with a signal which is vertically transmitted and vertically received (VV) and/or vertically transmitted and horizontally received (VH). This can

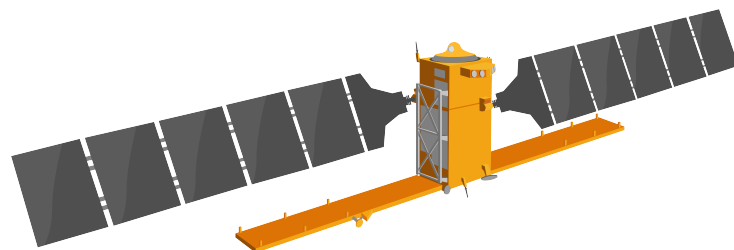


FIGURE 3.7: 3D model of the Sentinel-1A satellite.

be done in the default operation mode of the system, i.e., in Interferometric Wide-swath (IW) acquisition mode.

The Interferometric Wide (IW) swath mode is the main acquisition mode over land for Sentinel-1. It acquires data with a 250 km swath at 5×20 m spatial resolution (single look). As depicted in Figure 3.9, IW mode captures three sub-swaths using Terrain Observation with Progressive Scans SAR (TOPSAR). With the TOPSAR technique, in addition to steering the beam in range as in ScanSAR, the beam is also electronically steered from backward to forward in the azimuth direction for each burst, avoiding scalloping and resulting in homogeneous image quality throughout the swath. TOPSAR mode replaces the conventional ScanSAR mode, achieving the same coverage and resolution as ScanSAR, but with a nearly uniform SNR (Signal-to-Noise Ratio) and DTAR (Distributed Target Ambiguity Ratio). IW Single-Look Complex (SLC) products contain one image per sub-swath and one per polarisation channel, for a total of three (single polarisation) or six (dual polarisation) images in an IW product. Each sub-swath image consists of a series of bursts, where each burst has been processed as a separate SLC image. The individually focused complex burst images are included, in azimuth-time order, into a single sub-swath image with black-fill demarcation in between, similar to ENVISAT ASAR Wide ScanSAR SLC products.

The satellite is able to produce L1C products in SLC format or as multi-looked intensity images in ground range detected format (GRD) with 10×10 meters of pixel size. A second satellite, the Sentinel-1B, was launched on the 22th of April 2016. This additional

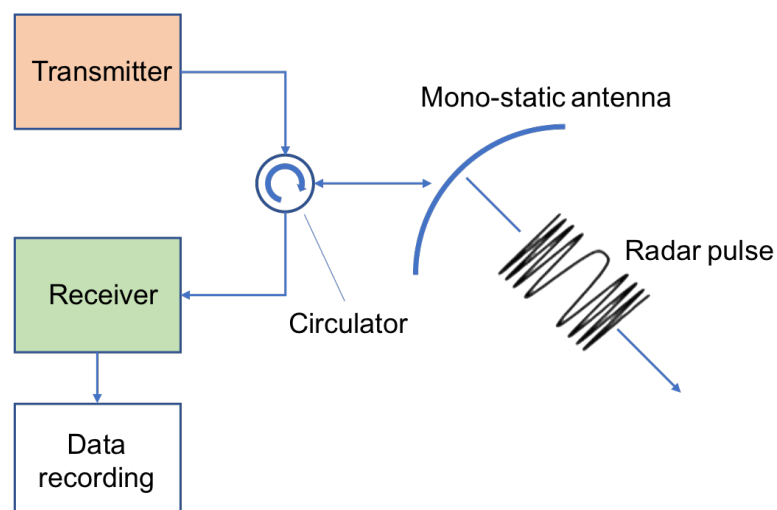


FIGURE 3.8: Basic radar block diagram.

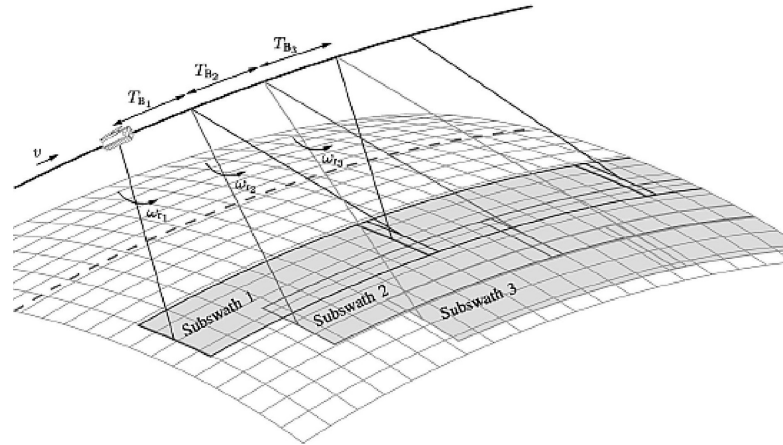


FIGURE 3.9: Sketch of the TOPSAR acquisition geometry. T_B is the burst duration and ω_r is the steering angle rate (image credit: DLR).

satellite, perfectly identical from a functionality point of view, uses the same orbit plane, thus, halving the revisit time and consequently doubling the number of acquisitions. This pair of satellites allows the production of SAR time series with very high temporal density, never had before at this resolution.

Note: on 23 December 2021, Copernicus Sentinel-1B experienced an anomaly related to the instrument electronics power supply provided by the satellite platform, leaving it unable to deliver radar data. Since then spacecraft operators and engineers have been working tirelessly to rectify the issue. Unfortunately, despite all concerted efforts, ESA and the European Commission announce that it is the end of the mission for Sentinel-1B. Copernicus Sentinel-1A remains fully operational and plans are in force to launch Sentinel-1C as soon as possible (scheduled for the second quarter of 2023). Until then, only Sentinel-1A data will be available to users, with 12 days revisit time.

3.4 Background of the proposed vegetation land cover mapping methodology

As deeply discussed in the introduction section of this manuscript, land cover (LC) mapping on wide areas is becoming an increasingly feasible tasks thanks to the availability of free multispectral and SAR data sets (e.g., by the Sentinel constellation [131]) and of cloud processing services (e.g., Google Earth Engine [132] and the Copernicus DIAS - Data and Information Access Services). Still, the challenges that the procedures designed

using these new data sets and tools are facing are far from being completely tackled. For instance, no general solution is available for the extraction of the most suitable features from sequences of data sets by heterogeneous sensors [133]. Similarly, the issue of the limited size of available training sets and the possibility/suitability of using existing land cover maps as starting point has been explored [79, 134], but with no final decision. Another issue is how to extract the same land cover classes when using different sensors, with different sensitivity and different spatial/spectral resolutions. To this aim, unsupervised approaches or transfer learning techniques [135] have been considered.

The main objective of the proposed methodology is the use of Sentinel-1 SAR time series for land cover classification at the regional level using only training points extracted from pre-existing coarser resolution maps, in a completely automated manner. As a matter of fact, global approaches to land cover mapping using satellite data are currently mostly limited to medium-resolution multispectral data sets. As seen in Chapter 1, typical examples are the 300 m GlobCover project [136], which exploits multispectral data recorded by the MERIS (MEdium Resolution Imaging Spectrometer) sensor and the 100 m Copernicus Global Land Service (CGLS) [137]. Only a few global land covers were extracted using SAR, and no complete land cover maps. Examples are water surfaces [43] using ENVISAT data, the Global Urban Footprint [138] from TerraSAR-X data, and the Forest/Non-Forest global map from ALOS/PALSAR data [37].

In order to fill this research gap, Sentinel-1 annual data sequences are exploited for the production of a global land cover map. To uniformly cover geographically wide areas, and potentially the whole Earth surface, the methodology is based on a progressive mapping of the tiles of the Sentinel-2 grid [139], used here for Sentinel-1 data partition as well. As target legend, a subset of the the CGLS legend is considered. Indeed, because of its rather coarse spatial resolution, the CGLS legend includes many mixed classes. Its legend was thus reduced to a subset of “pure classes”, which is in fact an improvement from the point of view of the mapping product. A randomly selected subset of points belonging to these classes in the Medium-Resolution Land Cover (MRLC) map is used as training set. This sampling approach is similar to the one presented in [134]; however, in that study the training set is built leveraging spectral clustering techniques applied to Sentinel-2 multispectral data, starting from a 30 m spatial resolution land cover map based on Landsat imagery (the CORINE land cover map).

The starting scientific question that this work addresses is how to use a year-long multitemporal SAR sequence from the Sentinel-1 constellation to effectively map land cover classes using as reference only an existing medium resolution map. This question translates into the two main points discussed here in the following: a) how to select a reliable set of training points from a medium resolution map, and b) how to use a multitemporal SAR sequence to discriminate among classes that are typically mapped using multispectral data.

Figure 3.10 summarizes the scheme of the proposed methodology. Starting from an annual sequence of pre-processed high-resolution SAR images, first a “seasonal” SAR time series (VH polarization only) is extracted, as better explained in the next sections, and a set of spatial features are computed from this reduced time series. Then, a second time series is added to the pool of features. This time series is composed by fifteen “24-days” composites (both VV and VH polarizations). The latter time series, also as explained in the next sections, is obtained by arithmetic average of the SAR acquisitions available within separated intervals of 24 days.

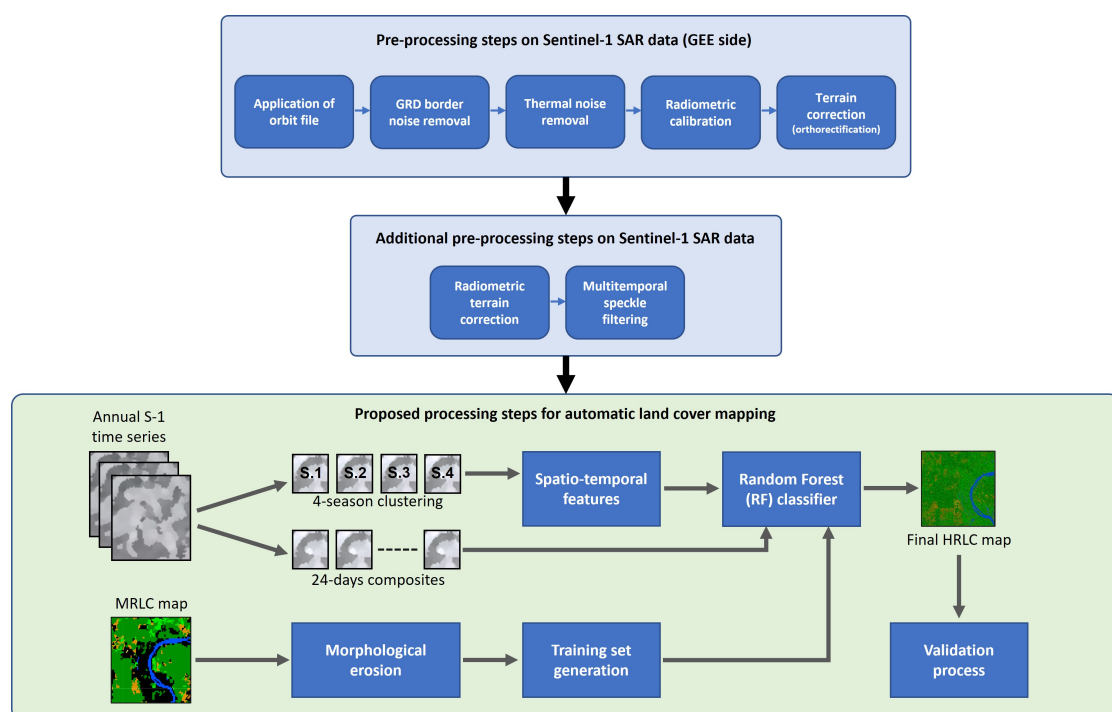


FIGURE 3.10: A simplified block diagram of the proposed land cover mapping procedure. Part of the pre-processing chain is pre-implemented in Google Earth Engine; whereas, the radiometric correction and speckle noise reduction steps were added to the chain.

3.5 SAR data pre-processing

Most of the processing steps involved in the presented methodology, and described in the next sections, rely on pre-processed Sentinel-1 SAR images provided by Google Earth Engine (GEE). GEE is an online cloud platform for scientific analysis and visualization of geospatial datasets, for academic, non-profit, business and government users. Earth Engine hosts satellite imagery and stores it in a public data archive that includes historical Earth images dating back more than forty years. The images, ingested on a daily basis, are then made available for global-scale data mining. Moreover, the platform also provides APIs and other tools to enable analysis of large data sets. The data sets from GEE are delivered as L1C products in Ground Range Detected (GRD) with 10 m of pixel spacing. Single-Look Complex (SLC) images are not available yet, due to current difficult management of complex numbers, typical of SLC images. For this work, Sentinel-1 (A and B) GRDH (High resolution GRD data) images were used.

GRD Images from the Sentinel-1 GEE archive are pre-processed with the Sentinel-1 Toolbox² (SNAP) in order to derive the backscatter coefficient σ^0 (sigma naught) in decibels (dB), which represents the target backscattering area (RCS or Radar Cross Section) per unit area. The scattering behaviour depends on the physical characteristics of the target: geometry and electromagnetic characteristics. The pre-processing chain used to obtain the backscatter coefficient for each pixel of the image can be summarized in 5 steps:

1. Application of orbit file, which updates the orbit metadata;
2. Removal of low intensity GRD border noise and invalid data on the edges of the scene;
3. Removal of additive thermal noise in sub-swaths to help reduce discontinuities between sub-swaths for scenes in multi-swath acquisition modes;
4. Radiometric calibration using sensor calibration parameters present in the GRD metadata in order to compute the backscatter intensity;
5. Range-Doppler terrain correction, which converts the data from ground range to σ^0 using the SRTM 30 meter or ASTER Digital Elevation Model (DEM). The latter is used for high latitudes, greater than 60° or less than -60° .

²<https://step.esa.int/main/toolboxes/snap/>

Since the standard Sentinel-1 pre-processing chain does not include radiometric terrain correction, we added an angular-based radiometric slope correction routine for Sentinel-1 SAR images, developed in [140]. This model leverages a well-established physical reference model which is also extended to simultaneously generate masks of invalid data represented by active layover and shadow affected regions.

The angular-based algorithm developed in [140] is a simplified model compared to more accurate pixel-area-based models, as it does not fully compensate for the radiometric distortions; in fact, this angular-based model does not account for the apparent heteromorphic relationship between map (geocoded image) and radar geometry. However, this model is currently the best option possible for GEE users, as pixel-area-based methods are not practical due to heavy memory usage and its consequent saturation.

The radiometrically corrected SAR products significantly improve the potential usage of Sentinel-1 imagery for a wide range of land applications, such as land cover classification, deforestation monitoring, the retrieval of bio-geophysical parameters as well as the combination of imagery from different geometries. From Figure 3.11 it is possible to observe how a Sentinel-1 SAR image benefits from the radiometric terrain correction described above.

In the procedure implemented in this work, once the Region of Interest (a Sentinel-2 tile according to [139]) and the year of interest are selected, all the SAR images in that year are considered as long as they cover at least 70% of the selected tile footprint. According to the study presented in [128] (published by the undersigned Author within this Ph.D. framework and whose main outcomes are described in Section 3.5.1), the use of the whole annual temporal series is not necessary for land cover mapping, and temporally aggregated versions of it are more suitable. Leveraging on those results, the selected set of SAR images is grouped into quarterly clusters that resemble, although roughly, the seasonal cycle of the different land cover types.

The four “seasonal” clusters, each obtained by averaging in time all possible SAR images acquired within three-months time windows, are then subject to speckle noise reduction exploiting a multitemporal denoising filter based on the one presented in [141], which appears to provide better results than a spatial filter applied independently to each SAR image. The procedure, depicted in Figure 3.12, basically consists in the estimation of a “super-image”, obtained as arithmetic mean of all the SAR acquisitions within the year of interest (in case the number of images of the original stack is not large enough,

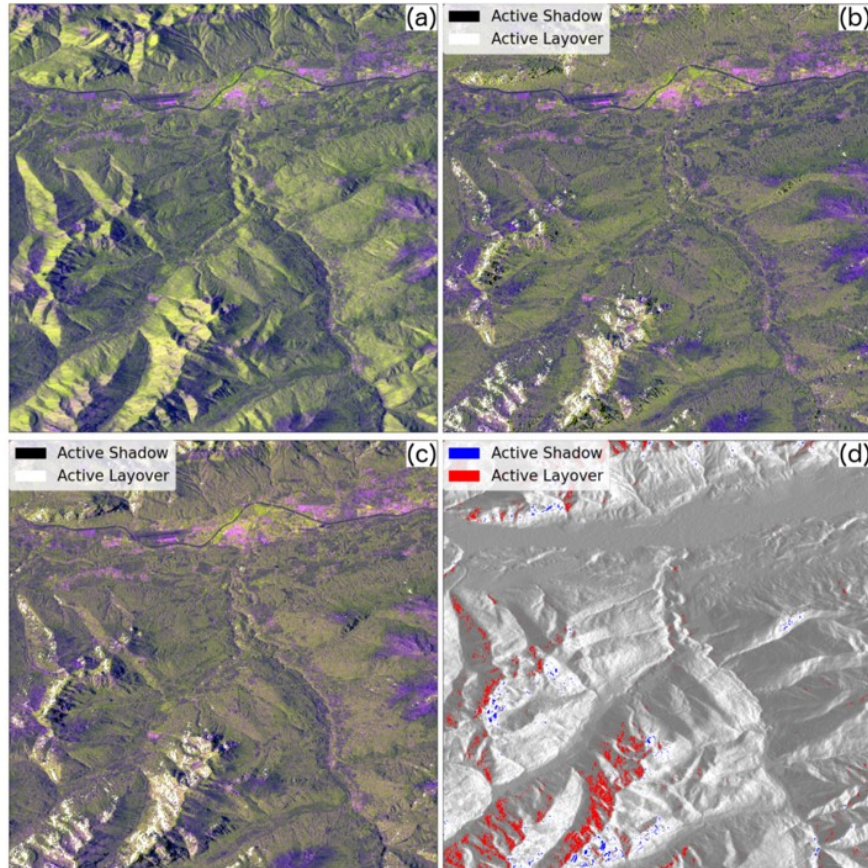


FIGURE 3.11: Sentinel-1 RGB color composite (Red: σ_{VV}^0 (dB), Green: σ_{VH}^0 (dB) Blue: VV/VH power ratio) over the region of interest before (a) and after correction with model 1 (b) and model 2 (c), as well as the difference of model 1–model 2 for the VV polarised bands stretched between -5 and 5 dB (d). Regions of active layover and shadow are overlaid in black and white (b,c) as well as in red and blue (d).

a spatial filtering step on the super-image is necessary). Then, the ratio between the original, noisy image at time t and the super-image is computed and spatially denoised exploiting a simple low-pass filter, with a moving 3×3 kernel; finally, each denoised ratio composite at time t is re-multiplied by the super-image. Due to the improved stationarity of the ratio images, multitemporal speckle-reduction techniques are demonstrated to be much more effective than denoising each image in the original multitemporal dataset. As mentioned above, after the multitemporal denoising filtering is applied, an artificial SAR composite time series made of four images is built by the arithmetic mean of all the acquisitions along each seasonal cluster.

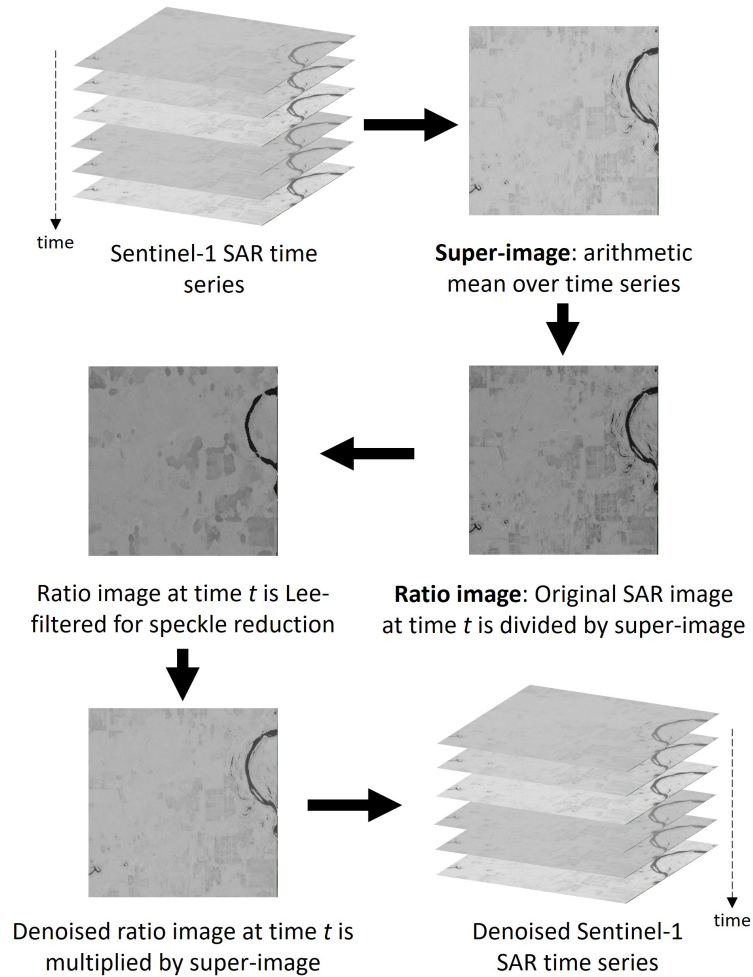


FIGURE 3.12: Algorithm of the multitemporal despeckle filtering used in the proposed land cover classification methodology.

3.5.1 Leveraging of aggregated SAR time series

This section is devoted to a brief analysis aimed at demonstrating that long time sequences of SAR data can be reduced in order to obtain a new, yet equally informative sequence that can be more easily processed.

in the article cited in [128] (published by this thesis' Author), a collection of Sentinel-1 images acquired in year 2018 has been selected, and a series of possible inputs have been considered to evaluate the performances of different aggregated time sequences. These inputs are:

1. A single image selected during the year (in good weather conditions);
2. A single image obtained by temporally averaging all the images for the whole year;

3. The whole sequence of images as a long multitemporal stack;
4. A multitemporal seasonal image where the annual collection was subdivided into four seasons and an arbitrary number N of images are evenly extracted from these groups of images and subsequently averaged in time.

In any of the above-mentioned cases, each Sentinel-1 image belonging to the original dataset was chosen according to the Sentinel-2 tiles' area coverage percentage. In this specific work ([128]), only SAR images overlapping at least 80% each tile footprint were selected. This also prevents the system from using acquisitions in different orbits, avoiding incidence angle issues which affects backscatter intensity and, thus, classification [142]. Different features have been extracted prior to the classification; specifically, if only VV or VH backscatter intensity information is used (so-called "single-band" case), spatial filters are used to compute features with the aim of exploring the spatial information hidden inside the SAR scenes. Namely, these features are the VV (or VH) original value, Lee-filtered, Mean, Median, Max, Min and MaxMin ($max - min$). Note that the "Lee-filtered" feature is an image obtained by applying the Refined Lee filter to the original SAR image. As an improved version of the well-known Lee filter, the Refined Lee filter follows the development in the k -Nearest Neighbour (kNN) algorithm, and is aimed at reducing speckle noise, thus improving SAR images [143].

Regarding the case of multiband image (both VV and VH polarizations), polarimetric features were computed as combination of bands, as they may provide greater classification results [144]. Namely, these polarimetric feature are VV original value, VH original value, Sum ($VV + VH$), Mean ($\frac{VV+VH}{2}$), Ratio ($\frac{VV}{VH}$) and Difference ($VV - VH$).

Regarding the classification model, a Random Forest (RF) classifier was employed, as it provides good results in many studies for vegetation classification purposes (see Chapter 2). Figure 3.13 shows the block scheme of the procedure which aims at assessing the classification potential when temporally aggregated versions of the original SAR time series are used for land cover purposes.

Examples of classification results for the test site in Amazonia (tile 21KUQ) are shown in Figure 3.14. It is possible to appreciate the effectiveness of the involvement of time series with respect to the use of a single image (considering only VV polarization in the example), mainly as a result of the drastically reduced speckle effects. Such effects are also reduced by using more than one image per season (in this case, 3 or 5).

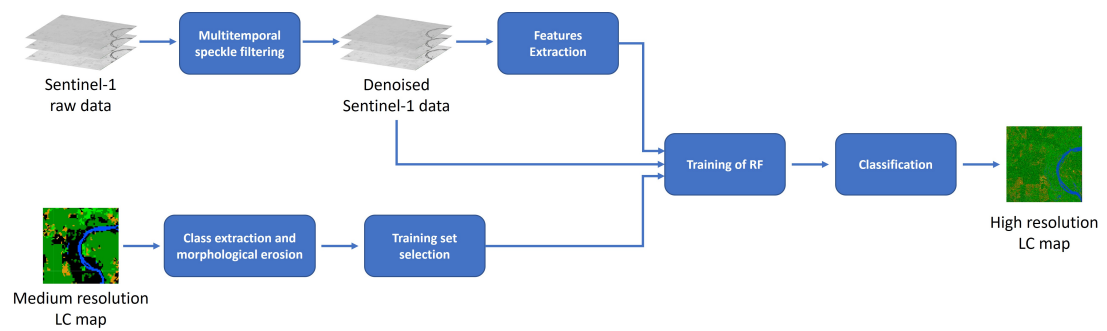


FIGURE 3.13: Overview of the classification model aimed at assessing the potential of temporally aggregated Sentinel-1 SAR time series.

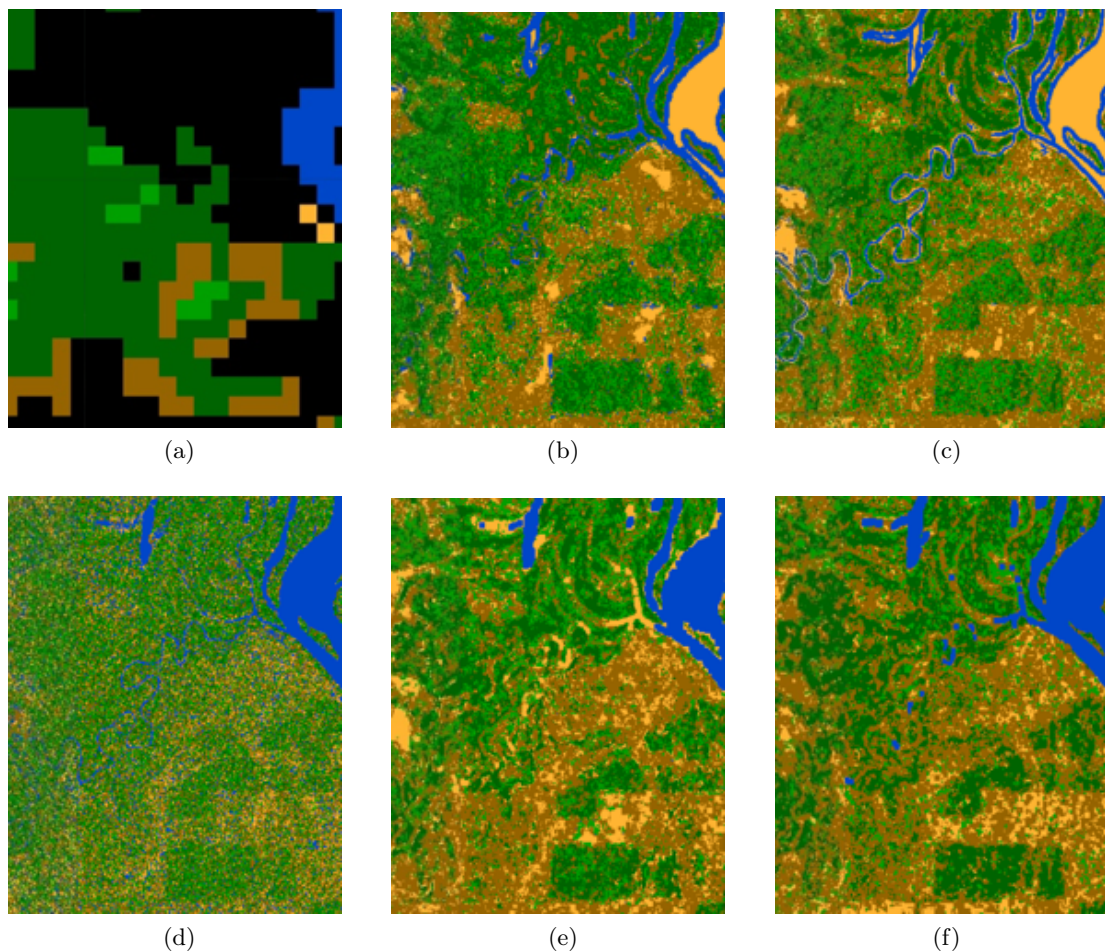


FIGURE 3.14: Visual comparison between (a) the 2018 European Space Agency (ESA) CCI LC map at 300 m spatial resolution and the LC maps obtained by using (b) a single scene acquired on 2018.04.27, (c) single image obtained averaging in time all available images for year 2018, (d) a multitemporal stack of all the 2018 images, (e) a set of 4 seasonal images obtained by averaging 3 images per season, (f) a set of 4 seasonal images obtained by averaging 5 images per season. Black areas in (a) represent classes discarded from the classification.

Land cover classification was also performed in other two regions, i.e., Africa and Siberia (tiles 37PCP and 42WXS, respectively), to test the effectiveness of temporally aggregated SAR time series. Classification results are reported in Table 3.2 for the considered different input data sets.

Referring to Table 3.2, it must be noted that, since the evaluation is provided against the original coarse land cover map (at 300 m scale), the absolute numbers are not meaningful. Therefore, only the improvements (in percentage) for different options of input SAR data are provided, considering as base map (i.e. worst result) the map obtained with a single scene in input to the classifier. The second column reports the results when a single image, obtained by averaging all the available scenes for year 2018, was used. In the third column, results are obtained when the input is an image composed by the temporal stack of all available images for year 2018. Whereas, in the fourth column, the annual Sentinel-1 sequence was split into four seasonal collections; for each season, $N = 3$ scenes were averaged in time, ending up with a time series made of four images which was provided as input. Finally, the last column shows classification results for a case similar to the previous one, but using $N = 5$ images per season averaged in time.

From Table 3.2, a relevant increase of effectiveness of the classification procedure is achieved in all test areas when time series are involved. As a matter of fact, the exploitation of the phenological information in SAR time series confirms state of the art vegetation mapping using radar data. Based on this relatively simple analysis, the main result is that, building a seasonal time series made of 4 composite images, where each image is obtained by temporally averaging the same number of scenes per season, the phenological information is preserved without using the whole annual image collection, thus reducing the overall computational effort. Moreover, referring to Figure 3.14, it is

Tile	Averaged image	Annual time series	Seasonal time series (N=3)	Seasonal time series (N=5)
21KUQ	+14.41	+10.7	+17.48	+19.89
37PCP	+1.76	+4.64	+2.41	+2.44
42WXS	+16.0	+9.29	+15.78	+15.9

TABLE 3.2: Classification improvements [%] with respect to the worst result, occurring when only a single SAR image is provided in input to the classifier.

notable the major capability by the classifier to discriminate water bodies when working on an averaged multitemporal sequence, while in all other cases water is barely distinguishable. This result suggests that multitemporal data has always an advantage, but the way the original SAR sequence may be best exploited depends on the class(es) to be mapped. This concepts will be particularly relevant in the next Chapter, where a water body classifier is developed.

3.6 Features extraction

The second step in the proposed procedure is the selection of the most useful input features for the classifier. As mentioned in previous sections, it is expected that despeckled SAR sequences are able to provide a better discrimination among different land cover types (as also observed in [92, 95, 103, 104, 145, 146]).

Exploiting the “seasonal” time series described in Section 3.5, a single mean composite image is computed by averaging in time all the images belonging to a specific season. Then, a set of textural features are computed from each of the four mean composites of the seasons: the spatial median, maximum, minimum and range. Each of these spatial statistical descriptors is derived using a kernel of 5×5 pixels. Figure 3.15 clarifies the procedure used to extract textural features from the aggregated, seasonal SAR time season.

Referring to Figure 3.15, it is possible to note that the total number of spatial features is equal to the number of seasons times the number of extracted textural features (i.e., 4 seasons times 5 textural features, for a total of 20 spatial features).

A set of temporal features are also extracted from the original stack of images, that are going to be used as input to the classifier. These features are represented by a new SAR time series, appropriately aggregated (based on findings from the technical literature).

In this case, first the complete collection is clustered into 24-days collections; then, each collection is denoised with the multitemporal denoising filter described above; finally, both the VV and VH polarizations are used to generate a time sequence per channel, where the sequence elements are obtained by the arithmetic mean of the images in each 24-days denoised cluster. In Figure 3.16 the procedure for extracting the aggregated SAR time series is schematized.

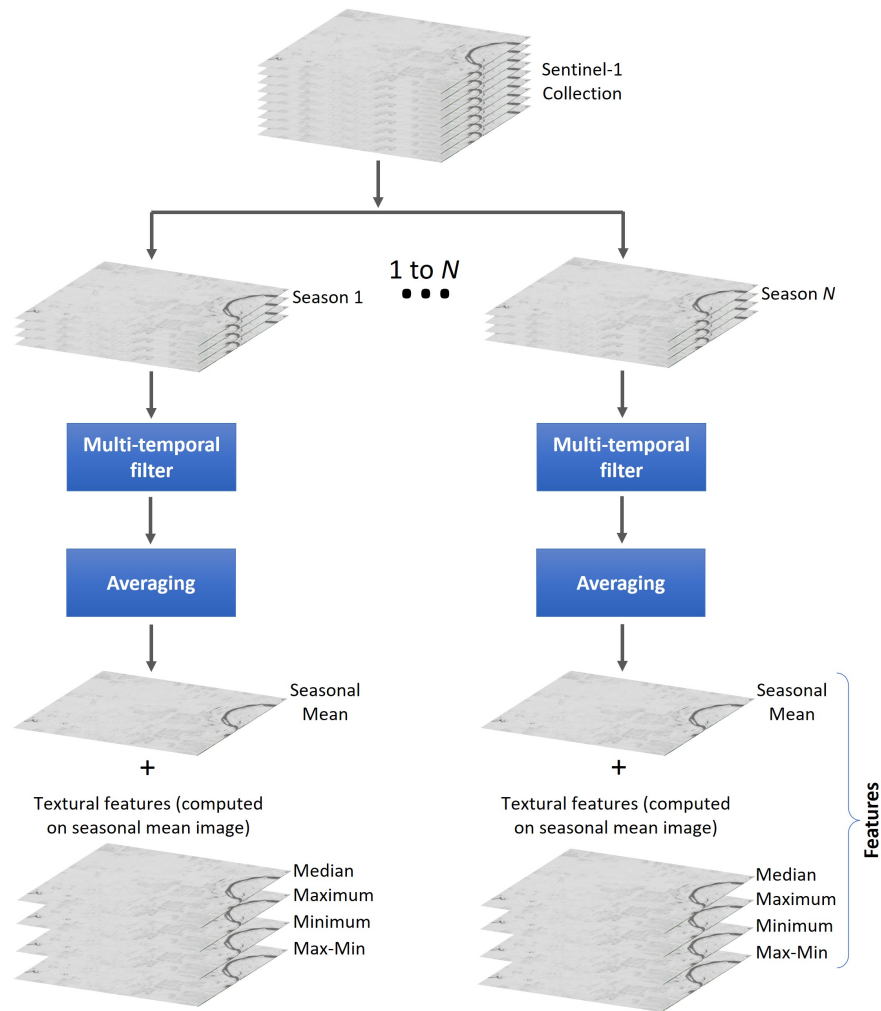


FIGURE 3.15: Extraction of textural features from seasonal mean composites, using a 5×5 kernel. Note that this features extraction procedure is not limited only to four seasons, but it can be applied on N seasonal collections.

The above mentioned seasonal spatial features, plus the 24-days based sequence (either VV or VH), are stacked and classified by means of a Random Forest (RF) classifier. The RF classifier is trained using a training set extracted, as mentioned in the following section, from the Copernicus Global Land Service (CGLS) medium resolution land cover (MRLC) map at 100 m scale, while its final classification result is a High-Resolution Land Cover (HRLC) map with 10 m posting.

3.7 Medium resolution (MR) training set

As in any supervised classification procedure, the selection of the training set plays a crucial role in the proposed procedure. As discussed in Chapter 1, since there are already

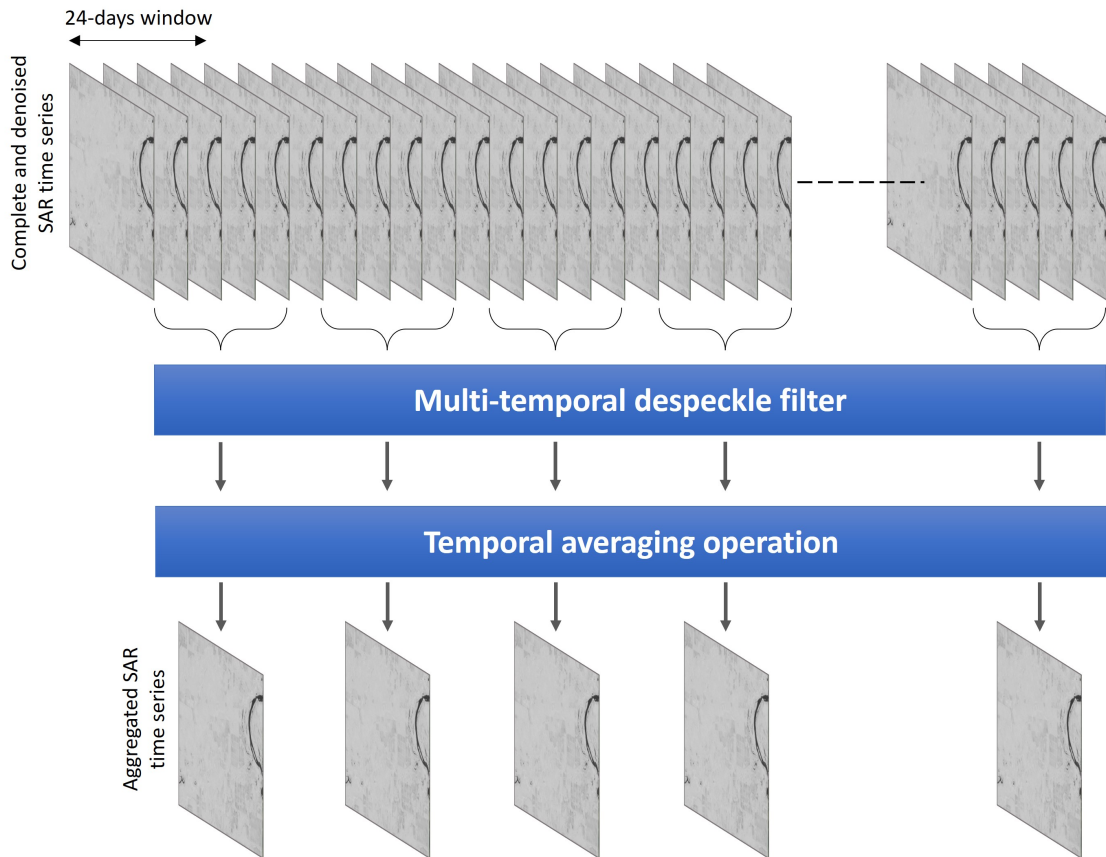


FIGURE 3.16: Extraction of temporal features from 24-days denoised clusters. Note that this procedure is applied to both VV and VH channels, separately (therefore two 24-days based collections are generated).

good quality global land cover maps available at medium spatial resolution, the idea is to exploit the information they contain.

Specifically, in this work the training samples are collected from the CGLS MRLC map at 100 m resolution. The CGLS is a product delivering a global land cover map at 100 m spatial resolution that provides a primary land cover scheme [137]. Together with discrete classes, the CGLS also includes continuous field layers for all basic land cover classes that provide proportional estimates for vegetation/ground cover for the different land cover types. These consistent land cover maps are provided for the period from 2015 to 2019 over the entire Earth, and are derived from the PROBA-V 100 m time series (a database of high quality land cover training sites and several ancillary data sets, reaching around 80% of accuracy across all years. Moreover, the CGLS is also planned to provide yearly updates, from 2020, through the use of the Copernicus Sentinels.

As mentioned in Section 3.4, the land use class set of this map is not suitable for a map

at finer spatial resolution. In fact, it includes many mixed land cover types. Therefore, a different yet related class set must be used for the new map, which includes only “pure” classes, i.e. classes representing only one land cover type. The new class set, reported in Table 3.3, is thus composed only by pure classes. Additionally, classes in the original MR set that cannot be reliably discriminated using SAR data are merged. As an example, the MR class set contains two classes named *evergreen broadleaf tree* and *deciduous broadleaf tree*, which are merged into a single class named *broadleaf tree*. In fact, according to [147], C-band signals are less reliable than L- and P-band SAR signals when biomass estimation is the task; this happens because only small branches (with section ranging from 0.8 to 1 cm) contribute most to the backscattered energy. On the other hand, thicker branches essentially contribute to backscattering attenuation and “forward scattering”. Moreover, the capability of C-band radar signals to discriminate forests from other types of vegetation is decreased, as small scattering elements characterize the majority of the herbaceous and crop species.

Here follows a brief description of the selected classes, according to the Food and Agriculture Organization (FAO) Land Cover Classification System (LCCS)³:

1. **Tree cover broadleaf**: primarily vegetated areas with a tree canopy cover of more than 50% at the time of fullest development. Snow and/or ice, open water or built-up areas cover less than 50% of the area. A tree is a woody, perennial or seasonal plant with a simple and well-defined stem, bearing a more or less defined

³<https://www.fao.org/home/en/>









Class ID	CGLS class(es)	Land cover type	Color
1	112, 114, 122, 124	Tree cover broadleaf	
2	111, 113, 121, 123	Tree cover needleleaf	
3	20	Shrubland	
4	30	Grassland	
5	90	Vegetation aquatic	
6	100	Lichens and mosses	
7	60	Bare areas	
8	80, 200	Open water	

TABLE 3.3: The class legend used in the proposed land cover mapping methodology.

crown (Ford-Robertson, 1971) and a minimum height of 5 m. Trees are broadleaved and come from the Angiospermae group.

2. **Tree cover needleleaf:** Primarily vegetated areas with a tree canopy cover of more than 50% at the time of fullest development. A tree is a woody, perennial or seasonal plant with a simple and well-defined stem, bearing a more or less defined crown (Ford-Robertson, 1971) and a minimum height of 5 m. Trees carry typical needle-shaped leaves and come from the Gymnospermae group.
3. **Shrubland:** Primarily vegetated areas with a shrub canopy cover of more than 50% at the time of fullest development. Snow and/or ice, open water or built-up areas cover less than 50% of the area. A shrub is a woody plant with persistent woody stems and without any defined main stem (Ford-Robertson, 1971), being less than 5 m tall.
4. **Grassland:** Primarily vegetated areas with an herbaceous cover of more than 50% at the time of fullest development. Snow and/or ice, open water or built-up areas cover less than 50% of the surface. Herbaceous plants are defined as plants without persistent stem or shoots above ground and lacking definite firm structure (Scoggan, 1978).
5. **Vegetation aquatic:** Primarily vegetated areas with trees, shrubs, grasslands or lichens and mosses covering more than 50% of the area flooded by water for more than 4 months throughout the year. The water can be saline, fresh or brackish.
6. **Lichens and mosses:** Primarily vegetated areas with a cover of more than 50% at the time of fullest development. Snow and/or ice, open water or built-up areas cover less than 50% of the surface. Mosses are a group of photo-autotrophic land plants without true leaves, stems or roots (Gray, 1970). Lichens are composite organisms formed from the symbiotic association of fungi and algae (Gray, 1970).
7. **Bare areas:** Areas where the sum of vegetation cover is less than 50% at the time of fullest development. Snow and/or ice, open water or built-up areas cover less than 50% of the surface. Bare rock areas, sands and deserts are classified as bare areas. Extraction sites (open mines and quarries) and salt flats covered by water for less than 5 months are classified as bare areas.

8. **Open water (permanent)**: Areas where open water covers at least 50% of the surface and remains for more than 9 months a year, except in special circumstances (particularly dry year, construction of dams, etc.). Snow and/or ice and built-up areas cover less than 50% of the surface. Water bodies can be natural or artificial. Water can be saline, fresh or brackish.

Starting from the MRLC map including only the classes to be recognized in the new map, a morphological erosion processing step is applied separately to each class layer. This step, performed using a 3×3 pixels kernel, aims at avoiding the selection of training points on the border of the classified area, which might be mixed pixels at medium spatial resolution. To avoid undersampling of classes that have only few pixels in the scene, if the abundance of a class after the erosion appears to be less than the number of samples to be extracted (e.g., less than 500 pixels), the original class extent is entirely recovered and used for sampling. Figure 3.17 shows how the erosion operation performs on a small region within the Amazon tile (21KUQ).

The eroded version of the MRLC map is then used to derive more reliable training points, by means of an innovative algorithm here described in the next section.

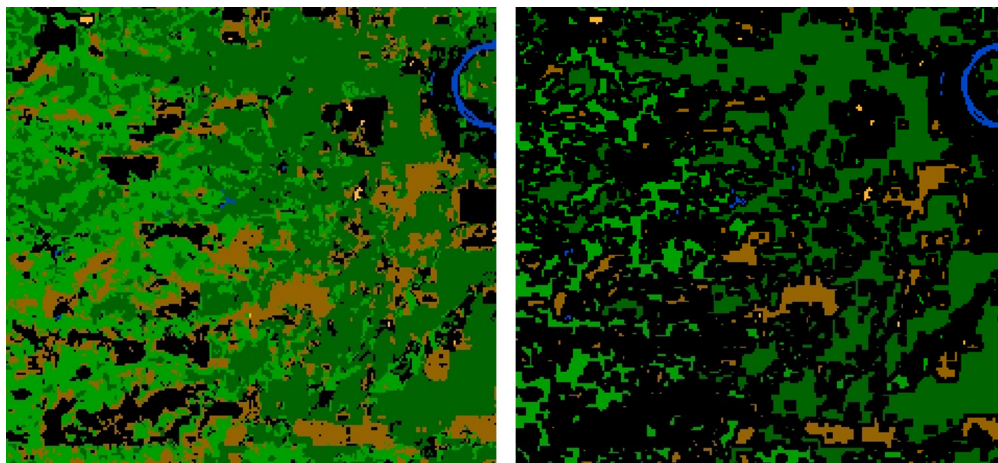


FIGURE 3.17: Visual example of how the erosion operation works on the MRLC map, based on a 3×3 pixels kernel. The left image is the original, non eroded map, while the right one is the erosion output. Note that in both maps, black regions represent classes that were not selected to be classified.

3.7.1 High-resolution training set generation

Due to great effort in building reliable training data sets, semi-supervised methodologies have been developed that aim at optimizing the selection of training samples, achieving better results at a lower cost. These so-called “active learning” procedures consists of iteratively proposing training points to an operator until a satisfying classification accuracy is achieved. However, these approaches are not applicable when land cover mapping at large scale is the task. In fact, generally a very large number of samples characterizing each single class is needed; moreover, it is also mandatory to have photo-interpretation expertise all around the world. Therefore, in this section a fully automated training set generation procedure is proposed, aimed at collecting reliable training samples virtually in any region of the Globe, without any human-based intervention.

Figure 3.18 summarizes the processing steps aimed at obtaining points whose reliability is much higher than a simple stratified random sampling performed on the original MRLC map, either eroded or not.

The first step consists of extracting a class from the MRLC map and then generate a set of training points (seeds) to be used as input for a k -Means clusterer applied to the stack of SAR-based features described in Section 3.6. Note that the k -Means clustering is implemented according to the “Weka” open source machine learning software [148] and starts from a representative subset of the data to generate a model aimed at making predictions on the whole data set. The trained clustering model is then used to extract $k = 2$ clusters inside the original MR class boundaries, whose associated land cover types are not know in advance.

At this point, the originally selected seeds belonging to a single land cover class in the MR map is split into two clusters. Only the most abundant cluster is retained and a large number of samples (4000 in this implementation) are randomly selected to sample the stack of SAR features. Each of the 4000 sampled pixels is associated to a features vector of the form:

$$\mathbf{p}_k^i(n) = [p_k^i(1), p_k^i(2), \dots, p_k^i(N)] \quad \text{with} \quad \mathbf{p}_k^i(n) \in \mathbb{R}^N \quad (3.1)$$

where N is the number of features that define the N -dimensional feature space (that train the RF classifier), and $p_k^i(n)$ is the value of the n -th feature element in the vector

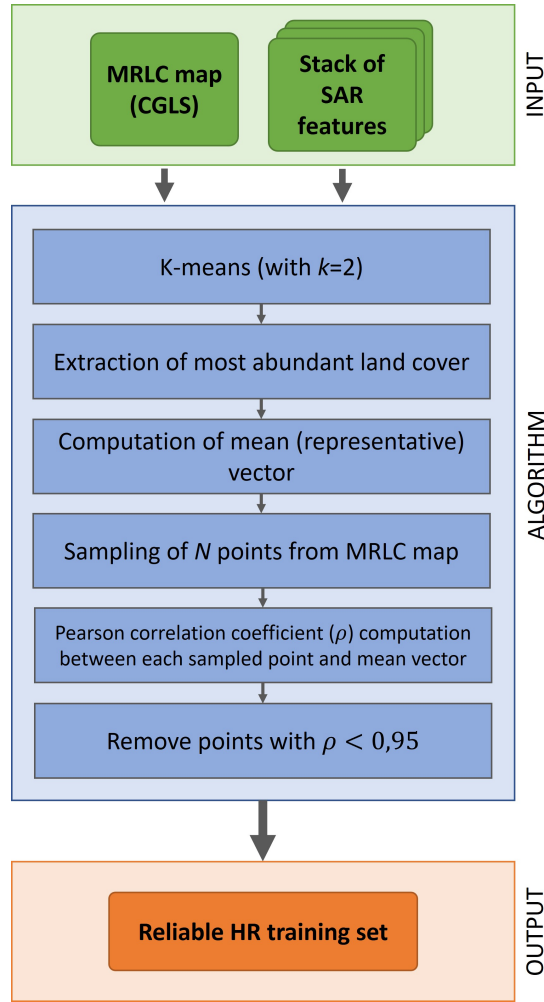


FIGURE 3.18: Block diagram of the high-resolution training set generation procedure.

$\mathbf{p}_k^i(n)$ associated to the k -th pixel, which belongs to the i -th class.

All these vectors are then reduced to a single vector by an element-wise mean. This mean vector is considered as the “representative” vector for that particular class. Therefore, if the i -th class is considered, the associated mean features vector can be written as:

$$\bar{\mathbf{f}}^i(n) = [\bar{f}^i(1), \bar{f}^i(2), \dots, \bar{f}^i(N)] \quad \text{with} \quad \bar{\mathbf{f}}^i(n) \in \mathbb{R}^N \quad (3.2)$$

Finally, each of the extracted 4000-features vectors, having the form of the vector in Equation (3.1) is compared with the i -th representative vector of Equation (3.2) by computing the Pearson correlation coefficient (ρ). Eventually, only the points with correlation $\rho \geq 0.95$ are kept to be part of the final random forest training set for that

specific class. This procedure is iterated for all the classes in the selected legend that are present in the region of interest, according to the MRLC map.

Figure 3.19 shows the main outputs of the training set generation procedure described above. Specifically, Figure 3.19a shows the initial situation, where the MRLC map is just eroded. Then, as shown in Figure 3.19b, a specific class from the original MRLC map is selected, and a given number of clusters ($k = 3$ in the example in the figure) are extracted within the class boundaries using a k -Means clustering model, trained based on the stack of SAR features. Lastly, 3.19c shows the selected cluster, which represents the most abundant cluster extracted by the k -Means. This final cluster is then associated to the original MR class (thus, they are labelled with the same class ID) and used for sampling at 10 m scale.

3.8 Results and discussion

The entire workflow described in the previous sections was implemented leveraging the great computational power offered by Google Earth Engine, a powerful cloud computing platform aimed at processing and analysing huge amounts of remotely sensed data and GIS data in general.

To test the methodology, all four regions of interest described in Section 3.2 (Siberia, Italy, Brazil and Africa) were used to evaluate the robustness of the proposed approach in areas with very different land covers and climate typologies.

As explained in Section 3.5, for each case study, all the Sentinel-1 acquisitions covering

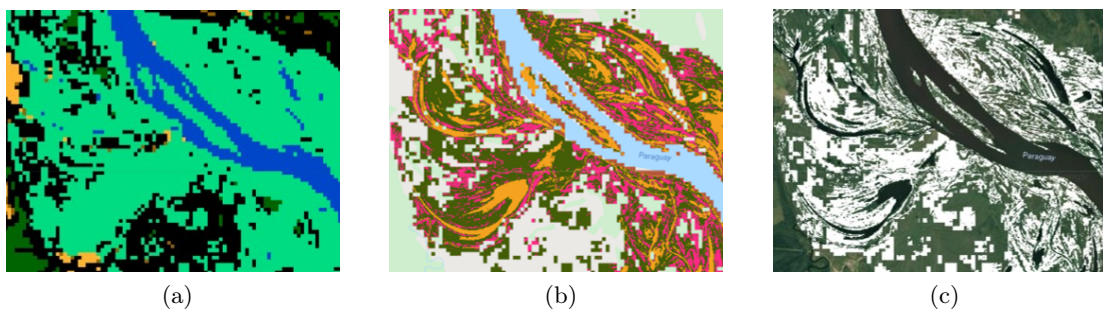


FIGURE 3.19: Main outputs of the training set generation procedure: in (a) is shown the eroded MRLC map; in this example, the aquatic vegetation is selected and clustered (b) using a k -Means clusterer with $k = 3$. Finally, in (c) the most abundant cluster is extracted and sampled with 10 m scale.

at least 70% of the tile in 2019 are considered. This high overlap ratio is selected to avoid the use of images acquired from different orbits, therefore avoiding incidence angle issues affecting backscatter intensity and, consequently, the classification results. Such overlap ratio it is also necessary to prevent the training set to be chopped to a subset, due to SAR images covering only a small part of the region of interest. To better understand this issue, the reader is referred to Figure 3.20. Starting from a given number of points extracted from the MR land cover map (all the red starting points in Figure 3.20), it is possible that the final training set is composed only by a tiny subset of them; this happens when the features images are cropped due, for example, to the relative orbit number. For the training process, it is mandatory that all the sampled points have the exact same number (and type) of features; from Figure 3.20, it is possible to notice that the only valid area corresponds to the intersection of all images' footprints. All the starting points falling outside this area are discarded because they cannot sample the same features of those belonging to the intersection region. For all these reasons, it is clear that selecting images that have a certain degree of overlap between their footprint and the region of interest boundaries is a relevant detail in order to build a consistent training set.

This selection results into a collection of 29 SAR images for Siberia, 38 for Italy, 32 for Amazonia and 25 for Africa (on average, this means one acquisition every 12 days). All the images are Ground Range Detected (GRD) and acquired in Interferometric Wideswath (IW) mode; both VV and VH descending orbit data sets were selected.

Once all the features are computed as described in Sections 3.6 and 3.7.1, all the features vectors were classified using the random forest (RF) classifier trained as mentioned above. Random forest is a one of the most powerful and most used supervised learning

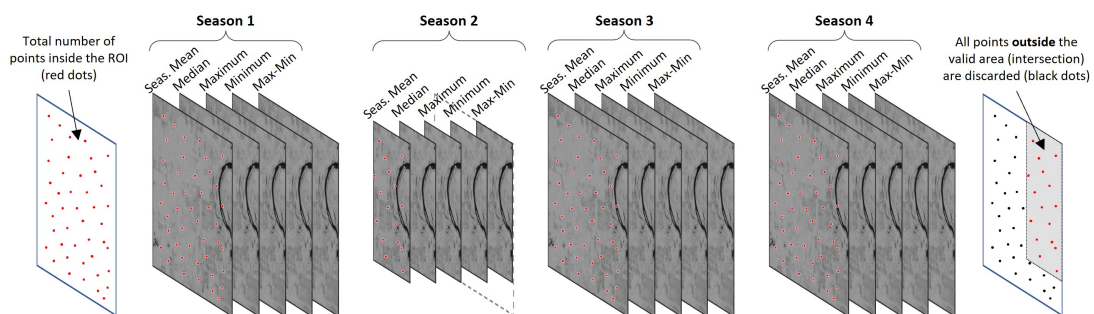


FIGURE 3.20: Chopping of training set issue caused by low overlapping degree between region of interest and each SAR image belonging to the original time series.

algorithms. It allows to quickly identify significant information from vast data sets. The biggest advantage of random forest is that it relies on collecting various decision trees to arrive at any solution. As depicted in Figure 3.21, this is an “ensemble algorithm” that considers the results of more than one algorithms of the same or different kind of classification.

After assuming to have a number m of features, its working principle can be summarized in the following steps:

1. Randomly chose k features such that $k < m$;
2. Among the k features, calculate the root node by choosing a node with the highest Information gain, which is a decrease of entropy (is the difference between the starting node uncertainty and the weighted impurity of the two child nodes);
3. Split the node into child nodes;
4. Repeat the previous steps n times;
5. End up with a “forest” made of n “trees”;
6. Perform Bootstrapping, i.e., combining the results of all Decision Trees.

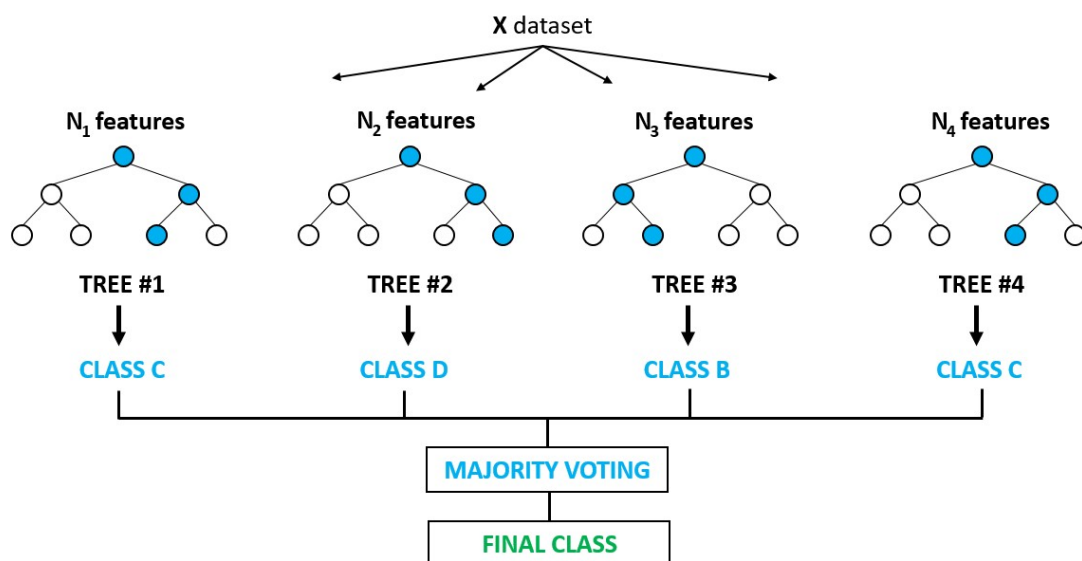


FIGURE 3.21: Simplified concept scheme of a random forest classifier.

Random forest classifiers are in general very robust to outliers, work fairly well on non-linear data, overfitting risks are reduced, runs very efficiently on large data sets and have better overall accuracy with respect to many other classifiers used for land cover mapping. However, RF classifiers are found to be biased while dealing with categorical variables, they are slow to train and they not suitable for linear methods with a lot of sparse features.

The RF classifier used in this work consisted of 60 decision trees (based on empirical testing), a number of variables per split equal to the square root of the total number of input features (as per scientific literature), and the fraction of input for bagging (per tree) was set to $1/2$ and each tree had a minimum leaf population equal to 1 (so that every new node has at least 1 point in its training set).

To validate the mapping results and provide a quantitative analysis, a total of 1350, 712, 1432 and 1709 High-resolution (HR) validation points for Siberia, Italy, Amazonia and Africa, respectively, were manually collected by experts in different institutions (most of them collaborate to the ESA CCI+ project). This HR set was extracted by visual interpretation from multispectral and multitemporal 10 m spatial resolution Sentinel-2 data sets and/or Very High Resolution single date SPOT-6/7 ortho images at 1.5 m spatial resolution; when available, ground panoramic images were inspected as well. The only exception is the training set generated for the Italian tile: in this case, together with interpretation of Sentinel-2 multispectral data, high-resolution imagery from Google Earth and visual inspection of the CGLS map at 100 m scale were used to derive training points. The spatial and class-wise distribution of the validation points for each test site is reported in Figure 3.22, while Figure 3.23 shows the trend of each class (when present) in multitemporal VH-polarized SAR data.

Qualitative classification results are shown for the selected tiles in Figure 3.24. It is possible to note that the new land cover product (in the last column) offers a significantly increased spatial detail of the classes with respect to the MRLC map. In other words, the new product is coherent with the coarser CGLS map at 100 m, used to select the training set, but improves its details. Please note that the black regions in the MRLC maps indicate areas labeled with mixed classes in the MR map, hence removed from this comparison (also the areas not covered by the tile of interest are filled with black color).

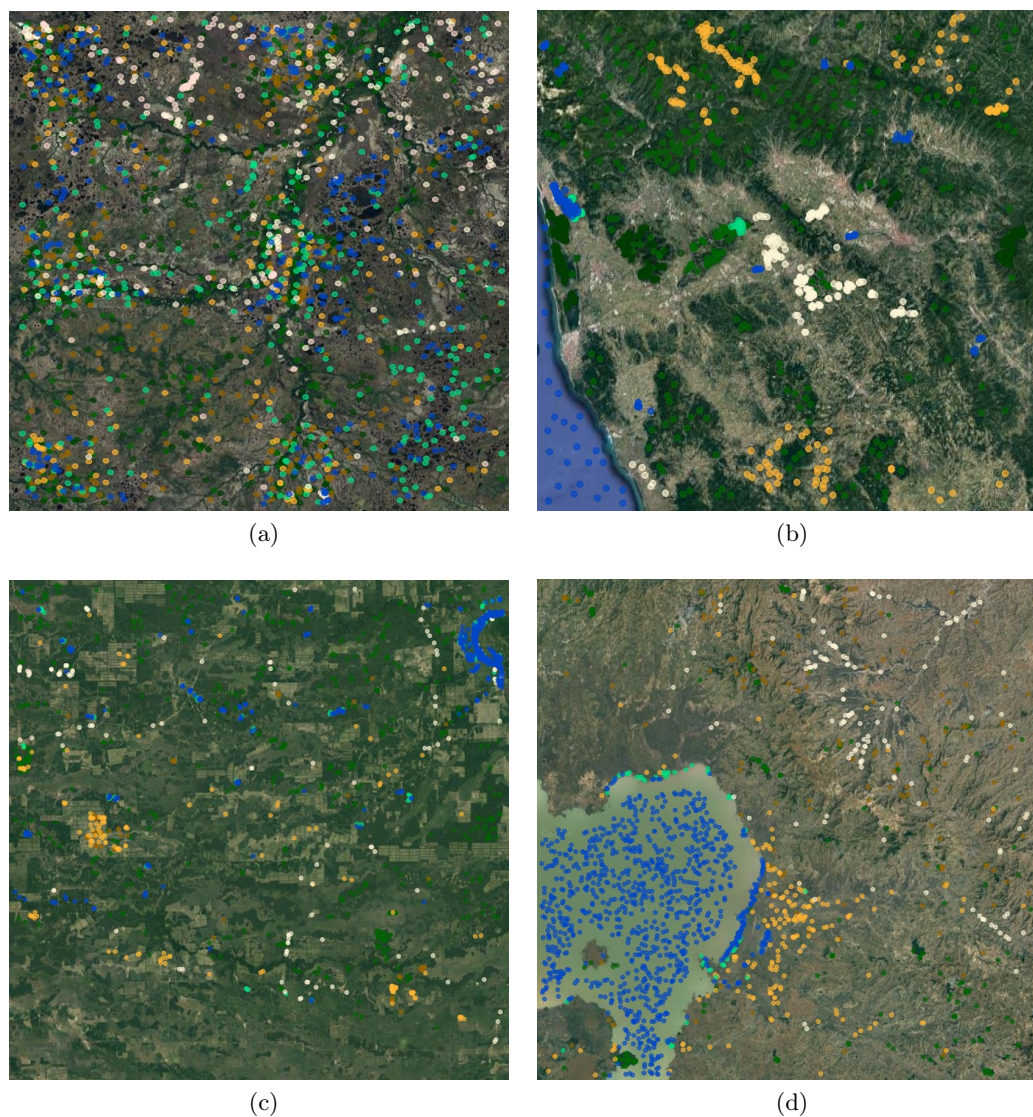


FIGURE 3.22: Spatial distribution of the validation points in (a) Siberia (tile 42WXS), (b) Italy (central Italy tile, 32TPP), (c) Amazonia (tile 21KUQ) and (d) Africa (tile 37PCP). The color code is reported in Table 3.3

To further appreciate the increased spatial resolution of the final product of the proposed procedure, in Figure 3.25 it is possible to observe the classification of a very small portion of each test site. The aim of this figure is to provide a qualitative comparison between the MRLC map used to train the RF classifier and the obtained result in areas which are significant. In particular, in the African HR map it is possible to observe the much more outlined area of aquatic vegetation surrounding the lake; also, small broad-leaved trees are now visible to the East of the scene. Regarding the Amazonian tile, lots of important spatial details are visible: small river branches, as well as the regular square-shaped regions, due to (sadly) deforestation activities. In these areas, current grassland

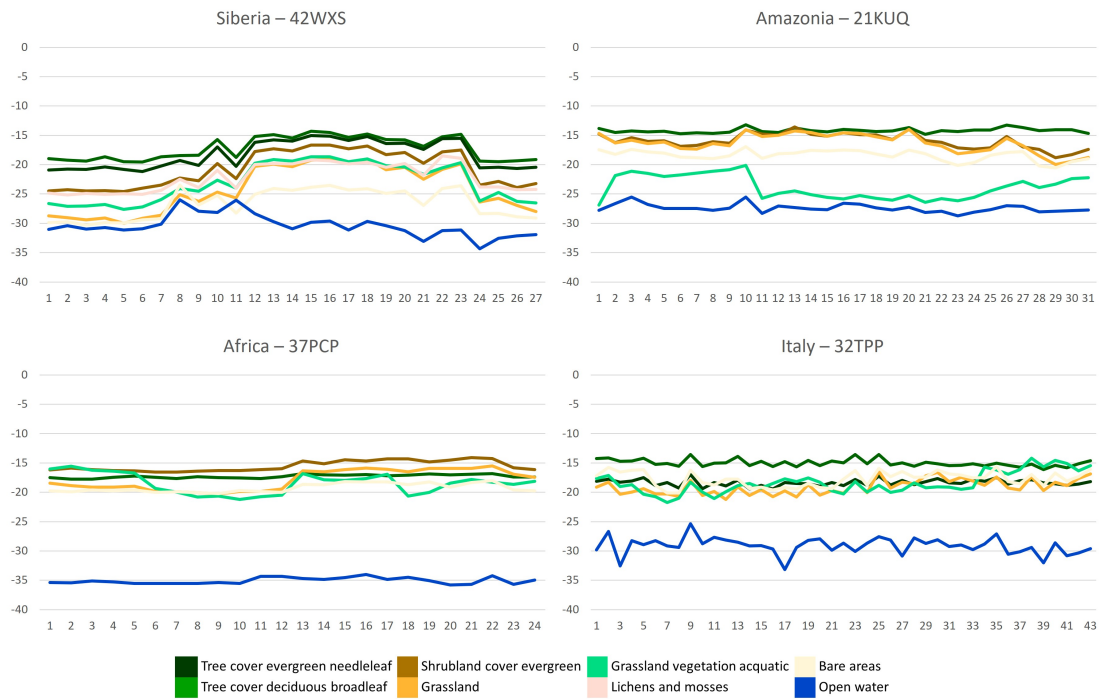


FIGURE 3.23: Phenology tracking of classes in multitemporal Sentinel-1 SAR data (note that the tiles do not always contain the same number of classes).

cover (yellow) replaced previous dense vegetation (dark green) zones. Whereas, in the Italian tile, the enhanced spatial resolution of the HR map highlights very small water bodies, surrounded by thin layers of grassland. Also, many agricultural fields boundaries are clearly distinguishable (even if not classified as actual crop fields, since this class was neither selected from the MRLC map nor classified). Finally, looking at the Siberian tile, small water bodies and grassland areas are well visible and separated. Moreover, a large variety of land cover types emerge where the two river branches split, types that are invisible in the MR map.

Table 3.4 reports, finally, the quantitative analysis of the maps extracted in the four test areas, using the above mentioned manually extracted validation sets. For each tile and test site, this table shows the achieved overall accuracy (OA) values together with the number of samples used to validate each class (px), as well as the corresponding producer (pa) and the user accuracy (ua) values for each of class. The producer accuracy is the map accuracy from the point of view of who generated the map (the producer); this refers to how often are real features on the ground correctly shown on the classified map, or the probability that a certain land cover of an area on the ground is classified as such. On the other hand, the user Accuracy is the accuracy from the point of view of who uses

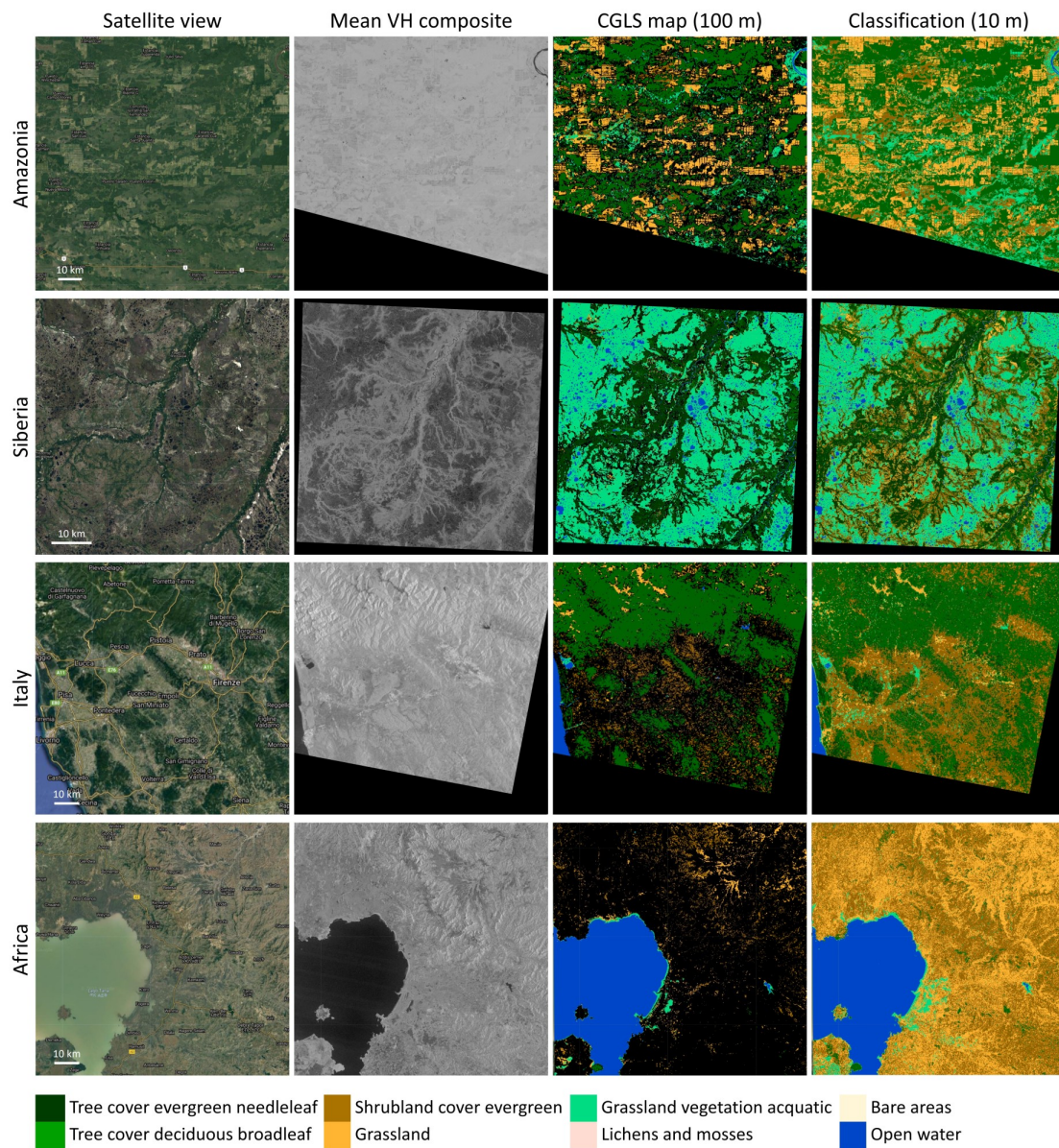


FIGURE 3.24: Qualitative results for the four test areas. Columns refer to 1) the Google Satellite basemap view, 2) the annual mean composite derived by all the VH-channel images overlapping the tile of interest, 3) the CGLS map at 100 m resolution and 4) the obtained classification result with 10 m pixel spacing.

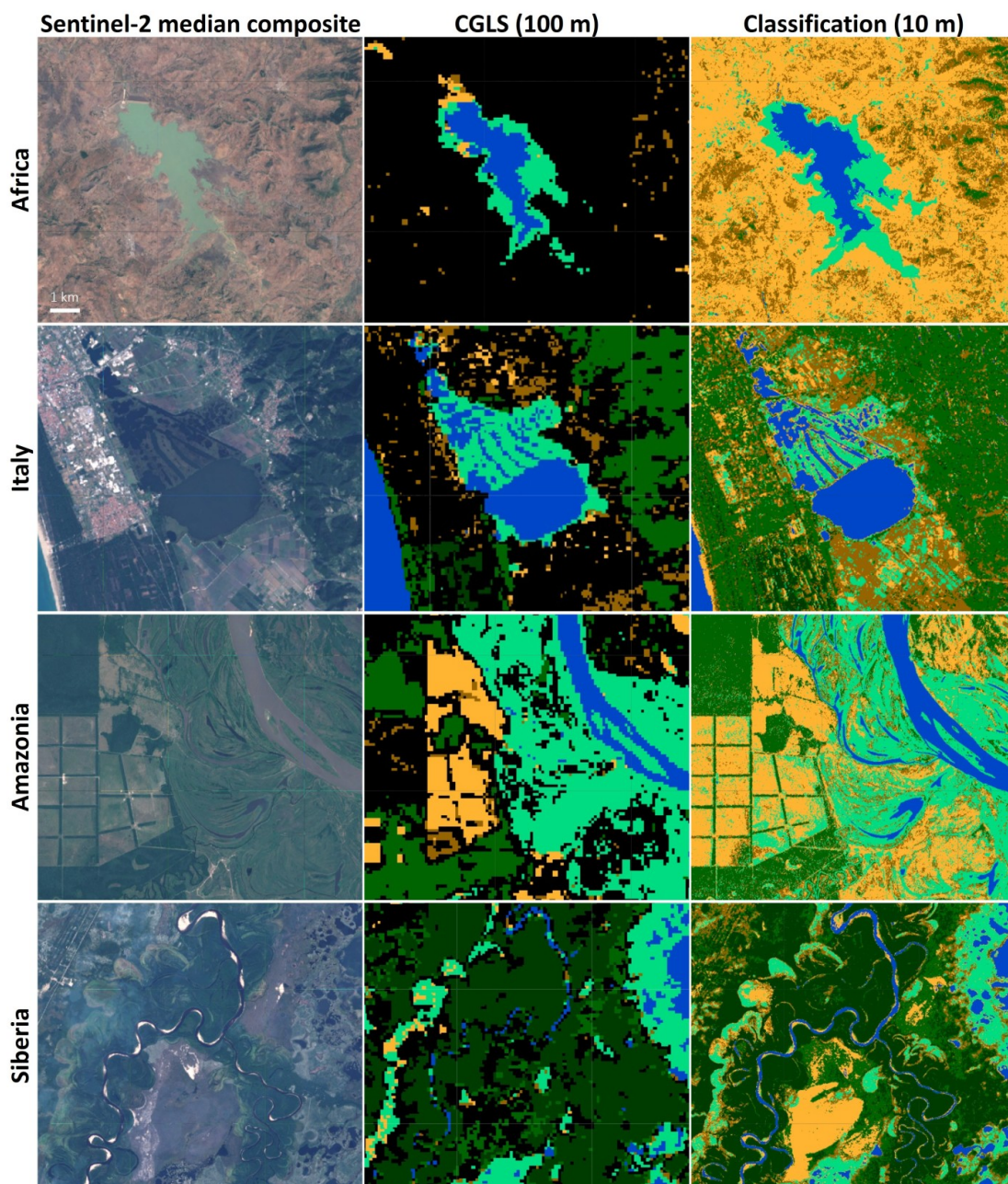


FIGURE 3.25: Small sample areas inside each test site: on the left a multispectral Sentinel-2 image of each area, at the center the CGLS map, and on the right the result of the proposed procedure.

the map (the user), and not the map maker. The user accuracy essentially tells how often the class on the map will actually be present on the ground, also referring to the “reliability” of the map.

All the values in Table 3.4 were computed for both the original MRLC map used in this work (the CGLS at 100 m resolution) and for the results of the proposed procedure (labeled “this work” in the table).

LC	Siberia										Italy										Amazonia										Africa									
	CGLS		this work		CGLS		this work		CGLS		this work		CGLS		this work		CGLS		this work		CGLS		this work		CGLS		this work		CGLS		this work									
	px	pa	ua	OA	px	pa	ua	OA	px	pa	ua	OA	px	pa	ua	OA	px	pa	ua	OA	px	pa	ua	OA	px	pa	ua	OA	px	pa	ua	OA								
1	-	-	-	-	258	94.6	84.3	91.9	77.7	486	70.4	90.7	92.2	98.2	302	8.8	96.4	37.4	95.8	-	-	-	-	-	-	-	-	-	-	-	-									
2	300	55.6	38.5	74.7	196	49.8	98	60.2	95.2	-	-	-	-	-	-	-	-	-	-	-	-	-	-	-	-	-	-	-	-	-	-									
3	300	7.6	56	51	-	-	-	-	-	79	17.7	41.1	11.4	39.1	152	14.4	52.3	44.1	26.5	-	-	-	-	-	-	-	-	-	-	-	-									
4	150	6	52	24.7	107	56	97.6	70	80.4	176	67.6	66.1	92.6	70.9	193	7.7	42.8	68.4	43.3	-	-	-	-	-	-	-	-	-	-	-	-									
5	300	57.6	30.4	47	35	20	63.6	45.7	80	145	78.6	31	67.6	47.1	61	60.6	22.5	41	21.4	-	-	-	-	-	-	-	-	-	-	-	-									
6	-	-	-	-	-	-	-	-	-	-	-	-	-	-	-	-	-	-	-	-	-	-	-	-	-	-	-	-	-	-	-									
7	-	-	-	-	-	-	-	-	-	-	-	-	-	-	-	-	-	-	-	-	-	-	-	-	-	-	-	-	-	-	-									
8	300	50.3	92	93	116	92.1	85.3	87.1	91	546	46.9	98.1	86.6	91.8	1001	86.6	100	91.4	99.9	-	-	-	-	-	-	-	-	-	-	-	-									

TABLE 3.4: Accuracy results for the selected test site using independently extracted high resolution validation points. The table reports the overall accuracy (OA) values for the CGLS map and for the maps produced by the proposed procedure, the number of validation pixels per class (px) and the class producer's accuracy (pa). Note: the symbol “-” means there are no MR points in that tile for a specific class.

Moreover, to better understand the consistency of the high-resolution reference points collected by the experts within the CCI+ project, from Table 3.4 it is possible to observe that the overall accuracy was also computed against the medium resolution CGLS land cover map at 100 m spatial resolution, for each considered test region, in order to provide a quantitative estimation of “how good” the HR validation points are with respect to the MR land cover map used to build the training set. Based on this evaluation, it turned out that, in general, the quality of the HR validation dataset is relatively low, if compared to the MR map used in the training process; since the training and validation processes are carried out using two completely different data sets (which are not directly comparable), this fact justifies the relatively low accuracy values obtained, on average, over the test sites. Despite this, a very clear take away message from the numbers of Table 3.4 is that the proposed methodology allows to achieve significantly higher accuracy values on the independent HR validation set than the CGLS map. This increment is equal to 18.4% for Siberia, 5.9% for Italy, 24.2% for Brazil and 16.8% for Africa. Note that Italy achieved the lowest improvement because the validation points were manually extracted also using the support of the CGLS map (therefore, the result is slightly biased). The methodology was able to achieve on average 71% overall accuracy and standard deviation equal to 14.2%. Such high variation is mainly due to the results obtained in the Siberian tile (50.5% OA); this was in fact a very challenging region, as snow, ice and clouds cover the tile of interest for almost 3/4 of the year, thus, even radar data was not able to reliably track the phenology of the classes present in the area. If this region was discarded from the evaluation of the classifier performance, the average overall accuracy could have reached values around 79-80%, with associated low standard deviation values (around 5%). Still, to provide a clear and transparent evaluation of both strengths and weaknesses/limitations, the Siberian tile was kept.

These results are somehow coherent with the different accuracy levels achieved by other global land cover products at 30 m spatial resolution. Accuracy values significantly vary depending on the considered land cover type; for example, in the case of classes associated to “pure” spectral properties or that occupy a large proportion of the considered region of interest such as forests, croplands and water bodies, generally high accuracy values can be found. On the other hand, complex classes such as shrubland, grassland, wetland and many others are very often confused with other types of land covers. Quantitatively speaking, the *forest* class achieved 94% OA for the GLC_FCS30 map,

76.5% OA for the FROM_GLC30 map and 83.6% OA for the GlobeLand30 map. The classification carried out in this work does not account for a single “forest” class but considers, instead, two different types of forest: broadleaved and needleleaved trees; in this case, the obtained accuracy values were, on average, 73.8% and 67.5%, respectively. Moreover, for broadleaved trees the accuracy could be much higher, around 92%, due to the fact that this class is very rare in the considered African tile and, therefore, it is subject to classification errors which decrease the mapping accuracy. Regarding the *shrubland* class, the accuracy values were lower, i.e., 56.8% for the GLC_FCS30, 33.9% for the FROM_GLC30 and 72.6% for the GlobeLand30. The proposed methodology reached 35.5% accuracy for this class, as it is very difficult to detect in radar data; in the Amazonian tile the accuracy of the shrubland class achieved only 11.4% accuracy (which contributed to decrease the overall accuracy for this class), as almost all the classes are barely distinguishable both in spatial and temporal SAR features (see Figure 3.26). Lastly, regarding the *vegetation aquatic* class, accuracy values were around 61.8% for the GLC_FCS30 map, 3.3% for FROM_GLC30 map and 52.6% for the GlobeLand30; the proposed classification methodology was able to achieve, on average, 50.3% accuracy. Also in the case of aquatic vegetation, such class is in general very hard to distinguish in SAR data, as it is confused with many other land covers. It was not possible to make a similar comparison for the other classes mapped in this work, due to legends incompatibilities. Note that the above accuracy values achieved by the 30 meters products were computed based on different validation data sets, thus, they are not fully comparable with the results obtained in this work.

Cohen’s kappa coefficient k was also computed for each test site. The k coefficient basically provides information related to how much better a classifier is performing over the performance of a classifier that simply guesses randomly according to the frequency of each class. It is defined as follows:

$$k = \frac{p_o - p_e}{1 - p_e} = 1 - \frac{1 - p_o}{1 - p_e} \quad (3.3)$$

where p_o is the observed agreement and p_e is the expected agreement. Cohen’s kappa coefficient is always less than or equal to 1. Values of 0 or less, indicate that the classifier is completely useless. However, there is no standardized way to interpret its values: in

[149], the Authors provide a way to characterize values, which accords with the following scheme:

- $k \leq 0 \rightarrow$ no agreement;
- $0 < k \leq 0.2 \rightarrow$ slight agreement;
- $0.2 < k \leq 0.4 \rightarrow$ fair agreement;
- $0.4 < k \leq 0.6 \rightarrow$ moderate agreement;
- $0.6 < k \leq 0.8 \rightarrow$ substantial agreement;
- $0.8 < k \leq 1 \rightarrow$ almost perfect agreement

The estimated k coefficient was 0.76 for Amazonia, 0.55 for Africa, 0.7 for Italy and 0.38 for Siberia.

Despite the MR map was obtained using multispectral data and the new result is based only on SAR data, the SAR-base methodology achieves better results thanks to the exploitation of spatio-temporal features and to the intelligent training point selection procedure.

Please note that the numbers in Table 3.4 refer to one specific result of the procedure, because the first step for training point selection is a random extraction of points from the MRLC map using the procedure shown in Section 3.7.1. To understand the impact of this random seed, a cross-validation was carried out, and it was found that the overall accuracy values are stable, with very small standard deviations within the range [0.5 - 1] %.

To understand the source of the classification errors, in Figure 3.26 the mean features vectors for the training set of each class in each considered region are depicted. The plots in Figure 3.26 are divided in three groups: the trend of the spatial features, the trend of the VH-polarized temporal features and the trend of the VV-polarized temporal features. Although only the average behaviour per class is shown, it is clear that, apart from water, all the vegetated land covers have a similar pattern. Still, the small differences are enough to enable a decent discrimination of the different land cover classes. Based on the HR validation points - independently extracted by experts - the produced land cover maps appear to be very promising, except than for Siberia. As a matter of fact,

discriminating classes in Siberia is complicated by the long cold season during which the soil is covered with snow and ice. These harsh conditions effectively reduce the amount of multitemporal SAR images useful to discriminate among different land cover types. Still, the proposed methodology achieves good results for specific land covers (for instance, the producer accuracy for *shrublands* increases by 43% with respect to the MRLC map).

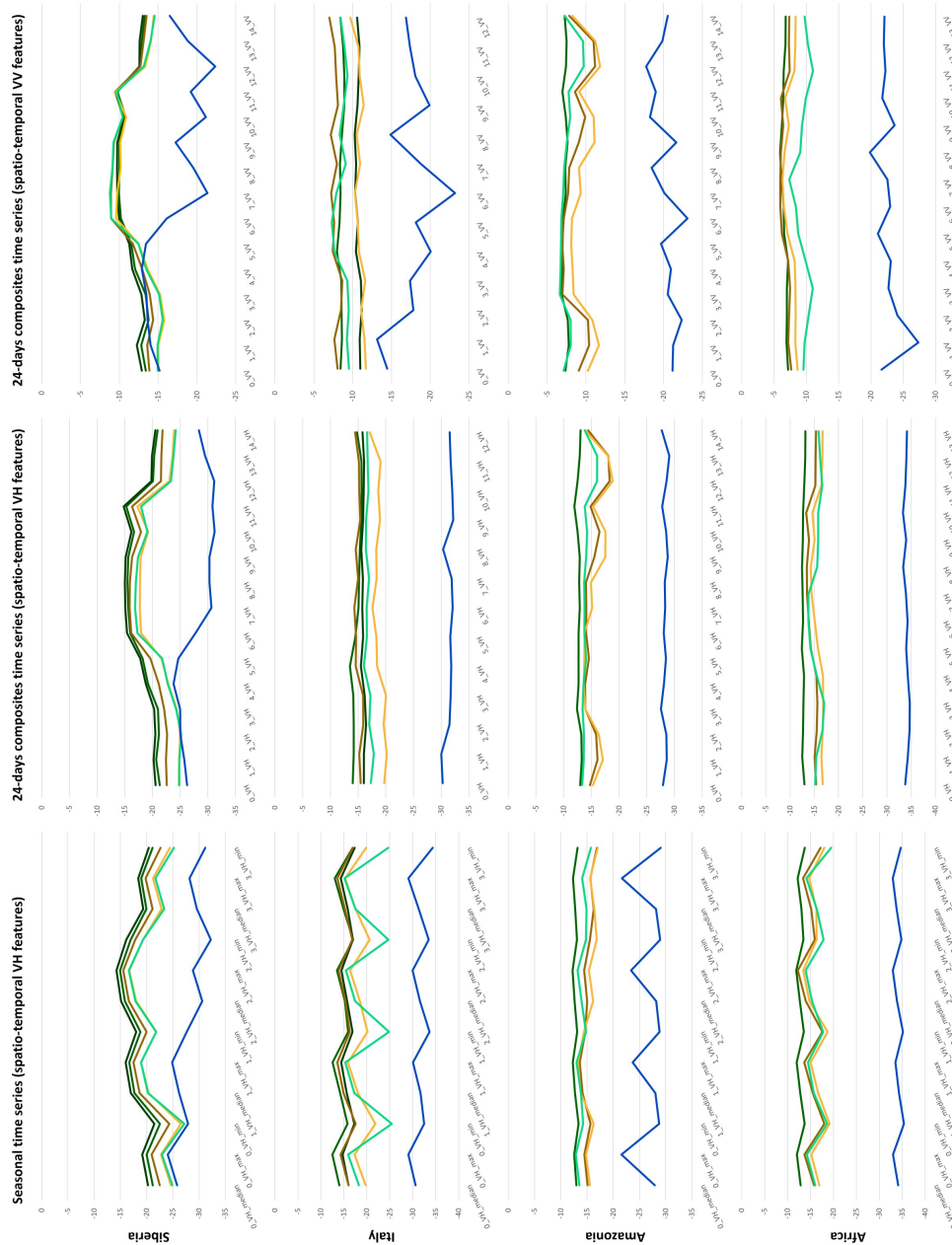


FIGURE 3.26: Mean feature vectors for each class in each test site (class color legend as in Table 3.3).

Another very important point that can be observed from Table 3.4 regards the complete absence of classes number 7 and 8, corresponding to “lichens and mosses” and “bare areas”, respectively.

Regarding lichens and mosses, unfortunately, such land cover type was not present within the medium resolution land cover map used to build the training set (the CGLS at 100 m scale), for any of the four considered regions. In fact, if a class is not present in the MRLC product (i.e., there are no pixels associated to that land cover), then it is not considered in the overall accuracy computation (so HR validation points of that class are discarded). However, since reference points representing lichens and mosses were manually collected in the Siberian tile, we decided to show such land cover in Table 3.4 anyways, even if it has never been mapped. Note that this approach was applied, in general, for all the classes and in all test sites; if the total number of MR pixels of a specific class is very low (e.g., less than 10 pixels), then this class is excluded from the validation process, even if HR reference points were available. This is, for example, visible for class number 1 (broadleaf trees) in Siberia; the number of MR pixels was considered insufficient to reliably train the classifier and, therefore, it was completely discarded from accuracy computation (despite a certain number of HR validation points were available for this class).

On the other hand, the bare areas class was treated differently. In this case, in fact, bare areas are present almost in all the regions of interest. However, the number of medium resolution pixels representing this class is quite low (not low enough to be discarded by the classifier) and, after collecting them to be part of the training set, they are all discarded by the high-resolution training set generation procedure, described in Section 3.7.1. Considering, for instance, the African tile, it is possible to note in Table 3.4 that the bare areas class is missing. In this case, the number of MR pixels belonging to this class was equal to 43, thus, very low; then, after subdividing the whole class into two sub-classes through the k -Means clustering, the number of remaining pixels associated to bare areas (and used to build the mean, representative vector) amounts to 14, preventing to correctly reconstruct the statistics of the bare areas class; for this reason, if the correlation coefficient ρ used to select points whose features are similar to those belonging to the representative vector is set to high values (i.e., $\rho = 0.95$ in the proposed algorithm), none of the original 43 pixels can satisfy such constraint. All the pixel features belonging to the bare areas class are, in fact, considered not similar enough to the representative features, thus, all 43 pixels are discarded from the training set generation procedure.

In order to include this class in the classification, despite its scarcity, it is necessary to decrease the correlation constraint; experiments showed a value of $\rho = 0.8$ could allow the classifier to consider such class. However, since this value is globally applied inside the classification procedure, the overall classifying performance is affected; this is likely due to the fact that a high level of confusion is introduced by the inclusion of the bare arees class in the procedure, and also because “dirtier” training points are collected for each of the other classes.

Of course, both the selection of the degree of similarity (correlation coefficient) and the exclusion of classes based on a low number of MR training points (e.g., broadleaf trees in Siberia) represent an important trade-off of the proposed mapping approach that deserves to be deeply explored.

3.8.1 Comparison with other training set generation procedures

Three different training set generation approaches have been tried, to evaluate their performances within the presented land cover mapping methodology. This brief section is devoted to the comparison in terms of achieved accuracy in three different cases:

1. Training set generation using the procedure described in Section 3.7.1;
2. Training set generation based only on the morphological erosion of the MRLC map;
3. Training set generation based on the MRLC map eroded using the Multiclass Border Reduction Filter (MBRF) described in [79].

Similarly to the scope of this thesis work, the paper reported in [79] aims at locally train a classifier using an automated selection of training points from existing (but outdated) land cover maps. The classifier used in the cited work is based on optical data acquired by the Medium Resolution Imaging Spectrometer (MERIS), a programmable spectrometer on board the Envisat mission.

In general, a classical erosion filter may remove too many pixels, at the risk of completely remove those classes that do not homogeneously cover large areas (e.g., urban areas) or present linear shapes (e.g., thin rivers). To overcome this issue, this work developed a

Multiclass Border Reduction Filter (MBRF) that is able to remove pixels on the boundaries, while keeping at least one pixel among each group of adjacent pixels. Therefore, all the original classes are preserved also in the eroded version of the LC map.

The working principle of the MBRF filter can be summarized in two steps (per class): first, the number of pixels belonging to the class of the central pixel inside a moving kernel is registered; then, the central pixel is set to “no data” if it did not reach the largest count of neighbours amongst the pixels that belong to the same class inside the moving kernel.

At the end of the procedure, the MBRF removed 5% less pixels than the classical erosion filter. Such percentage belongs to those classes that are much less frequent or present in linear patterns.

Carrying on with the comparison, in Table 3.5 are reported the achieved overall, producer and user accuracy, together with the k coefficient for each of the three cases described at the beginning of this section, and for each test area.

		Siberia						Italy						Amazonia						Africa					
		CGLS			this work			CGLS			this work			CGLS			this work			CGLS			this work		
		OA	pa	ua	OA	pa	ua	OA	pa	ua	OA	pa	ua	OA	pa	ua	OA	pa	ua	OA	pa	ua			
Case 1	LC																								
	1	-	-	-	258	94.6	84.3	91.9	77.7	77.7	486	70.4	90.7	92.2	98.2	98.2	302	8.8	96.4	37.4	37.4	95.8			
	2	300	55.6	38.5	196	49.8	98	60.2	95.2	95.2	-	-	-	-	-	-	-	-	-	-	-	-			
	3	300	7.6	56	-	-	-	-	-	-	79	17.7	41.1	11.4	39.1	39.1	152	14.4	52.3	44.1	44.1	26.5			
	4	150	6	52	107	56	97.6	70	80.4	80.4	176	67.6	66.1	92.6	70.9	70.9	193	7.7	42.8	68.4	68.4	43.3			
	5	300	57.6	30.4	35	20	63.6	45.7	80	80	145	78.6	31	67.6	47.1	47.1	61	60.6	22.5	41	41	21.4			
	6	-	-	-	-	-	-	-	-	-	-	-	-	-	-	-	-	-	-	-	-	-			
	7	-	-	-	-	-	-	-	-	-	-	-	-	-	-	-	-	-	-	-	-	-			
8	300	50.3	92	116	92.1	85.3	87.1	91	91	546	46.9	98.1	86.6	91.8	91.8	1001	86.6	100	91.4	91.4	99.9				
		OA 47.1 - k=35.4			OA 74.1 - k=64.9			OA 78 - k=70.4			OA 65.8 - k=50.6														
Case 2	LC																								
	1	-	-	-	87.2	86.2	86.2	86.2	86.2	86.2	91.8	91.8	98	98	98	98	35	35	95.5	95.5	95.5	95.5			
	2	-	-	-	74.4	87.9	87.9	87.9	87.9	87.9	-	-	-	-	-	-	-	-	-	-	-	-			
	3	300	36.6	68	-	-	-	-	-	-	14.7	14.7	51.5	51.5	51.5	51.5	80.2	80.2	29.1	29.1	29.1	29.1			
	4	150	4	14	69.7	90.4	90.4	90.4	90.4	90.4	91.7	91.7	50	50	50	50	38.3	38.3	31.4	31.4	31.4	31.4			
	5	300	50.3	38.8	57.1	23.8	23.8	23.8	23.8	23.8	48	48	64	64	64	64	86.8	86.8	24.6	24.6	24.6	24.6			
	6	-	-	-	-	-	-	-	-	-	-	-	-	-	-	-	-	-	-	-	-	-			
	7	-	-	-	-	-	-	-	-	-	-	-	-	-	-	-	-	-	-	-	-	-			
8	300	83.3	94.3	53.4	92.5	92.5	92.5	92.5	92.5	90	90	78.2	78.2	78.2	78.2	85.7	85.7	99.5	99.5	99.5	99.5				
		OA 46.1 - k=37			OA 80.9 - k=74			OA 77 - k=71.1			OA 71.3 - k=53.2														
Case 3	LC																								
	1	-	-	-	84.5	90.4	90.4	90.4	90.4	90.4	90.8	90.8	98	98	98	98	24.9	24.9	100	100	100	100			
	2	-	-	-	83.1	81.9	81.9	81.9	81.9	81.9	-	-	-	-	-	-	-	-	-	-	-	-			
	3	300	66.6	36.6	-	-	-	-	-	-	15.6	15.6	45	45	45	45	88.8	88.8	29.9	29.9	29.9	29.9			
	4	150	10	15.4	70.6	88.5	88.5	88.5	88.5	88.5	87.6	87.6	49.7	49.7	49.7	49.7	51.8	51.8	81.3	81.3	81.3	81.3			
	5	300	47.3	40.5	51.4	46.1	46.1	46.1	46.1	46.1	54.9	54.9	61.8	61.8	61.8	61.8	86.8	86.8	26.3	26.3	26.3	26.3			
	6	-	-	-	-	-	-	-	-	-	-	-	-	-	-	-	-	-	-	-	-	-			
	7	-	-	-	-	-	-	-	-	-	-	-	-	-	-	-	-	-	-	-	-	-			
8	300	93.6	88.3	87.9	93.6	93.6	93.6	93.6	93.6	88.5	88.5	80.4	80.4	80.4	80.4	85.7	85.7	99.6	99.6	99.6	99.6				

TABLE 3.5: Accuracy results for the selected test site using independently extracted high resolution validation points. The table reports the overall accuracy (OA) values for the maps produced by the proposed procedure, the number of validation pixels per class (px) and the class producer's accuracy (pa) in three different cases. Case 1 refers to the application of the training set generation procedure, as described in Section 3.7.1; Case 2 reports the results when only a classical morphological erosion filter is applied to the MRLC map; Case 3 shows the values obtained using applying a Multiclass Border Reduction Filter (MBRF) on the MRLC map. Note: the symbol “-” means there are no MR points in that tile for a specific class.

From the comparison table it is possible to observe that case 1 (i.e., the proposed methodology described in Section 3.7.1) outperforms the other two approaches for all the considered test areas, except from Italy, using the same HR validation dataset, manually extracted by experts.

3.8.2 Selection of features suitable for land cover mapping

This section intends to briefly justify the choice of the final input features, described in Section 3.6. Prior to the final decision regarding which features are the most useful for characterizing land cover, several experiments were carried out. To carry out these experiments, a stratified random sampling procedure was applied on the CGLS land cover map at 100 m scale in order to generate independent, non-overlapping training and validation sets. Before sampling, the CGLS was only eroded to avoid collecting points over transition regions. Since the overall accuracy is not computed on the manually extracted, high quality and high-resolution validation set, such computed statistic is not intended for actual validation purposes. Still, by keeping unaltered the entire classification system and changing only the set of input features, it is possible to understand the impact of the selected features in terms of classification performance.

Table 3.6 shows how accuracy values change as a function of the set of input SAR features. In the table, four cells are highlighted in greenish colour to indicate that the SAR features configuration was considered as the optimal one. As a matter of fact, for the test sites located in Amazonia, Africa and Italy, the overall, producer and user accuracy values were among the highest. For Siberia, the highest values are reached for configuration no. 10; however, the number of features in this case is 84 which, compared to those of configuration no. 13 (46) is almost twice. The overall accuracy for Siberia was about 77.60% and 75.15% in the case of configurations no. 10 and 13, respectively; since such values are similar, the configuration with fewer input features was selected (no. 13).

Different is the case of the test site located in Amazonia, whose highest overall accuracy is achieved thanks to configuration no. 7 (75.97%). However, results are similar to those obtained using configuration no. 13 (75.75%); for this reason, we decided to use the latter configuration even for the Amazonian site, in order to exploit the same configuration for any region of interest. The objective is, in fact, to build a classifier that works “fairly”

well worldwide, which means that the classifier will perform better in certain areas of the World, and worse in others.

Given all the above considerations, the vegetation mapping model described in the previous sections is tuned based on the input SAR features corresponding to configuration no. 13 of Table 3.6.

TABLE 3.6: Accuracy results obtained by changing the set of input SAR features.

Begin of Table 3.6: Accuracy vs. input features						
ID	# Features	Features	Amazonia	Siberia	Africa	Italy
1	28	<p>For each seasonal composite obtained by averaging each despeckled seasonal collection:</p> <ul style="list-style-type: none"> • Original despeckled VH seasonal image • Lee-filtered image • spatial mean • spatial median • spatial maximum • spatial minimum • Difference Max-Min 	<p>OA:72.07% PA:61.77% UA:61.71%</p>	<p>OA:75.69% PA:70.17% UA:72.72%</p>	<p>OA:85.42% PA:60.85% UA:71.09%</p>	<p>OA:67.54% PA:58.64% UA:70.16%</p>
2	24	<p>For each seasonal composite obtained by averaging each despeckled seasonal collection:</p> <ul style="list-style-type: none"> • Original despeckled VH seasonal image • spatial mean • spatial median • spatial maximum • spatial minimum • Difference Max-Min 	<p>OA:73.16% PA:63.63% UA:64%</p>	<p>OA:74.82% PA:69.70% UA:71.52%</p>	<p>OA:85.07% PA:62.28% UA:70.39%</p>	<p>OA:69.29% PA:58.41% UA:62.41%</p>
3	28	<p>For each seasonal composite obtained by simply averaging each seasonal collection:</p> <ul style="list-style-type: none"> • Original despeckled VH seasonal image • Lee-filtered image • spatial mean • spatial median • spatial maximum • spatial minimum • Difference Max-Min 	<p>OA:73.80% PA:64.21% UA:64.65%</p>	<p>OA:74.65% PA:69.22% UA:72.6%</p>	<p>OA:84.39% PA:60.04% UA:68.59%</p>	<p>OA:65.21% PA:53.93% UA:60.58%</p>

Continuation of Table 3.6						
ID	# Features	Features	Amazonia	Siberia	Africa	Italy
4	24	For each seasonal composite obtained by simply averaging each seasonal collection: <ul style="list-style-type: none"> • Original despeckled VH seasonal image • spatial mean • spatial median • spatial maximum • spatial minimum • Difference Max-Min 	OA:74.24% PA:69.36% UA:72.62%	OA:74.47% PA:69.36% UA:72.62%	OA:85.59% PA:63.03% UA:72.38%	OA:66.08% PA:56.39% UA:62.01%
5	20	For each seasonal composite obtained by simply averaging each seasonal collection: <ul style="list-style-type: none"> • Original despeckled VH seasonal image • spatial median • spatial maximum • spatial minimum • Difference Max-Min 	OA:74.24% PA:63.42% UA:63.92%	OA:72.74% PA:67.8% UA:70.72%	OA:86.10% PA:64.67% UA:74.86%	OA:66.52% PA:55.15% UA:60.55%
6	20+15	For each seasonal composite obtained by simply averaging each seasonal collection: <ul style="list-style-type: none"> • Original despeckled VH seasonal image • spatial median • spatial maximum • spatial minimum • Difference Max-Min • Extra: 24-days composites (15 images) 	OA:73.59% PA:62.14% UA:64.03%	OA:74.47% PA:68.84% UA:73.11%	OA:84.9% PA:60.62% UA:73.41%	OA:74.34% PA:62.5% UA:62.77%
7	16+15	For each seasonal composite obtained by simply averaging each seasonal collection: <ul style="list-style-type: none"> • spatial median • spatial maximum • spatial minimum • Difference Max-Min • Extra: 24-days composites (15 images) 	OA:75.97% PA:66.78% UA:69.68%	OA:75.17% PA:69.81% UA:74.44%	OA:85.07% PA:61.02% UA:70.45%	OA:75.65% PA:62.91% UA:63.72%

Continuation of Table 3.6						
ID	# Features	Features	Amazonia	Siberia	Africa	Italy
8	16+30	<p>For each seasonal composite obtained by simply averaging each seasonal collection:</p> <ul style="list-style-type: none"> • spatial median • spatial maximum • spatial minimum • Difference Max-Min • Extra: 12-days composites (30 images) 	<p>OA:75.32% PA:66.87% UA:68.39%</p>	<p>OA:75.17% PA:69.38% UA:75%</p>	<p>OA:85.93% PA:62.95% UA:75.18%</p>	<p>OA:75.21% PA:63.99% UA:69.86%</p>
9	16+N	<p>For each seasonal composite obtained by simply averaging each seasonal collection:</p> <ul style="list-style-type: none"> • spatial median • spatial maximum • spatial minimum • Difference Max-Min • Extra: All N images available for the ROI 	<p>OA:74.67% PA:64.91% UA:66.96%</p>	<p>OA:75.17% PA:69.38% UA:75%</p>	<p>OA:74.67% PA:64.91% UA:66.96%</p>	<p>OA:78.37% PA:68.35% UA:84.33%</p>
10	84	<p>For each monthly composite (12 in total):</p> <ul style="list-style-type: none"> • Original despeckled VH monthly image • Lee-filtered image • spatial mean • spatial median • spatial maximum • spatial minimum • Difference Max-Min 	<p>OA:74.67% PA:66.87% UA:69.47%</p>	<p>OA:77.60% PA:72.81% UA:76.03%</p>	<p>OA:85.76% PA:62.91% UA:72.89%</p>	<p>OA:78.69% PA:67.98% UA:71.83%</p>
11	217	<p>For each of the N available images for the ROI:</p> <ul style="list-style-type: none"> • Original VH image • Lee-filtered image • spatial mean • spatial median • spatial maximum • spatial minimum • Difference Max-Min 	<p>OA:74.67% PA:66.05% UA:67.95%</p>	<p>OA:73.43% PA:74.02% UA:74.02%</p>	<p>OA:87.13% PA:68.45% UA:78.65%</p>	<p>OA:79.72% PA:64.96% UA:71.64%</p>

Continuation of Table 3.6						
ID	# Features	Features	Amazonia	Siberia	Africa	Italy
12	16+15	For each seasonal composite obtained by simply averaging each seasonal collection: <ul style="list-style-type: none"> • spatial median • spatial maximum • spatial minimum • Difference Max-Min 	OA:74.89% PA:64.47% UA:68.29%	OA:72.22% PA:67.15% UA:71.45%	OA:86.96% PA:67.78% UA:80.61%	OA:76.52% PA:65.31% UA:79.24%
13	16+30	For each seasonal composite obtained by simply averaging each seasonal collection: <ul style="list-style-type: none"> • spatial median • spatial maximum • spatial minimum • Difference Max-Min • Extra: 24-days VV&VH composites (15 × 2 images) 	OA:75.75% PA:67.37% UA:69.58%	OA:75.17% PA:70.39% UA:73.85%	OA:87.65% PA:67.54% UA:80.25%	OA:81.73% PA:74.13% UA:85.08%
14	20	For each VV-polarized seasonal composite obtained by simply averaging each seasonal collection: <ul style="list-style-type: none"> • Original VV seasonal image • spatial median • spatial maximum • spatial minimum • Difference Max-Min 	OA:73.16% PA:62.96% UA:63.11%	OA:67.70% PA:63.22% UA:68.47%	OA:85.07% PA:61.64% UA:73.14%	OA:62.60% PA:51.74% UA:75.46%
14	20+20	For each VV- and VH-polarized seasonal composite obtained by simply averaging each seasonal collection: <ul style="list-style-type: none"> • Original VV (VH) seasonal image • spatial median • spatial maximum • spatial minimum • Difference Max-Min 	OA:74.89% PA:64.74% UA:64.69%	OA:76.04% PA:71.39% UA:73.79%	OA:87.47% PA:69.1% UA:79.46%	OA:76.52% PA:68.96% UA:79.57%

End of Table 3.6: Accuracy vs. input features

Chapter 4

Inland water body monitoring and mapping¹

Similarly to what has been done in the previous Chapter for the development of a vegetation land cover mapping application, in this fourth Chapter an algorithm that aims at classifying inland water bodies has been developed and described in detail.

4.1 Background of the proposed inland water body mapping methodology

As discussed previously in Chapter 1, in the context of climate change studies, there exist great interest in mapping and monitoring land cover types and their changes at the global scale. Indeed, it is necessary to produce high resolution land cover maps for consecutive years in order to better observe and analyse changes in terms of extent and/or transition of the classes, thus characterizing the effects of climate change from the local to the global scale. The most useful maps for land cover types of interest at the global scale

¹this chapter is based on material published in the works:

- [44] Marzi, David, and Paolo Gamba. “Inland Water Body Mapping Using Multitemporal Sentinel-1 SAR Data.” *IEEE Journal of Selected Topics in Applied Earth Observations and Remote Sensing* 14 (2021): 11789-11799.
- [150] Marzi, David, and Paolo Gamba. “Wide-Scale Water Bodies Mapping Using Multi-Temporal Sentinel-1 Sar Data.” *2021 IEEE International Geoscience and Remote Sensing Symposium IGARSS*. IEEE, 2021.

for climate change initiatives and their connection with Earth Observation (EO) sensors have been provided by projects funded by the ESA Climate Change Initiative (CCI).

To obtain these maps, data from multiple satellite sensors have been employed, namely multispectral, hyperspectral, and microwave passive radiometers, as well as lidar and radar active sensors. Since each source of data has its own pros and cons, it is not possible to reliably map all classes with a single type of data. For instance, optical systems (multi- and hyper-spectral sensors) are suitable to recognize surface materials by measuring their reflectance at different wavelengths, typically ranging from the visible to the infrared. For this reasons, optical data are widely used in vegetation mapping, agricultural applications, and soil characterization [151].

As mentioned in Section 2.2, due to its typical spectral signature, water is also well-distinguishable in optical data, and several water indices have been designed to detect water bodies by means of optical data such as the Normalized Difference Vegetation Index (NDVI), Normalized Difference Water Index (NDWI), Modified Normalized Difference Water Index (MNDWI) and the Automated Water Extraction Index (AWEI) [107]. Still, constant monitoring of any land cover type using optical sensors is a real challenging task in cloudy areas.

Thanks to the efforts of many researchers and the use of multispectral and radar data sets, several projects aimed at producing water body maps at the global scale were developed. These products (sorted by increasingly coarser spatial resolution) are summarized in Table 4.1 and subdivided in data sets dedicated only to water class and data sets which contain multiple information on different classes, among which, water surfaces.

The Water and Wetness product [152] from the European Commission Copernicus project is generated based on the fusion of multi-temporal optical satellite imagery and SAR data and represents a thematic product that shows water occurrence from 2009 to 2018; the Landsat Dynamic Surface Water Extent (DSWE) [153] is a multi-band raster layer representing per-pixel surface water inundation; the JRC Global Surface Water Mapping Layers [27] data set contains maps of the location and persistence of surface water over the last 35 years, also providing statistics on the extent and change of those water surfaces; the Global Surface Water Dynamics product [28] highlights estimates of open surface water extent and change from 1999 to 2020; the Global WaterPack [154] is a 250 m resolution data set revealing dynamics of global inland water bodies on a daily basis and represents the surface water map product having the highest temporal resolution

with respect to all other products of Table 4.1; the Global Forest Change Water Cover (GFCC30WC) [155] data set provides surface-water information and was derived from water bodies masks in the GFCC Tree Cover (GFCC30TC) and Forest Cover Change (GFCC30FCC) products based on a classification-tree model; the Copernicus Global Land Service (CGLS) [137] delivers a global land cover map that includes many classes, including water surfaces; finally, the GlobCover Land Cover maps by the ESA CCI project [156] provide global annual Land Cover maps and, contrary to all other land cover types, water bodies are mapped with the Envisat Advanced Synthetic Aperture Radar (ASAR).

Previous works proposed methodologies for water body extraction using SAR data by means of supervised classifications [117], thresholding techniques using quad-pol data [118], SAR and optical data fusion [157] and signature analysis in the feature space [43, 119].

Following, a very brief recall about the current state-of-the-art in water body monitoring and mapping (see Chapter 2, Section 2.2 for details). In [119] the authors demonstrated that the joint use of Sentinel-1 time series data and a metric based on the product of co- and cross-polarized channels can lead to an efficient support of the so-called “smart

Data set	EO sensor(s)	Resol.	Ref. year(s)
Copernicus Land Monitoring Service – High Resolution Layer Water and Wetness (v2) [152]	Landsat-5, -6, -7 and -8, Sentinel-1A, ENVISAT-ASAR)	20 m	2009 - 2018
Landsat Dynamic Surface Water Extent (DSWE) [153]	Landsat-4, -5, -7, -8	30 m	1982 - present (2021)
JRC Global Surface Water Mapping Layers (v1.3) [27]	Landsat-5, -7, -8	30 m	1984 - present (2021)
Global surface water dynamics [28]	Landsat-5, -7, -8	30 m	1999 - 2020
Global WaterPack [154]	MODIS Terra & Aqua	250 m	2013 - 2015
Global Forest Cover Change Water Cover (GFCC30WC) [155]	Landsat-7, MODIS	30 m	2000
Copernicus Global Land Cover Layers (CGLS-LC100 collection 3) [137]	PROBA-V	100 m	2015 - 2019
GlobCover Land Cover Maps [156]	MERIS, Envisat-ASAR	300 m	1992 - 2018

TABLE 4.1: Available global water surface products subdivided in two groups and sorted by increasingly coarser spatial resolution: the first group relates to projects focusing only on water bodies extraction; whereas, the second group is devoted to projects aimed at generic Land Cover (LC) mapping.

water management”; in particular, the proposed methodology, based on two steps, allows to efficiently extract waterlines and retrieve water surfaces.

The study in [120] compares 10 different feature combinations to train a supervised support vector machine (SVM) model. The conclusion of the study states that optical indices are not useful as expected and, from the accuracy point of view, the best SAR configuration for detecting water is the single-channel VH-polarised intensity data, with an average overall accuracy of 98.07%.

Another interesting study is reported in [121], where a k -Means clustering approach is employed with a number of extracted clusters $k = 15$. The methodology extracts features starting from a yearly Sentinel-1 time-series obtained by averaging ascending and descending orbit images separately within each month (ending up with 12 two-average-composites per year), and VV and VH intensity data are used as inputs. Eventually, the temporal average backscatter value is computed for each cluster and a specific threshold is applied to obtain the “water” class. Compared to the methodology proposed in this paper, the work in [121] lacks the flexibility to be applied to other regions of interest because it does not exploit any initial set of water points. Moreover, the parameters are tailored to the specific area of interest.

All in all, as also stated at the end of the scientific literature carried out in Chapter 2, the studies analyzed from the technical literature have limitations, related to lack of automatism (e.g., manual sampling of training samples), the impossibility to apply the methodologies to other study regions without a-priori information (e.g., because they have thresholds and decision steps calibrated for specific regions of interest), the high computational cost of working on quad-pol images, or the reduced classification capability over cloudy regions when optical data is employed. Moreover, the main characteristics of the global water products listed in Table 4.1 suggest that the limitations of those data sets are mostly related to the spatial resolution, which is coarser than the result obtainable with the proposed approach. Finally, almost no products use the great potential in terms of both spatial and temporal resolution of Sentinel-1 data.

Given all the above considerations, the objective of this part of the thesis work is to use data sets that have never been used to generate annual water surfaces maps with an unprecedented spatial resolution. Specifically, a novel fully-automated water surface mapping algorithm is presented, able to deal with any region of the World, with no limitation in size and no prior information about the area. This is possible thanks to

the use of Sentinel-1 SAR data sequences, and the exploitation of previous medium resolution global land cover maps for an initial training sample collection. The entire, fully automated procedure has been implemented in Google Earth Engine (GEE).

The proposed unsupervised water body extraction processing chain is summarized in Figure 4.1, and is meant to be applied to a stack of multitemporal SAR data. First, a multitemporal denoising step is performed on the sequence of all the ascending and descending SAR images overlapping (completely or partially) the selected tile, aiming at reducing the effect of speckle noise. Then, a set of statistical and temporal features are computed to guide the k -Means clustering algorithm. Finally, a few post-processing steps (such as morphological operations and steep slope removal) are applied to the classified result to improve the final water surface mapping accuracy.

4.2 SAR data pre-processing for water detection

Before actual use, all the data must undergo several pre-processing steps. These steps - similar to those applied for the vegetation land cover classifier - are summarized in Figure

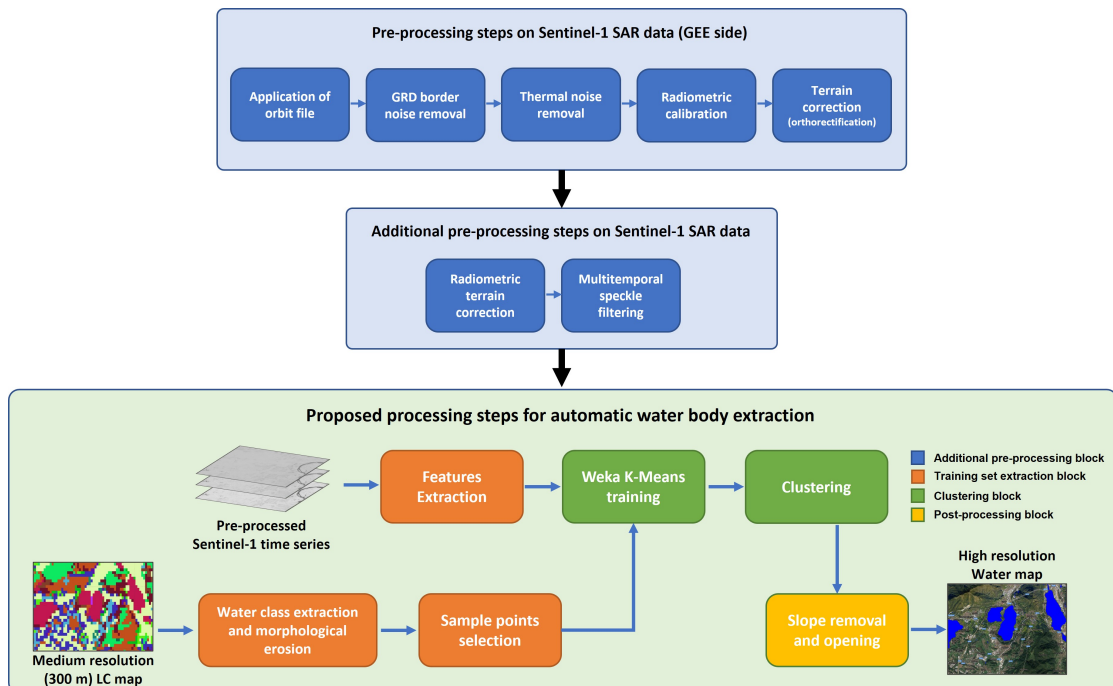


FIGURE 4.1: Overview of the complete procedure designed to extract water bodies from Sentinel-1 SAR data sequences.

4.1 and include: application of orbit file, GRD border noise removal, thermal noise removal, radiometric calibration and Range-Doppler terrain correction (orthorectification) using SRTM30 or ASTER DEM for regions located at more than 60 degrees latitude. All these steps are directly applied by the Google Earth Engine cloud computing platform. Since the standard Sentinel-1 pre-processing chain does not include radiometric terrain correction, we added an angular-based radiometric slope correction routine for Sentinel-1 SAR images, developed in [140]. The idea behind such correction is to exploit an established physical reference model which is also extended to simultaneously generate masks of invalid data represented by active layover. The radiometrically corrected SAR products significantly improve land cover mapping on a large scale, especially over morphologically complex regions (e.g., mountains).

The radiometrically corrected SAR products significantly improve the potential usage of Sentinel-1 imagery for a wide range of land applications, such as land cover classification, deforestation monitoring, the retrieval of bio-geophysical parameters as well as the combination of imagery from different geometries.

Moreover, the proposed procedure exploits a multitemporal speckle noise filter, applied to the sequence of Sentinel-1 SAR images according to [141]. As already described in the previous Chapter, the filtering algorithm starts with the estimation of a “super-image” obtained by averaging all the SAR images of the multitemporal stack. Then, the ratio between each original and noisy image and the super-image is computed; the result of this ratio is denoised with a 7×7 low-pass filter kernel (note: the original procedure used spatial Lee filter for this step, which was replaced with a simpler, yet effective low-pass filtering step); finally, each low-pass-filtered image is re-multiplied by the super-image (see Figure 3.12 for details).

4.3 Extraction of water-related SAR features

Based on findings from the technical literature, in the proposed water extraction algorithm we rely only on the VH intensity data, that has been proven to be the best selection in terms of classification accuracy in [120]. More specifically, the following VH-based temporal features are computed, on a per-pixel basis, from the denoised SAR time series:

- Three-months composites named “quarter composites”. These composites are obtained by averaging in time all the available SAR images within a temporal window that roughly corresponds to a quarter of a year;
- The overall annual mean composite;
- The overall minimum composite;
- The overall maximum composite;
- The overall temporal variance.

In Figure 4.2 the block scheme of the features extraction procedure is depicted.

Among all the above mentioned features, variance and minimum are particularly important when water monitoring and mapping is the objective. In fact, contrary almost all other types of land covers, water bodies are characterized by very high temporal variability (hence, variance) and very low minimum backscatter intensity along the year [43].

The main difference between this approach and the one in [43] is the use of the so-called “quarter composites”, a possibility due to the high revisit frequency of Sentinel-1 constellation. Quarter composites helps to better discriminate between water and other similar classes. For instance, many agricultural fields are flooded several times along the corresponding crop growth season (e.g., rice fields); therefore, their annual mean,

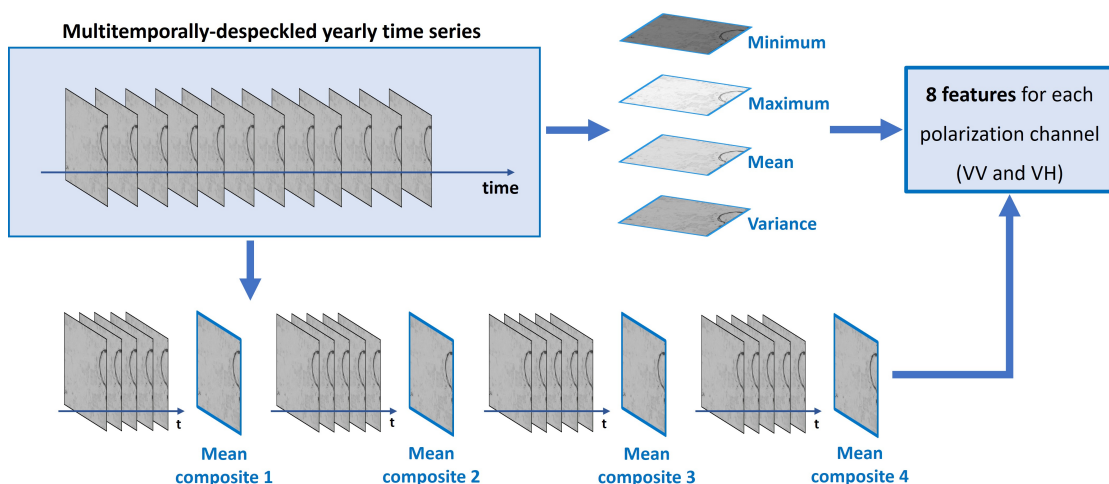


FIGURE 4.2: Set of features extracted from a Sentinel-1 time series, suitable for water detection in SAR data.

minimum backscatter and temporal variability parameters may be very close to those of water bodies. The selected four composites allow to recognize the temporal pattern along the year due to the variability of specific land cover types (e.g., because of the phenology in case of vegetation). Indeed, differently from a water body, agricultural fields will show significant phenological variations along the year and this helps the classifier to recognize such fields as non-water. Such discrimination may be more difficult if only annual (or multi-annual) values are used.

4.4 Training the k-means model

The features extracted in Section 4.3 are used to sample a balanced set of *water* and *non-water* points derived from coarse maps, such as the medium resolution CGLS map (at 100 m scale). The procedure for the extraction of training points is outlined in Figure 4.3.

First a binary mask from the MRLC map of water bodies is extracted (4.3b) and eroded with a 3×3 sliding kernel to increase the likelihood of sampling “pure” water pixels (4.3c). In the case the erosion procedure ends up with no water pixels in the considered tile, the original (not eroded) mask is restored and used for sampling. Whereas, if the tile of interest contains no water pixels in the MR map at all, an empty image (all zeroes) is provided in output. To sequentially extract a map all over the world, the Sentinel-2 tile system is used [139], and $\sim 10000 \text{ km}^2$, i.e., ~ 100 million pixels at 10 m resolution, are analyzed at a time. Finally, a stratified random sampling is applied to the binary mask to generate water and non-water points in a ratio of 1:3. Specifically, in the proposed algorithm 1000 and 3000 points are collected for water and non-water class, respectively.

These training points are then used as initial seeds for the *k*-Means clustering algorithm, and the model extracted from them is eventually used to cluster all points belonging to the wide area of interest. Note that the *k*-Means algorithm implemented in GEE is based on the “Weka” open source machine learning software [148], optimized to work with very large data sets (like the ones of this work). Starting from a representative subset of the data (the above high-resolution training set), the Weka *k*-Means algorithms generates a model that is then used to make predictions on the full data set.

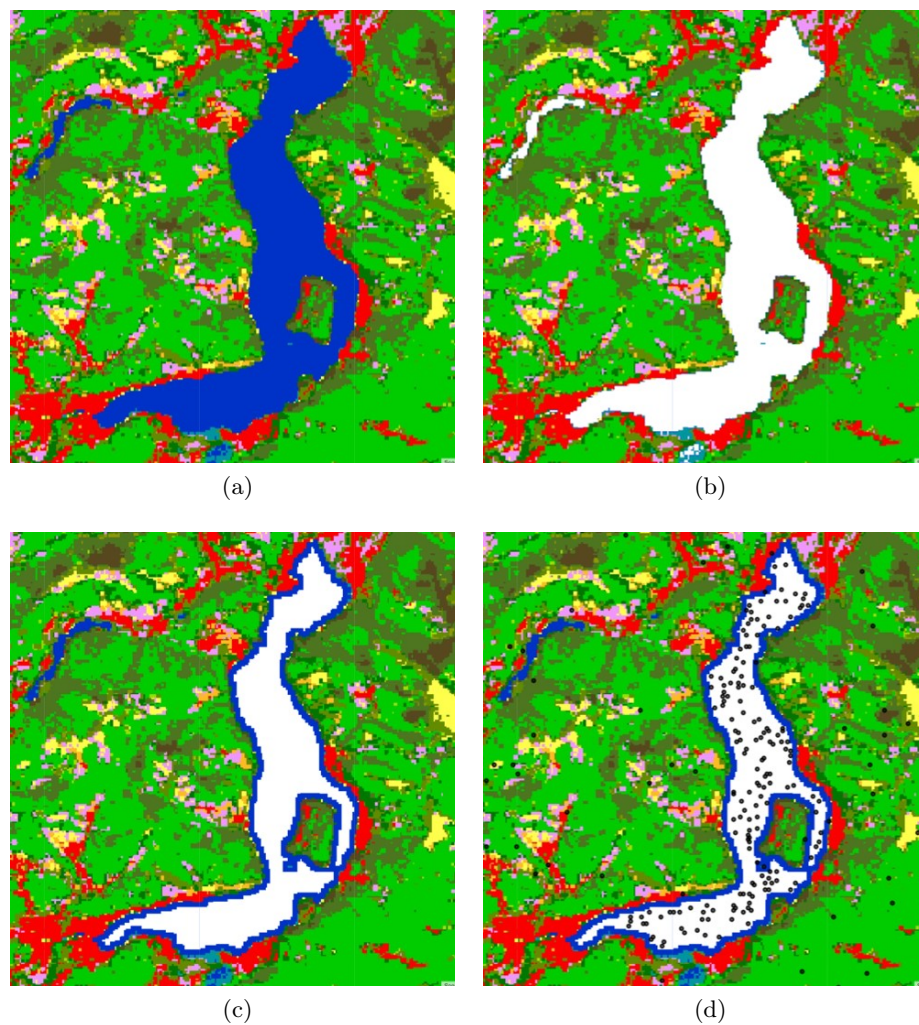


FIGURE 4.3: Main outcomes of the training set generation procedure: (a) shows the original CGSL map at 100 m spatial resolution; the “water” class is then extracted (b) from the MR map and eroded (c). Finally, the eroded water class is randomly sampled inside and outside water regions (d) to generate a balanced set of points. The Iseo Lake, located in the Lombardy region in North Italy, was used in this example.

Even if it may look counter intuitive, the k -Means algorithm is run with $k = 4$; this means that each training pixel is automatically assigned to one among four (unknown) clusters. The number of clusters comes from the idea that inside the initial mask (and near water bodies) there may be essentially four main land cover types: water, vegetation, bare or impervious soil.

Indeed, we experimentally found that the use of only $k = 2$ clusters leads in many cases to confusion between water and some of these classes. By increasing k , the k -Means model performs a more reliable clustering since the potentially confusing classes are clustered in different non-water clusters. This results in a more robust discrimination of water bodies

from the other land cover types, and drastically reduces the number of false positives. Since the k -Means model makes no assumptions on the distribution of the data (as it is essentially an optimization problem), it is a suitable approach to deal with multitemporal SAR composites, whose statistical characteristics are very complex.

Moreover, in order to avoid oversampling the water class when the tile include wide open water areas (such as portions of seas and oceans), the shoreline/coastline data from the Global Self-consistent, Hierarchical, High-resolution Geography Database (GSHHG) is used to mask out open water from all Sentinel-1 images [158] before the clustering is applied. The GSHHG is a free, high-resolution geography data set containing the “World Vector Shorelines (WVS)”, a shapefile of the shorelines of the entire Earth, available at different spatial resolutions. For the proposed water body mapping algorithm, the “high resolution” shapefile is used, obtained by using the Douglas-Peucker lines-reduction algorithm to reduce the maximum number of vertices of the “full resolution” shapefile by 80% (hence, reducing the size of the dataset). This step was necessary first of all to avoid oversampling the water class, but also to avoid sampling of open water bodies, whose SAR features are not similar to those of inland water bodies (such as lakes and rivers). For instance, due to the persistent presence of waves, the minimum SAR backscatter value is not low enough to be associated to an inland water body (which in general is more stable in time). Experiments showed that open water is sometimes confused with vegetation, due to similar mean backscatter values that are in common with the two classes. Therefore, thanks to the GSHHG dataset, it is possible to prevent open water from being classified, as it would represent a strong source of errors. In this way, only water not farther than 300 m from the shores are involved in the classification procedure.

4.5 Automatic water cluster extraction

Being an unsupervised learning algorithm (i.e., there is no labelled data for clustering), the k -Means model performs the division of objects into clusters that share similarities (features). The nature, i.e., the associated land cover type, of each generated cluster is not known in advance. In many previous works, once the clusters have been generated, human intervention is needed in order to extract the cluster associated to the land cover of interest, by photo-interpretation and experience. Of course, this approach strongly lacks of automatism and is time consuming.

In the proposed water mapping algorithm, once the four clusters have been extracted, a simple yet effective method is applied to automatically select the one representing the water class (procedure summarized in Figure 4.4). To this aim, the original water mask derived from the CGLS land cover map is converted from raster to vectors (in order to obtain a multi-polygon layer representing water boundaries in the MR map). Then, to ensure the operations to be performed only inside the boundaries of the water class, a negative buffer of 100 m is applied to the vectorized water mask; at this point, a frequency histogram at 20 m scale is computed over the 4-cluster result, within the multi-polygon boundaries. Since the frequency histogram shows frequencies for each cluster, i.e., how many times each cluster occurs inside the vector layer in terms of number of pixels, we assumed the cluster associated with highest frequency to be representative of the water class. Such cluster is eventually extracted as the final high resolution water map.

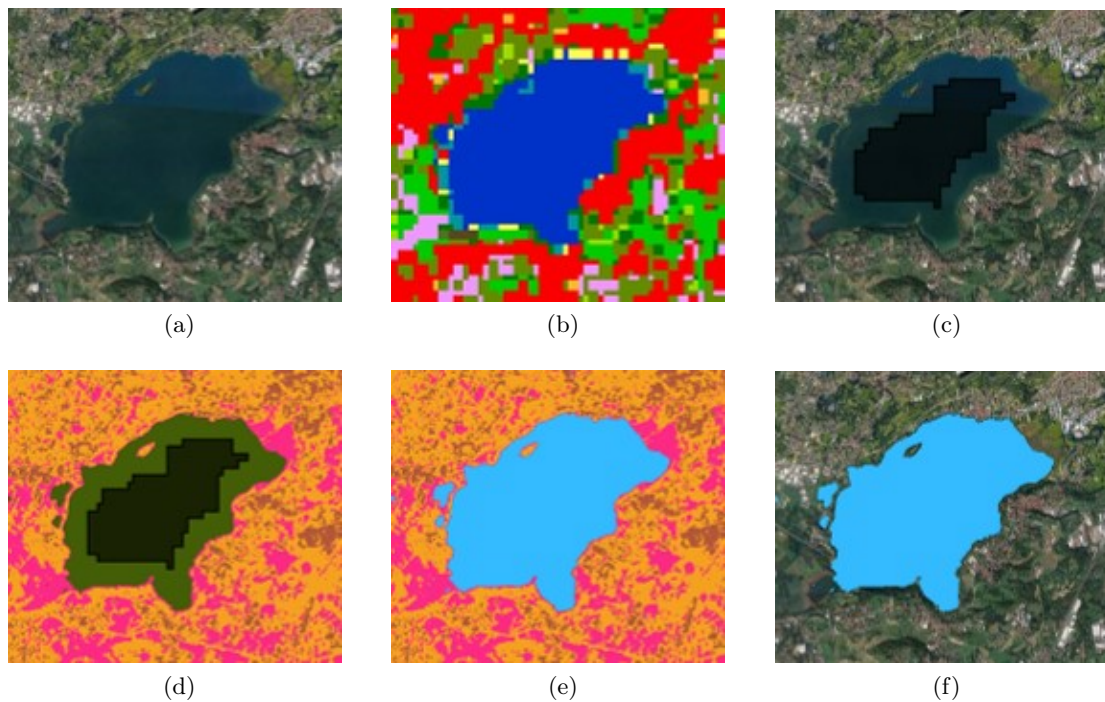


FIGURE 4.4: Main steps of the water cluster selection procedure: (a) shows the satellite view of the example scene; the (b) CGLS map at 100 m resolution is loaded, and a negatively buffered (100 m) multi-polygon layer (c) is generated. Then, a frequency histogram is computed over the clustered result (d) inside the multi-polygon layer. The most frequent cluster is then associated to the water class (e), and extracted as the final HR water map (f).

4.6 Post-processing of the clustering result

To increase the reliability of the water mapping algorithm, the final high-resolution water map derived in the previous Section undergoes a few post-processing steps to get rid of isolated pixels and residual false positive occurrences. As discussed in Section 4.2, a radiometric terrain correction pre-processing step was applied to the whole stack of Sentinel-1 images in order to account for slope-induced backscatter differences, which are mainly caused by hills and mountains due to the natural slanted acquisition geometry of SAR systems.

Notwithstanding the great effectiveness of the radiometric terrain correction in reducing the backscatter dependency to the terrain geometry, such approach represents a simplified angular-based model and have some limitations which translate into residual topographic effects. These effects are mainly related to the inaccuracy of the used DEM, the assumption of homomorphism between map (geo-coded imagery) and radar geometry, and the image geometry approximations [140]. Moreover, unlike the radiometric terrain correction model chosen for this work, pixel-area-based slope correction models - which account for actual topology between map and radar geometry - are proven to be more accurate and suitable to address this issue [97]. However, such algorithms are impractical to use within Google Earth Engine, since the area of the pixel should be computed on-the-fly, causing long run-times and/or memory saturation issues.

Due to the residual topographic effects described above, false positive occurrences may persist over steep-sloped regions. A simple slope masking proved to be enough to get rid of the remaining false positives over these regions. To this aim, a steep-slope masking using the ALOS World 3D - 30m (AW3D30 [159]) Digital Surface Model (DSM) from the JAXA Earth Observation Research Center is applied. The ALOS DSM is a globe-covering raster data set where each pixel represents height-above-sea level at 30 m spatial resolution. To derive slopes from the elevation data, the local gradient is computed using the 4-connected neighbors of each pixel. The resulting product was finally used to mask out terrain pixels with slope greater than 8 degrees. To visually appreciate the effects of such additional slope masking procedure, the reader is referred to Figure 4.5.

To further improve the final result, an “opening” morphological operation with a 3×3 kernel is applied to the above described slope-filtered result. The effect of the opening operation is the removal of foreground (bright) pixels. Contrary to a simple erosion,

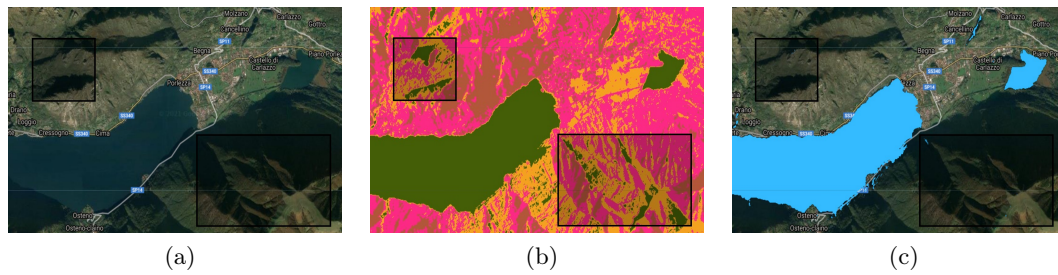


FIGURE 4.5: Benefits of the slope filtering: (a) shows the satellite view of the scene, while (b) and (c) show how false positive occurrences were removed, hence improving classification results.

which may be too disrupting, the opening operation is defined by an erosion followed by a dilation; therefore, at the cost of a slight loss of spatial details, the spatial resolution is $30 \times 30 \text{ m}^2$, while the posting of the final result is 10 m.

4.7 Results and discussion

The presented methodology for water body mapping was tested mainly over three (very diverse) study sites to assess the robustness and reliability of the proposed methodology in situations with very few common features. These regions, presented in Section 3.2, are located in Siberia (tile 42WXS, Figure 3.4), northern Italy (tile 32TNR, Figure 3.5 and Amazonia (tile 21KUQ, Figure 3.2).

On these areas, multitemporal Sentinel-1 SAR data were used. It is worth noticing that the incidence angle in Interferometric Wide Swath (IW) mode ranges from 29.1 to 46 degrees across the range direction; however, even if the incidence angle variation heavily affects backscatter intensity, for water detection purposes such variation is not very critical, thanks to the strong dominance of mirror reflection backscatter mechanism over flat regions. Moreover, since the data has been subject to radiometric terrain correction, incidence angle related effects are even more attenuated.

The year considered in this work is 2019 and 27, 60 and 31 IW VH-polarized SAR images acquired over Siberia, Italy and Amazon, respectively, were considered for the analysis. Note that the number of available images intersecting (even partially) the region is much larger; however, only images overlapping at least 70% of one of the test areas were considered.

Figure 4.6 shows the final classification results at 10 m spatial resolution over tiny areas inside the selected test regions compared with the CGLS map (100 m spatial resolution). By visual comparison, it is clear that the water areas delineated in the medium resolution maps are confirmed in the high resolution (HR) map extracted by the proposed approach. Moreover, in the latter, water pixels inside very small water bodies and narrow river branches are also extracted, while they are not visible in the other maps.

A more detailed, but still qualitative analysis is shown in Figure 4.7, where the analysis is enlarged to compare samples of the extracted maps with the water layer of the Globcover (300 m spatial resolution), the Copernicus Global Land Cover map (100 m spatial resolution) and the JRC Global Surface Water Mapping Layer (30 m spatial resolution). A visual comparison confirms that using the technique proposed in this thesis, a map consistent with those available is obtained, with the potential to disclose more details due to the finer spatial resolution.

Referring to Figure 4.7, from left to right, it is provided the visual comparison among the water layer of the Globcover map (300 m spatial resolution), the Copernicus Global Land Cover (CGLS) map (100 m), the JRC Global Surface Water Mapping Layer (30 m) and the results of the proposed approach (10 m). The considered zoomed areas are located in Amazonia (-22.728, -57.93142), Siberia (64.1333, 72.9079), Italy (45.161, 9.8607), Italy (45.0084, 8.7647), Mexico (22.0452, -105.5576), Gabon (0.0923, 9.6849) and Italy (45.4823, 12.5104). Background images are taken from the Google Satellite basemap and the coordinates are expressed in decimal degrees (EPSG:4326, WGS 84; ellipsoidal 2D CS; axes: latitude, longitude; orientations: north, east; UoM: degree).

4.7.1 Consistency analysis

To quantitatively prove the *consistency* between the new HR result of this work and the existing maps, a random sample of the Globcover, Copernicus and JRC water maps was extracted and compared with those of the generated 10 m water map. Specifically, up to 1000 pixels for both the *water* and *non-water* classes were selected. The confusion matrices for the study cases with respect to each compared data sets are shown in Table 4.2. Note that before sampling the reference maps, they were all up-sampled to 10 m and eroded using a square kernel with radius of 50 m, in order to avoid pixels in transitional areas.

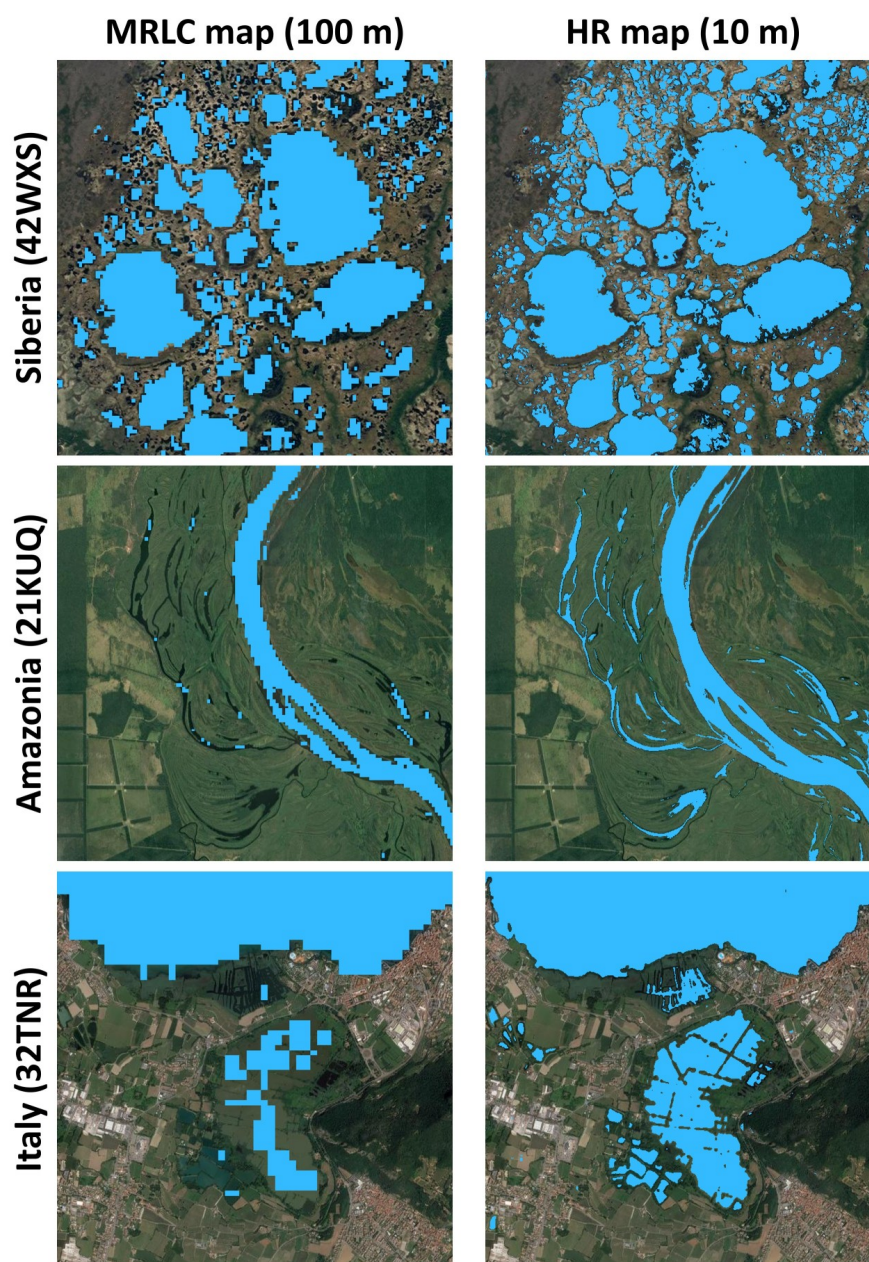


FIGURE 4.6: Qualitative results over very small areas inside the considered tiles. The images on the left show samples from the 100 m spatial resolution water layer in the CGLS map; the images on the right show instead the output of the proposed methodology with a spatial resolution of 10 m in Siberia (top), Amazon (middle) and Italy (bottom). In all the cases, water regions are colored in light blue and overlapped to the Google Satellite basemap.

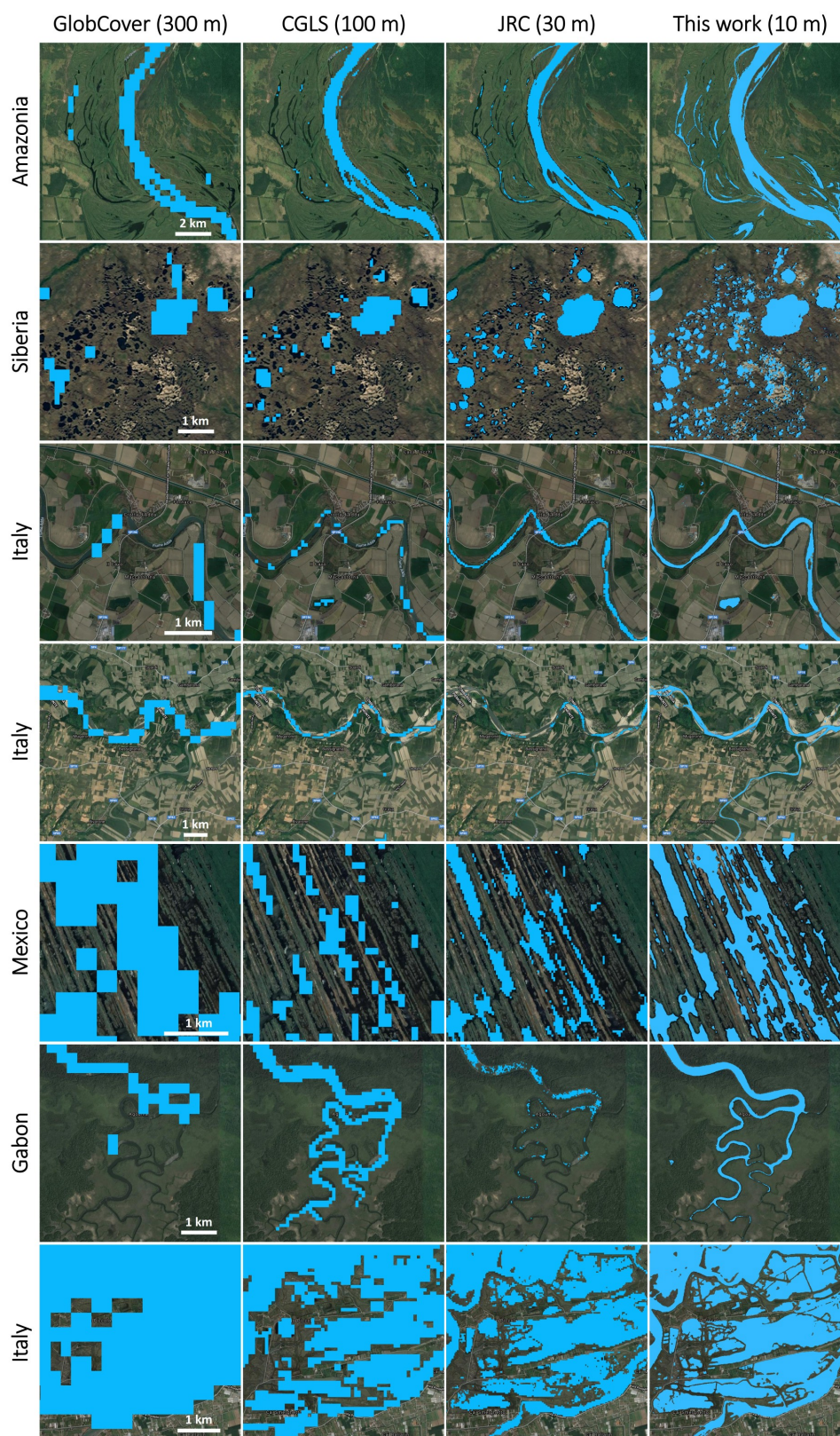


FIGURE 4.7: From left to right, visual comparison among the water layer of the Globcover, the Copernicus Global Land Cover (CGLS) map, the JRC Global Surface Water Mapping Layer and the results of the proposed approach (10 m).

		Siberia		Amazonia		Italy	
		W	NW	W	NW	W	NW
CCI	W	805	194	205	84	840	160
	NW	45	955	8	966	1	993
CGLS	W	881	119	922	78	952	48
	NW	63	937	8	968	5	987
JRC	W	909	90	952	48	985	15
	NW	54	946	4	979	5	992

TABLE 4.2: Confusion matrices for the three regions of interest, generated based on test points collected from the three different reference maps: the CCI Globcover (300 m), the CGLS (100 m) and the JRC (30 m). “W” and “NW” stand for water and non-water respectively.

From the confusion matrices, the producer accuracy for both the *water* (PA_w) and *non-water* (PA_{nw}) classes and the overall accuracy (OA) values were computed as a way to evaluate the consistency between the maps obtained by the proposed technique and the reference maps. All the results are summarized in Table 4.3. Even if these results do not provide a real validation, but only a comparison between the extracted water body maps and the pre-existing and coarser resolution water maps, they are extremely promising since, on average, the OA is around 96.2% when the best water map in terms of spatial resolution, the JRC map, is adopted as reference.

4.8 Validation of the proposed method on the Lombardy region

Since the analysis carried out in the previous section only provided a measure of consistency between the obtained HR water maps and different MR water maps, the aim of this section is to accurately validate the methodology developed in this thesis, and provide a meaningful and reliable quantitative analysis of the final high resolution water product. To do so, a validation procedure was carried out exploiting the ground truth dataset available for the whole Lombardy region, located in northern Italy.

		Siberia	Amazon	Italy
CCI	PA_w	80.6	71	84
	PA_{nw}	95.5	99.2	99.4
	OA	88	92.7	91.9
CGLS	PA_w	88.1	92.2	95.2
	PA_{nw}	93.7	99.2	99.5
	OA	91	95.6	97.3
JRC	PA_w	91	95.2	98.5
	PA_{nw}	94.6	99.6	99.5
	OA	92.8	97.4	98.5

TABLE 4.3: Overall accuracy (OA), *water* producer accuracy (PA_w) and *non-water* producer accuracy (PA_{nw}) for each study case using CCI Globcover (300 m), the CGLS (100 m) and the JRC (30 m) map as references (all the values are in percentage [%])

Depicted in Figure 4.8, the region has an extent of 23863 km² and is characterized by a large number of water bodies with very different characteristics, such as big rivers with their tributaries and narrow branches and numerous very large and small lakes of glacial origin. Additionally, the morphology of the area is quite variable, from the main Po valley to hilly and Alpine mountainous areas.

All the described characteristics of the Lombardy region were considered challenging enough to test our methodology and provide an accurate validation analysis. Moreover, the whole area is covered by official land use data, provided by the Regional Territorial Information Infrastructure. In particular, we used the DUSAF (Destinazione d’Uso dei Suoli Agricoli e Forestali - Agricultural and Forestry Land Use) catalog of year 2018, a huge, detailed geographic database containing information on many different land cover types [160]. In its latest version (DUSAF 6.0), a greater level of detail has been added thanks to the exploitation of very-high spatial resolution SPOT6/7 satellite images (1 pixel = 1.5 m).

The DUSAF 6.0 land cover legend is structured according to 5 hierarchic levels: the first three consist of the classes present in the Corine Land Cover project [161], while the last two levels describe classes typical of the Lombardy region. The first level is in turn divided in five “fundamental” classes and, among these, the “water bodies” class.

Since the DUSAF 6.0 reference dataset comes with a spatial resolution of 1.5 m, it is necessary to make it compatible (in terms of map content) with the 10 m spatial

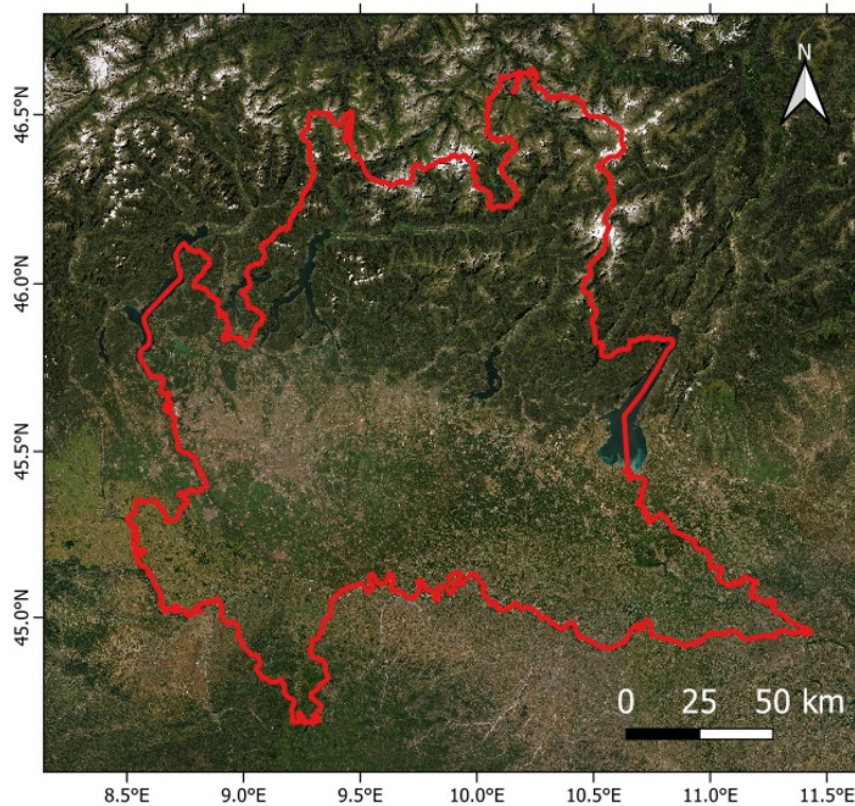


FIGURE 4.8: The Lombardy region, northern Italy. Red solid line represents the political boundaries of the region.

resolution of the extracted map. To this aim, a negative buffer on the vector data representing the reference water bodies was applied. By doing so, Two typologies of water bodies that cannot be detected by definition in Sentinel-1 SAR data were excluded from the validation experiment to avoid any negative bias. The first set is composed of very small water bodies with size less than one Sentinel-1 pixel, i.e. $\sim 100 \text{ m}^2$. The second set is composed of long and thin water bodies, such as very narrow river branches with a width smaller than the spatial resolution of the SAR sensor.

Figure 4.9 provides a visual comparison between the considered validation set and the map extracted in this work, generated by classifying nine $100 \times 100 \text{ km}^2$ tiles, which were necessary to cover the whole region (namely, these tile are 32TMQ, 32TMR, 32TMS, 32TNQ, 32TNR, 32TNS, 32TPQ, 32TPR, 32TPS). Starting from the validation set, a total of 20.000 points, equally distributed between water and non-water classes, were collected. All these points were then used to sample the classification result, build a confusion matrix and compute the producer, user and overall accuracy. Specifically, a cross-validation was performed by repeating the procedure 10 times, changing the random

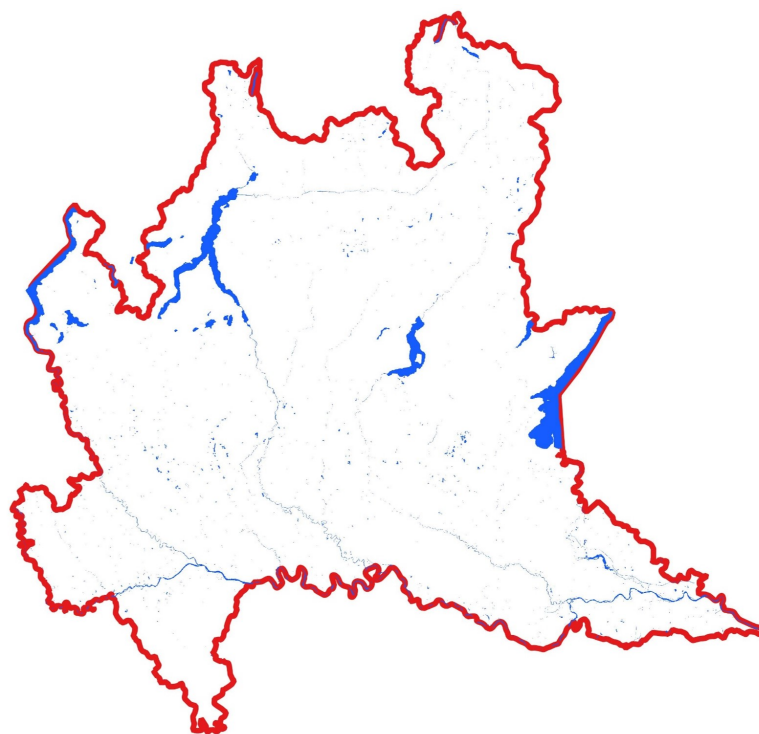
locations of the validation samples in order to prove the precision of the classification procedure.

The methodology was able to achieve, on average, an overall accuracy of 94.6%, with a standard deviation of the order of 10^{-3} , meaning that the OA is not affected by the change of the location of the validation samples (thus, demonstrating the high precision of the algorithm). The producer's accuracy is, on average, 89.4% and 99.8% for *water* and *non-water* classes, respectively.

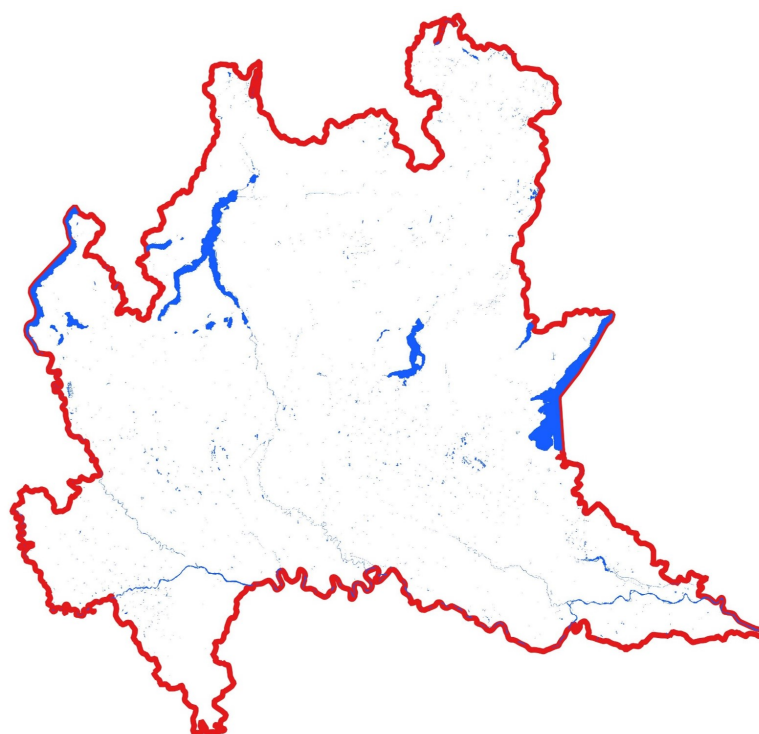
To further assess the limits of the proposed classification procedure, examples of omission occurrences for the water class were investigated. To this aim, a map highlighting all the points over which the proposed method fails to extract water bodies was built. On average, 9.3% of actual water class are not extracted by the proposed procedure. The spatial distribution of these points was thus analyzed to better understand under which conditions the extraction fails. From Figure 4.10 it is possible to observe the distribution of omitted water points in the region after classification.

There are two notable cases. The first one is due to the complex terrain morphology: Figure 4.11a shows an example in a lake whose boundaries are characterized by steep and overhanging hilly banks. In such conditions, SAR images suffer from strong foreshortening and layover effects - the latter is dominant in this area. The second source of omission errors, depicted in Figure 4.11b, is due to the presence of small and/or long and thin water bodies. In this case, such bodies are not extracted or they are classified as thin lines of pixels which tend to disappear when applying the final opening step that was included to reduce false positives. Other cases of omission may also be represented by thin rivers surrounded by vegetation laying upon them.

Overall, the developed water body monitoring and mapping methodology achieved very good results and was also published on one of the top-of-the-line remote sensing Journals [44].



(a)



(b)

FIGURE 4.9: Visual comparison between (a) the validation set and (b) the extracted water bodies map for the whole Lombardy region. Both sets are presented in blue, whilst the red solid line represents the boundaries of the Lombardy region (the white background allows to better highlight water bodies and the differences between the two sets).

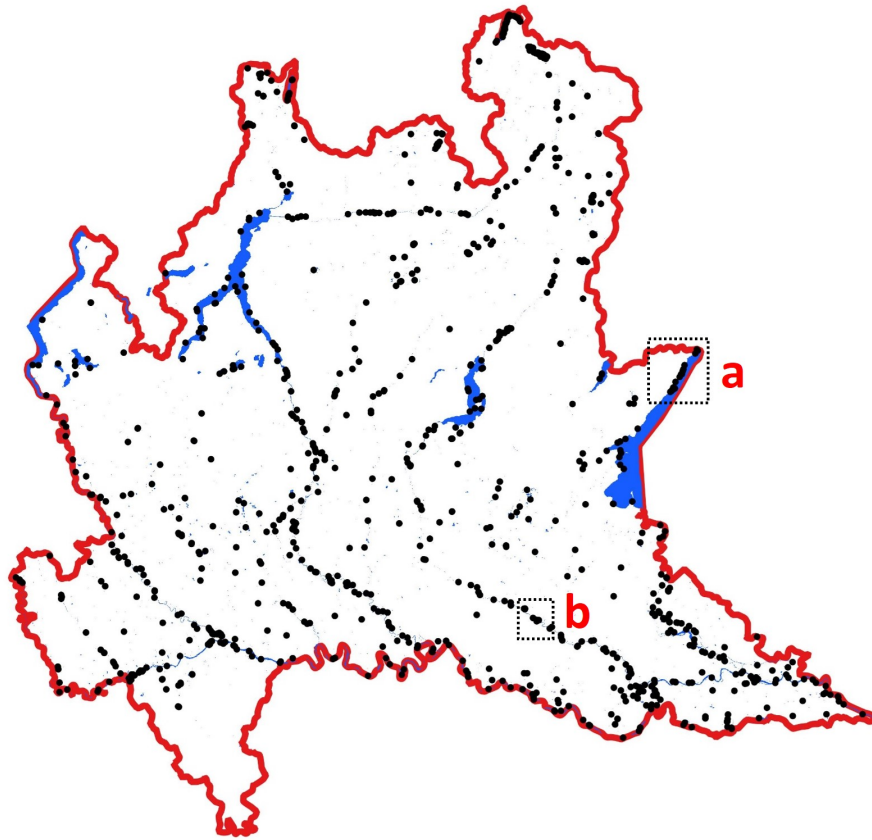


FIGURE 4.10: Spatial distribution of omitted water points (black dots) for a specific classification run. Red solid line represents the boundaries of the Lombardy region and blue areas represent water bodies from the DUSAF 6.0 dataset. Black dashed boxes “a” and “b” show examples of foreshortening/layover effects and morphological operation issues, respectively (see Figure 4.11).

4.9 The ESA WorldWater Round Robin²

During the development of the water body monitoring and mapping algorithm described in the previous sections, we had the privilege to participate in a Round Robin organized by the European Space Agency (ESA). The “WorldWater” project³ was about a Round Robin aiming at the inter-comparison of Earth Observation algorithms for surface water detection, using free and open satellite data such as Sentinel-1, Sentinel-2 and Landsat 8. The project was supported by several international organizations, including CNES (Centre national d’études spatiales), NASA (National Aeronautics and Space

²this chapter is based on material published in the work: [162] Tottrup, Christian, et al. “Surface Water Dynamics from Space: A Round Robin Intercomparison of Using Optical and SAR High-Resolution Satellite Observations for Regional Surface Water Detection.” *Remote Sensing* 14.10 (2022): 2410.

³<https://worldwater.earth/>

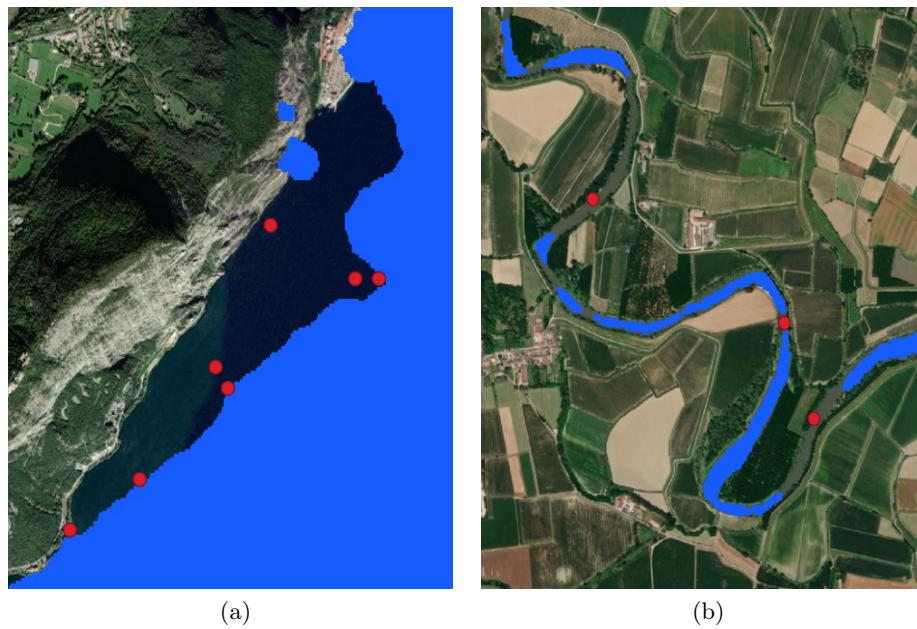


FIGURE 4.11: Spatial distribution of omitted water points for a specific classification run. Case 1: foreshortening and layover; case 2: small water bodies not extracted or canceled by morphological operations. Omission points lay on the background image which is represented by the Google Maps layer (over which the boundaries of the Lombarardy region, in red, are superimposed).

Administration), EARSC (European Association of Remote Sensing Companies), CEOS (Committee on Earth Observation Satellites) and GEO (Group on Earth Observations).

The main objectives of the Round Robin were to provide a better understanding of the pros and the cons of EO-based approaches for monitoring and mapping inland water bodies extent, compare different algorithms and identify shortfalls and areas of further research. All the important outcomes of the Round Robin experience are available in the published paper, referenced in [162].

The participants were asked to produce monthly maps of surface water presence at 10 m spatial resolution in 5 (very) different $100 \times 100 \text{ km}^2$ sized test sites, for 2 consecutive years (from July 2018 to June 2020), for a total of 120 water maps to be produced. Moreover, participants were also allowed to use ancillary data sets under the condition they were publicly available, such as DEMs and a priori surface water maps (e.g., the Copernicus DEM and the JRC-GSWE). As shown in Figure 4.12 these sites are located in Colombia, Gabon, Greenland, Mexico and Zambia.

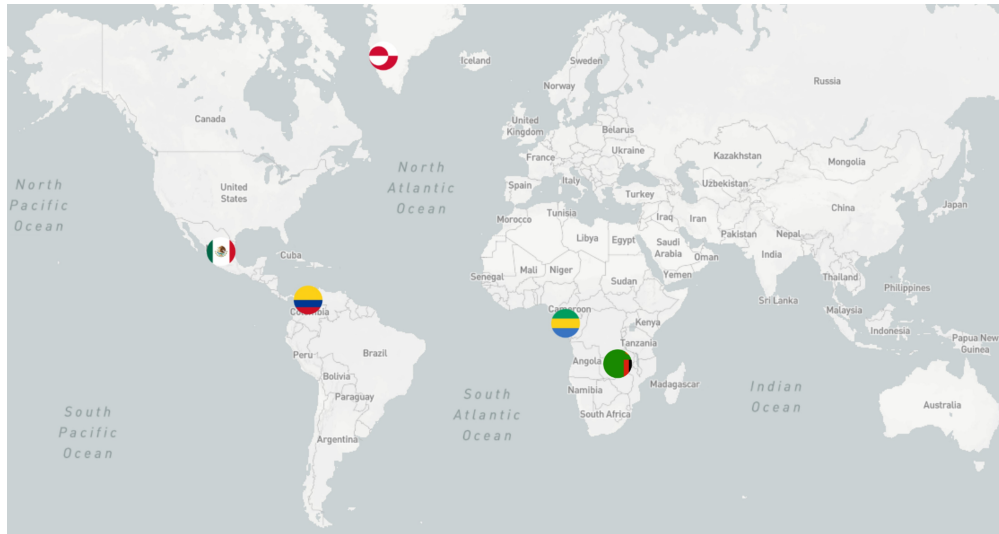


FIGURE 4.12: Overview of the WorldWater pilot Countries and test sites: Colombia, Gabon, Greenland, Mexico and Zambia.

Following, a brief description of the test sites, in terms of their morphological characteristics and water bodies variety:

1. **Colombia** (Figure 4.13a): this region is located in the central eastern part of Colombia and is characterized by mountainous areas with complex river system and intensive farmlands;
2. **Gabon** (Figure 4.13b): this site is located in Western Gabon and is characterized by a lagoon system with numerous narrow rivers and lakes;
3. **Greenland** (Figure 4.13c): the Ice sheet test site is located at the ice sheet margin in Southwestern Greenland and includes an extremely dense network of inland lakes and supra glacial lakes;
4. **Mexico** (Figure 4.13d): located in central Mexico, this area is characterized by inland dry forest region, mixed with agricultural land;
5. **Zambia** (Figure 4.13e): this challenging test site represents a very complex region, dominated by seasonally- or permanently-flooded grasslands.

The five test sites used for intercomparison represent very different conditions, which can also be inferred by looking at multiannual water occurrence maps for the respective test sites (see Figure 4.14). Site variability is, on the one hand, dictated by geographic

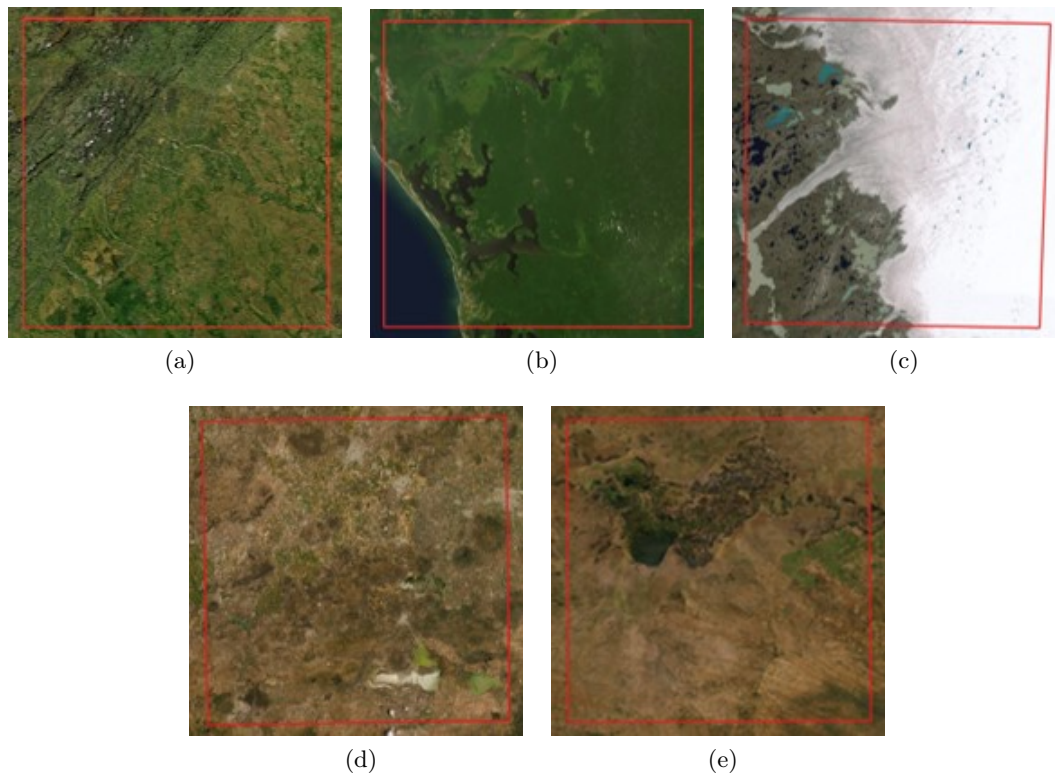


FIGURE 4.13: All the test sites used in the ESA WorldWater Round Robin.

location and, on the other hand, by surface water characteristics. The latter is clearly shown in the water occurrence maps, which show the differences between test sites in terms of size and type of water bodies, as well as the relative distribution of permanent and seasonal water (Figure 4.14).

All the water detection models participating at the Round Robin were evaluated individually and in cross-comparison using independent reference data collected from each test site. As discussed in the introductory sections of this thesis, a fundamental premise

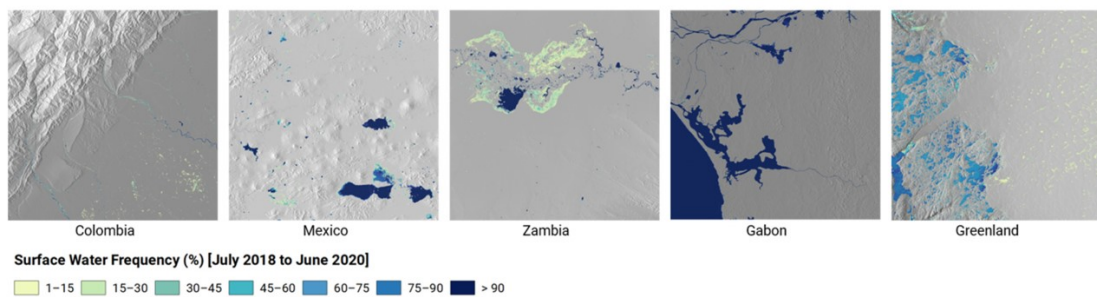


FIGURE 4.14: Overview of the WorldWater pilot Countries and test sites: Colombia, Gabon, Greenland, Mexico and Zambia.

for sound scientific validation is to use reference data of higher quality than the product to be validated. There are two ways to ensure higher quality in the reference data: the first way is to use a reference dataset having better resolution with respect to the dataset used for results production; whereas, the second approach aims at using a more accurate measurement or interpretation than being used for results production.

In the case of this Round Robin validation, a two-step approach was followed:

1. Sample-based validation (i.e., pixel-based) and labelling using the production imagery (verification by higher method);
2. Object extraction accuracy (i.e., area-based) and using Very High Resolution (VHR) PlanetScope data (3 m spatial resolution) as a reference (verification by higher data).

The sample-based validation has the advantage of delivering reference data, which can be directly matched (in space and time) to the validation input, whereas the PlanetScope data offer the advantage of better capturing and, hence, better evaluation of smaller and narrower water bodies and features. Still, the acquisition and interpretation of PlanetScope data is costly, and their representation is therefore restricted in space and time.

In a final step, the temporal consistency of the optical, SAR, and dual sensor-mapping approaches were evaluated by comparing the total areal water extent mapped within each test site and across the monthly time series. Each validation and evaluation step is described in more detail in the two next sections.

4.9.1 Sample-based validation

Stratified random sampling was used to generate reference points over each 100×100 km² test site and within three strata across the land–water continuum: permanent water, seasonal water, and non-water.

The three strata were generated from the 30 m spatial resolution JRC-GSWE long-term water occurrence and defined according to the following thresholds:

- Permanent water: $> 90\%$

- Seasonal water: $> 0\%$ and $< 90\%$
- Non-water: $= 0\%$

The aim was to have a minimum of 50 samples in each stratum, while using subsequent sample size allocations to provide a proportional allocation of samples in better accordance with the actual area of the different strata within each test site. In addition, the expected variance within each stratum was also considered; i.e., the transitional strata are expected to have the highest variance, and why it has a higher sample allocation.

In total, 7980 samples were allocated across the five test sites and assigned to be either water or non-water by two independent and experienced interpreters using blind visual interpretations of monthly Sentinel-1 and -2 composites. To harmonize and achieve consistent reference labelling, a standard validation interface was used to ensure interpreters were looking at same area and using the same reference data and the predefined set of classes. In cases where the interpreters disagreed, a quality manager intervened to seek consensus. If consensus could not be agreed upon, the sample was rejected. For each sample we extracted, the respective water classifications and the final set of samples were used to derive standard metrics for accuracy assessments, i.e., overall accuracy (OA), producer accuracy (PA), and user accuracy (UA). For this analysis, all pixels in the individual Round Robin classifications not classified as water were considered to be non-water; i.e., the non-water class also included pixels being masked (e.g., due to clouds).

4.9.2 Object extraction accuracy

In general, stratified sampling under-sample Small Water Bodies (SWB) due to the fact that they represent only a tiny fraction of the total water area, even if the number of such SWB is larger than the number of large water bodies. To deal with this issue, the Round Robin validation team complemented the conventional stratification, sampling, and confusion matrix-type accuracy assessments with an evaluation of object extraction accuracy based on area-based accuracy metrics and the use of higher spatial resolution but single date (i.e., time-limited) PlanetScope data [163]. The acquired data was PlanetScope Level 3B (Ortho Scene Product) at 3 m spatial resolution, with 4 spectral bands (Red, Green, Blue and Near-Infrared). The PlanetScope data was acquired within the

coverage of each of the test sites and for two areas of approximately 25 km².

For each PlanetScope image, a supervised Gradient Boosting (lightGBM) algorithm [164] was used to generate water masks using the convolution layers derived from spatial filtering of Planet imagery as the explanatory variables and manually derived training samples for water and land (i.e., non-water) as the response variable. At the end of the process, all water masks were manually checked and corrected to ensure high quality. Once analyzed, the PlanetScope data was used to evaluate the object extraction accuracy of the water classifications derived using Sentinel data.

The accuracy evaluation of object extraction is based on object matching, and the focus is on two elements related to this concept: object matching and area-based accuracy measures [165]. Referring to Equation (4.1) The main idea of object matching is to estimate the maximum overlap area by computing the coincidence degree, A_{max} , between two objects:

$$A_{max} = \frac{1}{2} \left(\frac{A_{C,i} \cap A_{R,j}}{A_{C,i}} + \frac{A_{C,i} \cap A_{R,j}}{A_{R,j}} \right) \quad (4.1)$$

where $A_{C,i}$ is the area of the i -th evaluated object, $A_{R,j}$ is the area of the j -th reference object and $A_{C,i} \cap A_{R,j}$ is the intersection area. Naturally, two objects (i.e., the evaluated object and the candidate reference object) are considered a matching pair if the area of the coincidence degree is maximum, i.e., $A_{max} = 1$.

The maximum overlap object matching is also complemented by three area-based accuracy measures: correctness, completeness and quality. Correctness (A_{cor}) is defined as the ratio of the correctly extracted area A_C and the whole extracted area A_{DC} ; whereas, completeness (A_{com}) refers to the ratio of the correctly extracted area to the reference area A_{RC} .

Correctness and completeness range from 0 to 1; if A_C completely corresponds to A_{DC} or A_{RC} , then the value is 1. On the contrary, if there is no overlap between A_C and A_{DC} or A_{RC} then the value is 0. For instance a large A_{DC} value leads to a small correctness value, while a small A_{RC} translates into a large completeness value. To deal with this issue, in Equation (4.2) is defined the quality A_{qual} , which is designed to provide a measure of quality by balancing correctness and completeness:

$$A_{qual} = \frac{A_C}{A_{DC} + A_{RC} - A_C} \quad (4.2)$$

A_{qual} can range from 0 to 1: if the water extraction results are the same as the reference data, then $A_{qual} = 1$; on the contrary, if none of the extracted water area overlaps with the reference water area, then $A_{qual} = 0$. The advantage of area-based accuracy measures compared to the sample-based validation relates to the fact that the confusion matrix of the latter depends on the total pixel number. In contrast, area-based accuracy measures rely only on the evaluation, as reference objects are independent from the total number of pixels.

4.9.3 Results and discussion

Figure 4.15 shows the classification results aggregated by input data type (multispectral, SAR, multispectral+SAR). It is possible to observe that joint use of optical and SAR data generally outperforms single sensor approaches.

For instance, in Colombia the joint use of optical and SAR sensors led to the best results in terms of overall accuracy; however, SAR and optical models performed better in terms of both user and producer accuracy. In Gabon, SAR-based algorithms worked better than the other models in terms of overall accuracy, while optical-based models performed better in Colombia and Zambia in terms of PA and UA, respectively. In Mexico, OA and UA are almost the same among all the models, apart from a drop in PA values for the optical data models, compared with the SAR and dual sensor models.

The observed differences in UA and PA are mainly related to the specific characteristics of each site. For instance, the higher UA achieved in Gabon and Colombia using SAR data provides an indication of the benefit of using SAR in cloudy regions. On the contrary, SAR achieves lower UA in Zambia and Mexico due to commission errors caused by dry and sandy surfaces. Also, the optical model faced limitations in these areas: in fact, it was noted that sun glint in certain months caused erroneous cloud masking for certain processors, hence contributing to lowering the PA for the optical-based models.

The Zambia site is dominated by the Kafue flats, an extensive wetland ecosystem subject to variable flooding and with a sharp contrast to the surrounding drier landscape, where fire is a major natural factor impacting the landscape. Such dynamic nature and many confounding factors (e.g., fires and emergent vegetation) make Zambia a particularly challenging site. Here, dual sensor approaches displayed their strongest potential in balancing the individual strengths and weaknesses of optical and SAR data.

In Greenland, the topography and light conditions are the main challenges. For optical data, this translates into higher commission errors due to shading effects and low sun angles. SAR-based models are better at dealing with these issues because it works independent of sunlight; moreover, by using ascending and descending SAR scenes, the part of the landscape that can be monitored is increased. Still, the influence of low-backscatter areas (e.g., exposed river beds and in snow dominated landscapes) make SAR-based models suffer from commission errors and lower PA.

Regarding the object extraction accuracy analysis, 3 m spatial resolution PlanetScope water classification maps, depicted in Figure 4.16, were utilized. From Figure 4.17, which summarizes the obtained results, it is possible to note that models that include multispectral data perform better than those based on SAR data only. The lowest overall accuracy was obtained in the Colombian site, where is also possible to observe the difference between the best optical-based models and the best SAR-based models. Moreover, the highest object extraction accuracy is achieved in Zambia, which (together with Greenland) has the largest share of water bodies within the test sites. Figure 4.17 also shows that the optical data model outperforms SAR data models in all test sites, except for Gabon (whereas, Greenland achieved similar results for single- and dual-sensor based approaches).

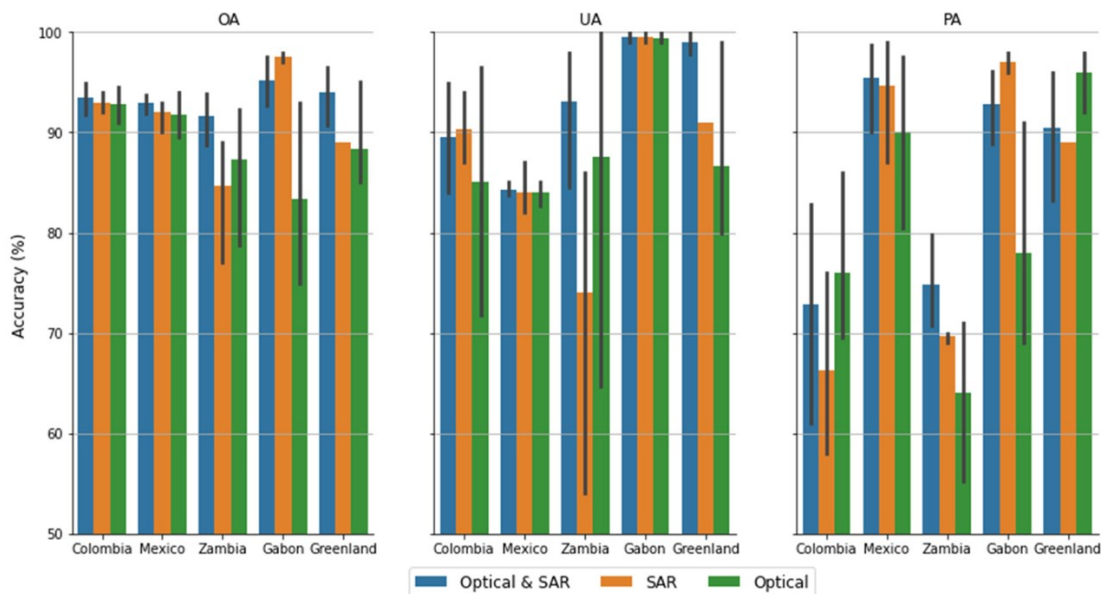


FIGURE 4.15: Accuracy statistics from the WorldWater Round Robin test sites, individually and overall, summarized by model input data type (OA = Overall Accuracy; UA = User Accuracy; PA = Producer Accuracy).

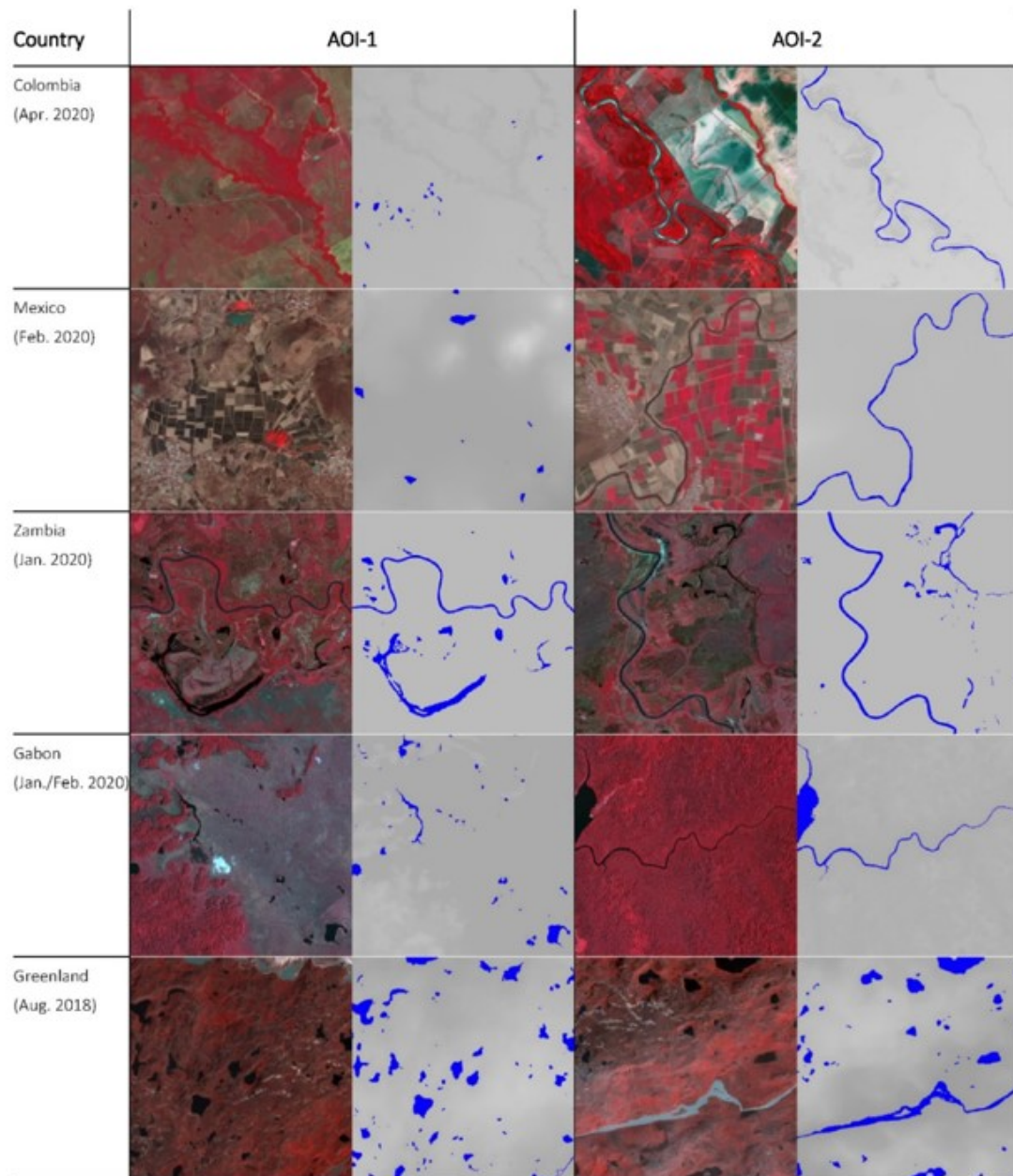


FIGURE 4.16: False colour PlanetScope QuickLooks and associated water classifications for each test site used in the object-based validation approach.

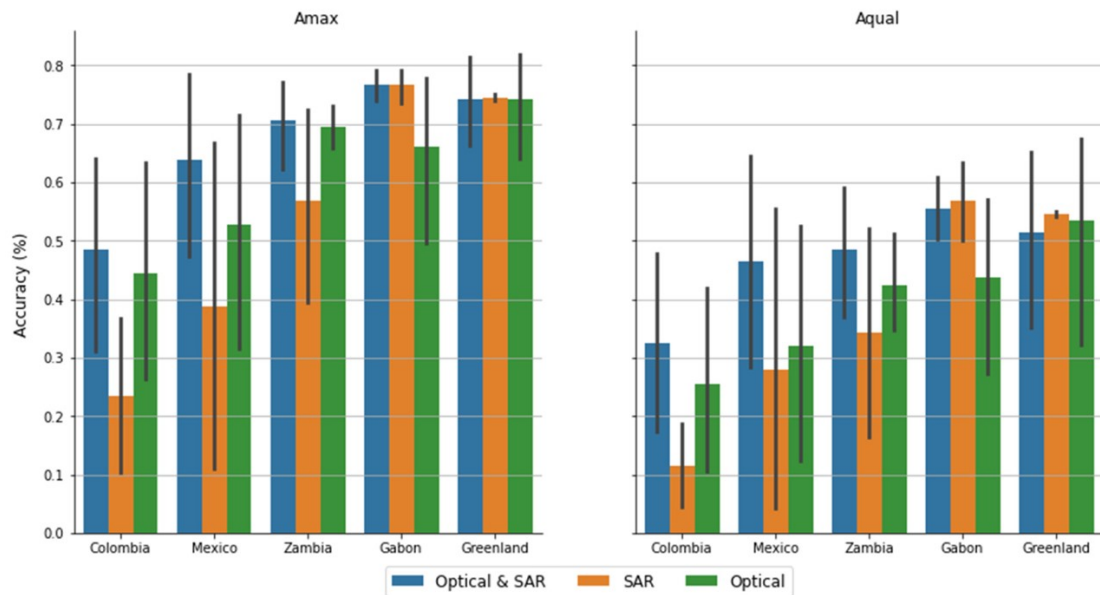


FIGURE 4.17: False colour PlanetScope QuickLooks and associated water classifications for each test site used in the object-based validation approach.

Findings from the object extraction accuracy analysis indicate that using or integrating optical data into the water detection algorithm is vital in order to achieve accurate water object definitions. In Colombia, the average water body size/width is smaller compared to other sites; for this reason, the difference between the optical-based algorithms and SAR-based approaches is the largest. This is explained by the characteristics of the input data, with key spectral water detection bands from Sentinel-2 available only in 10 m spatial resolution, while the true spatial resolution of Sentinel-1 is understood to be closer to 20 m (with 10 m pixel spacing). There are also some differences between the optical- and the SAR-based approaches in Mexico, which is likely caused by the dry environment and a landscape dominated by large dry areas and sandy surfaces. In contrast, the difference between optical and SAR is much less pronounced in Zambia and Gabon; this may be likely related to the larger average size of the water bodies (Zambia) and the dense tropical forest landscape causing a strong land–water contrast (Gabon).

Regarding the water mapping algorithm developed in this thesis (Chapter 4), the performances of the proposed approach are extremely promising. The validation procedure carried out in the framework of the WorldWater Round Robin provided evidence of the scientific robustness of the developed methodology, which was proved to be one of the best SAR-based models.

Results concerning the sample-based validation are reported in Table 4.4, whilst those obtained by means of the object extraction accuracy are reported in Table 4.5. Comparison between the proposed model (model “J”) and all the other Round Robin participants can be accessed at <https://www.mdpi.com/article/10.3390/rs14102410/s1>.

Lastly, in Figure 4.18 examples of water body extraction over the five test site, to visually appreciate the outcomes of the proposed algorithm, are reported.

4.9.4 Takeaway messages

The first very important lesson learnt during the Round Robin was that satellite-based surface water monitoring systems are vital to supporting more evidence-based planning and management of water resources, and to provide the ability of efficiently report and

	PA_w	PA_{nw}	UA_w	UA_{nw}	OA
Zambia	88	95	82	97	93
Mexico	83	99	98	91	93
Colombia	76	98	87	95	94
Gabon	98	98	99	96	98
Greenland	89	88	91	86	89
Average	86.8	95.6	91.4	93	93.4

TABLE 4.4: Results from the ESA WorldWater project validation process. “w” and “nw” stand for water and non-water respectively, whereas PA, UA and OA stand for Producer Accuracy, User Accuracy and Overall Accuracy respectively (in percentage [%]).

	A_{max}	A_{qual}	OA
Zambia	0.73	0.55	0.40
Mexico	0.43	0.37	0.16
Colombia	0.19	0.11	0.02
Gabon	0.79	0.63	0.49
Greenland	0.75	0.55	0.41
Average	0.58	0.44	0.3

TABLE 4.5: Summary of object extraction accuracies. The accuracy metrics are maximum overlap area (A_{max}) and quality (A_{qual}) as a joint balanced measure of correctness (A_{cor}) and completeness (A_{com}). The overall score is the product between A_{max} and A_{qual} .

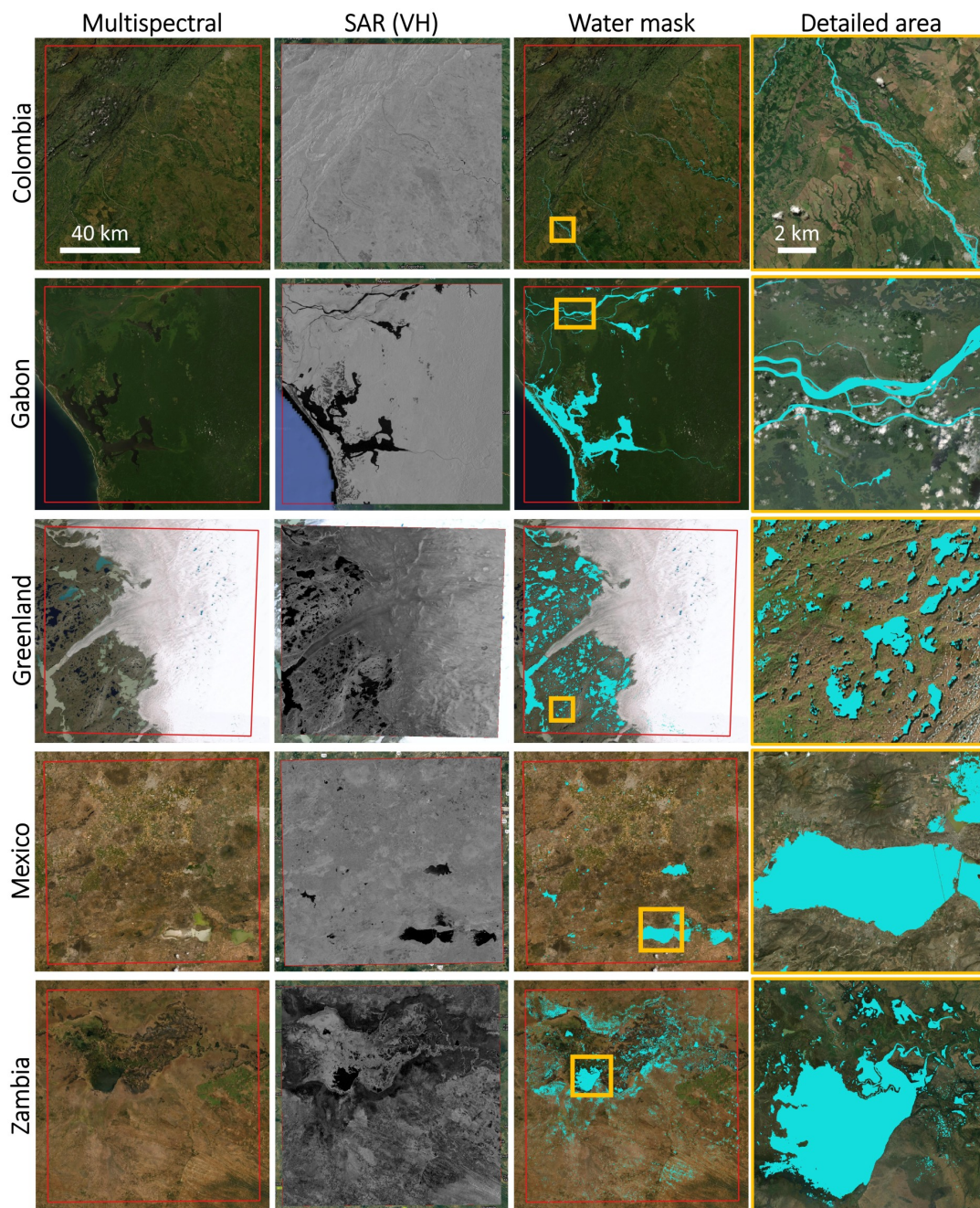


FIGURE 4.18: Qualitative results for the five WorldWater Round Robin test sites: Colombia (tile 18NYL), Gabon (tile 32MND), Greenland (tile 22WET), Mexico (tile 14QKH) and Zambia (35LNC). Background optical images are taken from the Google Satellite basemap, except for the second column, which shows the annual mean VH composite image for each tile of interest (the grey-scale composite is obtained by setting -30 dB and 0 dB for minimum (black) and maximum (white) σ^0 values respectively). The scale bar is shown only once for full view of the tiles and for the detailed, zoomed region.

act in response to the global water agenda.

In the framework of the ESA WorldWater Round Robin, 14 different EO-based models for surface water monitoring and mapping were analyzed and evaluated. The whole experience showed that single sensors models are able to produce very accurate and consistent results under almost ideal conditions. On the other side, joint use of optical and SAR data allows to achieve more accurate and consistent water maps.

The main outcomes of this exercise allow to bear several important perspectives for formulating a new best practice where multispectral and SAR data are used in a synergistic way in order to achieve the highest accuracy possible. However, even is accuracy is a very critical and important factor for selecting a surface water detection approach, there exist other important aspects, such as computational efficiency, simplicity and ease of implementation; these aspects all contribute to increase understanding, maintainability and scalability.

It has been shown that, for larger scales across diverse ecological gradients, synergistic models are better; on the other hand, at the local scale SAR data is the preferred source of data because they allow to effectively and promptly monitoring water extents during natural events, such as floods during cloudy periods. Whereas, optical data alone is preferred when the task is to monitor the status of reservoirs and small water bodies during periods when clouds do not represent an issue.

For all these reasons, instead of claiming the “best” water detection model, it is recommended more flexibility and options to build and/or adapt methods that are suitable for individual user needs in terms of management goals, environmental settings and scale of study.

To conclude, the Round Robin experience demonstrated that EO data and methods for monitoring surface water dynamics are available and successfully applied in many contexts all around the World.

4.10 Seasonal water body monitoring and mapping

This very brief section is devoted to the analysis of the capability of the proposed water body monitoring and mapping algorithm to discriminate permanent water bodies from temporary/seasonal ones. The objective of the methodology described at the beginning

of Chapter 4 was to generate annual high resolution *permanent* water bodies maps over a specific region of interest. In the case of annual maps, the multitemporal stack of four “quarter composites” (see Section 4.3) was essential to characterize water bodies, hence being able to separate this class from other classes which may represent sources of confusion; this was possible thanks to the fact that such reduced SAR time series is able to reconstruct the phenology of the different land cover types.

However, during the Round Robin described in Section 4.9, it was required to generate *monthly* water maps for two consecutive years. Given this constraint, it was no longer possible to take advantage of the quarter composites. To generate monthly water map, the quarter composite was removed from the feature space, while the minimum, maximum, mean and variance features were kept.

During the experiments carried out within the Round Robin framework, this new setup unlocked the possibility to generate maps of both permanent and temporary water bodies, which represent a very important distinction for climate change scientists. Unfortunately, it was not possible to develop this topic and go deep into it, as such activity require much more effort and time, which cannot fit into the framework of the present thesis. However, few preliminary results are presented, in order to show the potential of the developed water mapping algorithm to discriminate permanent and temporary water bodies.

First of all, it is necessary to define what is a permanent water body and a temporary/seasonal one. To this aim, referring to official definition from the FAO Land Cover Classification System (LCCS)⁴, these two classes are defined as follows:

- **Permanent water:** Areas where open water covers at least 50% of the surface and remains for more than 9 months a year, except in special circumstances (particularly dry year, construction of dams, etc.). Snow and/or ice and built-up areas cover less than 50% of the surface. Water bodies can be natural or artificial. Water can be saline, fresh or brackish;
- **Seasonal water:** Areas where open water covers at least 50% of the surface and remains between 5 and 9 months a year, except in special circumstances (particularly dry year, construction of dams, etc.). Snow and/or ice and built-up areas

⁴<https://www.fao.org/3/x0596e/x0596e00.htm>

cover less than 50% of the surface. Water bodies can be natural or artificial. Water can be saline, fresh or brackish.

Based on the above definitions, a modified water body methodology has been designed. Figure 4.19 shows the modified block scheme for seasonal water body mapping. The idea of such procedure is to subdivide the entire, despeckled SAR time series into monthly time series, ending up with $N = 12$ smaller SAR sequences made of all the available SAR images within each single month for a specified year of interest. It is however important to keep in mind that, for some regions in the World, it is not always possible to build 12 smaller sequences, due to coverage issues; for instance, experiments carried out in the Siberia revealed the complete absence of SAR images in some months along the year. Therefore, even if $N = 12$ is the ideal condition, in general N may be smaller.

From each of the N time series, four temporal composite images are then computed, namely: the minimum, maximum, mean and variance composites. These temporal statistics are then used as input features within a k -Means clusterer, which is instantiated from scratch for each month. The only thing in common with all the instantiated classifiers is the set of seed points, which is extracted from the CGLS map at 100 m resolution, as per Section 4.4. At this point, each k -Means classifier generates a water map which represents the situation of water bodies for a specific month.

Then, as depicted in Figure 4.20, all the N generated maps (in the form of binary masks where 0s and 1s represent non-water and water, respectively) are used to build a single, annual water map where permanent and seasonal water bodies are separated. To this aim, first the N water maps (each representing one month) are stacked considering N as the temporal dimension. As mentioned above, N can range between 1 and 12, where 1 is the worst possible case and 12 is the best one. Then, the number of water occurrences are counted along the N -axis, for each single pixel, ending up with a map of per-pixel water occurrences. In this map, each pixel is associated to a value n , where $n \in [1, 12]$. At this point, each pixel of the previous result is divided by the total number N of monthly maps, to obtain the amount of time water is present along the year on a per-pixel basis. In this new result, each pixel p is associated to a number $(\frac{n}{N})$ which is used to label such pixel as water or non-water, based on the following rules:

- If $t_{inf} \leq \frac{n}{N} \leq t_{sup}$ then $p \rightarrow$ **Seasonal**;

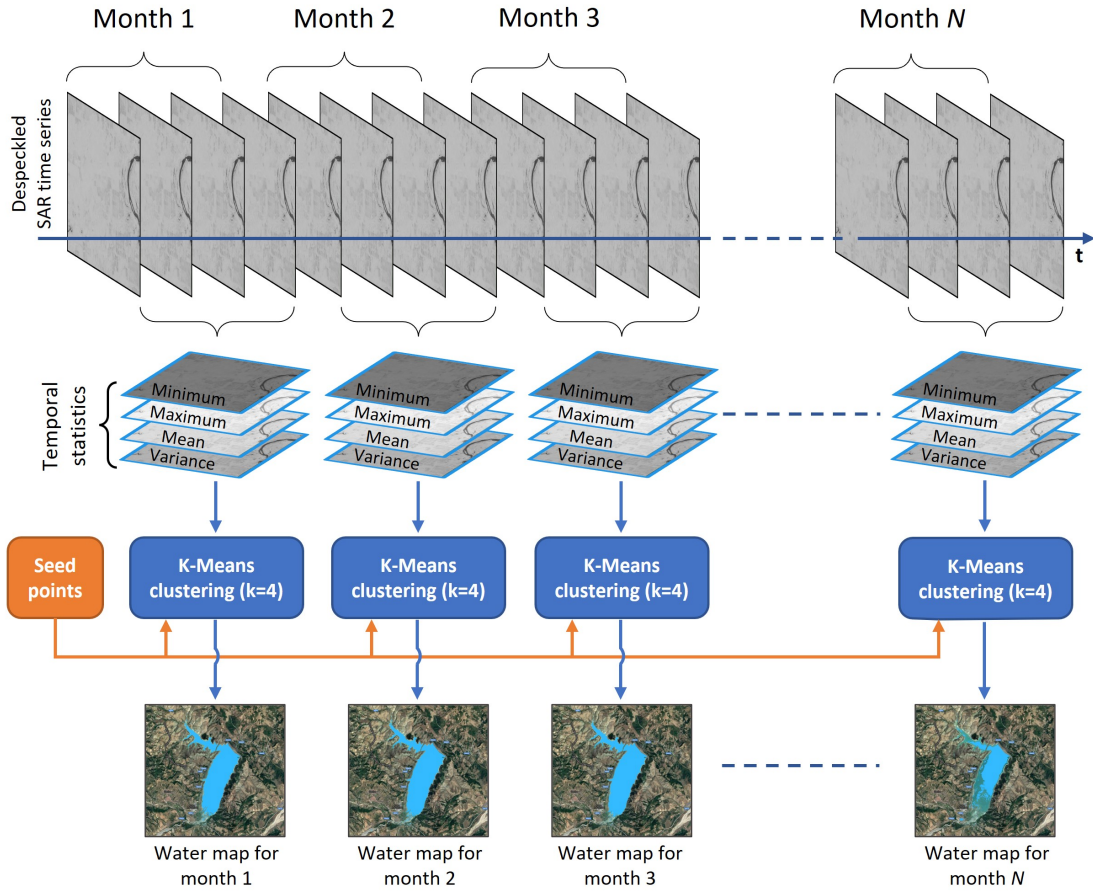


FIGURE 4.19: Scheme of the proposed seasonal water body mapping algorithm (which is a variation of the original water body mapping model).

- If $\frac{n}{N} > t_{sup}$ then $p \rightarrow$ **Permanent**;
- If $\frac{n}{N} < t_{inf}$ then $p \rightarrow$ **Non-water**

Where $t_{inf} = \frac{5}{12} = 0.4167$ and $t_{sup} = \frac{9}{12} = 0.75$.

So, based on the FAO definition of permanent and seasonal water bodies, if a pixel is labelled as “water” 11 times (not necessarily in a row) out of 12, then $\frac{n}{N} = \frac{11}{12} = 0.9167 > t_{sup} = 0.75$ (i.e., the pixel eventually labelled as permanent water body). In this way, it is possible to assign to permanent/seasonal water class a pixel based on the percentage of time such pixel is labelled as “water” in the monthly maps, given any number N of maps. Of course, the lower the number of maps, the less reliable is the final permanent/seasonal water map.

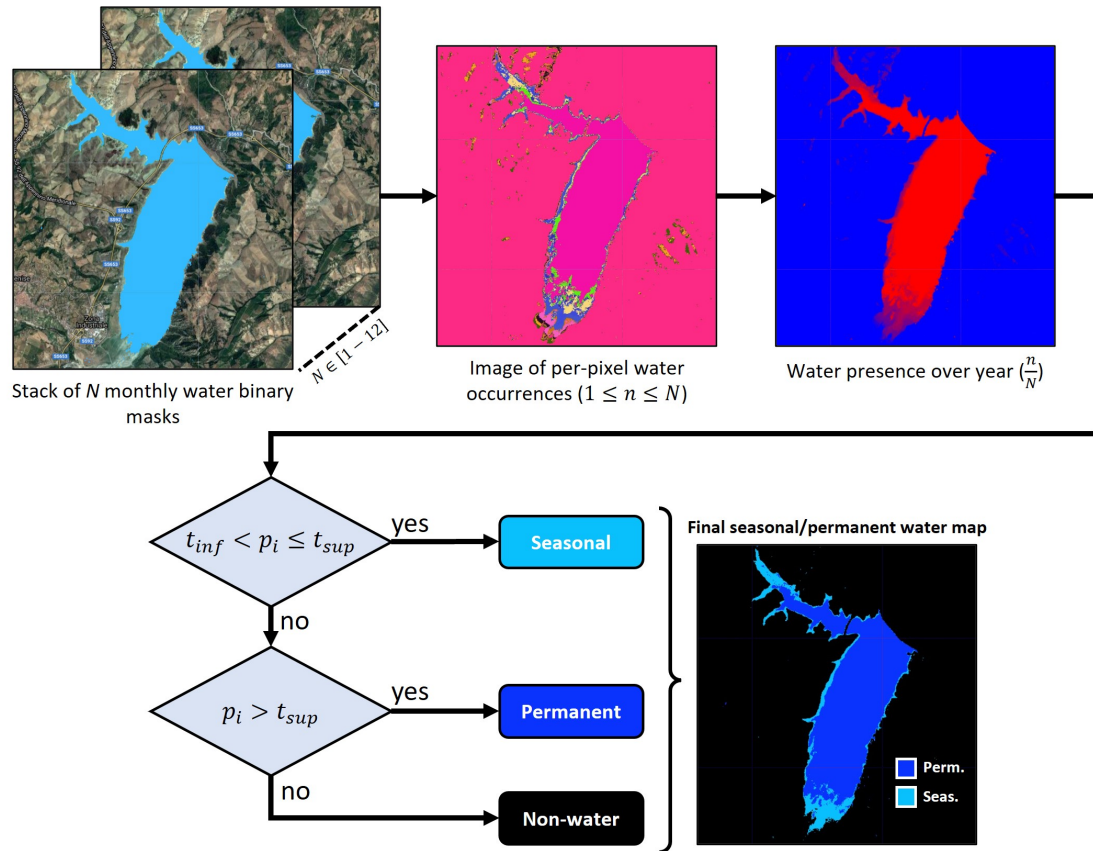


FIGURE 4.20: Final stage of the permanent/seasonal water body mapping algorithm, that aims at generating the final water map based on the frequency of water presence, per pixel.

4.10.1 Example of permanent and seasonal water body mapping: the Monte Cotugno reservoir

In this section, some preliminary qualitative results related to permanent/seasonal water body mapping are presented. The area of interest, where experiments were carried out, is located in the Potenza province, Basilicata region, South Italy. Specifically, the algorithm was tested over the Monte Cotugno reservoir, the biggest clay dam in Europe (Figure4.21).

Applying the algorithm depicted in Figure 4.19, 12 water maps were generated for year 2019. To visually appreciate the water maps extracted for each month, these were grouped together in Figure 4.22. From this figure is possible to observe how the extent of the water body surface changes in time, from January to December 2019. In particular, it is interesting to note that the surface extent decreases from August to December, while it begins to increase from January.

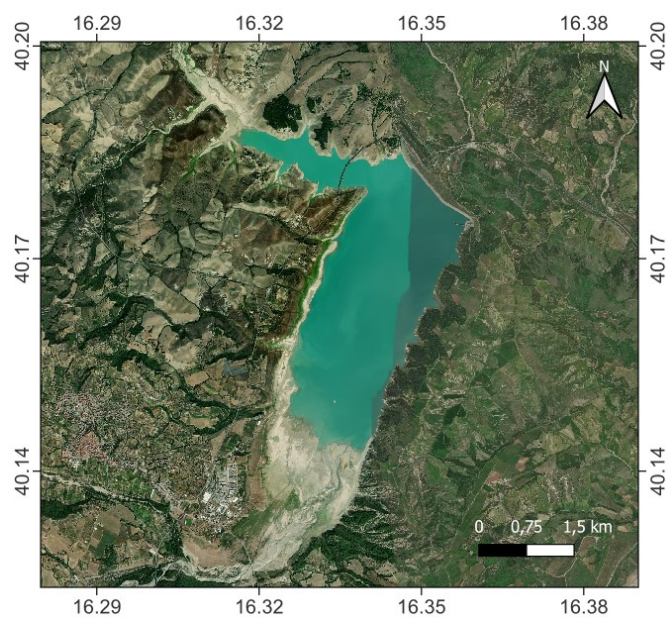


FIGURE 4.21: The Monte Cotugno reservoir in the Potenza province, Basilicata region, South Italy.

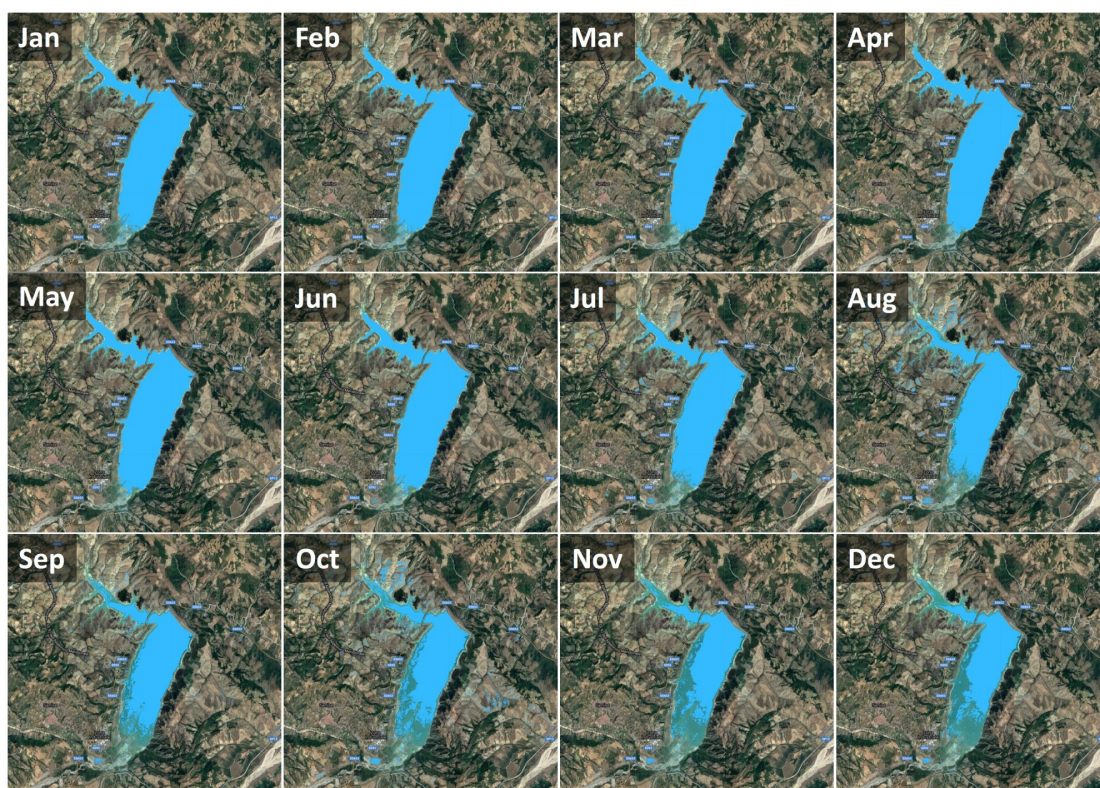


FIGURE 4.22: The Monte Cotugno reservoir in the Potenza province, Basilicata region, South Italy.

All these maps are then used as input to the algorithm schematized in Figure 4.20, which aims at producing the final, high-resolution permanent/seasonal water map reported in Figure 4.23. The final map visually matches the expected behaviour of the reservoir: the frequency of water pixels located in the South, North and on the West parts of the reservoir is around 6-7 over 12. This means that all these pixels are labelled as “seasonal water”.

Lastly, another interesting feature that can be exploited based on the described methodology, regards the possibility to generate vector layers that track, month by month, the situation of the water body extent. Figure 4.24 shows an example of GIS layer useful to analyse the annual trend at a glance.

Given all the obtained results, the developed methodology has demonstrated to possess the potential to reliably generate water body maps, where permanent and seasonal water type are distinguished. Future works on this topic will include the collection of ground truth data, to quantitatively assess the proposed algorithm.

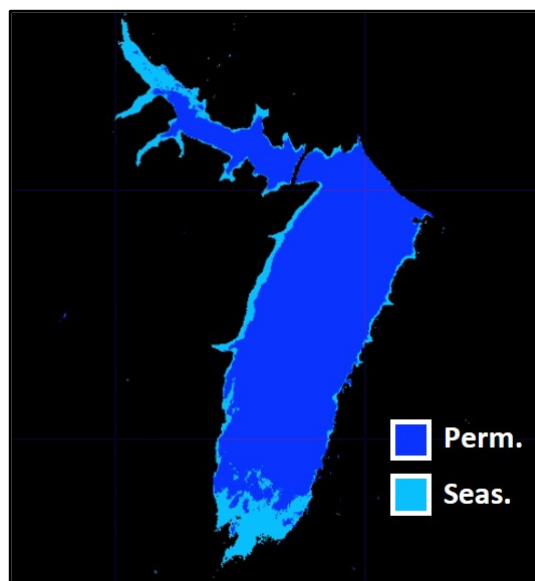


FIGURE 4.23: Final high resolution (10 m) permanent/seasonal water body map generated over the Monte Cotugno reservoir.

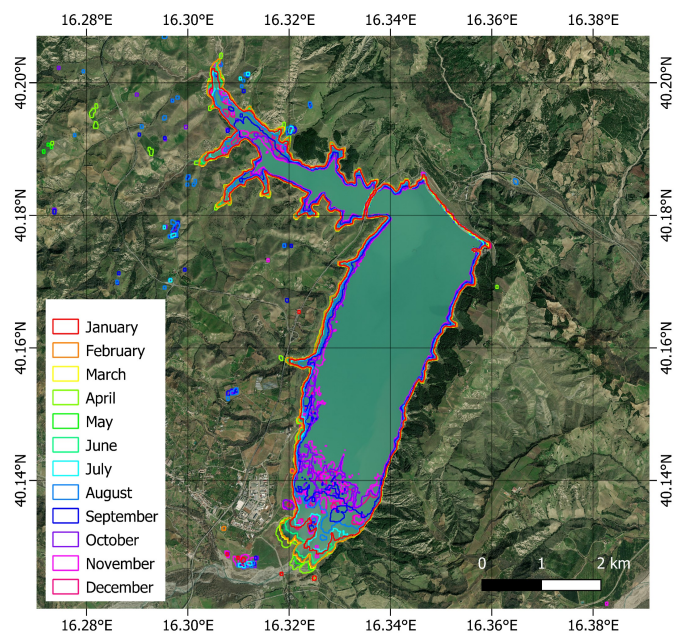


FIGURE 4.24: Vector layer showing the extent of the analyzed water body for each month (year of interest: 2019). Note that there are some false positive occurrences around the reservoir, due to the absence of post-processing steps.

Chapter 5

Organic farming characterization¹

In the present Chapter, the last topic of this thesis is presented and analyzed: the characterization of organic farming practices using both spaceborne, multitemporal optical and radar data.

The objective of *organic farming* is to produce food using natural substances and processes, which ensure limited environmental impact and foster maintenance of biodiversity, regional ecological balances, soil fertility, water quality etc. [169]. Rice is an interesting example in relation with the European context in general and the Italian case in particular. Italy alone, indeed, accounts for about 53% in weight of the total European Union (EU) rice production, and exports more than 45% in weight of its domestic output, thus playing a primary role in the European rice market. Most of the Italian rice production takes place in North-Western Italy, with the province of Pavia, providing alone just above one third of the total domestic rice production thanks to its 82000 hectares of rice paddy fields; the nearby Piedmont region contributes slightly less than half the

¹this chapter is based on material published in the works:

- [49] Marzi, David, and Fabio Dell’Acqua. “Mapping European Rice Paddy Fields Using Yearly Sequences of Spaceborne Radar Reflectivity: A Case Study in Italy.” *Earth* 2.3 (2021): 387-404.
- [166] Marzi, David, and Fabio Dell’Acqua. “An experiment on extended, satellite-based traceability of organic crops in North-Western Italy.” 2022 IEEE International Geoscience and Remote Sensing Symposium IGARSS. IEEE, 2022.
- [167] Marzi, David, Cristian Garau, and Fabio Dell’Acqua. “Identification of rice fields in the Lombardy region of Italy based on time series of Sentinel-1 data.” 2021 IEEE International Geoscience and Remote Sensing Symposium IGARSS. IEEE, 2021.
- [168] Marzi, D., and F. Dell’Acqua. “Space-based monitoring of organic rice: The ESA KSA project “Vialone” contributes to supporting an Italian high-tier product.” Proceedings of the GTTI Radar and Remote Sensing Workshop. 2019.

total. Other significant contributors include the Veneto, Emilia-Romagna, Sardinia and Calabria regions. However, data from the Italian National Statistics Institute (ISTAT) reports that, per each Italian citizen, traditional agriculture introduces on average into the environment more than 70 kg of pesticides, weedicides and chemical fertilizers; the situation is similar in other developed countries, and the need to change the approach is becoming increasingly clear. Consumer awareness on health and environment impacts of rice consumption [170] is indeed growing, and so the appeal of organic products. Although the environmental effects of organic farming have not yet been explored to their very end and some aspects are controversial [171], it surely generates a positive impact through for example the ban on pesticides, that contributes to a cleaner environment.

On the downside, organic food is generally more expensive than traditional food due to more costly production practices and lower yields [172], yet still accepted by the consumer because of its features. Demanding, selective, environment-aware consumers are available to pay far higher prices per unit in exchange for products that are supposedly more healthy and more sustainable. Specifically in the case of rice, the organic product can be sold at a unit price up to five times higher than traditional one.

In this framework, “fake organic” rice, i.e. traditional rice fraudulently declared and sold as organic, represents a great, albeit illegal, revenue opportunity for unscrupulous farmers. The astonishing speed of growth in the number of “green” farms is a factor in suspicion arising about the veracity of some organic compliance statements. These episodes may dent the appeal of the “organic” label to the consumer, thus damaging the vast majority of genuine organic producers.

Increasing public awareness about the problem calls for not only legal, but also technological countermeasures. This may include monitoring from space of the reportedly organic fields to expose possible lack of compliance that may have been missed by the field surveys of certifying authorities. These latter cannot be pervasive, and thus may happen to leave blind spots. In space-based observation, temporal and spatial resolutions make it virtually impossible to directly detect from space a single forbidden operation the very moment it is carried out, like e.g. rolling a tractor to spread weed-killer substances. Still, a number of parameters exist that are visible from space and can provide significant clues about possible non-compliance.

In Chapter 2 (Section 2.3), an overview of the methodologies that can be useful to characterize crop management using satellite data was given. More importantly, the fact

that no previous studies on monitoring of organic farming practices have been carried out was highlighted. Despite this, the technical literature on conventional crop monitoring and mapping using satellite data provided us with the tools that may be successfully exploited for organic crop monitoring purposes.

In this Chapter, three main topics are discussed:

1. Detection of weed-killer activities by analyzing their short/long-term effects on crops using optical data;
2. Assessment of the type of tillage technique using SAR data.
3. Detection of fertilization operations using optical data;

The first two topics were developed within the framework of the Italian Space Agency (ASI) “MultiBigSARData” project (Section 5.1), while the last one was carried out within the Joint Research Centre (JRC) “Geospatial Intelligence Against Nitrate Pollution” (GEOINT) project (Section 5.4.1).

5.1 The Italian Space Agency (ASI) “MultiBigSARData” project

The “MultiBigSARData” project is part of a very important methodological framework, i.e., the field of research dedicated to the use of time sequences of SAR data for the characterization of phenomena with both high spatial and temporal resolution. The project aims, in fact, at obtaining a multifrequency, multitemporal and multiresolution description of the same phenomenon using a combination of L- C- and X-band SAR data. Thanks to the combination in three different directions of spectral resolution (w.r.t. the wavelength), spatial resolution (w.r.t. the dimension) and temporal resolution (w.r.t. the acquisition frequency), it is possible to extract information regarding events that cover different temporal and spatial scales, and which have different features in the given frequencies.

The aim of this project is to identify, adapt and develop methodologies that best combine with respect to the time, spatial and spectral axes the data acquired from different sensors, thus allowing to exploit all their potential in a synergistic way. This project has

the potential to significantly impact many different areas. For instance, in the field of urban remote sensing, the use of data from multiple sensors allows to promptly identify any change due to the construction or even the redevelopment (change of scope) of a building, a neighborhood or a urban environment. In case of cropland monitoring, the use of multifrequency data may improve the identification of different scattering mechanisms which are related to the geometric characteristics of the crops, but also to their health status. Also target detection algorithms may benefit from the joint use of multisource SAR data, as the use of different satellites - that make the whole SAR time series denser - allow to better identify events that can be caught only in a specific time window. Finally, regarding the control of the environment in terms of risk management and defence, the possibility of combining information from different times and from different sources is essential at the decision level. Similarly, even land cover and land use classification methodologies can benefit from the use of multifrequency, multitemporal and multiresolution data.

To summarize, the “MultiBigSARData” serves a triple purpose:

- Implementation of a procedure for the appropriate combination of multisensor SAR data in a single sequence, aimed at enriching multitemporal sequences acquired in the same band with different spatial resolution, or in different bands with same spatial resolution;
- Implementation of procedures to analyze multisensor SAR data at different frequencies in order to obtain from the overall sequence useful temporal information for the characterization of a particular event, in terms of its changes in time and of its bio-physical characteristics;
- Implementation of a procedure for the joint classification of multifrequency and multiresolution SAR data for the characterization of phenomena in which the analysis at different wavelengths and/or polarizations is more important than revisit time, due to the nature of the event itself.

Within the framework of this project, the present thesis focussed on the characterization of crop fields, specifically, on organic crops, with the support of optical data.

5.2 Detection of weed-killer activities using optical data

In this Section, the capabilities of Sentinel-2 multispectral data to detect weed-control chemical treatments on crops are explored. Together with many other organic-related parameters, these treatments represent a key aspect from an organic certification point of view; in fact, weed control involve chemical products in conventional rice fields, an approach which is forbidden in organic farming practices. Hence, these assessments are extremely significant in verifying whether the previously declared organic cultivation was factual or less so.

5.2.1 Space-based monitoring of organic compliance on rice

Earth observation satellite technology enables collection of data on crop fields and consequent generation of information that may be profitably integrated into the process of checking organic compliance. The same pool of information can also be used to expand traceability information on organic products.

As mentioned in Chapter 2, Section 2.3.2, several aspects of organic rice cultivation that may be monitored and assessed from space were identified and are here briefly recalled. A first, important technical detail regards the sequence of crops; in a 4- to 5-year cycle, the practice of organic rice cultivation is characterized by the so-called “crop rotation”, which is mandatory for qualifying the cultivation practice as organic. When rice cultivation is paused, the field must be sowed with other crops that help implementing natural weed management and maintaining soil fertility [173], or kept fallow when it does not make agronomic or economic sense to seed other crops as is sometimes the case in some farms in northern Italy. In order to assess such practice, classification algorithms can be used, based on either supervised or unsupervised techniques.

Examples of classification algorithms include statistical decision trees like in [174], where the capabilities of Google Earth Engine (GEE) cloud platform for large scale crop mapping using Landsat-8 optical imagery are investigated, comparing the proposed decision trees with other reference methods on a standard agricultural benchmark dataset in Ukraine; random forests like in [175], where parameter tuning is also discussed, or in [176], where large-scale mapping is addressed with the connected big data issues; unmixing algorithms like in [177], where a parametric mixture model is proposed to describe satellite data monitoring crop development in the US Corn Belt; crop growth

models like in [178] where both spaceborne multispectral and radar data are ingested by a suitable model that accurately predicts cash crop yields for insurance purposes; finally, machine learning techniques were also proposed as in [179] where a multilevel DL architecture is presented, targeting land cover and crop type classification from multi-temporal, multisource satellite imagery. Another key aspect subject to monitoring from space, and representing a major challenge in organic paddy field management, is weed control [180]. This latter can be achieved using different field management techniques strictly related with water management, which include false seeding, weeder harrowing, green mulching, transplanting, manual cleaning.

A third fundamental aspect differentiating organic production from non-organic one is water management. This is about planning inflow and drainage of water from the paddy field chamber, and consequently about monitoring water level in the field. From a technical point of view, it is not possible to reliably detect water depth from satellite, still, it is possible to determine the moment in time when the inflow and outflow of water takes place; it has been indeed demonstrated in literature [181]) that flood water in the field can be detected even from optical satellites.

Since the management of water is strictly correlated to the specific agronomic technique used, this assessment is extremely significant in verifying whether the previously declared organic technique was actually implemented or not. This aspect can be successfully assessed by exploiting radar data. In fact, monitoring of water is reliable and effective using space-borne radar data [44, 182, 183]); moreover, radar signals are insensitive to weather conditions and can therefore provide data in cloudy conditions as well [184].

5.2.2 Study area

As mentioned in the previous Section, collaboration with local farmers in the Pavia and Vercelli areas, northern Italy, granted us the composition of an interesting pool of ground truth (GT) information for year 2018. Specifically identified rice paddy fields were translated into GIS polygons reflecting the boundaries of each field. Then, as depicted in the block diagram of Figure 5.1, the polygons were used for isolating responses from each single field, spatially averaging them within each polygon and composing the related NDVI time series for each field. The NDVI spectral index, whose value can range from -1 to 1, is computed based on red (RED) and near-infrared (NIR) bands, according to Equation (5.1).

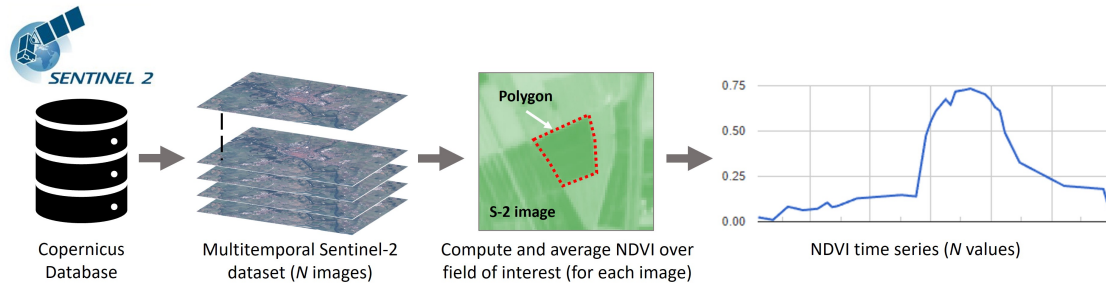


FIGURE 5.1: Scheme of the NDVI time series extraction procedure.

$$NDVI = \frac{NIR - RED}{NIR + RED} \quad (5.1)$$

The operation of building GT information leveraged legitimate weed control and fertilization activities in conventional rice fields, as the focus of our research is to assess whether such operations are detectable from space. For obvious reasons, building a statistically significant sample of “fake” organic rice fields is tricky; however, one can take advantage of legitimate weed control and fertilization activities in conventional rice fields, as the objective is to assess whether they are detectable from space.

In particular, the goal of the analysis described in this Section is to determine the ability of Copernicus’ Sentinel-2 satellites to spot out the effects of weed-management chemical products on rice crops.

The GT dataset is composed of 14 rice paddy fields with sizes varying between 0.9 ha and 8 ha, with an average of about 3.9 ha, and covering a total area of roughly 58 ha. Each field was labelled with a conventional name, reported together with additional details in Table 5.1; the related GIS polygons are represented in Fig. 5.2. It is important to keep in mind that weeding dates are not systematically recorded in the farm operations log. Hence, such dates can only be estimated based on the sowing date, which is instead recorded in writing.

Starting from the GT information, we clustered all fields into three groups based on the sowed rice variety, thus generating the *S. Andrea*, *Luna CL* and *Sole* clusters. Clustering helps carrying out a more focussed analysis, as each variety has its own features and may lead to different temporal trajectories. For example, both *Sole* and *Luna* are somehow precocious, but *Luna* can be sowed a bit later and with a slightly lower density. *S. Andrea* is sowed even later, and the plant is somehow taller. These different features are expected

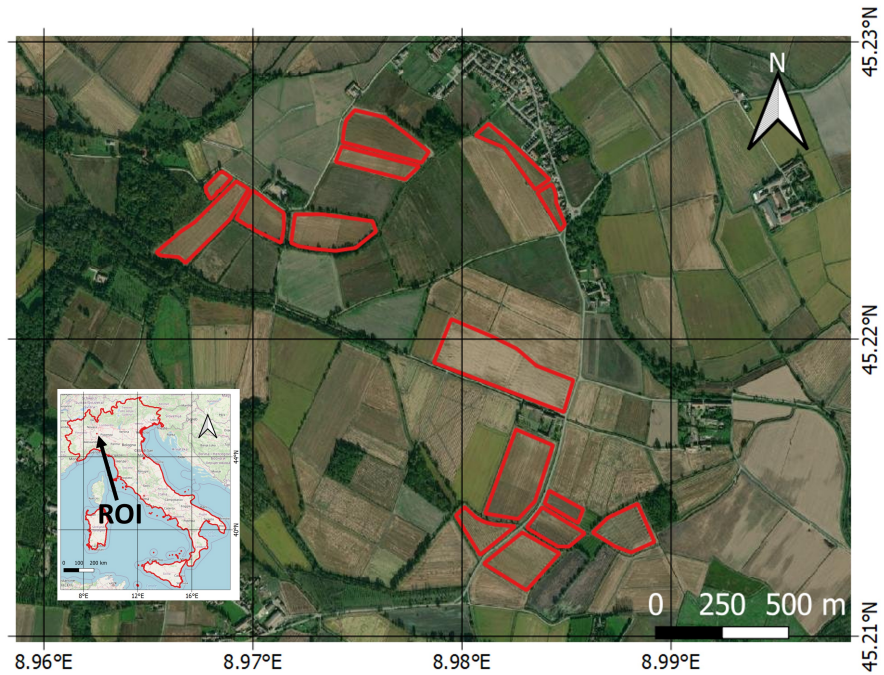


FIGURE 5.2: Ground truth (GT) polygons representing conventional rice fields.

Field ID	Lat., Long.	Rice var.	Type of sowing	Sowing	Weeding
Essiccatoio	45.215, 8.982	SA	Water	15/5	12/6
Triangolo	45.213, 8.981	SA	Water	15/5	12/6
Platani	45.212, 8.983	SA	Water	15/5	12/6
Bandi	45.213, 8.988	SA	Dry	11/5	11/6, 15/6
Baccanino	45.223, 8.967	LCL	Water	21/5	14/6, 9/7
Cabina	45.225, 8.968	LCL	Water	21/5	14/6, 10/7
Baccano	45.224, 8.970	LCL	Water	21/5	14/6, 10/7
Vigna	45.223, 8.973	LCL	Water	21/5	14/6, 10/7
Prosoni	45.225, 8.975	LCL	Dry	19/5	22/5, 11/6, 14/6, 10/7
Cerine	45.226, 8.975	LCL	Water	24/5	14/6, 10/7
Orti	45.218, 8.984	SO	Dry	17/5	21/5, 11/6, 16/6, 13/7
Marcite	45.213, 8.984	SO	Water	17/5	15/6, 12/7
Pasquale 1	45.225, 8.982	SO	Water	24/5	14/6, 12/7
Pasquale 2	45.224, 8.984	SO	Dry	17/5	21/5, 11/6, 14/6, 12/7

TABLE 5.1: Rice fields and corresponding geo-location, sowed variety (SA = S. Andrea, LCL = Luna CL, SO = Sole), type of sowing (dry-seeding or water sowing), sowing date and weeding dates. Geographic coordinates are expressed in decimal degrees.

to impact on their appearance in satellite data. NDVI time series were generated on each field by averaging per-pixel NDVI values within the boundaries of the field. In order to give the reader an idea of the magnitudes involved, we computed some statistics over the NDVI values of individual fields at two representative dates, i.e. 15th August 2018 (*Summer* statistics) and 11th November 2018 (*Winter* statistics). In *Summer*, single-field averages range between 0.775 and 0.880, with single-pixel values spread from 0.412 to 0.895. Standard deviations among pixels in individual fields range between 0.012 and 0.068 with an average of 0.03, which suggests a good degree of homogeneity despite a few outliers in single-pixel values. Relative Standard Error (RSE) values range between 0.261 and 1.555%, with an average of 0.704%. Although shifted to generally lower values, *Winter* statistics show similar trends. Single-field averages range between 0.1 and 0.233, with single-pixel values ranging from 0.014 to 0.397. Standard deviations among pixels in individual fields range between 0.021 and 0.091 with an average of 0.039, i.e. slightly less homogeneous than summer, but still stable. RSE values range between 1.877 and 11.609%, with an average of 4.638%, reflecting the decrease in homogeneity with respect to summer. All these statistics were summarized in Table 5.2.

The stability of values across the fields, especially in summertime, hints that the analysis described in the next chapter rests on a statistically robust sample.

5.2.3 Sentinel-2 multispectral data

This constellation was chosen, among many others, because it offers a very welcome open policy on its data, while at the same time featuring spatial and temporal resolutions that are fine enough for our purposes [185, 186].

Sentinel-2 is a wide-swath, high-resolution, multi-spectral imaging mission supporting Copernicus Land Monitoring studies, including the monitoring of crops. In this work,

	Single-field mean	Single-pixel values	Std. dev. of single-pixel values	Mean single-pixel std. dev.	Relative std. err.	Average relative std. err.
Summer	0.775-0.88	0.412-0.895	0.012-0.68	0.03	0.261-1.555	0.704
Winter	0.1-0.233	0.014-0.397	0.021-0.091	0.039	1.887-11.609	4.638

TABLE 5.2: NDVI values statistics of the individual fields at two representative dates.

Level-1C processed Sentinel-2 images were used, each containing 13 spectral bands representing Top-Of-Atmosphere (TOA) reflectance. In addition to this set of bands, three useful bands containing cloud masks (QA10, QA20 and QA60) are provided.

Regarding data level, atmospheric-corrected L2A data offers better accuracy than L1C data in reflectance estimation, which is important in the agricultural context for example for interpretation of growth patterns and evapo-transpiration monitoring [187]. After weighing the pros and cons, we still preferred to use level-1C data, for a number of reasons. The investigation does not focus on estimated reflectance but rather on NDVI, which is more robust to (moderate) atmospheric bias thanks to its inherent normalization process. Each Level-1C product is composed of a “tile”, i.e. a 100×100 km² ortho-image in UTM/WGS84 projection, containing pixels conveying Top Of Atmosphere (TOA) reflectance values on the 13 bands of Sentinel-2 MSI, and results from the following pre-processing steps:

- Projection of the image in cartographic geometry by using a Digital Elevation Model (DEM);
- Per-pixel conversion from radiance to Top Of Atmosphere (TOA) reflectance values;
- Image resampling to 10, 20 and 60 m depending on the resolution of the spectral bands;

Details on Sentinel-2 multispectral instrument (MSI) are provided in Table 5.3. As mentioned above, the NDVI index is computed based on red and near-infrared bands which, in the case of Sentinel-2 data, translates into band 4 (B4) and band 8 (B8) respectively. At 664.5nm (for S-2A) / 665nm (for S-2B), indeed, B4 fits best the definition of “red band”, and at 835.1nm (S-2A) / 833nm (S-2B) B8 fits best the definition of “infrared band” required for NDVI computation. Both bands come at a spatial resolution of 10 m, hence the resulting NDVI map is generated at such resolution.

5.2.4 Results and discussion

Chemical products are usually leveraged for weed control and fertilization purposes in conventional rice cultivation as they afford increased crop yields, albeit at a cost to the environment. Unlike for conventional rice cultivation, such products in organic farming

Band	Description	Resolution	Wavelength
B1	Aerosols	60 m	443.9 nm (S2A) / 442.3 nm (S2B)
B2	Blue	10 m	496.6nm (S2A) / 492.1nm (S2B)
B3	Green	10 m	560nm (S2A) / 559nm (S2B)
B4	Red	10 m	664.5nm (S2A) / 665nm (S2B)
B5	Red Edge 1	20 m	703.9nm (S2A) / 703.8nm (S2B)
B6	Red Edge 2	20 m	740.2nm (S2A) / 739.1nm (S2B)
B7	Red Edge 3	20 m	782.5nm (S2A) / 779.7nm (S2B)
B8	NIR	10 m	835.1nm (S2A) / 833nm (S2B)
B8A	Red Edge 4	20 m	864.8nm (S2A) / 864nm (S2B)
B9	Water vapor	60 m	945nm (S2A) / 943.2nm (S2B)
B10	Cirrus	60 m	1373.5nm (S2A) / 1376.9nm (S2B)
B11	SWIR 1	20 m	1613.7nm (S2A) / 1610.4nm (S2B)
B12	SWIR 2	20 m	2202.4nm (S2A) / 2185.7nm (S2B)
QA10	Always empty	10 m	
QA20	Always empty	20 m	
QA60	Cloud mask	60 m	

TABLE 5.3: Spectral bands for the Sentinel-2 sensors (S2A & S2B).

are forbidden. We investigated whether such use could be revealed through the analysis of NDVI time series acquired over the previously mentioned study sites. For completeness of information, it is worth mentioning that *Sole* and *Luna* fields employed the Clearfield ([188]) weeding technology, whereas *S.Andrea* fields were treated with selective herbicides. For more details about common weeding practices, see also [189].

Yellowing of weeds consequent to weedkiller application is expected to shift the observed spectral mix away from the high values of NDVI that characterize vegetation. The research question is whether a minority of yellowing weeds mixed with a majority of healthy rice plants on a visible water/mud background is sufficient to push the NDVI value off the range of random variations due to measurement errors.

In trying to answer this question, we first split the GT into separate clusters, each containing one variety. Fields containing the same variety were subject to farming operations on the same dates, so each cluster is composed of homogeneous samples in this respect.

Starting from the *S.Andrea* cluster, in Figure 5.3 the NDVI series for the three fields are reported. It is clearly noticeable a plunge in the mean value of the NDVI in all fields after the application of chemical products for weed management (yellow vertical line). The next measurements were made by Sentinel-2 on 16th Jun, 21st Jun and 26th Jun, i.e., after 4, 9 and 14 days respectively from the weeding date (12th Jun). Visible effects

of the applied weedkiller usually emerge 10 to 20 days after its application; the observed decrease in NDVI matches this time frame, suggesting that the effects do visibly reflect into the NDVI trend.

Proceeding with our analysis, we considered the second cluster of rice fields where the *Luna CL* variety was sowed. The NDVI time series of the six fields are reported in Figure 5.4. Even in this case, we can observe very interesting behaviours. On 14th Jun all fields underwent a weeding treatment; in the following, a similar trend to to the cases of Figure 5.3 is observed, consisting of an analogous plunge in the sequence of mean NDVI values. Not all fields, however, responded with the same pattern. In particular, for fields *Baccanino*, *Baccano* and *Vigna* we can observe a slump in the NDVI values seven days after the treatment of the 14th Jun; a second drop is observed between 26th Jun and 1st Jul (12 and 17 days after treatment respectively). Between the two dates where decreases in NDVI values were recorded (i.e., between 21st Jun and 26th Jun) we can note an increase which, apparently, conflicts with the considerations previously made for the first cluster of fields. It is however important to remember that the natural growth cycle of rice results into a strong, positive contribute to NDVI; weedkillers are becoming increasingly selective, and they do not affect rice vigour significantly anymore.

This particular cluster of rice fields also represents a controversial study case generated by the lack of information. As discussed at the beginning of this chapter, suppression of cloudy pixels resulted into unevenly spaced time sequences; relevant loss of information

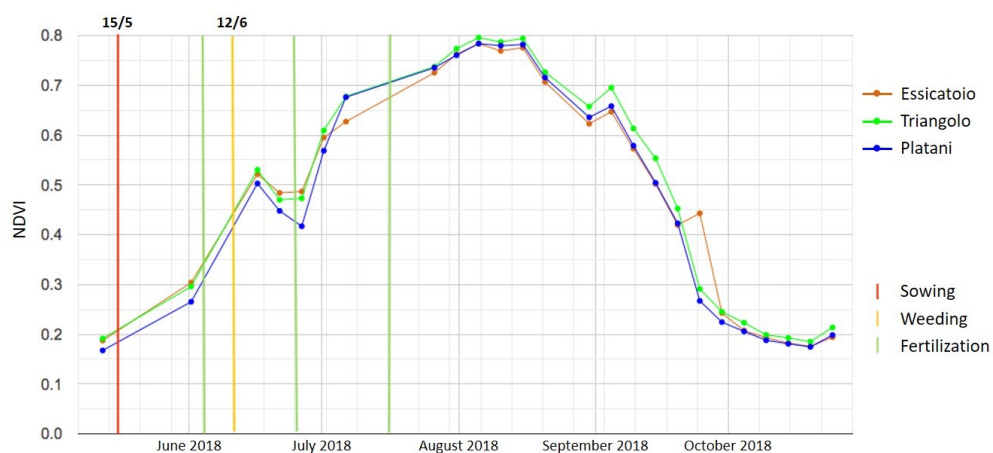


FIGURE 5.3: NDVI time series of all fields sowed with the S. Andrea rice variety. Coloured vertical lines mark the dates where major agricultural operations were carried out.

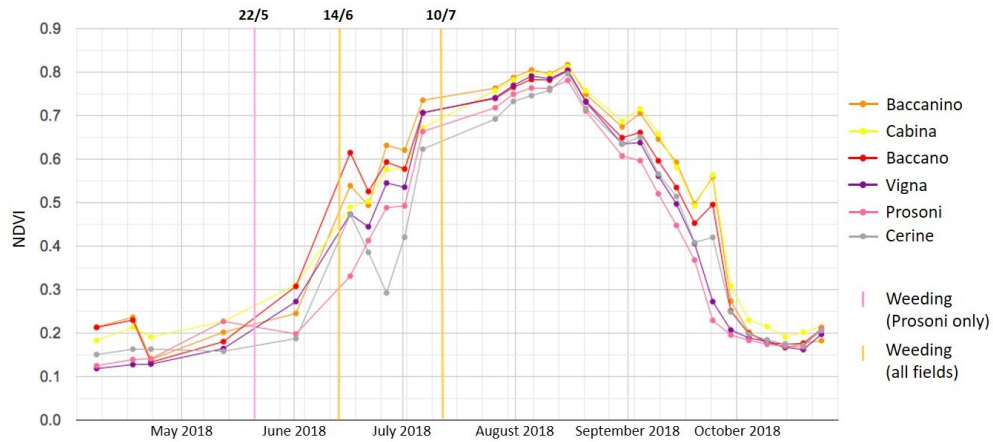


FIGURE 5.4: NDVI time series of all fields sowed with the Luna CL rice variety. Coloured vertical lines mark the dates where major agricultural operations were carried out.

was witnessed between July and August 2018 due to frequent cloud coverage. In Figure 5.4, this issue impacts on the second weeding activity (10th Jul), where the time series presents a gap of 20 days between 6th Jul and 26th Jul due to three cloudy scenes (11th, 16th and 21st Jul) in a row. Such lack of data makes it impossible to draw consistent conclusions regarding possible variations of the NDVI time series caused by the use of chemical products on the 10th of July.

Another interesting aspect of Figure 5.4 is represented by the *Prosoni* field. This rice field is the only one receiving an additional chemical treatment significantly in advance of all the others (vertical pink line on 22nd May). The NDVI mean value decreased between 12nd May and 1st Jun only on this rice field, confirming that a temporary inversion of trend is a good indicator of a weeding treatment, including at an early stage. Moreover, the *Prosoni* NDVI curve remains consistently below the other curves. A reasonable interpretation is if a rice field is treated with weedkillers immediately after the sowing date, the growth of the invasive plants' sprouts is stopped, and the positive NDVI contribution of weeds is consistently missing or reduced on the rest of the sequence. In fact, the plunge consequent to the weeding on 14th Jun is lower on *Prosoni* than on any other field. Another possible factor is the direct effect of the treatment on the rice status.

The last analysed cluster is the one sowed with *Sole* variety. The NDVI time series for each rice field in the cluster are reported in Figure 5.5. Also in this case it is possible to observe trends similar to all previous cases. Weeding treatments were applied on 21st

May only on fields *Orti* and *Pasquale_2* (red vertical line in Figure 5.5); whereas, the next treatments were applied between 11 Jun and 16 Jun (first yellow vertical line) and between 12nd Jul and 13rd Jul (second yellow vertical line) on all fields in the cluster. Once more it is possible to observe a fall of the NDVI value only for fields *Orti* and *Pasquale_2*, while for *Pasquale_1* and *Marcite* the value is respectively almost constant (due to sowing on 24th May) and slightly increased (due to sowing on 17th May). An interesting consequence related to the two latter fields is highlighted after the second, common weeding period (11th Jun to 16th Jun). We can in fact observe that both *Pasquale_1* and *Marcite* NDVI values rapidly decrease after weedkiller application on mid June, due to the decay of greater amounts of weeds in the rice fields; this is not observed in *Orti* and *Pasquale_2* where the first weeding carried out on 21 May had hampered the development of weeds.

Finally, after the second weedkiller application between 12th and 13th Jul, the situation is similar to the second Cluster (“Luna CL” rice variety of Figure 5.4). The frequent cloud coverage in July 2018 prevents observation of the relevant tract of NDVI trend, and we can only guess that the small increase between the last acquisition before weeding, and the first after it, is due to rice.

To add some quantitative data, an evaluation of the cases in Figure 5.5 led to the following results. The average increase of NDVI from emergence to maturity is 0.0875 per month, with a standard deviation of 0.025. Assuming a Gaussian distribution of values, this means that 99% of times the average increase per month lies between 0.1625 and 0.0125 ($\mu \pm 3\sigma$) per month. The average plunge of NDVI after a weeding operation is -0.05, far

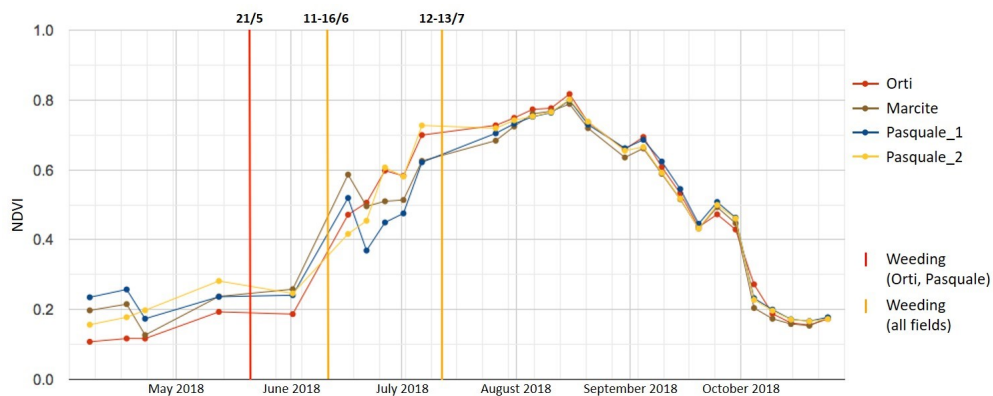


FIGURE 5.5: NDVI time series of all fields sowed with the Sole rice variety. Coloured vertical lines mark the dates where major agricultural operations were carried out.

below the $\mu - 3\sigma$ limit. This suggests the event is detectable by a thresholding operation on each incremental value for a single field.

This work investigates possible methods for satellite-based monitoring of organic crops to enhance their traceability information, with special regards to supporting organic compliance claims. Based on this first analysis carried out on multispectral data alone for a cluster of rice paddy fields in Northern Italy, it is possible to conclude that weeding operations can be detected, as they result in significant deviations from the typical bell-shaped trajectory of the NDVI time series observed on rice fields.

Naturally, an organic field is a very complex system, whose management and monitoring cannot be effectively carried out relying on satellite data alone, even when a multitude of sources are available and frequent revisiting is offered [190]. Organic cultivation involves intricate management strategies and smart handling of contingencies, that may not be reduced to a single, pre-determined model. Human-in-the-loop techniques may help in effective collection of data, especially if organized in a large-scale service under the Copernicus hat [191]. Direct interaction with the managing farmer is still necessary to understand the multifaceted aspects of organic management as it applies to the specific, considered fields.

Notwithstanding the complexity of the problem, it has been demonstrated that space-borne Earth observation has a potential to provide independent support to organic cultivation claims for rice paddy fields. This work is the first in a series, which will investigate visibility of organic compliance from space using different types of remotely sensed data, including radar and passive microwave sensing.

5.3 Tillage assessment using SAR data

In this section is devoted to the presentation of preliminary results towards assessing the type of tillage applied to a cropland, again in the framework of space-based collection of extended traceability information for organic agricultural products. As mentioned in Chapter 2 (Section 2.3.2), a very important aspect that characterizes organic farming is the type of used tillage technique. As a matter of fact, tillage can be performed mainly in two ways, resulting in diverse impacts on soil properties, hence, on SAR backscattered signals; the typical tillage technique used in conventional farming relies on the overturning of big clods, which causes relatively strong backscatter signals due

to volumetric scattering mechanisms. Whereas, in organic farming, the preferred tillage technique is known as “minimum tillage”; in this case, stubble burial and overturning of clods is minimized, hence, the registered SAR backscatter signal is weaker than the previous case, as the volumetric backscatter mechanism is less dominant.

The approach described in this section relies on the link between tillage practice and the resulting level of surface roughness after processing. Minimal tillage induces low levels of roughness, whereas ploughing causes significant roughness, partly mitigated by subsequent harrowing but still significantly higher than for minimal or mild tillage. The typically high sensitivity of radar backscatter to surface roughness of the observed target closes the link with satellite data. To turn this link into an actionable algorithm, a suitable model connecting radar response to surface roughness has to be selected.

5.3.1 Backscattering models

Being related to the acquisition geometry of the SAR system, incidence angle, polarization and wavelength directly affect SAR signals and measurements. However, even the target strongly affects the signal; in fact, all the parameters which are related with the target properties, such as conductivity, water content and geometric characteristics interact with the impinging electromagnetic wave.

In the literature there exist several models that link the measured SAR signal to soil (the target) parameters. These backscattering models can be grouped in three main categories:

- Physical backscattering models;
- Empirical backscattering models;
- Semi-empirical backscattering models.

With respect to the latter two models, physical models provide the most complete and accurate description of the relationship between SAR measurements and target parameters. However, such models are often very complex and difficult to use. For this reason, generally empirical and semi-empirical backscattering models are preferred.

One of the most widely used physical models is the so-called “Integral Equation Model” (IEM) [192]. This model provides the most complete description of the relationship

between the backscattered radar signal, sensor parameters (angle of incidence, polarization, frequency, etc.) and soil-related parameters (dielectric constant, correlation length, standard deviation of surface height, etc.). In general, soil parameters provide an “index of roughness” that allows to evaluate the level of roughness of the soil. The IEM can be in fact used to simulate backscattering values on bare soils and, therefore, its use is suitable in case of agricultural fields before the emergence of sprouts (which is the condition when tillage is applied). The IEM model describes the backscattered SAR signal σ_{pq}^0 as the sum of two terms: a partial signal generated by single reflection (σ_{pq}^S) and a second partial signal generated by multiple reflections (σ_{pq}^M), as shown in Equation (5.2).

$$\sigma_{pq}^0 = \sigma_{pq}^S + \sigma_{pq}^M \quad (5.2)$$

Referring to Equation (5.2), p is the “transmitting” polarization (either vertical V or horizontal H), while q is the “receiving” one (either vertical V or horizontal H). Since most of the natural surfaces are characterized by fairly low roughness values, the fundamental hypothesis of the IEM model is that the whole σ_{pq}^0 is determined only by the single-reflection component σ_{pq}^S . Under this condition, the expression describing the relationship between the backscattering signal, sensor and ground parameters is as follows (Equation (5.3)):

$$\sigma_{pq}^0 = \frac{k^2}{2} e^{-2k_z^2 s^2} \sum_{n=1}^{\infty} s^{2n} |I_{pq}^n|^2 \frac{W^{(n)}(-2k_x, 0)}{n!} \quad (5.3)$$

where $k_z = k \cos \theta$, $k_x = k \sin \theta$ (with θ incidence angle), k is the wave number defined as $k = \frac{2\pi}{\lambda}$ and s is the standard deviation of the surface roughness height. The term I_{pq}^n is function of the incidence angle, the soil dielectric constant and the Fresnel reflection coefficient, while $W^{(n)}(-2k_x, 0)$ is the Fourier transform of the n -th power of the surface auto-correlation function (which may be described by a Gaussian or exponential function, based on the type of soil).

Since the backscatter coefficient is given (i.e., we have the measurement done by the radar satellite), the IEM model is inverted to extract the needed soil parameters. However, this inversion is very difficult, due to its complexity and the high number of soil variables that have to be known or hypothesized.

An empirical model which is based on the IEM is the Oh model [193]. This model was generated based on a very large dataset made of a wide variety of soils with different dielectric constant values and roughness levels. Specifically, the Oh model analyzes the interaction between the so-called “cross-polarized” ratio, defined as $q = \frac{\sigma_{HV}^0}{\sigma_{VV}^0}$, and soil parameters (and also acquisition geometry parameters). The authors showed the very low sensitivity of the model in terms of water content of the soil, while, on the other hand, the ratio q was found to be very sensitive to the roughness of those types of soil, regardless of their water content. The mathematical expression of the Oh model is reported in Equation (5.4):

$$q = \frac{\sigma_{HV}^0}{\sigma_{VV}^0} = 0.23\sqrt{\Gamma_0} \left[1 - e^{-ks} \right] \quad \text{with} \quad \Gamma_0 = \left| \frac{1 - \sqrt{\epsilon_r}}{1 + \sqrt{\epsilon_r}} \right| \quad (5.4)$$

where k is the wave number, s is the standard deviation of the surface roughness height, ϵ_r is the relative dielectric constant of the soil and Γ_0 is the Fresnel reflectivity coefficient (at nadir). The Oh model also provides an expression for the “co-polarized” ratio $p = \frac{\sigma_{HH}^0}{\sigma_{VV}^0}$. Notwithstanding the easier mathematical form compared to the IEM, this model requires both polarimetric SAR data and soil parameters, which makes this model hardly employable.

The model described in [194], namely, the Dubois model, is an empirical model that reduces the number of soil-related variables to only two: dielectric constant (as a function of water content) and standard deviation of the surface roughness height; the main advantage of this model is that the correlation length is not involved, as it represents a soil parameter particularly difficult to accurately measure (and is affected by the measure itself). Equations (5.5) and (5.6) define the Dubois model for HH- and VV-polarized signals:

$$\sigma_{HH}^0 = 10^{-2.75} \frac{\cos^{1.5} \theta}{\sin \theta^5} 10^{0.028\epsilon \tan \theta} (ks \sin^{1.4} \theta) \lambda^{0.7} \quad (5.5)$$

$$\sigma_{VV}^0 = 10^{-2.35} \frac{\cos^3 \theta}{\sin \theta} 10^{0.046\epsilon \tan \theta} (ks \sin^3 \theta)^{1.1} \lambda^{0.7} \quad (5.6)$$

where θ is the incidence angle, ϵ is the real part of the dielectric constant of the soil, s is the standard deviation of the surface roughness height, k is the wave number and λ is

the wavelength in [cm].

Since VH signals are weaker than VV ones over bare soils, the Dubois model did not provide a description for cross-polarized data. Moreover, the model does not account for the topology of the area of interest, and the fact that does not consider the correlation length of the surface reduces its reliability.

In [195] an improved version of the Dubois model is provided. With this empirical model, namely the Baghdadi model, strong over- or under-estimations of radar backscattering coefficients observed with the Dubois model according to soil moisture, surface roughness and incidence angle are clearly eliminated. Moreover, the Baghdadi models provides with a description of cross-polarized signals, such as HV. The set of the new expression defining the model is defined by Equations (5.7), (5.8) and (5.9).

$$\sigma_{HH}^0 = 10^{-1.287} (\cos \theta)^{1.227} 10^{0.009 \cot(\theta)m_v} (ks)^{0.86 \sin(\theta)} \quad (5.7)$$

$$\sigma_{VV}^0 = 10^{-1.138} (\cos \theta)^{1.528} 10^{0.008 \cot(\theta)m_v} (ks)^{0.71 \sin(\theta)} \quad (5.8)$$

$$\sigma_{HV}^0 = 10^{-2.325} (\cos \theta)^{-0.01} 10^{0.011 \cot(\theta)m_v} (ks)^{0.44 \sin(\theta)} \quad (5.9)$$

In [196], a significant difference was highlighted between the measured backscatter values and those simulated via IEM. This is mainly related to the correlation length parameter, difficult to measure with sufficient accuracy. The Authors then built a semi-empirical model replacing field-measured correlation length with a fitting parameter (L_{opt}), which depends on surface roughness (s) and radar configuration (angle, polarization, frequency, etc.). Subsequent studies confirmed better estimation of backscatter values using such parameter, as it ensured a good fit between the backscattering coefficient provided by the SAR sensor and the backscattering coefficient simulated by the IEM model.

Notwithstanding the validity of the presented backscattering models, they all present some limitations. First, they all require numerous input parameters, related to both radar sensor and soil surface. Therefore, the precise analysis of the relationship between actual surface roughness and SAR signal is not trivial and several errors and discrepancies are introduced. Moreover, these models are often difficult to invert and, as a consequence, soil parameters are non easily obtainable. Finally, many soil parameters are often very

difficult to measure accurately in situ (e.g., the correlation length), leading to significant differences between the measured and simulated backscatter coefficients.

An improved version of [196] was finally selected for this work, i.e. a semi-empirical model [67] combining the effects of surface roughness s and correlation length CL . It models the backscatter coefficient based on a single roughness parameter, $Z_S = Hrms^2/CL$. Z_s is the product of s times the ratio s/CL , which represent a slope factor [197]; the intuition behind this parameter is to introduce a slope effect for σ^0 estimation. The authors identified a strong correlation between Z_s and the measured backscatter coefficients σ_0 . The use of a single surface roughness parameter that strongly correlates with the IEM physical model and the straightforward inversion permitted by its relatively simple mathematical form were the key factors in selecting this model as visible from its expressions in Equations (5.10) and (5.11):

$$\sigma_{VV}^0 = 0.5 (kZ_s)^{0.84} \frac{\cos^4 \theta}{\sin^3 \theta} \alpha_{VV}^2 \quad (5.10)$$

$$\sigma_{HH}^0 = 3.2110^{p(\theta)} (kZ_s)^{q(\theta)} \frac{\cos^4 \theta}{\sin^3 \theta} \alpha_{HH}^2 \quad (5.11)$$

with

$$\alpha_{HH} = R_{\perp} = \frac{\cos \theta - \sqrt{\epsilon_r - \sin^2 \theta}}{\cos \theta + \sqrt{\epsilon_r - \sin^2 \theta}} \quad (5.12)$$

$$\alpha_{VV} = (\epsilon_r - 1) \frac{\sin^2 \theta - \epsilon_r(1 + \sin^2 \theta)}{[\epsilon_r \cos \theta + \sqrt{\epsilon_r - \sin^2 \theta}]^2} \quad (5.13)$$

where R_{\perp} is the Fresnel coefficient for HH polarization, ϵ_r is the dielectric constant (real part), k is the wave number defined as $k = 2\pi/\lambda$ and θ is the incidence angle. Finally, the polynomials $q(\theta)$ and $p(\theta)$ are function of θ and are defined as $q(\theta) = 2.6289\theta^2 - 3.2561\theta + 1.969$ and $p(\theta) = 2.303\theta^2 - 2.3217\theta$.

For this work VV-polarized SAR data was used, so the backscatter coefficient σ_{VV}^0 is the input and the inversion of (5.10) is straightforward:

$$Z_s = \left[\sigma_{vv}^0 \frac{\sin \theta^3}{\sin \theta^4} \frac{1}{k^{0.84} 0.5 \alpha_{vv}^2} \right]^{\frac{1}{0.84}} \quad (5.14)$$

where Z_s , the final roughness parameter, is measured in [cm].

5.3.2 Data and case study

5.3.2.1 Data

In this work, we leveraged Copernicus' free and open data policy in using Sentinel-1 SAR data. The reader is referred to Chapter 3, Section 3.3, for a deep description of these data.

In this work the focus was the analysis of surface roughness based on time series of VV-polarized data acquired in Interferometric Wide Swath (IW) mode. As schematically reported in Figure 5.6, for each case study described in the next section, the multitemporal image collection covering the whole calendar year is loaded in Google Earth Engine. The selected data undergo several pre-processing steps, including application of orbit file, GRD border noise removal, thermal noise removal, radiometric calibration and terrain correction (orthorectification) using SRTM30, or ASTER DEM for regions located at more than 60° latitude. Pre-processing are directly performed by the Google Earth Engine cloud computing platform [198]. More details on typical trends for SAR reflectivity in rice paddy fields can be found in [49].

Next, the spatially averaged value of computed backscatter coefficients σ_{VV}^0 is computed over each single crop field at each given date. A typical example of σ_{VV}^0 time sequence over a rice paddy field is reported in Figure 5.7. Based on the computed σ_{VV}^0 time series, the maximum value along time is derived, and used as input in (5.14) to derive Z_s . As a matter of fact, the peak of backscatter intensity recorded during the season is likely caused by the tilled soil, whose roughness after such operation reflects into stronger scattering than other soil conditions, including fully emerged rice.

The incidence angle θ was computed on each parcel based on the geometric parameters of the maximum-backscatter SAR image selected as described above. The last critical soil-related parameter is the dielectric constant; as for soil roughness, relative permittivity also affects the overall backscattered SAR signal. The dielectric constant is in turn

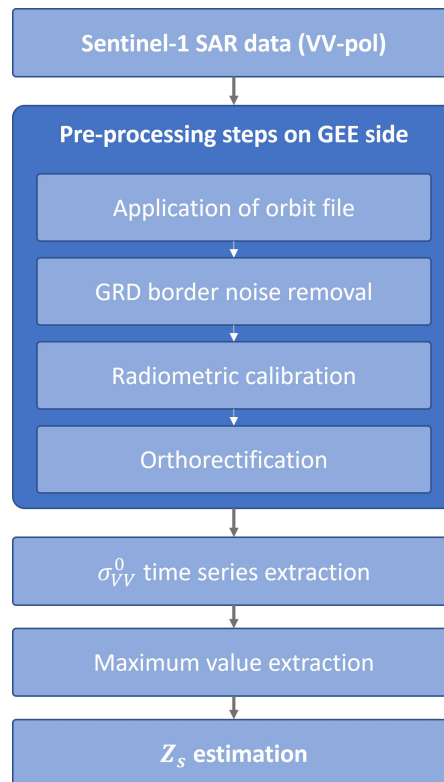


FIGURE 5.6: Procedure for the extraction of the roughness index parameter Z_s .

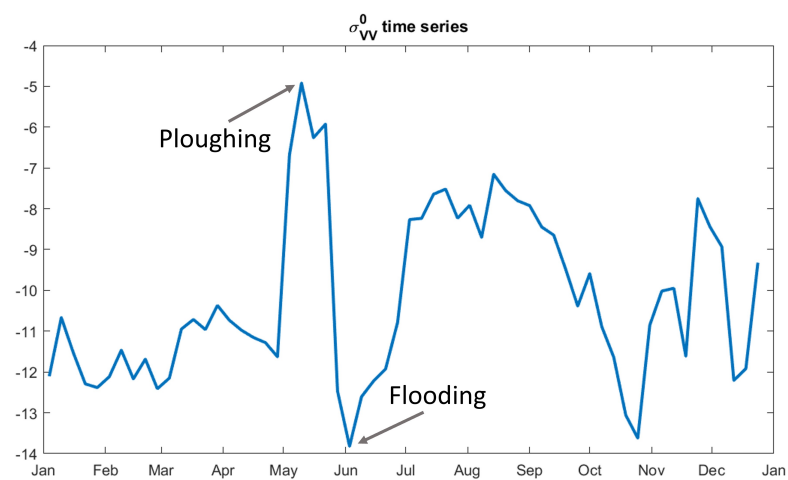


FIGURE 5.7: Typical paddy field SAR backscatter time series. Vertical axis values are in dB.

affected by wetness condition of the soil (for example, the dielectric constant decreases as the soil becomes dry). For this reason, estimating dielectric constant values using SAR data is not trivial, as inversion of backscattering models is required, and change detection techniques are needed to derive soil moisture from SAR data.

Since a more rigorous activity on dielectric constant retrieval cannot fit in the present thesis work, for this preliminary study on surface roughness estimation we decided to fix the dielectric constant value. Based on findings from the related scientific literature, we set $\epsilon_r = 50$, as this was the value estimated for rice fields using dual-pol (VV, VH) Sentinel-1 SAR data [199, 200]. The methods described in the articles showed an acceptable agreement between the estimations made using SAR data and in situ measurements made with a Ground Penetrating Radar (GPR), a technology used for measuring pavement layer thickness.

5.3.2.2 Case study

The utilized study site is described in Section 5.2.2 and depicted in Figure 5.2. Thanks to our collaboration with local farmers, in this area we identified 14 paddy fields managed with traditional approaches in year 2018 and we built a GIS layer with polygons describing field boundaries. These polygons were ingested in the Earth Engine platform and used to select Sentinel-1 data from solar year 2018. This dataset was the basis for building the related σ_{VV}^0 time series, detecting the tillage period by identifying a local reflectivity maximum in spring, considering the corresponding σ_{VV}^0 and deriving Z_s from it using the model as described in Equation (5.14). Results are summarized in Table 5.4.

Referring to Table 5.4, it can be noted that maximum backscatter values are generally around -5.7 dB, corresponding to roughness parameter values around 0.0747 cm. Such value of Z_s is consistent with those in [197], where the authors showed that Z_s ranges from 0.068 to 1.92 cm for bare farmland; please note that despite being expressed in [cm] unit, as defined by the underlying maths, the value expressed by Z_s should not be interpreted as a physical length.

For sake of comparison the model was also applied to two very different land cover classes, namely urban areas and water. 14 more polygons in the case study area were identified for each of these latter classes, and the same procedure was applied to these polygons.

ID	σ_{VV}^0	Z_s	Date	ID	σ_{VV}^0	Z_s	Date
0	-6.47	0.057	16 Apr	7	-4.95	0.094	4 May
1	-5.81	0.069	16 Apr	8	-4.00	0.110	4 Apr
2	-5.35	0.076	16 Apr	9	-4.51	0.104	4 May
3	-6.58	0.057	16 May	10	-5.61	0.072	16 Apr
4	-5.15	0.084	16 Apr	11	-5.96	0.067	16 Apr
5	-5.46	0.078	4 Apr	12	-5.93	0.070	4 May
6	-6.94	0.056	4 Apr	13	-7.11	0.050	4 Apr

TABLE 5.4: Roughness parameter estimation for each rice field. σ_{VV}^0 max is the maximum backscatter coefficient of the entire times series in decibels [dB], Z_s is the surface roughness parameter in centimeters [cm] and the “Date” column reports the date at which the maximum backscatter value was registered along the rice growth season (year 2018).

The statistics of Z_s values for the three classes are reported in the boxplot in Figure 5.8. Some interesting facts can be noted:

1. standard deviation for the analysed rice paddy fields is smaller than for other classes; this is consistent with the fact that all fields are managed under traditional agricultural practices, which include ploughing and harrowing;
2. the three classes are completely separated, even considering outliers (see max and min of each class in Fig 5.8);
3. on the Z_s axes, classes appear in an order which is consistent with the levels of complexity of surface shape (largest for urban, smallest for water bodies)

Current results are not sufficient to support classification of tillage type based on the identified model, because no counter-examples with minimal tillage were available. Yet Z_s values obtained on sample fields are consistent with literature, and encourage to further pursue the objective by collecting additional ground truth data including on organic-run rice paddy fields.

5.3.3 Preliminary conclusions

In this work, some preliminary steps towards assessing the type of tillage applied to a given farmland parcel are presented, in the framework of space-based collection of

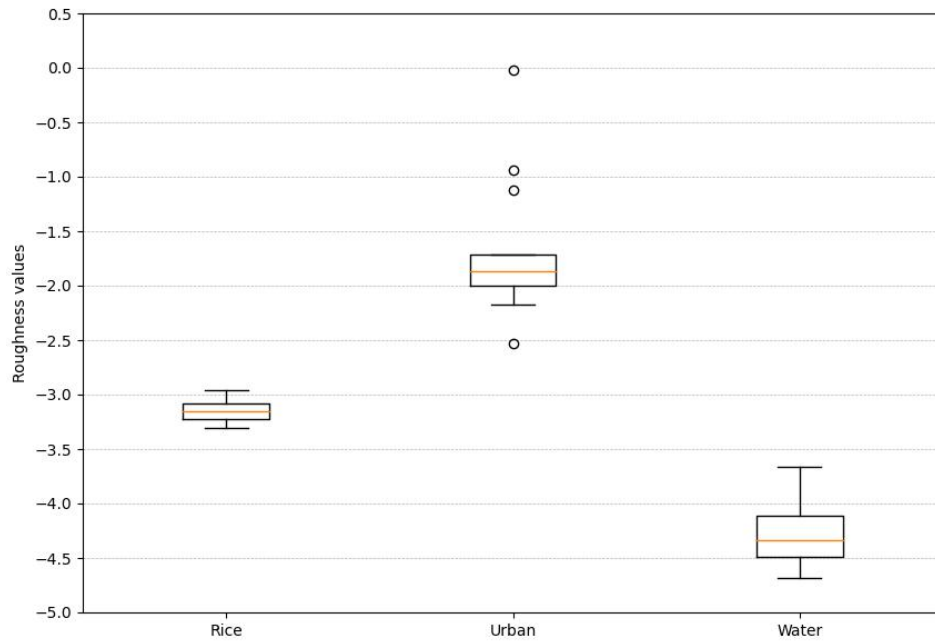


FIGURE 5.8: Boxplot of roughness values Z_s for paddy fields, urban areas and water. Z_s is in \log_{10} units for clearer visualization.

extended traceability information for organic agricultural products. A suitable model has been identified that links radar backscatter to post-tillage surface roughness. This latter provides clues regarding the approach adopted in tillage, a key selection in organic agriculture practices. Experiments were conducted using Sentinel-1 data on a group of rice paddy fields in Northern Italy, and on other land cover classes for comparison. Results suggest that the model is effective in retrieving surface roughness at key dates, and it represents a good starting point for further investigation. The next planned development steps will include combining different sources of radar data on the same areas; by doing so, it is expected both accuracy and reliability of roughness estimates will increase significantly. Moreover, a larger pool of samples will help determine separability of different tillage techniques, representing an important piece of information in the context of high-tier organic food traceability.

5.4 Detection of fertilization operations using multispectral data

5.4.1 The Joint Research Centre (JRC) “Geospatial Intelligence Against Nitrate Pollution” (GEOINT) project

The issue of nutrient pollution from agriculture has been an ongoing challenge for decades [201]. In particular, the use of nitrogen (N) fertilizers can result in losses of nitrate (NO_3^-) to surface and groundwater and emissions of nitrous oxide (N_2O) and ammonia (NH_3) to the atmosphere, contributing to climate change and poor air quality.

In the European Union (EU), policies have been developed that aim at addressing nutrient pollution from agriculture. Policies have also been developed that have indirect effects on nutrient pollution, for instance, by protecting ecosystems and habitats. Other regulations came into force, in order to ensure that the nutrient cycle is managed in a more sustainable and efficient manner.

One of the most important countermeasures against nutrient pollution implemented in Nitrate Action Programmes (NAPs) are the so-called “fertilizer closed periods”. Closed periods are specific time periods along the year when the use of fertilizing products (either organic or inorganic) is prohibited, with the aim of reducing losses of NO_3^- . This countermeasure is useful since there are specific periods during the year when losses of Nitrogen are more likely; such periods occur when the terrain contains significant amounts of soluble nitrogen, i.e., when the water content in soils exceed a certain threshold, above which water cannot be retained anymore (or lost through evapotranspiration). Generally, these conditions are caused by heavy rainfall periods, occurring in low-temperature seasons, during which agriculture is limited and farmlands are bare. Such conditions match the ones characterizing winter months, thus representing the most risky period. Hence, prohibiting the application of nitrogen-based fertilizers during winter helps avoiding N losses and limit N_2O emissions. In [202] it has been shown that closed periods help in reducing risks of organic material run-off, N_2O and NH_3 emissions.

Given this context, the Joint Research Centre (JRC) Geospatial Intelligence Against Nitrate Pollution (GEOINT) project aims at assessing whether farmers comply with the regulations described above (closed periods) or there are infringement cases, using satellite technologies. Specifically, the idea of this project is to leverage spaceborne EO

data to detect cow manure applications during winter months, when nitrates leaching is more likely.

The next Sections are devoted to analyze the potential of multispectral satellite data in detecting cow manure applications over agricultural fields, within the framework of the GEOINT project.

5.4.2 Scientific literature review on manure detection using spaceborne data

While reviewing the state-of-the-art methodologies for spotting out manure application over agricultural fields, we faced both a criticality and an opportunity. On the one hand, scientific literature strictly focussing on the problem turned out to be definitely scarce, on the other hand some similar problems are known in the remote sensing arena and former knowledge can be leveraged to develop new methodologies and applications, useful to the satellite remote sensing community. Both aspects are treated in this Section.

Scientific papers specifically addressing the problem of satellite-based detection of manure application are very few. The most relevant single paper encountered in the literature review was one by Dodin et al. [63], which aimed at monitoring both frequency and location of exogenous organic matter (EOM) applications on farmland. EOM applications, despite being typically unreported, generate relevant impacts both in agronomic terms (e.g., yield potential, soil carbon storage) and ecological terms (e.g., pollution from nitrate leaching and ammonia volatilization).

In the cited work, the Authors evaluated the potential of Sentinel-2 data for detecting EOM amendments, such as Green Waste Compost (GWC) and livestock manure. In particular, the spectral shift resulting from GWC and manure application was investigated. To this aim, multispectral Sentinel-2 image pairs were analysed before and after EOM application over six crop fields in the Versailles Plain, France. Results showed that multitemporal Sentinel-2 series report significant spectral differences before and after application events.

A significant decrease in reflectance values in the visible and near-infrared (NIR) regions of the electromagnetic spectrum was indeed observed after EOM spreading. With reference to Table 5.3 that contains nomenclature and information related to all Sentinel-2 bands, it was observed that the largest reflectance decrease occurred for bands B8 (NIR)

and B8A (Red Edge 4), whereas the smallest decrease occurred in band B12 (SWIR 2). The plot in Figure 5.9 shows such decrease of reflectance values before (on 25 Jul) and after (on 2 Aug) a manure treatment which took place on the 28th of July.

The Authors then developed a more specific approach by defining five tailored Exogenous Organic Matter Indices ($EOMI_{1...5}$), whose performances were then evaluated individually:

$$EOMI_1 = \frac{B_{11} - B_{8a}}{B_{11} + B_{8a}} \quad (5.15)$$

$$EOMI_2 = \frac{B_{12} - B_4}{B_{12} + B_4} \quad (5.16)$$

$$EOMI_3 = \frac{(B_{11} - B_{8a}) + (B_{12} - B_4)}{B_{11} + B_{8a} + B_{12} + B_4} \quad (5.17)$$

$$EOMI_4 = \frac{B_{11} - B_4}{B_{11} + B_4} \quad (5.18)$$

$$NBR2 = \frac{B_{11} - B_{12}}{B_{11} + B_{12}} \quad (5.19)$$

In terms of performances, the study showed the $EOMI_2$ index, defined by Equation (5.16) yielded the largest statistical distance (based on the Euclidian distances computations made between the before and after indices values distributions). This means that the

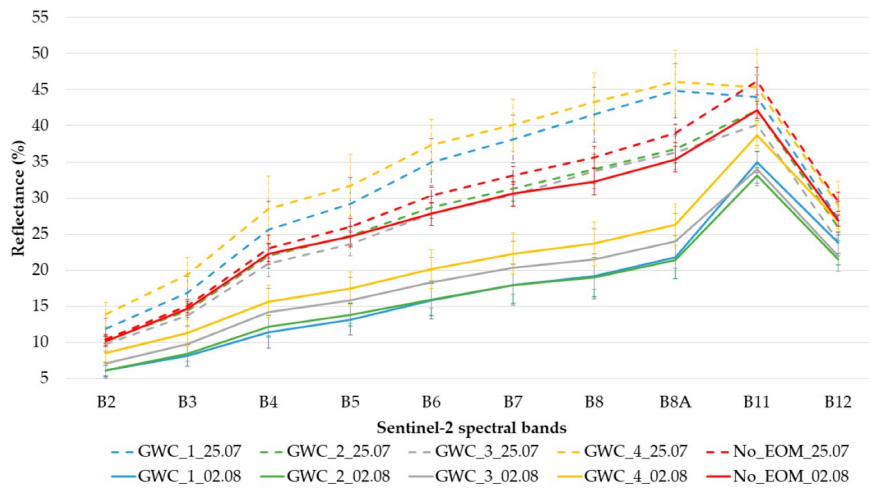


FIGURE 5.9: Reflectance values decrease after EOM treatment over five sites (four with GWC and one without EOM treatment). Image source: [63]

EOMI₂ index was the one that better discriminated fields with and without EOM spreading. The boxplot in Figure 5.10 shows the EOMI₂ for each field's set of pixels before and after EOM spreading.

From the plot of Figure 5.10, it is possible to observe that EOMI₂ values increases after the EOM treatment (in case of GWC). Moreover, the index is very low for the “control field” (the one without EOM amendment, named No_EOM) for all three dates, with a mean value of 0.1.

Regarding the applications of cattle manure (CM), two treated field have been analyzed in this work. As for the GWC case, reflectance values decreased both in the visible and NIR spectrum regions after manure application (as depicted in Figure 5.11).

Note that both CM fields were treated with manure, but the CM_1_Tilled was also tilled and sowed. As shown in Figure 5.11, in the case of the tilled field, the largest reflectance decrease occurs for bands B8 and B8A; whereas, the largest increase occurs for band B12. Another interesting finding of the work is related to the fact that, in the case of GWC and sheep manure, these EOM treatments can be detected at a minimum rate of 15 t/ha (when EOM is placed on the surface of the field and not buried).

Another interesting study that emerged from the scientific literature is reported in [203]. Here the authors propose a method that aims at using remotely sensed data for detection

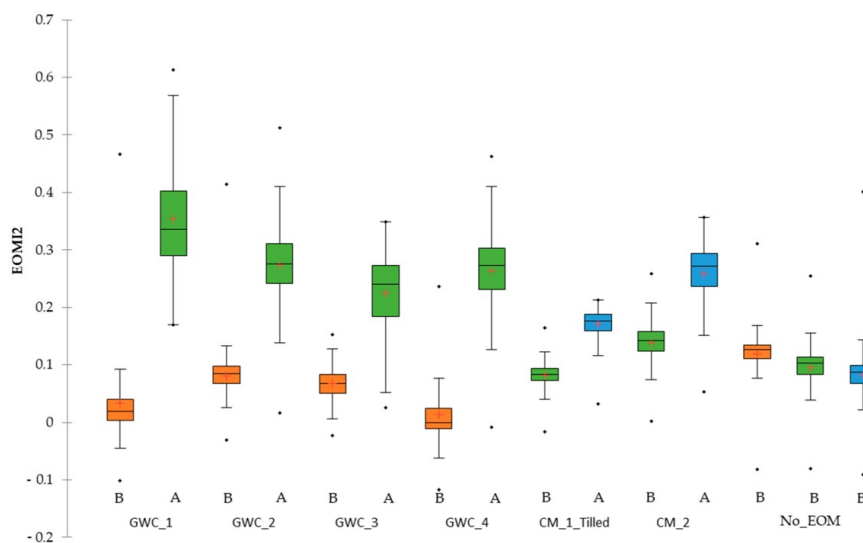


FIGURE 5.10: Boxplots of EOMI₂ pixels values before (B) and after (A) EOM spreading. The Sentinel-2 acquisition dates are 25 Jul (orange), 2 Aug (green) and 4 Aug (blue). Image source: [63]

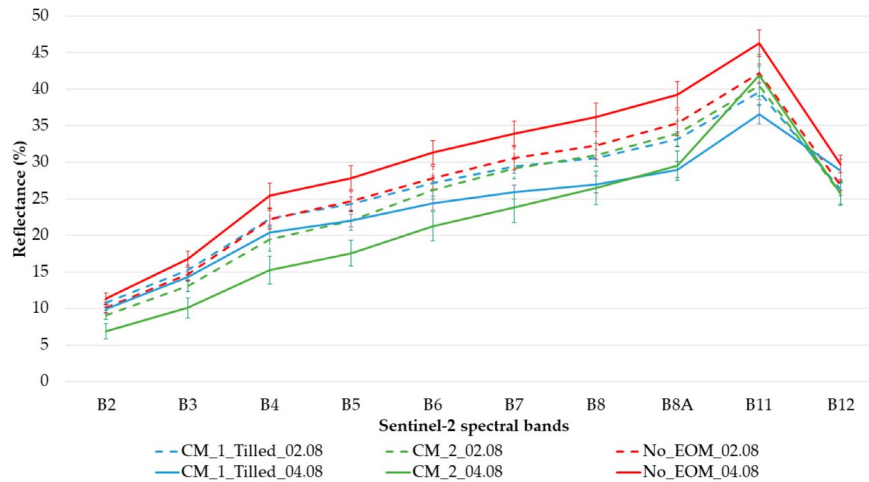


FIGURE 5.11: Mean reflectance of sample fields before (2 Aug) and after (4 Aug) cattle manure application. Image source: [63]

of environmentally hazardous cattle-breeding facilities in the Caserta Province, Southern Italy.

Pollutants generated by manure, litter and process wastewater can negatively affect human health and the environment. As a matter of fact, many diseases found in manure are easily transferrable to humans, including Salmonellosis, Tuberculosis and Leptospirosis. Such an environmental condition is particularly relevant to the Caserta Province, due to the high number of buffalo breeding facilities.

In this work, both optical and SAR data were employed. The optical data comes from the GeoEye-1 (0.5 m spatial resolution after pan-sharpening), whereas COSMO-SkyMed satellite (3 m spatial resolution) was used as the SAR source of data. As depicted in Figure 5.12, the methodology relies on the detection of two main classes: manure areas and metal roofs (of the facilities). The choice of these two classes comes from the need to identify new facilities that are unknown to the official census, as the number of unregistered buffalo breeding farms is increasing in the study region.

The methodology aims at discriminating the two classes mainly based on their spectral content. On the other side, SAR data was used to reduce false positive occurrences over highly urbanized areas. This may not be relevant to our case, where farmland can be assumed to have been mapped accurately, and the problem is just to detect manure application. Binary decision trees were used to classify the two different materials. The choice of using such binary trees was an improvement of [204], where the same authors



FIGURE 5.12: Typical buffalo breeding farm. Yellow boxes contain manure areas, whereas green boxes represent metal roofs. Image source: [203]

of this work used a maximum likelihood classifier based on Gaussian models that worked on many different classes. This choice made it possible to reduce the cost of data and to simplify the design of the algorithms. The decision tree classifier performs multistage classifications using different binary decisions in order to assign each single pixel to one of the two classes. To further improve classification performances, false positive occurrences were filtered out based on the following criteria:

- Removal of regions smaller than 8000 m^2 in the case of roofs;
- Removal of regions smaller than 800 m^2 in the case of manure.

An example result of this work can be observed in Figure 5.13.

The result showed in Figure 5.13(d) was then used in a GIS system to verify whether a recognized farm matches with an entry of the cadastral database or not. In the latter case, the farm is labelled as “unregistered”, and an in-situ verification procedure is activated.

5.4.2.1 Target Detection in Hyperspectral data

Section 5.4.2 focussed on methods specifically developed for manure detection. Other approaches are however possible, leveraging existing solutions to more general problems that can be applied, either as they are or adapted to the specific problem. For example, detection of manure from space can be potentially tackled by target detection techniques,

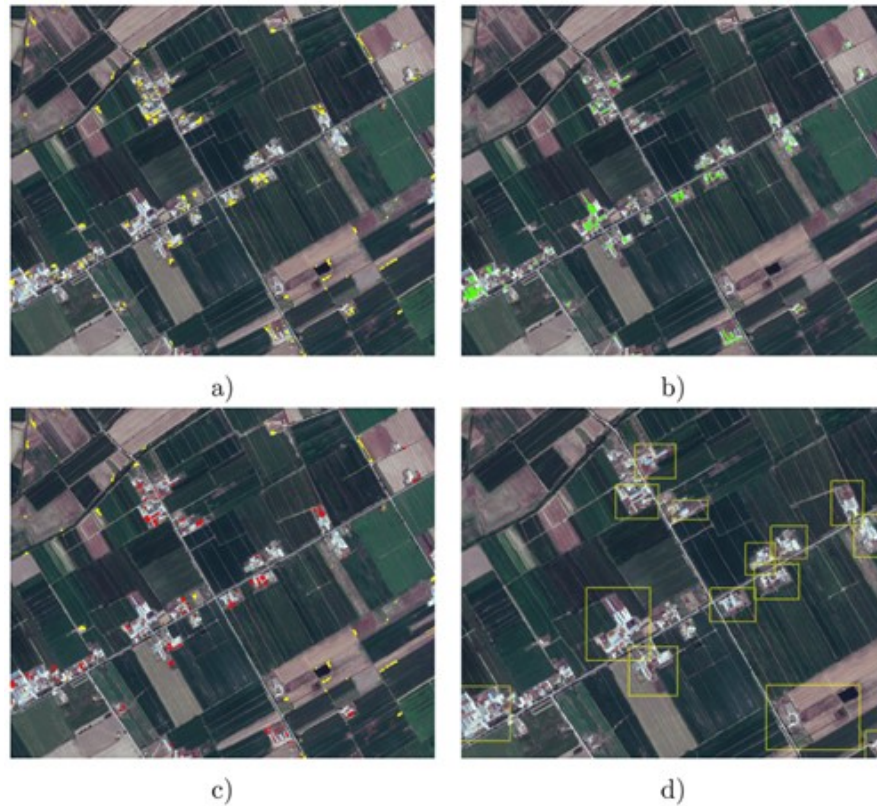


FIGURE 5.13: Classification product based on the described work and intermediate results. a) shows the detection of manure areas. b) shows the detection of metal roofs. In c) the detected manure areas were filtered based on a proximity analysis applied on metal roofs. Finally, in d) photointerpretation was carried out to recognize buffalo breed facilities.

as such task can be reduced to the identification of just two classes: manure (the “target”), and non-manure (the “background”). Target detection is a very specific class of problems in Remote Sensing that usually involves hyperspectral data. The goal of target detection methods is to identify a specific spectral signature, among many, non-interesting other ones in the scene. In our case, the target class is manure.

Detection algorithms and hyperspectral images are used in several contexts, such as environment monitoring, mining, geology, soil and vegetation characterization and agriculture [205]. In the case of agriculture, spectral signatures of vegetation allow to monitor crops health (e.g., stress by pests, diseases, and nutrient deficiencies). Such monitoring, however, it is not straightforward due to the high spectral variability of targets and background. The problem related to how to model the spectral variability can be addressed by two main approaches: statistical models (which describe the background patterns statistically) and geometric models (which describe the background patterns geometrically).

The first category contains the following state-of-the-art algorithms:

- Adaptive Coherence Estimator (ACE). This is a model based on the main assumption that the background covariance matrix is known, allowing greater separation between target and background while suppressing false alarms [206];
- Constrained Energy Minimization (CEM). The CEM is filter with a finite impulse response, that is capable to minimize the energy of the resulting output generated by the background, allowing the target to be detected [207];
- Matched Filter (MF). The MF algorithm is based on the binary hypothesis test (background and target having the same covariance matrix) and is widely involved in target detection applications that use hyperspectral data [208].

The second category includes:

- Orthogonal Subspace Projection (OSP). This algorithm allows to remove the response of non-target pixels and applies a filter to find matches with the desired target. OSP uses a structured background model to characterize the spectral variability [206];
- Spectral Angle Mapper (SAM). The SAM algorithm is another widely used algorithm that allows to evaluate how similar are two spectra, by computing the angle between target and background vectors. It has low computational complexity and cost and is faster with respect to the other models [209].

In [205] it has been demonstrated that the ACE statistical model had the best performance in terms of spectral variability modelling of target and background.

Nowadays, the use of Machine Learning (ML)-based nor Artificial Intelligence (AI)-based approaches is proposed for almost every problem, including in Earth observation. We did not consider to use them in this case because they would need large amounts of positive and negative samples to train the algorithms; since collecting ground truth information is difficult and very little of it is available, we estimate training-dependent approaches are ineffective in this context. We thus decided not to further investigate this type of possible solutions.

The analysis carried out in these two last sections revealed an almost absolute lack of exhaustive work in this area; no relevant methodologies or established algorithms that can be used in a straightforward manner have been found during our investigation. Although no ready-to-use solution apparently exists, considering the clues that were collected, mediating them with our expertise and the specific features of the target class, our educated guess is methods [63] and [203] may be the best starting point to tackle the problem. As a matter of fact, these papers provide hints on how to leverage the spectral information of manure in order to detect it from space.

The next steps of this work will therefore focus on a pair of identified study cases, where the exact date of manure application was registered, and leverage the contents of the above-cited papers to further develop the methods and test their effectiveness. Specifically, the analysis will focus on the spectral shift caused by the transition from bare or vegetated soil towards manure cover, exploiting mainly Sentinel-2 multispectral data. It is worthwhile to add that neither of the above mentioned papers considered temporal information; very low revisit time satellites would enable to leverage very dense image time sequences to spot sudden changes in time over crop fields. future works are expected to experiment with time-dense sequences subject to availability of relevant satellite data.

5.4.3 Development of a manure detection methodology

This Section presents the proof of concept for a method aimed at detecting manure application from multispectral Earth observing satellite data, and discusses a case study where such method is applied. The size of the sample set used for the case study is very small, but results appear to be convincing nonetheless. The limited amount of samples is due to the difficulty in obtaining suitable ground truth information, which is not public, not frequently disclosed, and perishable if not collected at the time of production. Specifically, two case studies are presented to illustrate the grounds for the proposed methodology and support their relevance to the intended goal.

The two case studies consist of two crop fields for which manure application dates are known. As depicted in Figure 5.14(a), both sites are located in in the Lombardy region of northern Italy. The first field of interest, named FOI₁ from now on, has a size of 1,744 m^2 (0.1744 hectares) and is located in the Varese province (Figure 5.14(b)). This field consisted of bare soil at the time it was covered with manure on the 12th of April 2022.

The second crop field, named FOI₂ and reported in Figure 5.14(c), has a size of 32330 m² (3.23 hectares) and is located in the Pavia province. The field was characterized mainly by bare soil with sparse vegetation (grass) before manure application on the 31st of March 2022.

5.4.3.1 Analysis with Sentinel data

The methods identified from the literature leverage multispectral satellite data, and Sentinel-2 was the most obvious choice to replicate them. In fact, as described in Section 5.2.3, the Copernicus mission named Sentinel-2 consists of a satellite constellation made of two 180-degree phase-shifted units (Sentinel-2A and -2B), capable to produce fresh high-resolution (10 m) data every three to five days over any given location at mid-latitude. This short revisit time enables near-real-time monitoring of crop growth as well as other applications requiring regular and frequent re-acquisition. Each satellite is equipped with a multispectral instrument measuring radiance on 13 spectral bands, whose features are summarized in Table 5.3.

The spatial resolution ranges between 10 m and 60 m, depending on the considered band. In this work, we used Sentinel-2 Level-2A products obtained through the Google

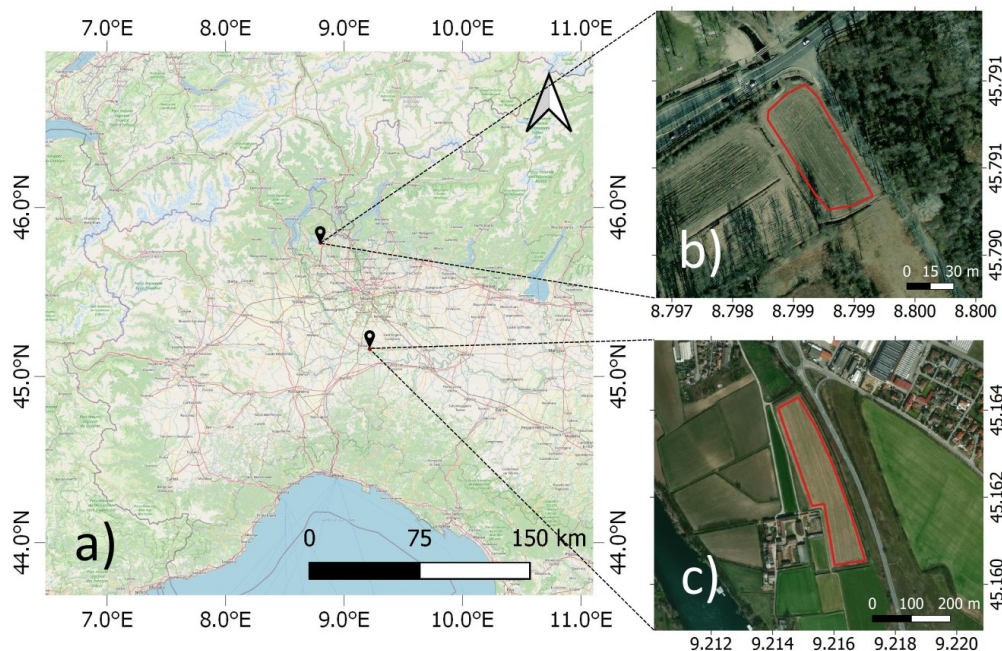


FIGURE 5.14: Test sites used to develop the manure detection algorithm.

Earth Engine geospatial cloud computing platform. Data at level L2A, derived from L1C products, are atmospherically corrected and provide estimates of surface reflectance values (Bottom-of-Atmosphere, or BOA, data). To analyze the effects on the spectral shifting caused by the transition from other agricultural land cover classes, such as bare soil or vegetation, to manure cover, we used pairs of images acquired before and after manure application, selecting the closest possible dates to manure application. Specifically, for FOI₁, the cloud-free Sentinel-2 L2A images closest to the manure spreading date were acquired on 11th April 2022 (before manure application) and on 16th April 2022 (after manure application). Whereas, for FOI₂ we selected images on the 22nd March 2022 (before manure application) and 11th April 2022 (after manure application), using the same criteria.

As it can be observed from Figure 5.15, after the application of manure, reflectance values for both the analyzed fields decreased significantly in different regions of the electromagnetic (EM) spectrum, especially in the NIR region. In fact, the NIR band (band B8 of Sentinel-2), experienced a decrease of about 8.2% and 22.8% in fields FOI₁ and FOI₂, respectively, which correspond to the strongest decreases along both spectral signatures. The smallest decrease was recorded in band B2 (Blue) - which basically remains unaltered - and in band B5 (Red Edge 1) for FOI₁ and FOI₂, respectively. Whereas, for both fields, the reflectance value of band B12 (SWIR 2) increased by about 7.2% and 36.2% for FOI₁ and FOI₂, respectively.

The reason why the smallest reflectance values decrease occurs in different regions of the spectrum can be explained by the fact that the two crop fields have different land cover types prior to the application of manure. In fact, with respect to the mixture of bare and vegetated land covers of FOI₂, the bare soil of FOI₁ features higher reflectance values in the visible band and lower values in the NIR region of the EM spectrum. This is due to the fact that, compared to bare soil, vegetation reflects more energy in the NIR band, and less in the visible bands. Therefore, it is reasonable that the smallest decrease in FOI₁ and FOI₂ occurs around different regions of the EM spectrum. However, from Figure 5.15, the most interesting aspect is that the multispectral signature of manure in the case of two fields located in different regions and manured in different periods, is almost the same, regardless of the type of land cover present in the field before manuring. This is also supported by the fact that the computed Pearson's correlation coefficient between the two earliest post-manuring spectral responses is $\rho = 0.98$. This analysis supports the idea

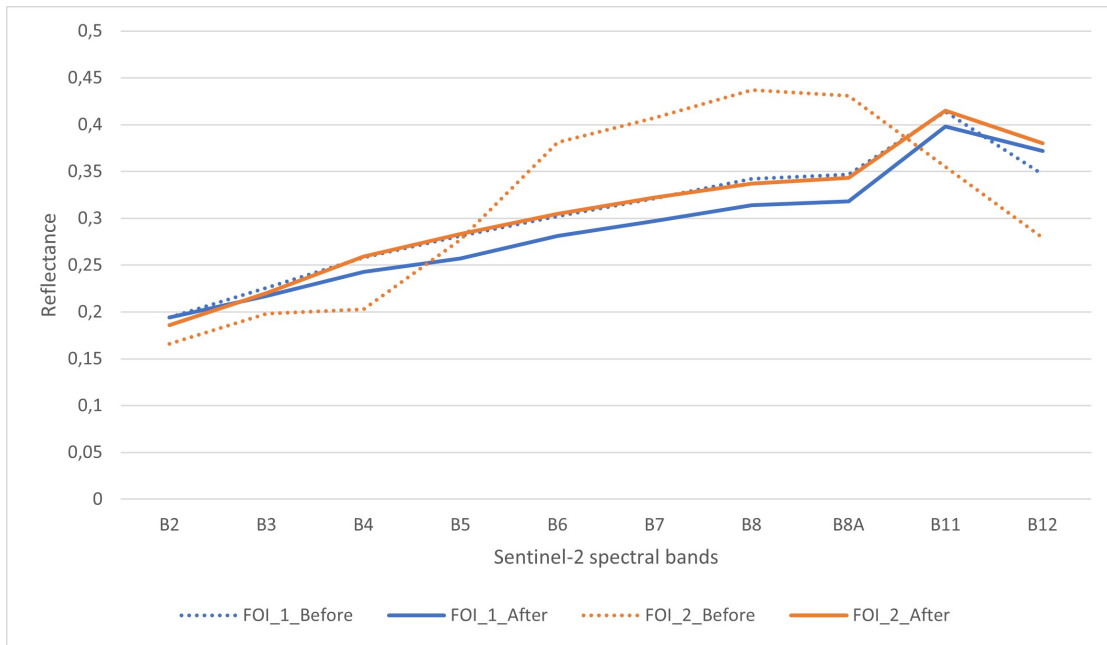


FIGURE 5.15: Average spectral shifts registered in the two fields of interest, before and after manure application.

that manure can potentially be detected over crop fields, using Sentinel-2 multispectral data and regardless of the land cover type before the application of manure.

For sake of completeness, in Figure 5.16 the true-color representation before and after manure application for both test sites is reported.

5.4.3.2 Analysis with Planet data

In addition to Sentinel-2 data, we considered also Planet data, featuring very high temporal resolution at high spatial resolution. Specifically, we used third generation, Sun-synchronous orbit PlanetScope satellites (also known as Dove-R or PSB.SD), each carrying an eight-band frame imager with butcher-block filter and providing coastal blue, blue, green I, green, yellow, red, red-edge and NIR stripes. Table 5.5 reports the details for each band, and whether they are interoperable with Sentinel-2 or not. These sensors provide images with Ground Sampling Distance (GSD) at nadir equal to 3.7 m, resampled to 3 m, with a daily revisit time (at nadir). The PlanetScope satellite fleet is operational from March 2020, and is capable of capturing 200 million km^2 per day. For this work, we used cloud-free images before and after the manuring event, for each of the two fields of interest. In particular, in the case of FOI₁ we used an image acquired

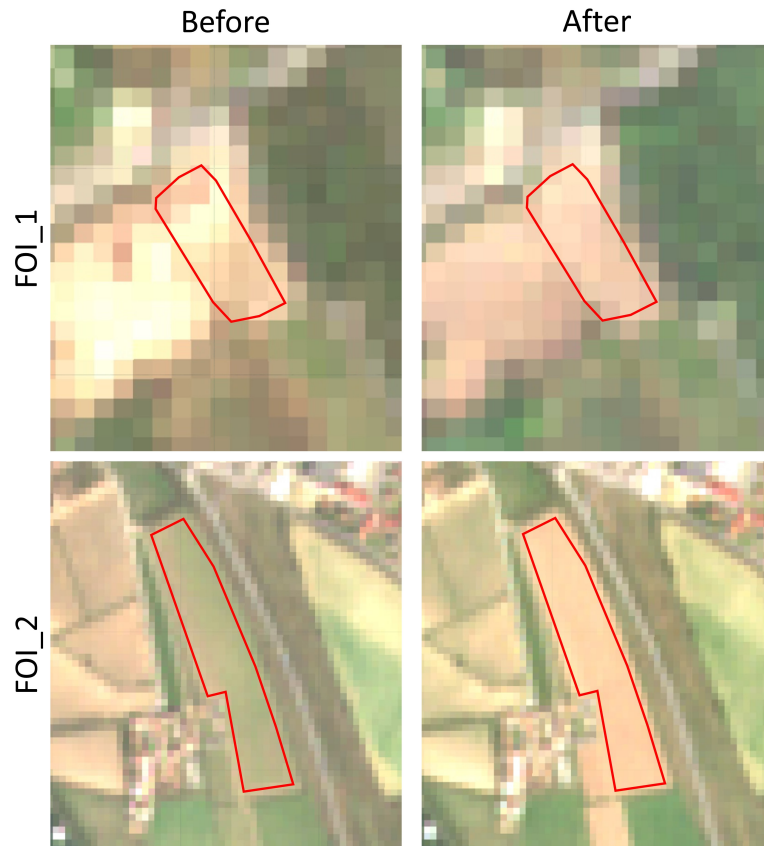


FIGURE 5.16: RGB composites of Sentinel-2 before and after images of the test sites.

on the 10th of April 2022 for pre-event, and one on the 15th of April 2022 for post-event. Whereas, for FOI₂ we used an image sensed on the 28th of March 2022, hence before manuring, and another one after manuring, acquired on the 5th of April 2022.

Spectral signatures in Planet data, before and after the date of manure application, were identified as reported in Figure 5.17. Even in this case one may note that reflectance

Band	Description	Resolution [m]	Wavelength [nm]	Interoperable with Sentinel-2
B1	Coastal Blue	3	443	Yes - with S-2 band B1
B2	Blue	3	490	Yes - with S-2 band B2
B3	Green I	3	531	No equivalent with S-2
B4	Green	3	565	Yes - with S-2 band B3
B5	Yellow	3	610	No equivalent with S-2
B6	Red	3	665	Yes - with S-2 band B4
B7	Red Edge	3	705	Yes - with S-2 band B5
B8	NIR	3	865	Yes - with S-2 band B8a

TABLE 5.5: Description of PlanetScope bands.

values decrease after manure spreading. Moreover, like for the case of Sentinel-2 data, the biggest differences are recorded in the NIR region of the EM spectrum. In particular, the biggest difference in reflectance values occurred in band B7, with a decrease of about 72%, and in band B8, with a decrease of 32%, for FOI₁ and FOI₂, respectively. Whereas, the smallest difference was registered in band B1 for both fields, with a decrease of about 28.8% and 9% for FOI₁ and FOI₂, respectively.

Similarly to what emerged from the analysis of the Sentinel-2 spectra, due to the presence of vegetation in FOI₂, the NIR band (B8) is associated with higher reflectance values than those of FOI₁, before manure application. Moreover, the before and after FOI₂ reflectance values are almost the same in the visible range, while they significantly shift in the NIR region. A change in the red band (B6) was also observed, with a remarkable increase of about 30%. Since Planet's B6 band is harmonized with Sentinel-2's B4 band, it is worth noticing that also the reflectance value of B4 in Sentinel-2 experiences a significant increase (see Figure 5.15). Regarding FOI₁, reflectance values are higher in the visible region due to the bare soil land cover, and the drop of values occurred in all Planet bands, but especially in bands B4 (Green), B6 (Red) and B7 (Red Edge). Finally, also in this case the two spectra recorded after manure application are quite similar; regardless of the previous land cover type, in fact, Pearson's correlation coefficient

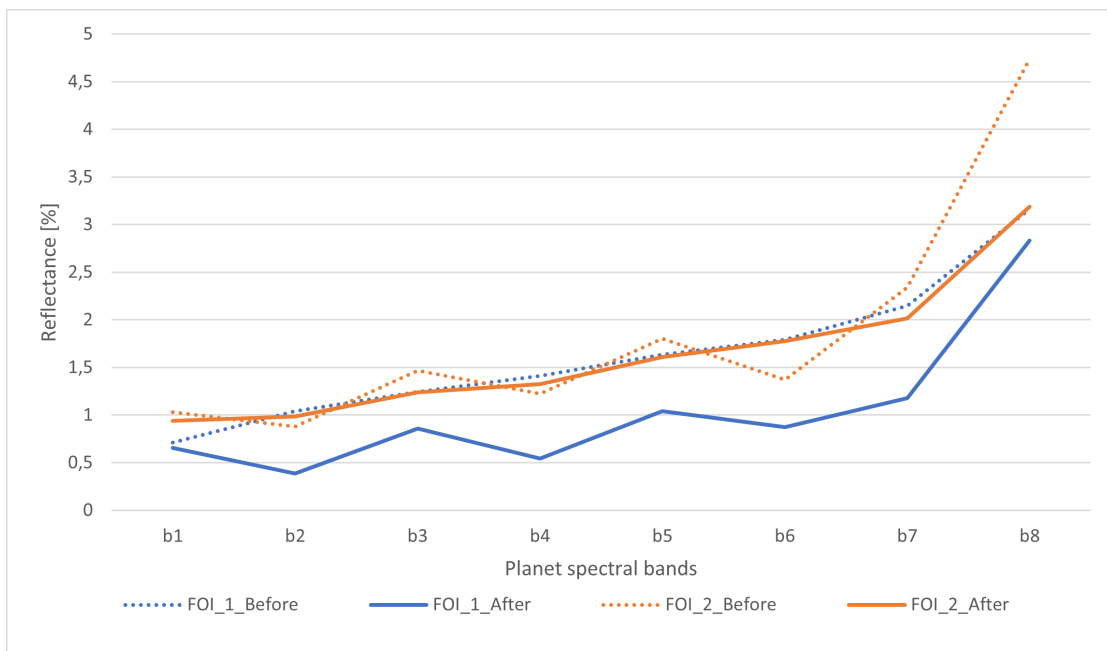


FIGURE 5.17: Average spectral shifts registered in the two fields of interest, before and after manure application (using Planet data).

between the two series of post-manuring spectral samples equals $\rho = 0.95$. However, the absence of SWIR bands, which have shown from the S-2 data analysis to be key in detecting manure application, are not available on Planet, so the EOMI index cannot be computed. Moreover, the absence of SWIR bands is not compensated by sufficiently distinctive features in the available bands. Considering all the above, we finally decided to discontinue experimenting with Planet data, notwithstanding the advantage of very high temporal resolution.

5.4.3.3 The proposed manure detection methodology

In this section a proposal on how to detect manure application based on the two study cases is presented. Specifically, the approach relies on time series analysis of EOMI values, focussing mainly on the increments of such index.

Before carrying out the actual EOMI time series analysis, a pre-processing step on the image collection is necessary to filter out cloudy images. The simplest approach is to leverage cloud cover information in metadata; Sentinel-2 imagery comes with a `CLOUDY_PIXEL_PERCENTAGE` property, expressing the percentage of cloudy pixels in the whole scene. This parameter can be used to filter out from a sequence all extensively clouded scenes. Such filtering, however, is very fast but not always effective: an image with high cloud cover percentage may still be cloud-free on the spot being analyzed, whereas an almost cloud-free image may have clouds exactly over the site of interest. A more effective approach disregards the overall cloud percentage and uses the specific cloudy pixel mask.

Another issue encountered in the cloud filtering step is occasional poor quality of the QA60 band content. The method used to identify clouded pixels, thus to build the QA60 band, is mainly based on thresholding applied to reflectance on band B2, considered together with SWIR bands B11 and B12 that help discriminating snow from clouds. Therefore, if a dataset is affected by radiometric calibration issues, this also affects the quality of the QA60 band. In Figure 5.18 an example of complete inconsistency between QA60 and visual evidence is reported; the cloud mask refers to level L2A Sentinel-2 image acquired on the 1st of January 2022. The effectiveness of the pixel-based cloud filtering process relies on the quality of cloud masks; still, the described incidents seem

to be rare enough for pixel-based selection to remain a better option with respect to metadata-based selection.

Radiometric calibration also caused critical issues with EOMI sequences. Specifically, some images generated unexpected values when processed to raise them from level L1C to level L2A, i.e., from TOA (Top Of Atmosphere) to BOA (Bottom of Atmosphere) reflectance values. The EOMI index showed unexplainably high values for the whole month of January 2022, so we decided to visually inspect the images acquired in that period. From Figure 5.19 it is possible to visually appreciate this issue and, in particular, it is noticeable that the problem lasts for almost the whole month of January. From the 26th of January the problem seems to be solved, and the radiometric values seem to be returned within their normal range.

Moreover, to cross-check that Sentinel-2 data was actually affected by calibration problems, we qualitatively compared Sentinel-2 L1C, L2A and Planet products as shown in Figure 5.20. This comparison was made essentially to verify whether a particular atmospheric condition may have impacted on the data, or maybe a calibration issue affected specifically S-2 data. Regarding the L1C products, it is noticeable that the correspondent true-color composites (RGB) do actually look as expected. Also the true-color Planet image composite shows the expected features. Whereas, the two L2A-processed products are clearly affected by radiometric calibration issues, as their true-color composites barely allow to distinguish their content.

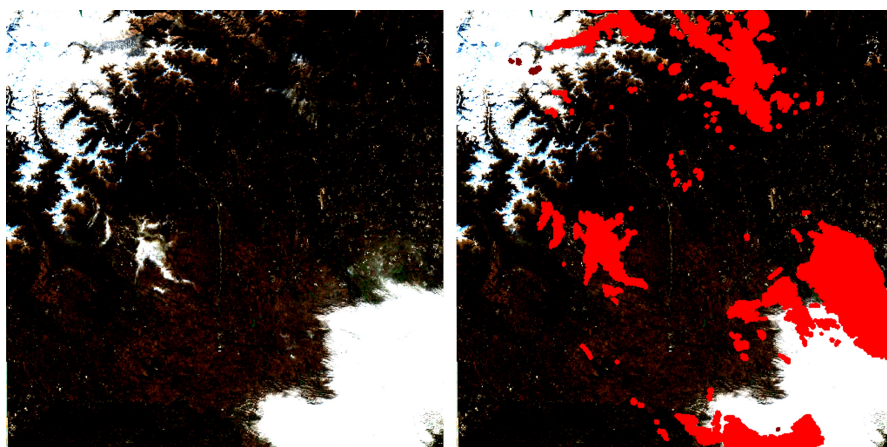


FIGURE 5.18: Example of bad quality cloud mask generated for the L2A Sentinel-2 image acquired on the 1st of January 2022.

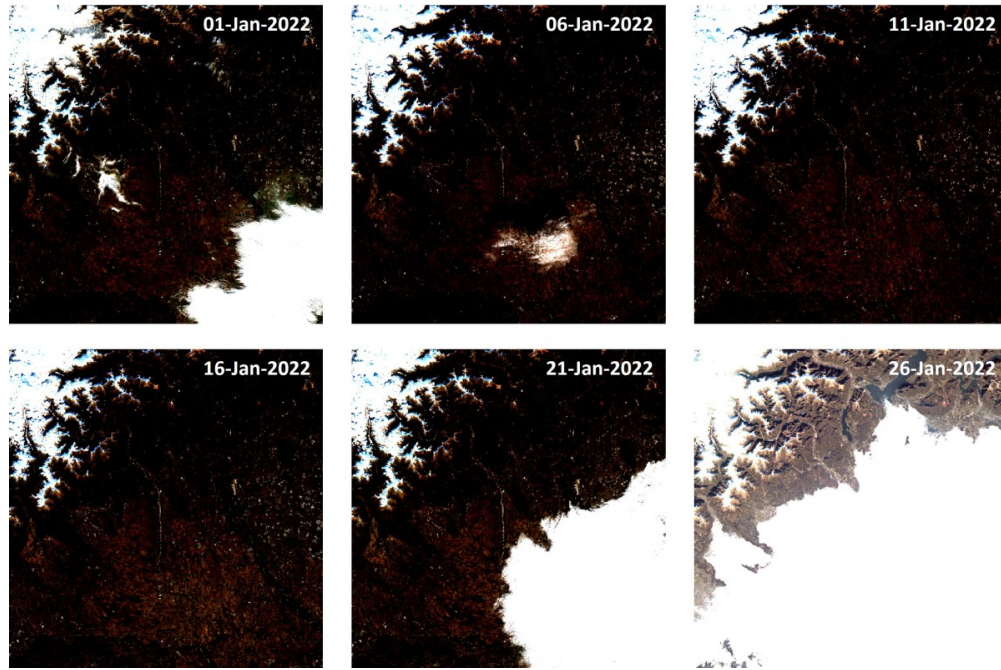


FIGURE 5.19: Radiometric calibration issues, encountered for both study sites and for the same period.

Finally, in Figure 5.21 we reported the histograms of the tile that incorporates FOI_1 , for the 1st of January and the 1st of May, to assess the distribution of spectral values. From Figure 5.21(a) it is possible to observe that bands B1, B2 and B3 feature strong outliers that may cause issues in statistical estimations, while Figure 5.21(b) shows a normal radiometric situation. In this work, all the images with obvious radiometric problems have been discarded from the final collection of images.

5.4.3.4 EOMI analysis

In this section, the analysis of the generated EOMI time series is carried out, first for FOI_1 and then for FOI_2 .

In Figure 5.22 the time series of mean EOMI values for the FOI_1 field is reported. Sequences for three different cases were reported. Specifically, Figure 5.22(top) shows the EOMI sequence without applying any type of cloud filtering. In this case, in correspondence of the strong EOMI drops where the field was completely covered by clouds, hampering manure detection.

Figure 5.22(middle) reports the EOMI sequence generated from a sequence of images with no more than 60% of overall cloud coverage. With respect to the previous situation

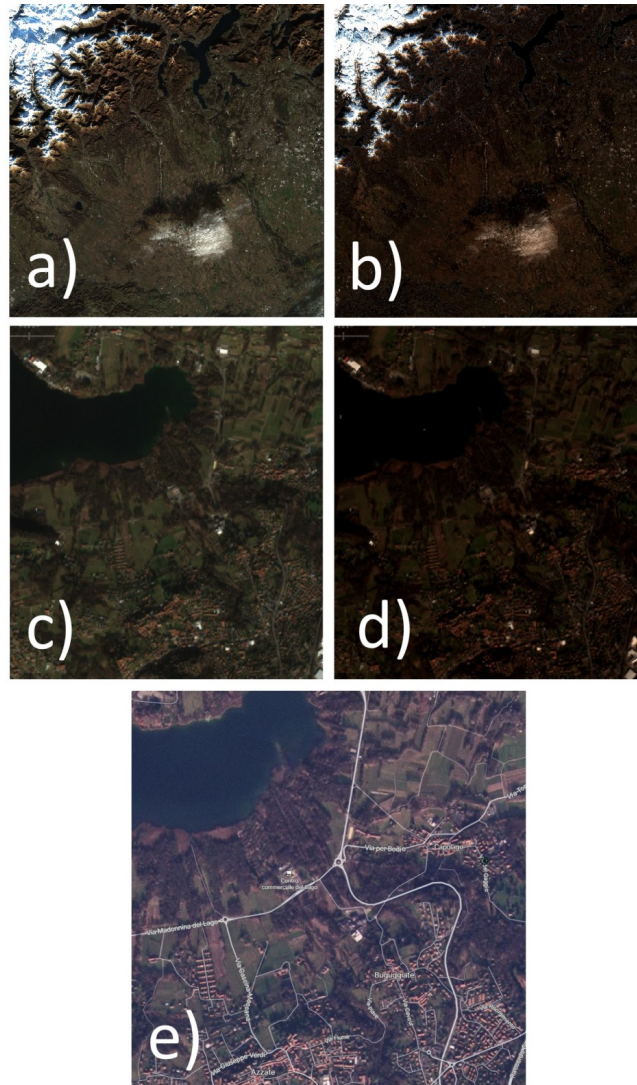


FIGURE 5.20: Visual comparison among different products. a) is the L1C RGB composite of the whole Sentinel-2 tile, b) is L2A RGB composite of the whole Sentinel-2 tile, c) and d) are zoomed regions around FOI₁ field, respectively, and e) is the RGB composite of a Planet image, acquired the same date as the Sentinel's ones (6th of January).

where no filtering was applied, the sequence appears now smoother and more regular. As discussed in Section 5.4.3.3, the drawback of filtering based just on image metadata is that invalid samples may be included, causing glitches in the EOMI value. Finally, in Figure 5.22(bottom) the EOMI time series obtained by pixel-based filtering is shown. As a matter of fact, this represents the best situation with respect to all considered cases. It can be noted that this sequence is populated with more samples with respect to the metadata filtering approach. This translates into a denser sequence of EOMI measurements, enabling more accurate tracking of index value changes.

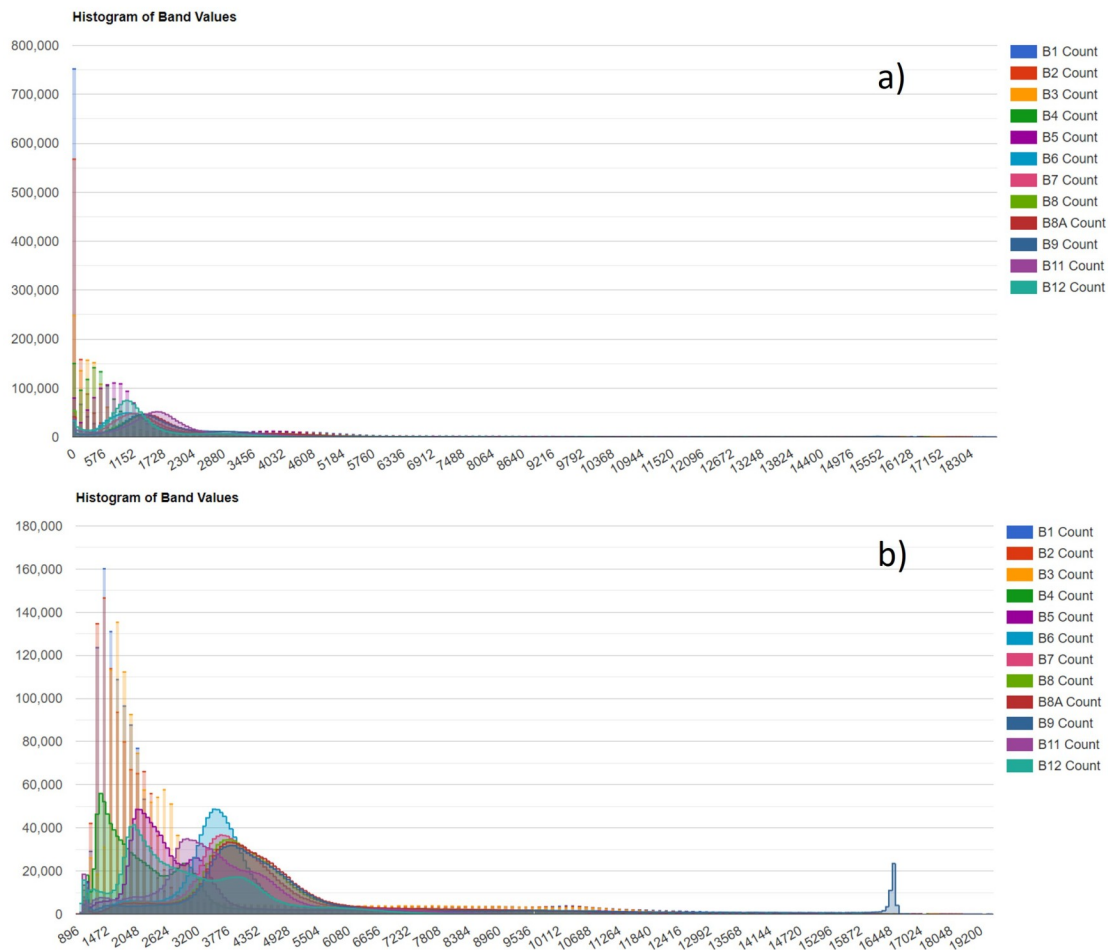


FIGURE 5.21: Histograms of spectral values a) before and b) after radiometric calibration issues.

Considering from now on the EOMI time series of Figure 5.22(bottom), it is possible to make some considerations. The most important aspect is that the EOMI index is capable of detecting the change from a previous land cover type, to manure cover. In fact, the mean EOMI value changed from 0.147 to 0.207, meaning an increase of more than 40%, between the 11th of April and the 16th of April, respectively. From Figure 5.23 it is possible to visually appreciate the overall increase of EOMI values in FOI₁.

The second consideration is that EOMI reaches its maximum immediately after manure spreading, which then decreases in subsequent acquisitions. Unfortunately, we do not possess ground truth from previous years, and thus we cannot assure the EOMI remains lower than its maximum value even in summer. However, since the main objective of this work is to spot out manure application operations in winter, this does not represent a critical aspect at the moment.

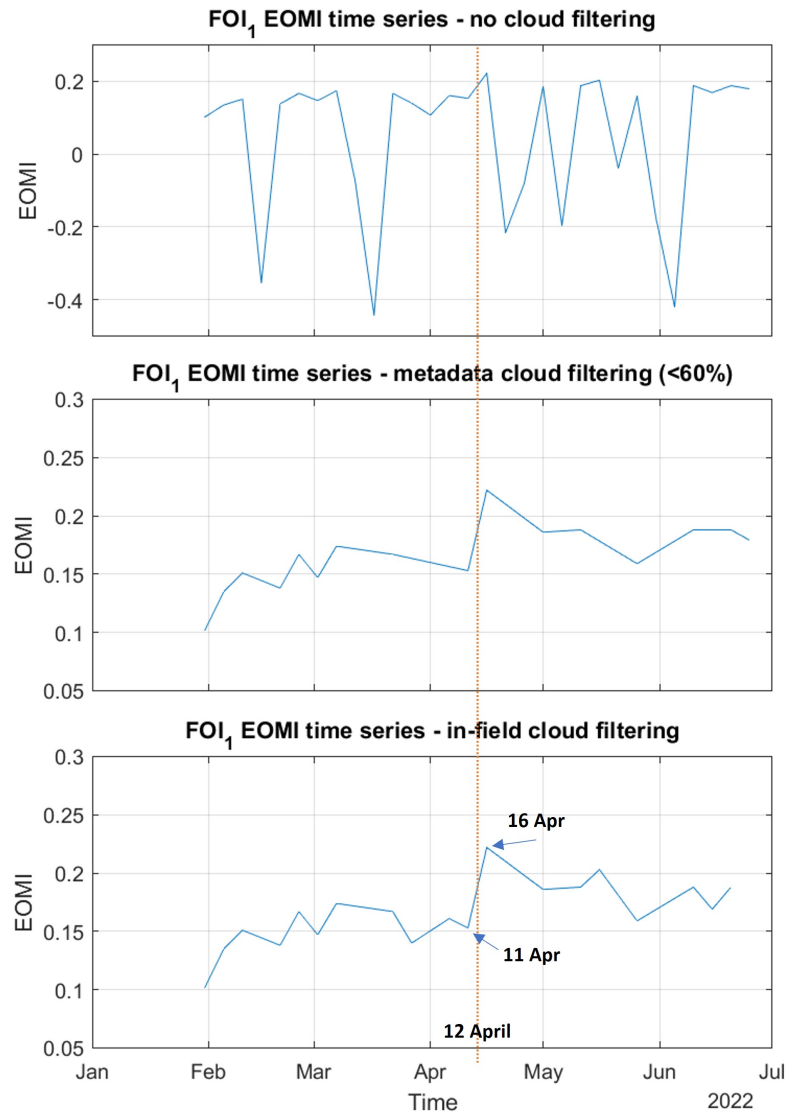


FIGURE 5.22: From top to bottom: 1) EOMI time series without any type of cloud filtering, 2) time series obtained by filtering the metadata to consider only images with 60% or less of overall cloud coverage, and 2) EOMI time series obtained by selectively filtering clouded pixels only inside the crop field (FOI₁).

Based on the above analysis, it is possible to conclude that a relatively simple algorithm detecting a sudden increase in the EOMI value can be a starting point for a precise manure detection methodology. In particular, once a peak EOMI value is detected within the EOMI time series extracted over a test field, it is possible to inspect the optical images before and after the date associated to the registered maximum value. A warning flag could be generated, and the field of interest could undergo additional analysis.

Similarly to what was done for FOI₁, let's first analyze the EOMI time series derived over

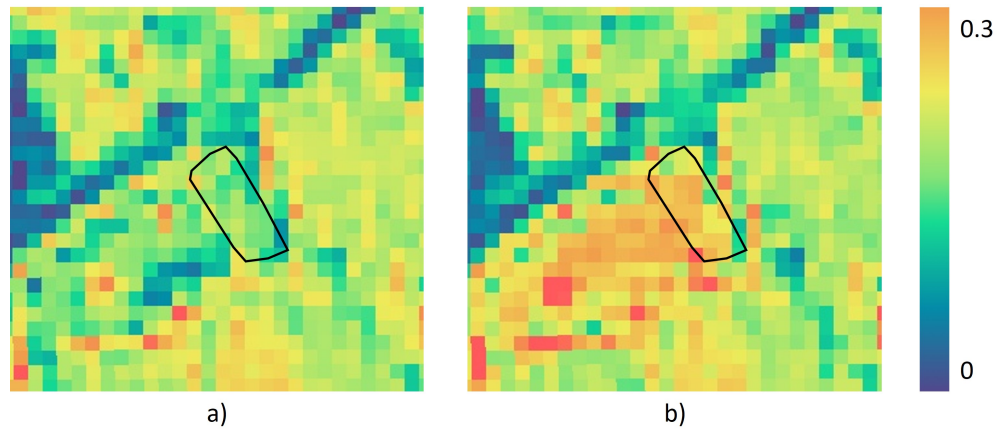


FIGURE 5.23: Map of EOMI values of FOI₁.

FOI₂. The value sequences for three different cloud-filtering procedures are reported in Figure 5.24. Figure 5.24(top) shows the sequence with no cloud filtering. Steep decreases of the EOMI index generally mean that the crop field is temporarily covered by clouds. Figure 5.24(middle) reports the sequence after removing all the images with over 60% cloud cover. In this case, it is possible to observe that notwithstanding the relatively strong filtering based on the metadata, there are still very low EOMI values caused by clouds. In fact, by visually inspecting the images acquired on the dates corresponding to the EOMI value drops, most of the clouds in the scene are concentrated in the area where FOI₂ belongs to. Figure 5.24(bottom) shows the sequence generated by eliminating all those images that are cloudy only on the field of interest. By doing so, it was possible to keep relevant samples only.

Considering the EOMI time series of Figure 5.24(bottom), it is possible to make some remarks. Similarly to what was observed for the first field, we can notice that the EOMI index increased significantly after manure application. In fact, from the 22nd of March to the 11th of April, the EOMI index recorded an increase of about 21%; specifically, the mean EOMI index increased from 0.157 to 0.19. From Figure 5.25 it is possible to visually appreciate the overall increase of EOMI values in FOI₂.

However, even if the index revealed a significant change between the two cloud-free dates (22nd of March and 11th of April), it is worth noticing that the maximum EOMI value is reached on the 16th of April, which is 16 days after manuring. Whereas, In FOI₁ the maximum value is reached only 4 days after manure spreading. This can be explained by the fact that the mix of manure is different in the two cases; for instance, it is possible

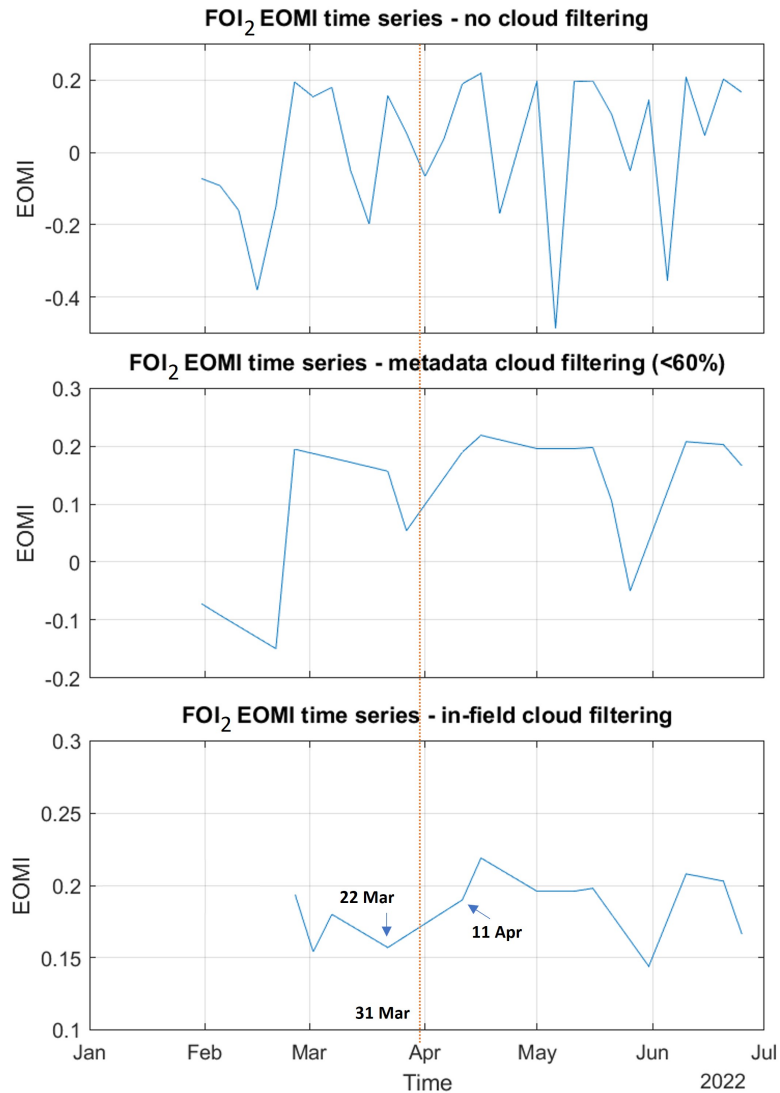


FIGURE 5.24: From top to bottom: 1) EOMI time series without any type of cloud filtering, 2) time series obtained by filtering the metadata to consider only images with 60% or less of overall cloud coverage, and 2) EOMI time series obtained by selectively filtering clouded pixels only inside the crop field (FOI₂).

that the nutrients that compose the manure mixture are long-releasing substances in FOI₂, while they are shortly released in FOI₁. Another possible explanation can be related to soil type; also in this case, different types of soil may react differently to the application of manure, absorbing its substances with different time rates. Still, we believe a delay of two weeks in the detection of manure can also generate a useful warning flag, aimed at activate further investigation on the field.

Based on the above considerations, we still suggest that the maximum EOMI value can be computed and used to warn the user about a potential manuring activity that took place around the date corresponding to the maximum value.

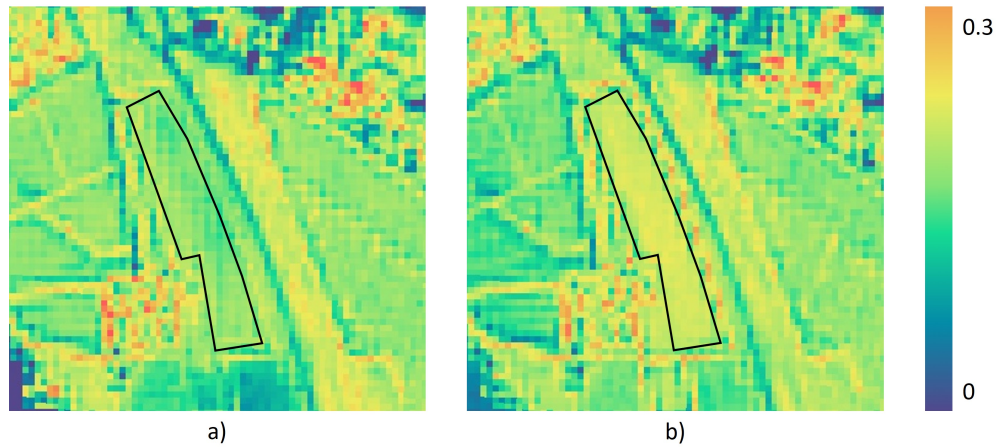


FIGURE 5.25: Map of EOMI values of FOI_2 .

As schematized in Figure 5.26, two methods for manure detection can be hypothesized, based on the intended application:

1. If manuring is to be detected solely for *recording purposes*: the most robust approach, based on the observations made, is to build the yearly EOMI value, find the yearly maximum and trace back to the previous local minimum. The manure event is expected between the local minimum and the next sample; the maximum of EOMI must be above 0.2, and the total increment above 0.05 for the event to be classified as manuring.
2. If manuring is to be detected in near-real-time for *alerting purposes*: the wait for a yearly series to build is too long. The approach in this case would involve identifying step increases between adjacent samples; if an increment greater than 0.03 is observed, an alert is raised.

The methods described above are believed to represent a suitable structure for a manure detection algorithm. A complete definition of a detection method would require tuning of the parameters (e.g. minimum EOMI increment to declare a manuring event), which cannot be done with the very small amount of samples available for our experiments.

5.4.3.5 An additional experiment

In this section we will briefly discuss some results obtained by applying our methodology to a new test field we identified near the city of Vigevano, in the agricultural province of

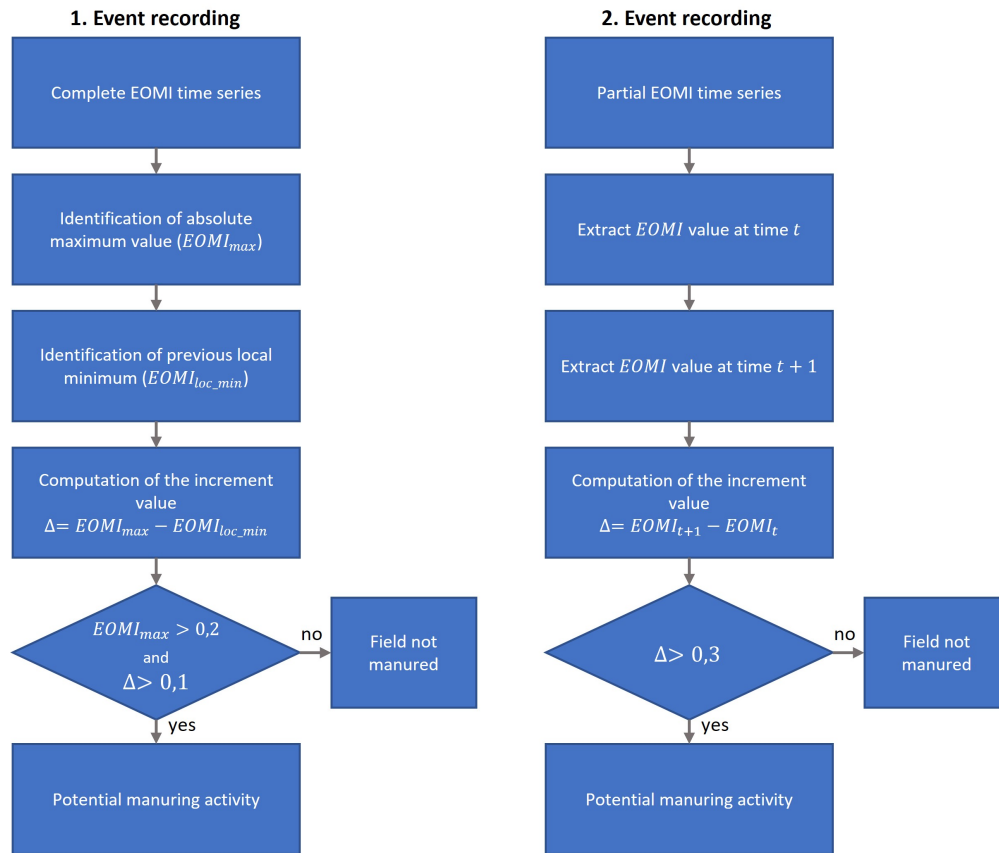


FIGURE 5.26: Two possible approaches aimed at spotting out potential manure spreading activities during winter months.

Pavia in northern Italy. This was done to assess the operation of the proposed method in real cases other than those used to build it. The test field is reported in Figure 5.27, together with the obtained results.

True-color Figures 5.27(a) and (b) show the situation of two crop fields, namely Field_1 and Field_2, on the 11th and the 16th of April 2022, respectively. Visual inspection reveals a significant change in both the fields between the two dates. Due to the typical brownish color visible in the second image, we assumed that manure was spread over the two fields. We then computed the per-pixel EOMI index for both images, and reported the results in the colour maps of Figures 5.27(c) and 5.27(d). From these maps, it is immediately noticeable that the EOMI values of the whole Field_1 field sharply increased, whilst those belonging to Field_2 barely changed. To further investigate this situation, we extracted the spectral responses before and after the supposed manuring operation for both fields. The results, reported in Figures 5.27(e) and 5.27(f), reveal quite an interesting fact. The reflectance values of Field_1, not only decreased significantly

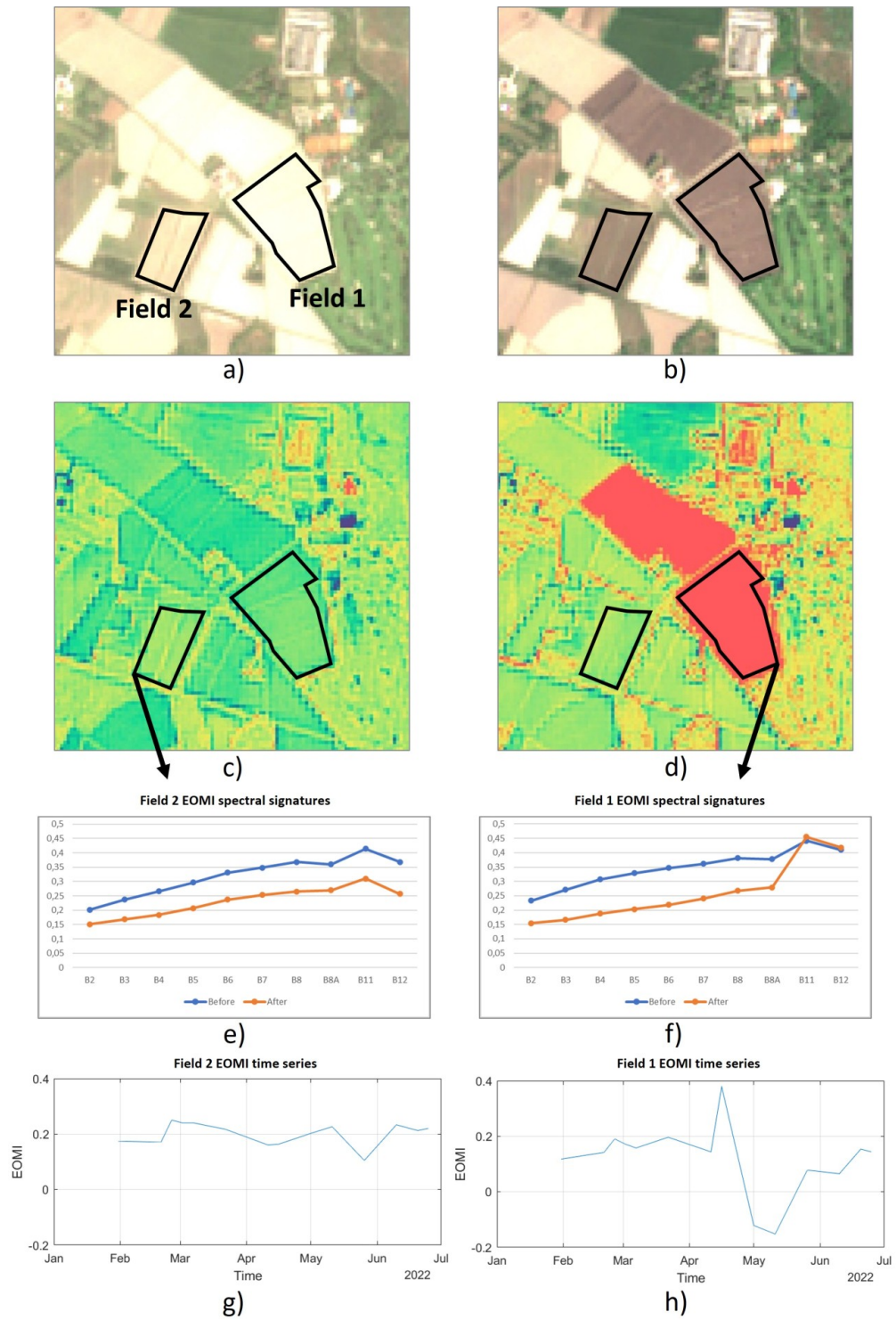


FIGURE 5.27: An additional site used to test the proposed manure detection algorithm.

in the visible and near-infrared regions of the spectrum, but bands B11 and B12 (SWIR bands of Sentinel-2) remained almost unaltered. On the other hand, the whole spectral signature of Field_2 dropped significantly, including reflectance values for the SWIR bands. This is a very interesting point, since both the study cases analyzed in the previous sections showed an increase SWIR reflectance together with an overall decrease in the visible and NIR regions. Based on these assumptions, we finally extracted the EOMI time series over the two fields to assess their behaviour in time. Figure 5.27(h) shows the EOMI time series for Field_1, and a clear peak of the index, corresponding to the maximum value of the series, was registered between the two considered dates. Whereas, for Field_2, the EOMI index is almost flat in the same period (Figure 5.27(g)).

Based on the developed methodology, we concluded that Field_1 was actually fertilized with manure, while Field_2 just undergone a ploughing operation, which caused the overturned soil to appear brown to the human eye. If the assumptions are correct, this test confirms that the proposed method can work on samples other than those used to develop it.

To conclude, in these sections the results of the literature search were presented, which led to identifying the EOMI, an index computed on multispectral satellite data; the EOMI index is in principle suitable to detect manuring events on farmland. In the two presented case studies, time series of the EOMI index have shown distinctive features on the occasion of known manuring events, with a sudden rise in value that may continue along two temporal samples. Based on the observations, a method for satellite-based manure detection has been proposed and tested on a third test case, where a manuring event was assumed from visual interpretation. The method proved capable of identifying a significant difference between two fields that visually appeared very similar while one of them featured an EOMI trend like those observed in the known manuring events. This does not constitute a proof that the method works, because we have no actual ground truth, however the observed temporal trajectory is very similar to those previously witnessed. In general, a key factor is the lack of an extensive set of samples with related ground truth on manuring events, so any conclusion in these circumstances is relatively weak. However, certainly these observation may help building an operational manure detection method based on multispectral spaceborne Earth observation data.

Chapter 6

Conclusions

6.1 Conclusions

This thesis describes the work carried out during my Ph.D. course in Electronic Engineering at the University of Pavia, Pavia, Italy.

The thesis starts in Chapter 1 with an introduction on the challenges related to land cover (LC) mapping and, more specifically, to land cover mapping using high-resolution (10-30 m) satellite data. Producing reliable LC maps is in fact a very complicated task in terms of product validation, due to rapid changes of the classes phenology. This aspect becomes even more relevant when LC mapping is performed over wide geographical areas. As a consequence, most previous studies focussed on monitoring and mapping land cover and land cover changes at the local scale and for short periods of time. For this reason, it is difficult to compare LC products and to quantify actual changes in a reliable manner. Moreover, in situ campaigns aimed at collecting reference data for model validation purposes are usually very expensive both in terms of time and financial resources, making the product validation process even more tough.

However, in recent years, several LC maps have been produced using different satellite data sources that have been used in LC monitoring and mapping algorithms to collect ground truth data. In this way, tuning and validation of models are carried out in a much more efficient and time saving way, as long as the used LC maps are reliable enough.

Chapter 1 carries on with the analysis of the pros and cons of using multitemporal satellite data. A review of the technical literature related to land cover mapping using time satellite data time series revealed that most studies leverage optical data, while only a

few employ SAR data due to their more complex nature and their inability (compared to optical data) to discriminate particular classes.

In this thesis work, the potential of using multitemporal data for land cover mapping purposes was explored and quantitatively assessed (when possible). Specifically, three main topics were tackled in this work: vegetation land cover mapping, inland water body extent mapping and characterization of farming practices over croplands (with a focus on organic agriculture). Regarding vegetation mapping, the exhaustive scientific literature review carried out in Chapter 2 revealed that optical data represent the most suitable source of data to characterize vegetated land covers. In fact, from the technical literature it is possible to find a wide variety of optical-based methodologies aimed at monitoring and mapping vegetation. On the other hand, a much smaller part of the literature is devoted to vegetation land cover mapping using SAR data; moreover, those studies that involve SAR data present several critical issues. Therefore, part of this thesis has been devoted to the assessment of the potential of multitemporal SAR data to characterize vegetated land covers.

Slightly different is the situation regarding water body mapping; in this case, it is possible to find a relatively large number of both optical- and SAR-based methodologies aimed at characterize water cover. However, all the analyzed approaches have many limitations. Given the demonstrated ability of SAR signals to detect water bodies (mainly thanks to the mirror reflection backscatter mechanism) and to penetrate almost any weather condition, in this thesis multitemporal SAR data were used to build a high-spatial and -temporal water mapping system that can be employed in any region of the World, overcoming the most severe limitations found in the technical literature.

In the case of both vegetation and water land covers, the works found in the literature presented the following issues: 1) lack of automatism, 2) the reference data sets are manually built based on experience and photo-interpretation (which is extremely time consuming), 3) it is not possible to transfer the generated models to other regions of interest without a priori information, 4) almost all the methodologies are tuned to work on small areas, 5) the use of optical data often reduces classification performances over cloud-covered regions, 6) many SAR-based models are usually inadequate to work in any region of interest due to locally-tuned pre-processing steps, 7) the generated land cover products do not meet the requirements of many applications (e.g., from a spatial and/or temporal point of view). Given this context, in Chapters 3 and 4 a SAR-based methodology for vegetation and water land cover mapping were developed, with the aim

of overcoming the limitations of the approaches found in the scientific literature. Regarding the last land cover type analyzed in this thesis, i.e., organic croplands, several farming practices were characterized with the most suitable source of data. In fact, depending on the parameter that needs to be monitored, optical or SAR data were employed. Among many variables that characterize organic crops, in this thesis three of them were analyzed: weed-killer activities, tillage techniques and fertilization operations. Based on findings from the technical literature, weed-killer and fertilization operations were monitored using multispectral data, while for assessing the type of tillage, multi-temporal SAR data were employed.

Regarding the developed vegetation mapping methodology, it has been shown that it is possible to obtain a significant land cover map in different regions of the World, using year-long sequences of Sentinel-1 SAR data; very encouraging results were obtained in four different locations, with very diverse environments and land covers. The presented work, which achieved on average 71% overall accuracy (with standard deviation $\sigma = 14.2\%$), represents a first step towards the possibility to obtain a global land cover map using solely SAR data. The accuracy obtained in the Siberian tile (50.5%) negatively affected the mean accuracy value, due to the strong limitations that characterize this area, such as snow and ice cover for nine months a year. If this test area was not considered in the overall model performance evaluation, the proposed methodology is able to achieve accuracy values near to 80%, with a much lower standard deviation (around 5%). However, it is important also to show the weaknesses of the approach. Moreover, the proposed methodology introduced an approach to automatically build training sets from existing medium-resolution land cover maps, reducing possible outliers and training a good classification model. The developed model was able to increase the overall accuracy of about 16% in average with respect to the medium resolution multispectral-based existing land cover map used to build the training set. Specifically, compared to the MRLC map, the proposed model was able to increase the accuracy of about 18.4% for Siberia, 5.9% for Italy, 24.2% for Amazonia and 16.8% for Africa.

Regarding the inland water body extent monitoring and mapping methodology described in this thesis, the proposed approach allows to extract water bodies in wide geographical areas, automatically generating clustering seeds from pre-existing coarser global water maps. The approach, based on multitemporal Sentinel-1 SAR data, enhances the capability to detect temporary water bodies and also limits the effects of speckle noise.

Moreover, the use of a DEM increases classification performances over morphologically complex regions that are typically dominated by mountains. A thorough validation performed on the water body map for the whole Lombardy region (North of Italy), using external reference information provided by the regional mapping authority, certifies that the proposed automatic methodology achieves overall accuracy values higher than 94%, with a slightly less good performance for water points than for non-water classes (89.4% vs. 99.8% producer accuracy, respectively). These results confirm the reliability of the proposed procedure, which has also been tested for consistency with similar global products. They also stress the robustness of the proposed extraction methodology on very wide areas, since nine $100 \times 100 \text{ km}^2$ tiles (each corresponding to the size of a single, conventional Sentinel-2 tile) were processed to characterize the whole of Lombardy. An additional validation test was also independently carried out by an expert validation team of the ESA WorldWater round robin over five $100 \times 100 \text{ km}^2$ test sites, using highly reliable VHR PlanetScope data. Notwithstanding the challenges represented by the diversities of the sites in terms of terrain complexity, climate and water bodies types, the presented model was able to achieve, on average, 93.4% overall accuracy. Finally, the proposed methodology showed great potential in detecting temporary/seasonal water bodies, which can be employed for monitoring, for example, small reservoirs and other water bodies that need to be constantly monitored.

The last topic, presented in Chapter 5, regards the identification of farming practices, with the aim of supporting organic production and organic compliance claims. This Chapter was divided in three main parts: the first part was about the development of a methodology capable of detecting weed-killer operations; the second part was devoted to the assessment of the type of utilized tillage technique by using multitemporal SAR data; finally, the last part dealt with the detection of fertilization operations to limit nitrate pollution.

Regarding the detection of weed-killer activities, it has been demonstrated that weeding operations can be detected using multispectral data, as long as the monitoring conditions are favourable (e.g., cloud coverage during the growing season). Since organic cultivation practices are characterized by intricate management strategies, future work may also involve Artificial Intelligence (AI) strategies, aimed at helping assessing organic compliance.

Some preliminary steps towards assessing the type of tillage applied to a given agricultural field were also presented. Specifically, a suitable backscattering model has been identified, which is able to link radar backscatter to post-tillage surface roughness. This latter provides clues regarding the approach adopted in tillage, which represents a key aspect in organic farming practices. Experiments were conducted using multitemporal Sentinel-1 SAR data on a set of rice fields in northern Italy. Results suggest that the model is effective in retrieving surface roughness at key dates, thus representing an excellent starting point for further investigation.

The last part of Chapter 5 was devoted to the development of an algorithm aimed at detecting fertilization operations exploiting multispectral data. In particular, a method for satellite-based manure detection has been proposed and tested, based on multitemporal Sentinel-2 data. It has been shown that, given the available information, the proposed methodology was able to detect manuring activities; however, due to the very limited test set, further tuning of the algorithm is required in order to build a more robust manure detection model, able to raise reliable warnings in case of actual fertilization activities.

6.2 Future work

Notwithstanding the promising results achieved by the models proposed in this thesis work, there exists large room for improvement. For example, regarding the presented vegetation land cover mapping methodology, the legend of the classes must be enlarged by characterizing “second level” land covers, such as the distinction between deciduous and evergreen vegetation types. If such discrimination is relatively easy using optical data, for SAR data it represents a challenge. Moreover, the training set generation procedure must be improved in order not to penalise the less abundant land cover types within the considered area. Finally, deep learning methodologies based on SAR time series should be analyzed to assess their classification capability compared to “classical” machine learning techniques, such as the one employed in this work.

Regarding the water body monitoring and mapping application developed in this thesis, experiments showed that improvements must be done in order to prevent strong classification errors in geographical areas mainly characterized by dry, sandy regions. Generally, in fact, sand causes the backscatter to drop below the Noise Equivalent Sigma Zero

(NESZ), often lying below water backscatter values. As a consequence, the methodology often confuses sand with water bodies. This aspect should be deeply analyzed in order to prevent it. Based on experiments carried out during the development of the water mapping model (that have not been reported in this thesis), it was found that the number of extracted clusters by the k -Means clusterer had a significant role on the classification performance, especially in desert regions. Therefore, a more dynamic approach must be designed, that automatically adapts the number of extracted clusters based on the land cover types distribution within the region of interest. Also different combinations of SAR features should be considered in order to evaluate their classification capabilities. Moreover, a more robust temporary water bodies mapping algorithm must be established, as in this work only preliminary results were shown.

Finally, regarding the approaches aimed at characterizing farming practices, a mission devoted to the collection of reference data is vital. In fact, most of the experiments were carried out on a very small ground truth dataset and, for this reason, despite all the conclusions that have been drawn are very promising, there are several weaknesses. Once a larger and reliable reference dataset has been generated, then all the developed models can be tuned and improved. A specific comment regards the tillage assessment in SAR data; in this particular case, results should be compared with in situ measurements of surface roughness which, however, are very expensive to do in terms of both time and resources. Regarding the fertilization detection algorithm, this was developed based only on two crop fields for which several information were available; notwithstanding the achieved good results, this is definitely not enough to claim the methodology as “reliable”. Finally, regarding the detection of weed-killer operations, it has been shown that clouds represent a critical issue for the developed detection algorithm; therefore, integration with other sources of data, e.g., SAR data, should be considered for improvements.

6.3 Published works during the Ph.D. course

- [210] D. Marzi, A. Sorriso, F. Dell’Acqua and P. Gamba, “Heterogeneous SAR Sequence Processing for Land Cover Mapping,” IGARSS 2022 - 2022 IEEE International Geoscience and Remote Sensing Symposium, 2022, pp. 5172-5175, doi: 10.1109/IGARSS46834.2022.9884205.
- [166] D. Marzi and F. Dell’Acqua, “An Experiment on Extended, Satellite-Based Traceability of Organic Crops in North-Western Italy,” IGARSS 2022 - 2022 IEEE

International Geoscience and Remote Sensing Symposium, 2022, pp. 4650-4653, doi: 10.1109/IGARSS46834.2022.9883883.

- [162] Tottrup, Christian, et al. “Surface Water Dynamics from Space: A Round Robin Intercomparison of Using Optical and SAR High-Resolution Satellite Observations for Regional Surface Water Detection.” *Remote Sensing* 14.10 (2022): 2410.
- [44] Marzi, David, and Paolo Gamba. “Inland Water Body Mapping Using Multitemporal Sentinel-1 SAR Data.” *IEEE Journal of Selected Topics in Applied Earth Observations and Remote Sensing* 14 (2021): 11789-11799.
- [129] Marzi, David, Shantanu Todmal, and Paolo Gamba. “Mapping Globally Using Multitemporal Sentinel-1 SAR: A Semiautomatic Approach.” 2021 IEEE International India Geoscience and Remote Sensing Symposium (InGARSS). IEEE, 2021.
- [49] Marzi, David, and Fabio Dell’Acqua. “Mapping European Rice Paddy Fields Using Yearly Sequences of Spaceborne Radar Reflectivity: A Case Study in Italy.” *Earth* 2.3 (2021): 387-404.
- [130] Sorriso, Antonietta, David Marzi, and Paolo Gamba. “A General Land Cover Classification Framework for Sentinel-1 SAR Data.” 2021 IEEE 6th International Forum on Research and Technology for Society and Industry (RTSI). IEEE, 2021.
- [150] Marzi, David, and Paolo Gamba. “Wide-Scale Water Bodies Mapping Using Multi-Temporal Sentinel-1 SAR Data.” 2021 IEEE International Geoscience and Remote Sensing Symposium IGARSS. IEEE, 2021.
- [167] Marzi, David, Cristian Garau, and Fabio Dell’Acqua. “Identification of rice fields in the Lombardy region of Italy based on time series of Sentinel-1 data.” 2021 IEEE International Geoscience and Remote Sensing Symposium IGARSS. IEEE, 2021.
- [128] Marzi, David, and Paolo Gamba. “Global Vegetation Mapping for ESA Climate Change Initiative Project Leveraging Multitemporal High Resolution Sentinel-1 SAR Data.” IGARSS 2020-2020 IEEE International Geoscience and Remote Sensing Symposium. IEEE, 2020.

Bibliography

- [1] Steffen Fritz, Linda See, and Felix Rembold. Comparison of global and regional land cover maps with statistical information for the agricultural domain in Africa. *International Journal of Remote Sensing*, 31(9):2237–2256, 2010.
- [2] Peter H Verburg, Kathleen Neumann, and Linda Nol. Challenges in using land use and land cover data for global change studies. *Global change biology*, 17(2): 974–989, 2011.
- [3] Ban Yifang, Peng Gong, and Chandra Gini. Global land cover mapping using Earth observation satellite data: Recent progresses and challenges. *ISPRS journal of photogrammetry and remote sensing (Print)*, 103(1):1–6, 2015.
- [4] PJ Mason, M Manton, DE Harrison, A Belward, AR Thomas, and DK Dawson. The second report on the adequacy of the global observing systems for climate in support of the UNFCCC. *GCOS Rep*, 82:74, 2003.
- [5] Zhiyong Lv, Tongfei Liu, Jón Atli Benediktsson, and Nicola Falco. Land cover change detection techniques: Very-high-resolution optical images: A review. *IEEE Geoscience and Remote Sensing Magazine*, 10(1):44–63, 2021.
- [6] Han Liu, Peng Gong, Jie Wang, Nicholas Clinton, Yuqi Bai, and Shunlin Liang. Annual dynamics of global land cover and its long-term changes from 1982 to 2015. *Earth System Science Data*, 12(2):1217–1243, 2020.
- [7] Congcong Li, Peng Gong, Jie Wang, Cui Yuan, Tengyun Hu, Qi Wang, Le Yu, Nicholas Clinton, Mengna Li, Jing Guo, et al. An all-season sample database for improving land-cover mapping of Africa with two classification schemes. *International Journal of Remote Sensing*, 37(19):4623–4647, 2016.
- [8] Xiao-Peng Song, Matthew C Hansen, Stephen V Stehman, Peter V Potapov, Alexandra Tyukavina, Eric F Vermote, and John R Townshend. Global land change from 1982 to 2016. *Nature*, 560(7720):639–643, 2018.
- [9] Céline Lamarche, Maurizio Santoro, Sophie Bontemps, Raphaël d’Andrimont, Julien Radoux, Laura Giustarini, Carsten Brockmann, Jan Wevers, Pierre Defourny, and Olivier Arino. Compilation and validation of SAR and optical data products for a complete and global map of inland/ocean water tailored to the climate modeling community. *Remote Sensing*, 9(1):36, 2017.
- [10] P Bicheron, M Leroy, C Brockmann, U Krämer, B Miras, M Huc, F Ninõ, Pierre Defourny, Christelle Vancutsem, O Arino, et al. Globcover: a 300 m global land cover product for 2005 using ENVISAT MERIS time series. In *Proceedings of the Recent Advances in Quantitative Remote Sensing Symposium: 25–29 September 2006. Valencia*, pages 538–542. Universitat de Valencia Valencia, 2006.

- [11] Mark A Friedl, Damien Sulla-Menashe, Bin Tan, Annemarie Schneider, Navin Ramankutty, Adam Sibley, and Xiaoman Huang. MODIS Collection 5 global land cover: Algorithm refinements and characterization of new datasets. *Remote sensing of Environment*, 114(1):168–182, 2010.
- [12] Matthew C Hansen, Ruth S DeFries, John RG Townshend, and Rob Sohlberg. Global land cover classification at 1 km spatial resolution using a classification tree approach. *International journal of remote sensing*, 21(6-7):1331–1364, 2000.
- [13] Thomas R Loveland, Bradley C Reed, Jesslyn F Brown, Donald O Ohlen, Zhiliang Zhu, LWMJ Yang, and James W Merchant. Development of a global land cover characteristics database and IGBP DISCover from 1 km AVHRR data. *International journal of remote sensing*, 21(6-7):1303–1330, 2000.
- [14] Jun Chen, Jin Chen, Anping Liao, Xin Cao, Lijun Chen, Xuehong Chen, Chaoying He, Gang Han, Shu Peng, Miao Lu, et al. Global land cover mapping at 30 m resolution: A POK-based operational approach. *ISPRS Journal of Photogrammetry and Remote Sensing*, 103:7–27, 2015.
- [15] Peng Gong, Jie Wang, Le Yu, Yongchao Zhao, Yuanyuan Zhao, Lu Liang, Zhenguo Niu, Xiaomeng Huang, Haohuan Fu, Shuang Liu, et al. Finer resolution observation and monitoring of global land cover: First mapping results with Landsat TM and ETM+ data. *International Journal of Remote Sensing*, 34(7):2607–2654, 2013.
- [16] Xiao Zhang, Liangyun Liu, Xidong Chen, Yuan Gao, Shuai Xie, and Jun Mi. GLC_FCS30: Global land-cover product with fine classification system at 30 m using time-series Landsat imagery. *Earth System Science Data*, 13(6):2753–2776, 2021.
- [17] ESA. *S2 Prototype Land Cover 20m Map of Africa 2016*, 2021 (accessed August 31, 2022). URL <https://2016africalandcover20m.esrin.esa.int/>.
- [18] B Chen, B Xu, Z Zhu, C Yuan, H Ping Suen, J Guo, N Xu, W Li, Y Zhao, JJSB Yang, et al. Stable classification with limited sample: Transferring a 30-m resolution sample set collected in 2015 to mapping 10-m resolution global land cover in 2017. *Sci. Bull*, 64:370–373, 2019.
- [19] ESA. *Worldwide land cover mapping*, 2022 (accessed August 31, 2022). URL <https://esa-worldcover.org/en>.
- [20] Aneta J Florczyk, Christina Corbane, Daniele Ehrlich, Sergio Freire, Thomas Kemper, Luca Maffenini, Michele Melchiorri, Martino Pesaresi, Panagiotis Politis, Marcello Schiavina, et al. GHSL data package 2019. *Luxembourg, EUR*, 29788(10.2760):290498, 2019.
- [21] Marcello Schiavina, Michele Melchiorri, Martino Pesaresi, Panagiotis Politis, S Freire, Luca Maffenini, Pietro Florio, Daniele Ehrlich, Katarzyna Goch, Pierpaolo Tommasi, et al. GHSL Data Package 2022. (*Journal not available*), 2022.
- [22] Xiaoping Liu, Guohua Hu, Yimin Chen, Xia Li, Xiaocong Xu, Shaoying Li, Fengsong Pei, and Shaojian Wang. High-resolution multi-temporal mapping of global urban land using Landsat images based on the Google Earth Engine Platform. *Remote sensing of environment*, 209:227–239, 2018.

- [23] Peng Gong, Xuecao Li, Jie Wang, Yuqi Bai, Bin Chen, Tengyun Hu, Xiaoping Liu, Bing Xu, Jun Yang, Wei Zhang, et al. Annual maps of global artificial impervious area (GAIA) between 1985 and 2018. *Remote Sensing of Environment*, 236:111510, 2020.
- [24] Xiao Zhang, Liangyun Liu, Changshan Wu, Xidong Chen, Yuan Gao, Shuai Xie, and Bing Zhang. Development of a global 30 m impervious surface map using multisource and multitemporal remote sensing datasets with the Google Earth Engine platform. *Earth System Science Data*, 12(3):1625–1648, 2020.
- [25] Min Feng, Joseph O Sexton, Saurabh Channan, and John R Townshend. A global, high-resolution (30-m) inland water body dataset for 2000: First results of a topographic–spectral classification algorithm. *International Journal of Digital Earth*, 9(2):113–133, 2016.
- [26] Dai Yamazaki, Mark A Trigg, and Daiki Ikeshima. Development of a global ~90 m water body map using multi-temporal Landsat images. *Remote Sensing of Environment*, 171:337–351, 2015.
- [27] Jean-François Pekel, Andrew Cottam, Noel Gorelick, and Alan S Belward. High-resolution mapping of global surface water and its long-term changes. *Nature*, 540(7633):418–422, 2016.
- [28] Amy H Pickens, Matthew C Hansen, Matthew Hancher, Stephen V Stehman, Alexandra Tyukavina, Peter Potapov, Byron Marroquin, and Zainab Sherani. Mapping and sampling to characterize global inland water dynamics from 1999 to 2018 with full Landsat time-series. *Remote Sensing of Environment*, 243:111792, 2020.
- [29] MK Gumma, PS Thenkabail, P Teluguntla, A Oliphant, J Xiong, RG Congalton, Kamini Yadav, and C Smith. NASA Making Earth System Data Records for Use in Research Environments (MEASURES) Global Food Security-Support Analysis Data (GFSAD) Cropland Extent 2015 South Asia, Afghanistan, Iran 30 m v001. (*Journal not available*), 2017.
- [30] Prasad S Thenkabail, Munir A Hanjra, Venkateswarlu Dheeravath, and Muralikrishna Gumma. A holistic view of global croplands and their water use for ensuring global food security in the 21st century through advanced remote sensing and non-remote sensing approaches. *Remote sensing*, 2(1):211–261, 2010.
- [31] Le Yu, Jie Wang, Nicholas Clinton, Qinchuan Xin, Liheng Zhong, Yanlei Chen, and Peng Gong. FROM-GC: 30 m global cropland extent derived through multisource data integration. *International Journal of Digital Earth*, 6(6):521–533, 2013.
- [32] Matthew C Hansen, Peter V Potapov, Rebecca Moore, Matt Hancher, Svetlana A Turubanova, Alexandra Tyukavina, David Thau, Stephen V Stehman, Scott J Goetz, Thomas R Loveland, et al. High-resolution global maps of 21st-century forest cover change. *science*, 342(6160):850–853, 2013.
- [33] JO Sexton, M Feng, S Channan, XP Song, DH Kim, P Noojipady, D Song, C Huang, A Annand, K Collins, et al. Earth science data records of global forest cover and change. *User guide*, 38, 2016.
- [34] Xiaomei Zhang, Tengfei Long, Guojin He, Yantao Guo, Ranyu Yin, Zhaoming Zhang, Han Xiao, Moxuan Li, and Bo Cheng. Rapid generation of global forest

- cover map using Landsat based on the forest ecological zones. *Journal of Applied Remote Sensing*, 14(2):022211, 2020.
- [35] Hugo Carrão, Paulo Gonçalves, and Mário Caetano. Contribution of multispectral and multitemporal information from MODIS images to land cover classification. *Remote Sensing of Environment*, 112(3):986–997, 2008.
- [36] Liheng Zhong, Peng Gong, and Gregory S Biging. Efficient corn and soybean mapping with temporal extendability: A multi-year experiment using Landsat imagery. *Remote Sensing of Environment*, 140:1–13, 2014.
- [37] Masanobu Shimada, Takuya Itoh, Takeshi Motooka, Manabu Watanabe, Tomohiro Shiraishi, Rajesh Thapa, and Richard Lucas. New global forest/non-forest maps from ALOS PALSAR data (2007–2010). *Remote Sensing of environment*, 155: 13–31, 2014.
- [38] Jeffrey W Cable, John M Kovacs, Jiali Shang, and Xianfeng Jiao. Multi-temporal polarimetric RADARSAT-2 for land cover monitoring in Northeastern Ontario, Canada. *Remote Sensing*, 6(3):2372–2392, 2014.
- [39] Marcus E Engdahl and Juha M Hyyppä. Land-cover classification using multi-temporal ERS-1/2 InSAR data. *IEEE Transactions on Geoscience and Remote Sensing*, 41(7):1620–1628, 2003.
- [40] Marc Simard, Susan S Saatchi, and Gianfranco De Grandi. The use of decision tree and multiscale texture for classification of JERS-1 SAR data over tropical forest. *IEEE Transactions on Geoscience and Remote Sensing*, 38(5):2310–2321, 2000.
- [41] Pauline Dusseux, Thomas Corpetti, Laurence Hubert-Moy, and Samuel Corgne. Combined use of multi-temporal optical and radar satellite images for grassland monitoring. *Remote Sensing*, 6(7):6163–6182, 2014.
- [42] Martin Whittle, Shaun Quegan, Yumiko Uryu, Michael Stüewe, and Kokok Yulianto. Detection of tropical deforestation using ALOS-PALSAR: A Sumatran case study. *Remote Sensing of Environment*, 124:83–98, 2012.
- [43] Maurizio Santoro and Urs Wegmüller. Multi-temporal SAR metrics applied to map water bodies. In *2012 IEEE International Geoscience and Remote Sensing Symposium*, pages 5230–5233. IEEE, 2012.
- [44] David Marzi and Paolo Gamba. Inland Water Body Mapping Using Multitemporal Sentinel-1 SAR Data. *IEEE Journal of Selected Topics in Applied Earth Observations and Remote Sensing*, 14:11789–11799, 2021.
- [45] Gianni Lisini, Andreas Salentinig, Peijun Du, and Paolo Gamba. SAR-based urban extents extraction: from ENVISAT to Sentinel-1. *IEEE Journal of Selected Topics in Applied Earth Observations and Remote Sensing*, 11(8):2683–2691, 2017.
- [46] Wenjin Wu, Huadong Guo, Xinwu Li, Laurent Ferro-Famil, and Lu Zhang. Urban land use information extraction using the ultrahigh-resolution Chinese airborne SAR imagery. *IEEE Transactions on Geoscience and Remote Sensing*, 53(10): 5583–5599, 2015.
- [47] Damian Bargiel and Sylvia Herrmann. Multi-temporal land-cover classification of agricultural areas in two European regions with high resolution spotlight TerraSAR-X data. *Remote sensing*, 3(5):859–877, 2011.

- [48] Alexandre Bouvet and Thuy Le Toan. Use of ENVISAT/ASAR wide-swath data for timely rice fields mapping in the Mekong River Delta. *Remote Sensing of Environment*, 115(4):1090–1101, 2011.
- [49] David Marzi and Fabio Dell’Acqua. Mapping European Rice Paddy Fields Using Yearly Sequences of Spaceborne Radar Reflectivity: A Case Study in Italy. *Earth*, 2(3):387–404, 2021.
- [50] Zhipeng Tang, Giuseppe Amatulli, Petri KE Pellikka, and Janne Heiskanen. Spectral Temporal Information for Missing Data Reconstruction (STIMDR) of Landsat Reflectance Time Series. *Remote Sensing*, 14(1):172, 2021.
- [51] Patrick Griffiths, Tobias Kuemmerle, Matthias Baumann, Volker C Radeloff, Ioan V Abrudan, Juraj Lieskovsky, Catalina Munteanu, Katarzyna Ostapowicz, and Patrick Hostert. Forest disturbances, forest recovery, and changes in forest types across the Carpathian ecoregion from 1985 to 2010 based on Landsat image composites. *Remote Sensing of Environment*, 151:72–88, 2014.
- [52] Mirela G Tulbure and Mark Broich. Spatiotemporal dynamic of surface water bodies using Landsat time-series data from 1999 to 2011. *ISPRS Journal of Photogrammetry and Remote Sensing*, 79:44–52, 2013.
- [53] He Yin, Dirk Pflugmacher, Robert E Kennedy, Damien Sulla-Menashe, and Patrick Hostert. Mapping annual land use and land cover changes using MODIS time series. *IEEE Journal of selected topics in applied earth observations and remote sensing*, 7(8):3421–3427, 2014.
- [54] Sandro Martinis, Simon Plank, and Kamila Ćwik. The use of Sentinel-1 time-series data to improve flood monitoring in arid areas. *Remote Sensing*, 10(4):583, 2018.
- [55] Davoud Ashourloo, Hamed Nematollahi, Alfredo Huete, Hossein Aghighi, Mohsen Azadbakht, Hamid Salehi Shahrabi, and Salman Goodarzdashti. A new phenology-based method for mapping wheat and barley using time-series of Sentinel-2 images. *Remote Sensing of Environment*, 280:113206, 2022.
- [56] Cristina Gómez, Joanne C White, Michael A Wulder, and Pablo Alejandro. Historical forest biomass dynamics modelled with Landsat spectral trajectories. *ISPRS Journal of Photogrammetry and Remote Sensing*, 93:14–28, 2014.
- [57] Mark Broich, Matthew C Hansen, Peter Potapov, Bernard Adusei, Erik Lindquist, and Stephen V Stehman. Time-series analysis of multi-resolution optical imagery for quantifying forest cover loss in Sumatra and Kalimantan, Indonesia. *International Journal of Applied Earth Observation and Geoinformation*, 13(2):277–291, 2011.
- [58] Steven E Franklin, Oumer S Ahmed, Michael A Wulder, Joanne C White, Txomin Hermosilla, and Nicholas C Coops. Large area mapping of annual land cover dynamics using multitemporal change detection and classification of Landsat time series data. *Canadian Journal of Remote Sensing*, 41(4):293–314, 2015.
- [59] João Andrade, John Cunha, João Silva, Iana Rufino, and Carlos Galvão. Evaluating single and multi-date Landsat classifications of land-cover in a seasonally dry tropical forest. *Remote Sensing Applications: Society and Environment*, 22: 100515, 2021.

- [60] Mailys Lopes, Pierre-Louis Frison, Sarah M Durant, Henrike Schulte to Bühne, Audrey Ipavec, Vincent Lapeyre, and Nathalie Pettorelli. Combining optical and radar satellite image time series to map natural vegetation: savannas as an example. *Remote Sensing in Ecology and Conservation*, 6(3):316–326, 2020.
- [61] Flávia de Souza Mendes, Daniel Baron, Gerhard Gerold, Veraldo Liesenberg, and Stefan Erasmi. Optical and SAR remote sensing synergism for mapping vegetation types in the endangered Cerrado/Amazon ecotone of Nova Mutum—Mato Grosso. *Remote Sensing*, 11(10):1161, 2019.
- [62] Manuela Hirschmugl, Carina Sobe, Janik Deutscher, and Mathias Schardt. Combined use of optical and synthetic aperture radar data for REDD+ applications in Malawi. *Land*, 7(4):116, 2018.
- [63] Maxence Dodin, Hunter D Smith, Florent Levavasseur, Dalila Hadjar, Sabine Houot, and Emmanuelle Vaudour. Potential of Sentinel-2 Satellite Images for Monitoring Green Waste Compost and Manure Amendments in Temperate Cropland. *Remote Sensing*, 13(9):1616, 2021.
- [64] Xavier Blaes, Guillaume Chomé, Marie-Julie Lambert, Pierre Sibiry Traoré, Antonius GT Schut, and Pierre Defourny. Quantifying fertilizer application response variability with VHR satellite NDVI time series in a rainfed smallholder cropping system of Mali. *Remote sensing*, 8(6):531, 2016.
- [65] Ana Navarro, Inês Silva, João Catalão, and João Falcão. An operational Sentinel-2 based monitoring system for the management and control of direct aids to the farmers in the context of the Common Agricultural Policy (CAP): A case study in mainland Portugal. *International Journal of Applied Earth Observation and Geoinformation*, 103:102469, 2021.
- [66] Marion Pause, Filip Raasch, Christopher Marrs, and Elmar Csaplovics. Monitoring glyphosate-based herbicide treatment using Sentinel-2 time series—a proof-of-principle. *Remote Sensing*, 11(21):2541, 2019.
- [67] Mehrez Zribi, Nicolas Baghdadi, and Christine Guérin. Analysis of surface roughness heterogeneity and scattering behavior for radar measurements. *IEEE transactions on geoscience and remote sensing*, 44(9):2438–2444, 2006.
- [68] Pei Zhan, Wenquan Zhu, and Nan Li. An automated rice mapping method based on flooding signals in synthetic aperture radar time series. *Remote Sensing of Environment*, 252:112112, 2021.
- [69] Olena Kavats, Dmitriy Khramov, Kateryna Sergieieva, and Volodymyr Vasyliiev. Monitoring harvesting by time series of Sentinel-1 SAR data. *Remote Sensing*, 11(21):2496, 2019.
- [70] Pavan Kumar Sharma, Pratyush Kumar, Hari Shanker Srivastava, and Thota Sivasankar. Assessing the potentials of multi-temporal sentinel-1 SAR data for paddy yield forecasting using artificial neural network. *Journal of the Indian Society of Remote Sensing*, 50(5):895–907, 2022.
- [71] Hoa Phan, Thuy Le Toan, Alexandre Bouvet, Lam Dao Nguyen, Tien Pham Duy, and Mehrez Zribi. Mapping of rice varieties and sowing date using X-band SAR data. *Sensors*, 18(1):316, 2018.

- [72] Mariana Belgiu and Lucian Drăguț. Random forest in remote sensing: A review of applications and future directions. *ISPRS journal of photogrammetry and remote sensing*, 114:24–31, 2016.
- [73] Cristina Gómez, Joanne C White, and Michael A Wulder. Optical remotely sensed time series data for land cover classification: A review. *ISPRS Journal of Photogrammetry and Remote Sensing*, 116:55–72, 2016.
- [74] Reza Khatami, Giorgos Mountrakis, and Stephen V Stehman. A meta-analysis of remote sensing research on supervised pixel-based land-cover image classification processes: General guidelines for practitioners and future research. *Remote Sensing of Environment*, 177:89–100, 2016.
- [75] Aaron E Maxwell, Timothy A Warner, and Fang Fang. Implementation of machine-learning classification in remote sensing: An applied review. *International Journal of Remote Sensing*, 39(9):2784–2817, 2018.
- [76] Prem Chandra Pandey, Nikos Koutsias, George P Petropoulos, Prashant K Srivastava, and Eyal Ben Dor. Land use/land cover in view of earth observation: data sources, input dimensions, and classifiers—a review of the state of the art. *Geocarto International*, 36(9):957–988, 2021.
- [77] Yong-Suk Lee, Sunmin Lee, and Hyung-Sup Jung. Mapping forest vertical structure in Gong-ju, Korea using Sentinel-2 satellite images and artificial neural networks. *Applied Sciences*, 10(5):1666, 2020.
- [78] Mahmoud Allam, Tarek Mahmoud, Ahmed Elsharkawy, and Bassem Sheta. Land Cover Mapping using Adaptive Decision Tree Algorithm for WorldView-2 High-Resolution Images. In *2021 International Telecommunications Conference (ITC-Egypt)*, pages 1–5. IEEE, 2021.
- [79] Julien Radoux, Céline Lamarche, Eric Van Bogaert, Sophie Bontemps, Carsten Brockmann, and Pierre Defourny. Automated training sample extraction for global land cover mapping. *Remote Sensing*, 6(5):3965–3987, 2014.
- [80] Michel ED Chaves, Michelle CA Picoli, and Ieda D Sanches. Recent applications of Landsat 8/OLI and Sentinel-2/MSI for land use and land cover mapping: A systematic review. *Remote Sensing*, 12(18):3062, 2020.
- [81] John W Rouse Jr, R Hect Haas, JA Schell, and DW Deering. Monitoring the vernal advancement and retrogradation (green wave effect) of natural vegetation, 1973.
- [82] Alfredo R Huete. A soil-adjusted vegetation index (SAVI). *Remote sensing of environment*, 25(3):295–309, 1988.
- [83] Alfredo Huete, Kamel Didan, Tomoaki Miura, E Patricia Rodriguez, Xiang Gao, and Laerte G Ferreira. Overview of the radiometric and biophysical performance of the MODIS vegetation indices. *Remote sensing of environment*, 83(1-2):195–213, 2002.
- [84] Stuart K McFeeters. The use of the Normalized Difference Water Index (NDWI) in the delineation of open water features. *International journal of remote sensing*, 17(7):1425–1432, 1996.

- [85] Luis Carrasco, Aneurin W O’Neil, R Daniel Morton, and Clare S Rowland. Evaluating combinations of temporally aggregated Sentinel-1, Sentinel-2 and Landsat 8 for land cover mapping with Google Earth Engine. *Remote Sensing*, 11(3):288, 2019.
- [86] Gerald Forkuor, Kangbeni Dimobe, Idriss Serme, and Jerome Ebagnerin Tondoh. Landsat-8 vs. Sentinel-2: examining the added value of sentinel-2’s red-edge bands to land-use and land-cover mapping in Burkina Faso. *GIScience & remote sensing*, 55(3):331–354, 2018.
- [87] Shangrong Lin, Jing Li, Qinhuo Liu, Longhui Li, Jing Zhao, and Wentao Yu. Evaluating the effectiveness of using vegetation indices based on red-edge reflectance from Sentinel-2 to estimate gross primary productivity. *Remote Sensing*, 11(11):1303, 2019.
- [88] Benjamin Jakimow, Patrick Griffiths, Sebastian van der Linden, and Patrick Hostert. Mapping pasture management in the Brazilian Amazon from dense Landsat time series. *Remote Sensing of Environment*, 205:453–468, 2018.
- [89] Paria Ettehadi Osgouei, Sinasi Kaya, Elif Sertel, and Ugur Alganci. Separating built-up areas from bare land in mediterranean cities using Sentinel-2A imagery. *Remote Sensing*, 11(3):345, 2019.
- [90] S Baeza, E Vélez-Martin, D De Abelleira, S Bancho, F Gallego, J Schirmbeck, S Veron, M Vallejos, E Weber, M Oyarzabal, et al. Two decades of land cover mapping in the Río de la Plata grassland region: The MapBiomass Pampa initiative. *Remote Sensing Applications: Society and Environment*, page 100834, 2022.
- [91] Luong Viet Nguyen, Ryutaro Tateishi, Hoan Thanh Nguyen, Ram C Sharma, Tu Trong To, and Son Mai Le. Estimation of tropical forest structural characteristics using ALOS-2 SAR data. *Advances in Remote Sensing*, 5(2):131–144, 2016.
- [92] Gaia Vaglio Laurin, Johannes Balling, Piermaria Corona, Walter Mattioli, Dario Papale, Nicola Puletti, Maria Rizzo, John Truckenbrodt, and Marcel Urban. Above-ground biomass prediction by Sentinel-1 multitemporal data in central Italy with integration of ALOS2 and Sentinel-2 data. *Journal of Applied Remote Sensing*, 12(1):016008, 2018.
- [93] Zhuli Xie, Yaoliang Chen, Dengsheng Lu, Guiying Li, and Erxue Chen. Classification of land cover, forest, and tree species classes with ZiYuan-3 multispectral and stereo data. *Remote Sensing*, 11(2):164, 2019.
- [94] Lu Zhang, Xiangxing Wan, and Bing Sun. Tropical natural forest classification using time-series Sentinel-1 and Landsat-8 images in Hainan Island. In *IGARSS 2019-2019 IEEE International Geoscience and Remote Sensing Symposium*, pages 6732–6735. IEEE, 2019.
- [95] Marius Rüetschi, Michael E Schaepman, and David Small. Using multitemporal sentinel-1 c-band backscatter to monitor phenology and classify deciduous and coniferous forests in northern switzerland. *Remote Sensing*, 10(1):55, 2017.
- [96] AO Varghese and AK Joshi. Polarimetric classification of C-band SAR data for forest density characterization. *Current Science*, pages 100–106, 2015.

- [97] David Small. Flattening gamma: Radiometric terrain correction for SAR imagery. *IEEE Transactions on Geoscience and Remote Sensing*, 49(8):3081–3093, 2011.
- [98] David Small. SAR backscatter multitemporal compositing via local resolution weighting. In *2012 IEEE International Geoscience and Remote Sensing Symposium*, pages 4521–4524. IEEE, 2012.
- [99] Kristof Van Tricht, Anne Gobin, Sven Gilliams, and Isabelle Piccard. Synergistic use of radar Sentinel-1 and optical Sentinel-2 imagery for crop mapping: A case study for Belgium. *Remote Sensing*, 10(10):1642, 2018.
- [100] DL Swets, BC Reed, JR Rowland, and SE Marko. A weighted least-squares approach to temporal smoothing of NDVI 1999 ASPRS Annual Conference, From Image to Information, Portland, Oregon, May 17–21, 1999. *Proceedings: Bethesda, Maryland, American Society for Photogrammetry and Remote Sensing, CD-ROM*, 1, 1999.
- [101] Arsalan Ghorbanian, Mohammad Kakooei, Meisam Amani, Sahel Mahdavi, Ali Mohammadzadeh, and Mahdi Hasanlou. Improved land cover map of Iran using Sentinel imagery within Google Earth Engine and a novel automatic workflow for land cover classification using migrated training samples. *ISPRS Journal of Photogrammetry and Remote Sensing*, 167:276–288, 2020.
- [102] Meisam Amani, Bahram Salehi, Sahel Mahdavi, Jean Elizabeth Granger, Brian Brisco, and Alan Hanson. Wetland classification using multi-source and multi-temporal optical remote sensing data in Newfoundland and Labrador, Canada. *Canadian Journal of Remote Sensing*, 43(4):360–373, 2017.
- [103] Alexander W Jacob, Fernando Vicente-Guijalba, Carlos Lopez-Martinez, Juan M Lopez-Sanchez, Marius Litzinger, Harald Kristen, Alejandro Mestre-Quereda, Dariusz Ziólkowski, Marco Lavalle, Claudia Notarnicola, et al. Sentinel-1 InSAR coherence for land cover mapping: A comparison of multiple feature-based classifiers. *IEEE Journal of Selected Topics in Applied Earth Observations and Remote Sensing*, 13:535–552, 2020.
- [104] Khanh Duc Ngo, Alex M Lechner, and Tuong Thuy Vu. Land cover mapping of the Mekong Delta to support natural resource management with multi-temporal Sentinel-1A synthetic aperture radar imagery. *Remote Sensing Applications: Society and Environment*, 17:100272, 2020.
- [105] Robert M Haralick, Karthikeyan Shanmugam, and Its’ Hak Dinstein. Textural features for image classification. *IEEE Transactions on systems, man, and cybernetics*, (Vol. not available)(6):610–621, 1973.
- [106] Hanqiu Xu. Modification of normalised difference water index (NDWI) to enhance open water features in remotely sensed imagery. *International journal of remote sensing*, 27(14):3025–3033, 2006.
- [107] Gudina L Feyisa, Henrik Meilby, Rasmus Fensholt, and Simon R Proud. Automated Water Extraction Index: A new technique for surface water mapping using Landsat imagery. *Remote Sensing of Environment*, 140:23–35, 2014.
- [108] Lian Feng, Chuanmin Hu, Xiaoling Chen, Xiaobin Cai, Liqiao Tian, and Wenxia Gan. Assessment of inundation changes of Poyang Lake using MODIS observations between 2000 and 2010. *Remote Sensing of Environment*, 121:80–92, 2012.

- [109] Ian Olthof. Mapping seasonal inundation frequency (1985–2016) along the St-John River, New Brunswick, Canada using the Landsat archive. *Remote Sensing*, 9(2):143, 2017.
- [110] Abbas Mohammadi, Justin Francis Costelloe, and Dongryeol Ryu. Application of time series of remotely sensed normalized difference water, vegetation and moisture indices in characterizing flood dynamics of large-scale arid zone floodplains. *Remote sensing of environment*, 190:70–82, 2017.
- [111] George H Allen and Tamlin M Pavelsky. Patterns of river width and surface area revealed by the satellite-derived North American River Width data set. *Geophysical Research Letters*, 42(2):395–402, 2015.
- [112] Mirela G Tulbure, Mark Broich, Stephen V Stehman, and Anil Kommareddy. Surface water extent dynamics from three decades of seasonally continuous Landsat time series at subcontinental scale in a semi-arid region. *Remote Sensing of Environment*, 178:142–157, 2016.
- [113] Mateo Gašparović and Tomislav Jogun. The effect of fusing Sentinel-2 bands on land-cover classification. *International journal of remote sensing*, 39(3):822–841, 2018.
- [114] Marjolein FA Vogels, Steven M De Jong, Geert Sterk, Harke Douma, and Elisabeth A Addink. Spatio-temporal patterns of smallholder irrigated agriculture in the horn of Africa using GEOBIA and Sentinel-2 imagery. *Remote Sensing*, 11(2):143, 2019.
- [115] Xiucheng Yang and Li Chen. Evaluation of automated urban surface water extraction from Sentinel-2A imagery using different water indices. *Journal of Applied Remote Sensing*, 11(2):026016, 2017.
- [116] Wei Jiang, Yuan Ni, Zhiguo Pang, Xiaotao Li, Hongrun Ju, Guojin He, Juan Lv, Kun Yang, June Fu, and Xiangdong Qin. An effective water body extraction method with new water index for sentinel-2 imagery. *Water*, 13(12):1647, 2021.
- [117] Esther O Makinde and Oluwaseun E Oyelade. Land cover mapping using sentinel-1 SAR satellite imagery of Lagos state for 2017. *Elsevier Proceedings*, 2(22):1399, 2018.
- [118] Md Rejaur Rahman and Praveen K Thakur. Detecting, mapping and analysing of flood water propagation using synthetic aperture radar (SAR) satellite data and GIS: A case study from the Kendrapara District of Orissa State of India. *The Egyptian Journal of Remote Sensing and Space Science*, 21:S37–S41, 2018.
- [119] Emanuele Ferrentino, Ferdinando Nunziata, Andrea Buono, Angelo Urciuoli, and Maurizio Migliaccio. Multipolarization time series of sentinel-1 SAR imagery to analyze variations of reservoirs’ water body. *IEEE Journal of Selected Topics in Applied Earth Observations and Remote Sensing*, 13:840–846, 2020.
- [120] Michael Schmitt. Potential of large-scale inland water body mapping from sentinel-1/2 data on the example of Bavaria’s lakes and rivers. *PFG–Journal of Photogrammetry, Remote Sensing and Geoinformation Science*, 88(3):271–289, 2020.

- [121] András Gulácsi and Ferenc Kovács. Sentinel-1-imagery-based high-resolution water cover detection on wetlands, Aided by Google Earth Engine. *Remote Sensing*, 12(10):1614, 2020.
- [122] Amir Behnamian, Sarah Banks, Lori White, Brian Brisco, Koreen Millard, Jon Pasher, Zhaohua Chen, Jason Duffe, Laura Bourgeau-Chavez, and Michael Battaglia. Semi-automated surface water detection with synthetic aperture radar data: A wetland case study. *Remote Sensing*, 9(12):1209, 2017.
- [123] Jose-Luis Bueso-Bello, Michele Martone, Carolina González, Francescopaolo Sica, Paolo Valdo, Philipp Posovszky, Andrea Pulella, and Paola Rizzoli. The global water body layer from TanDEM-X interferometric SAR data. *Remote Sensing*, 13(24):5069, 2021.
- [124] Richard Bamler and Philipp Hartl. Synthetic aperture radar interferometry. *Inverse problems*, 14(4):R1, 1998.
- [125] Hailong Tang, Shanlong Lu, Muhammad Hasan Ali Baig, Mingyang Li, Chun Fang, and Yong Wang. Large-Scale Surface Water Mapping Based on Landsat and Sentinel-1 Images. *Water*, 14(9):1454, 2022.
- [126] Silvia Valero, David Morin, Jordi Inglada, Guadalupe Sepulcre, Marcela Arias, Olivier Hagolle, Gérard Dedieu, Sophie Bontemps, Pierre Defourny, and Benjamin Koetz. Production of a dynamic cropland mask by processing remote sensing image series at high temporal and spatial resolutions. *Remote Sensing*, 8(1):55, 2016.
- [127] Kersten Clauss, Marco Ottinger, and Claudia Künzer. Mapping rice areas with Sentinel-1 time series and superpixel segmentation. *International journal of remote sensing*, 39(5):1399–1420, 2018.
- [128] David Marzi and Paolo Gamba. Global Vegetation Mapping for ESA Climate Change Initiative Project Leveraging Multitemporal High Resolution Sentinel-1 SAR Data. In *IGARSS 2020-2020 IEEE International Geoscience and Remote Sensing Symposium*, pages 4791–4794. IEEE, 2020.
- [129] David Marzi, Shantanu Todmal, and Paolo Gamba. Mapping Globally Using Multitemporal Sentinel-1 SAR: A Semiautomatic Approach. In *2021 IEEE International India Geoscience and Remote Sensing Symposium (InGARSS)*, pages 74–77. IEEE, 2021.
- [130] Antonietta Sorriso, David Marzi, and Paolo Gamba. A General Land Cover Classification Framework for Sentinel-1 SAR Data. In *2021 IEEE 6th International Forum on Research and Technology for Society and Industry (RTSI)*, pages 211–216. IEEE, 2021.
- [131] European Space Agency (ESA). *Copernicus Sentinel data 2020*. Retrieved from the *Copernicus Open Access Hub*, 2020. URL <https://scihub.copernicus.eu/>.
- [132] Noel Gorelick, Matt Hancher, Mike Dixon, Simon Ilyushchenko, David Thau, and Rebecca Moore. Google Earth Engine: Planetary-scale geospatial analysis for everyone. *Remote Sensing of Environment*, 2017. doi: 10.1016/j.rse.2017.06.031. URL <https://doi.org/10.1016/j.rse.2017.06.031>.

- [133] Tongdi He and Shengxin Wang. Multi-spectral remote sensing land-cover classification based on deep learning methods. *The Journal of Supercomputing*, pages 1–15, 2020.
- [134] Claudia Paris, Lorenzo Bruzzone, and Diego Fernández-Prieto. A novel approach to the unsupervised update of land-cover maps by classification of time series of multispectral images. *IEEE Transactions on Geoscience and Remote Sensing*, 57(7):4259–4277, 2019.
- [135] Yousra Hamrouni, Eric Paillassa, Véronique Chéret, Claude Monteil, and David Sheeren. From local to global: A transfer learning-based approach for mapping poplar plantations at national scale using Sentinel-2. *ISPRS Journal of Photogrammetry and Remote Sensing*, 171:76–100, 2021.
- [136] European Space Agency (ESA). *ESA GlobCover Project*, 2018 (accessed November 12, 2020). URL http://due.esrin.esa.int/page_globcover.php.
- [137] Marcel Buchhorn, Myroslava Lesiv, Nandin-Erdene Tsendbazar, Martin Herold, Luc Bertels, and Bruno Smets. Copernicus global land cover layers—collection 2. *Remote Sensing*, 12(6):1044, 2020.
- [138] Thomas Esch, Felix Bachofer, Wieke Heldens, Andreas Hirner, Mattia Marconcini, Daniela Palacios-Lopez, Achim Roth, Soner Üreyen, Julian Zeidler, Stefan Dech, et al. Where we live—A summary of the achievements and planned evolution of the global urban footprint. *Remote Sensing*, 10(6):895, 2018.
- [139] European Space Agency (ESA). *Sentinel-2 Data Products*, 2020 (accessed September 22, 2020). URL <https://sentinel.esa.int/web/sentinel/missions/sentinel-2/data-products>.
- [140] Andreas Vollrath, Adugna Mullissa, and Johannes Reiche. Angular-based radiometric slope correction for Sentinel-1 on google earth engine. *Remote Sensing*, 12(11):1867, 2020.
- [141] Weiying Zhao, Charles-Alban Deledalle, Loïc Denis, Henri Maître, Jean-Marie Nicolas, and Florence Tupin. Ratio-based multitemporal SAR images denoising: RA-BASAR. *IEEE Transactions on Geoscience and Remote Sensing*, 57(6):3552–3565, 2019.
- [142] Viktoriya Tsyganskaya, Sandro Martinis, Philip Marzahn, and Ralf Ludwig. SAR-based detection of flooded vegetation—a review of characteristics and approaches. *International journal of remote sensing*, 39(8):2255–2293, 2018.
- [143] Aiyeola Sikiru Yommy, Rongke Liu, and Shuang Wu. SAR image despeckling using refined Lee filter. In *2015 7th International Conference on Intelligent Human-Machine Systems and Cybernetics*, volume 2, pages 260–265. IEEE, 2015.
- [144] Saygin Abdikan, Fusun Balik Sanli, M Ustuner, and Fabiana Calò. Land cover mapping using sentinel-1 SAR data. In *The International Archives of the Photogrammetry, Remote Sensing and Spatial Information Sciences, Volume XLI-B7, 2016 XXIII ISPRS Congress*, 2014.
- [145] Saeed Khabbazan, Paul Vermunt, Susan Steele-Dunne, Lexy Ratering Arntz, Caterina Marinetti, Dirk van der Valk, Lorenzo Iannini, Ramses Molijn, Kees Westerdijk, and Corné van der Sande. Crop monitoring using Sentinel-1 data: a case study from The Netherlands. *Remote Sensing*, 11(16):1887, 2019.

- [146] Mateo Gašparović and Dino Dobrinić. Comparative assessment of machine learning methods for urban vegetation mapping using multitemporal sentinel-1 imagery. *Remote Sensing*, 12(12):1952, 2020.
- [147] Paolo Ferrazzoli and Leila Guerriero. Radar sensitivity to tree geometry and woody volume: A model analysis. *IEEE Transactions on Geoscience and Remote Sensing*, 33(2):360–371, 1995.
- [148] Eibe Frank, Mark Hall, Geoffrey Holmes, Richard Kirkby, Bernhard Pfahringer, Ian H Witten, and Len Trigg. Weka—a machine learning workbench for data mining. In *Data mining and knowledge discovery handbook*, pages 1269–1277. Springer, 2009.
- [149] J Richard Landis and Gary G Koch. The measurement of observer agreement for categorical data. *biometrics*, pages 159–174, 1977.
- [150] David Marzi and Paolo Gamba. Wide-scale water bodies mapping using multi-temporal sentinel-1 sar data. In *2021 IEEE International Geoscience and Remote Sensing Symposium IGARSS*, pages 6032–6035. IEEE, 2021.
- [151] Julie Transon, Raphaël d’Andrimont, Alexandre Maignard, and Pierre Defourny. Survey of hyperspectral earth observation applications from space in the sentinel-2 context. *Remote Sensing*, 10(2):157, 2018.
- [152] *Water and Wetness — Copernicus Land Monitoring Service*, 2018 (accessed August 31, 2022). URL <https://land.copernicus.eu/pan-european/high-resolution-layers/water-wetness>.
- [153] John W Jones. Improved automated detection of subpixel-scale inundation—Revised dynamic surface water extent (DSWE) partial surface water tests. *Remote Sensing*, 11(4):374, 2019.
- [154] Igor Klein, Ursula Gessner, Andreas J Dietz, and Claudia Kuenzer. Global WaterPack—A 250 m resolution dataset revealing the daily dynamics of global inland water bodies. *Remote sensing of environment*, 198:345–362, 2017.
- [155] Townshend, J. (2016). *Global Forest Cover Change (GFCC) Water Cover 2000 Global 30 m V001 [Data set]*, NASA EOSDIS Land Processes DAAC. Accessed 2021-06-03 from <https://doi.org/10.5067/MEASURES/GFCC/GFCC30WC.001>.
- [156] ESA. *Land Cover CCI Product User Guide Version 2. Tech. Rep.*, 017 (accessed August 31, 2022). URL maps.elie.ucl.ac.be/CCI/viewer/download/ESACCI-LC-Ph2-PUGv2_2.0.pdf.
- [157] Kabir Uddin, Mir A Matin, and Franz J Meyer. Operational flood mapping using multi-temporal sentinel-1 SAR images: a case study from Bangladesh. *Remote Sensing*, 11(13):1581, 2019.
- [158] Pål Wessel and Walter HF Smith. A global, self-consistent, hierarchical, high-resolution shoreline database. *Journal of Geophysical Research: Solid Earth*, 101 (B4):8741–8743, 1996.

- [159] Junichi Takaku, Takeo Tadono, Masanori Doutsu, Fumi Ohgushi, and Hiroki Kai. Updates of ‘AW3D30’ALOS Global Digital Surface Model with Other Open Access Datasets. *The International Archives of Photogrammetry, Remote Sensing and Spatial Information Sciences*, 43:183–189, 2020.
- [160] Regione Lombardia. *Dusaf 6.0 - Uso del suolo 2018*, 2020 (accessed August 31, 2022). URL <https://www.dati.lombardia.it/Territorio/Dusaf-6-0-Uso-del-suolo-2018/7rae-fng6>.
- [161] Copernicus. *CORINE Land Cover*, 2018 (accessed June 14, 2021). URL <https://land.copernicus.eu/pan-european/corine-land-cover>.
- [162] Christian Tottrup, Daniel Druce, Rasmus Probst Meyer, Mads Christensen, Michael Riffler, Bjoern Dulleck, Philipp Rastner, Katerina Jupova, Tomas Sokoup, Arjen Haag, et al. Surface Water Dynamics from Space: A Round Robin Inter-comparison of Using Optical and SAR High-Resolution Satellite Observations for Regional Surface Water Detection. *Remote Sensing*, 14(10):2410, 2022.
- [163] Planet Labs. *Planet Imagery and Archive*, (accessed August 31, 2022). URL <https://www.planet.com/products/planet-imagery/>.
- [164] Guolin Ke, Qi Meng, Thomas Finley, Taifeng Wang, Wei Chen, Weidong Ma, Qiwei Ye, and Tie-Yan Liu. Lightgbm: A highly efficient gradient boosting decision tree. *Advances in neural information processing systems*, 30, 2017.
- [165] Liping Cai, Wenzhong Shi, Zelang Miao, and Ming Hao. Accuracy assessment measures for object extraction from remote sensing images. *Remote Sensing*, 10(2):303, 2018.
- [166] David Marzi and Fabio Dell’Acqua. An experiment on extended, satellite-based traceability of organic crops in north-western italy. In *IGARSS 2022-2022 IEEE International Geoscience and Remote Sensing Symposium*, pages 4650–4653. IEEE, 2022.
- [167] David Marzi, Cristian Garau, and Fabio Dell’Acqua. Identification of rice fields in the lombardy region of italy based on time series of sentinel-1 data. In *2021 IEEE International Geoscience and Remote Sensing Symposium IGARSS*, pages 1073–1076. IEEE, 2021.
- [168] D Marzi and F Dell’Acqua. Space-based monitoring of organic rice: The ESA KSA project “Vialone” contributes to supporting an Italian high-tier product. In *Proceedings of the GTTI Radar and Remote Sensing Workshop*, 2019.
- [169] Joséphine Peigné, Marion Casagrande, Vincent Payet, Christophe David, F. Xavier Sans, José M. Blanco-Moreno, Julia Cooper, Kate Gascoyne, Daniele Antichi, Paolo Bàrberi, and et al. How organic farmers practice conservation agriculture in Europe. *Renewable Agriculture and Food Systems*, 31(1):72–85, 2016. doi: 10.1017/S1742170514000477.
- [170] Zeynab Jouzi, Hossein Azadi, Fatemeh Taheri, Kiumars Zarafshani, Kindeya Gebrehiwot, Steven Van Passel, and Philippe Lebailly. Organic farming and small-scale farmers: Main opportunities and challenges. *Ecological Economics*, 132:144–154, 2017.

- [171] Jacopo Bacenetti, Alessandra Fusi, Marco Negri, Stefano Bocchi, and Marco Fiala. Organic production systems: Sustainability assessment of rice in Italy. *Agriculture, Ecosystems & Environment*, 225:33–44, 2016.
- [172] Verena Seufert, Navin Ramankutty, and Jonathan A. Foley. Comparing the yields of organic and conventional agriculture. *Nature*, 485(1):229–232, 2012. doi: <https://doi.org/10.1038/nature11069>.
- [173] Pietro Barbieri, Sylvain Pellerin, and Thomas Nesme. Comparing crop rotations between organic and conventional farming. *Scientific reports*, 7(1):1–10, 2017.
- [174] Andrii Shelestov, Mykola Lavreniuk, Nataliia Kussul, Alexei Novikov, and Sergii Skakun. Large scale crop classification using Google earth engine platform. In *2017 IEEE international geoscience and remote sensing symposium (IGARSS)*, pages 3696–3699. IEEE, 2017.
- [175] R Saini and SK Ghosh. Crop Classification on Single Date Sentinel-2 Imagery Using Random Forest and Support Vector Machine. *International Archives of the Photogrammetry, Remote Sensing & Spatial Information Sciences*, 2018.
- [176] XM Zhang, GJ He, ZM Zhang, Yan Peng, and TF Long. Spectral-spatial multi-feature classification of remote sensing big data based on a random forest classifier for land cover mapping. *Cluster Computing*, 20(3):2311–2321, 2017.
- [177] Colin Lewis-Beck, Zhengyuan Zhu, Anirban Mondal, Joon Jin Song, Jonathan Hobbs, Brian Hornbuckle, and Jason Patton. A Parametric Approach to Unmixing Remote Sensing Crop Growth Signatures. *Journal of Agricultural, Biological and Environmental Statistics*, 24(3):502–516, 2019.
- [178] Tri D Setiyono, Emma D Quicho, Luca Gatti, Manuel Campos-Taberner, Lorenzo Busetto, Francesco Collivignarelli, Francisco Javier García-Haro, Mirco Boschetti, Nasreen Islam Khan, and Francesco Holecz. Spatial rice yield estimation based on MODIS and Sentinel-1 SAR data and ORYZA crop growth model. *Remote Sensing*, 10(2):293, 2018.
- [179] N. Kussul, M. Lavreniuk, S. Skakun, and A. Shelestov. Deep Learning Classification of Land Cover and Crop Types Using Remote Sensing Data. *IEEE Geoscience and Remote Sensing Letters*, 14(5):778–782, 2017.
- [180] Khawar Jabran and Bhagirath S Chauhan. Overview and significance of non-chemical weed control. In *Non-chemical weed control*, pages 1–8. Elsevier, 2018.
- [181] Luigi Ranghetti, Lorenzo Busetto, Alberto Crema, Mauro Fasola, Elisa Cardarelli, and Mirco Boschetti. Testing estimation of water surface in Italian rice district from MODIS satellite data. *International Journal of Applied Earth Observation and Geoinformation*, 52:284–295, 2016. ISSN 0303-2434. doi: <https://doi.org/10.1016/j.jag.2016.06.018>. URL <https://www.sciencedirect.com/science/article/pii/S0303243416301015>.
- [182] Donato Amitrano, Gerardo Di Martino, Antonio Iodice, Daniele Riccio, and Giuseppe Ruello. Unsupervised rapid flood mapping using Sentinel-1 GRD SAR images. *IEEE Transactions on Geoscience and Remote Sensing*, 56(6):3290–3299, 2018.

- [183] Evan R DeLancey, Jahan Kariyeva, Jerome Cranston, and Brian Brisco. Monitoring hydro temporal variability in Alberta, Canada with multi-temporal Sentinel-1 SAR data. *Canadian Journal of Remote Sensing*, 44(1):1–10, 2018.
- [184] MA Clement, CG Kilsby, and P Moore. Multi-temporal synthetic aperture radar flood mapping using change detection. *Journal of Flood Risk Management*, 11(2): 152–168, 2018.
- [185] Amanda Veloso, Stéphane Mermoz, Alexandre Bouvet, Thuy Le Toan, Milena Planells, Jean-François Dejoux, and Eric Ceschia. Understanding the temporal behavior of crops using Sentinel-1 and Sentinel-2-like data for agricultural applications. *Remote sensing of environment*, 199:415–426, 2017.
- [186] Joel Segarra, Maria Luisa Buchailot, Jose Luis Araus, and Shawn C Kefauver. Remote sensing for precision agriculture: Sentinel-2 improved features and applications. *Agronomy*, 10(5):641, 2020.
- [187] Diofandos G Hadjimitsis, G Papadavid, A Agapiou, K Themistocleous, MG Hadjimitsis, A Retalis, S Michaelides, N Chrysoulakis, L Toullos, and CRI Clayton. Atmospheric correction for satellite remotely sensed data intended for agricultural applications: impact on vegetation indices. *Natural Hazards and Earth System Sciences*, 10(1):89–95, 2010.
- [188] Edi Sudianto, Song Beng-Kah, Neik Ting-Xiang, Nestor E. Saldain, Robert C. Scott, and Nilda R. Burgos. Clearfield rice: Its development, success, and key challenges on a global perspective. *Crop Protection*, 49:40–51, 2013. ISSN 0261-2194. doi: <https://doi.org/10.1016/j.cropro.2013.02.013>. URL <https://www.sciencedirect.com/science/article/pii/S0261219413000495>.
- [189] Hansjoerg Kraehmer, Cyrille Thomas, and Francesco Vidotto. Rice production in Europe. In *Rice production worldwide*, pages 93–116. Springer, 2017.
- [190] Francesca Orlando, Sumer Alali, Valentina Vaglia, Elena Pagliarino, Jacopo Bacchetti, Stefano Bocchi, et al. Participatory approach for developing knowledge on organic rice farming: Management strategies and productive performance. *Agricultural Systems*, 178:102739, 2020.
- [191] Fabio Dell’Acqua and Daniele De Vecchi. Potentials of Active and Passive Geospatial Crowdsourcing in Complementing Sentinel Data and Supporting Copernicus Service Portfolio. *Proceedings of the IEEE*, 105(10):1913–1925, 2017.
- [192] Adrian K Fung, Zongqian Li, and Kun-Shan Chen. Backscattering from a randomly rough dielectric surface. *IEEE Transactions on Geoscience and remote sensing*, 30(2):356–369, 1992.
- [193] Yisok Oh, Kamal Sarabandi, and Fawwaz T Ulaby. An empirical model and an inversion technique for radar scattering from bare soil surfaces. *IEEE transactions on Geoscience and Remote Sensing*, 30(2):370–381, 1992.
- [194] Pascale C Dubois, Jakob Van Zyl, and Ted Engman. Measuring soil moisture with imaging radars. *IEEE transactions on geoscience and remote sensing*, 33(4): 915–926, 1995.

- [195] Nicolas Baghdadi, Mohammad Choker, Mehrez Zribi, Mohammad El Hajj, Simonetta Paloscia, Niko EC Verhoest, Hans Lievens, Frederic Baup, and Francesco Mattia. A new empirical model for radar scattering from bare soil surfaces. *Remote Sensing*, 8(11):920, 2016.
- [196] Nicolas Baghdadi, Mehrez Zribi, Simonetta Paloscia, Niko EC Verhoest, Hans Lievens, Frederic Baup, and Francesco Mattia. Semi-empirical calibration of the integral equation model for co-polarized L-band backscattering. *Remote Sensing*, 7(10):13626–13640, 2015.
- [197] Mehrez Zribi and Monique Dechambre. A new empirical model to retrieve soil moisture and roughness from C-band radar data. *Remote Sensing of Environment*, 84(1):42–52, 2003.
- [198] Google Earth Engine. *Sentinel-1 Algorithms*, 2021 (accessed April 08, 2021). URL <https://developers.google.com/earth-engine/guides/sentinel1#metadata-and-filtering>.
- [199] Harry M Jol. *Ground penetrating radar theory and applications*. elsevier, 2008.
- [200] S Putiamini, F Marpaung, and D Fernando. Estimation of Peatland Distribution Using Ratio Dual-pol from Sentinel-1A. *IOP Conference Series: Earth and Environmental Science*, 280(1):012012, 2019.
- [201] Annabel Sharma. The wicked problem of diffuse nutrient pollution from agriculture. *Journal of Environmental Law*, 32(3):471–502, 2020.
- [202] John Tzilivakis, DJ Warner, Andrew Green, and KA Lewis. A broad-scale spatial analysis of the environmental benefits of fertiliser closed periods implemented under the Nitrates Directive in Europe. *Journal of Environmental Management*, 299:113674, 2021.
- [203] Francesco Gargiulo, CESARIO VINCENZO ANGELINO, Luca Cicala, Giuseppe Persechino, and Massimiliano Lega. Remote sensing in the fight against environmental crimes: The case study of the cattle-breeding facilities in Southern Italy. *International Journal of Sustainable Development and Planning*, 11(5):663–671, 2016.
- [204] Angela Errico, Cesario Vincenzo Angelino, Luca Cicala, Giuseppe Persechino, Claudia Ferrara, Massimiliano Lega, Andrea Vallario, Claudio Parente, Giuseppe Masi, Raffaele Gaetano, et al. Detection of environmental hazards through the feature-based fusion of optical and SAR data: A case study in southern Italy. *International Journal of Remote Sensing*, 36(13):3345–3367, 2015.
- [205] Ariolfo Camacho Velasco, César Augusto Vargas García, and Henry Arguello Fuentes. A comparative study of target detection algorithms in hyperspectral imagery applied to agricultural crops in Colombia. *Tecnura*, 20(49):86–99, 2016.
- [206] Xiaoying Jin, Scott Paswaters, and Harold Cline. A comparative study of target detection algorithms for hyperspectral imagery. In *Algorithms and Technologies for Multispectral, Hyperspectral, and Ultraspectral Imagery XV*, volume 7334, page 73341W. International Society for Optics and Photonics, 2009.

-
- [207] Chein-I Chang, JihMing Liu, BinChang Chieu, Hsuan Ren, Chuin-Mu Wang, ChienShun Lo, Pau-Choo Chung, Ching-Wen Yang, and DyeJyun Ma. Generalized constrained energy minimization approach to subpixel target detection for multispectral imagery. *Optical Engineering*, 39(5):1275–1281, 2000.
- [208] Dimitris Manolakis, Eric Truslow, Michael Pieper, Thomas Cooley, and Michael Brueggeman. Detection algorithms in hyperspectral imaging systems: An overview of practical algorithms. *IEEE Signal Processing Magazine*, 31(1):24–33, 2013.
- [209] Fred A Kruse, AB Lefkoff, JW Boardman, KB Heidebrecht, AT Shapiro, PJ Barloon, and AFH Goetz. The spectral image processing system (SIPS)—interactive visualization and analysis of imaging spectrometer data. *Remote sensing of environment*, 44(2-3):145–163, 1993.
- [210] D Marzi, A Sorriso, F Dell’Acqua, and P Gamba. Heterogeneous sar sequence processing for land cover mapping. In *IGARSS 2022-2022 IEEE International Geoscience and Remote Sensing Symposium*, pages 5172–5175. IEEE, 2022.